

**ELECTRICAL AND COMPUTER ENGINEERING  
DEPARTMENT**



**CLEMSON UNIVERSITY**

CLEMSON, SC 29634-0915

**AFOSR Grant #F49620-96-1-0005**

Entitled

**ELECTROMAGNETIC FIELDS AND CURRENTS  
ON CONDUCTING BODIES EXCITED BY  
MODULATED LASER LIGHT—PART 2**

Submitted by

Chalmers M. Butler, Anthony Q. Martin,  
A. Kustepeli and C. Ozzaim  
Department of Electrical and Computer Engineering  
Clemson University  
Clemson, SC 29634-0915

Submitted to

**AIR FORCE RESEARCH LABORATORY**

Through

Department of the Air Force  
Air Force Office of Scientific Research (AFOSR)  
110 Duncan Avenue, Suite B115  
Bolling Air Force Base, DC 20332-0001

1 March 1999



**20001127 028**

**DTIC QUALITY INSPECTED 4**

# REPORT DOCUMENTATION PAGE

AFRL-SR-BL-TR-00-

Public reporting burden for this collection of information is estimated to average 1 hour per response, including the time for reviewing the data needed, and completing and reviewing this collection of information. Send comments regarding this burden estimate or any other aspect of this collection of information, including suggestions for reducing this burden to Washington Headquarters Services, Directorate for Information Operations and Reports, 1215 Jefferson Davis Highway, Suite 1204, Arlington, VA 22202-4302, and to the Office of Management and Budget, Paperwork Reduction Project (0704-0188), Washington, DC 20503.

ing and  
on, including  
VA 22202-4302.

1. AGENCY USE ONLY (Leave blank)		2. REPORT DATE 25 March 1999		3. REPORT TYPE AND DATES COVERED Final Technical, 1 Dec. 1995 - 31 Dec. 1998	
4. TITLE AND SUBTITLE  Electromagnetic Fields and Currents on Conducting Bodies Excited by Modulated Laser Light - Parts 1 & 2				5. FUNDING NUMBERS AFOSR Grant F49620-96-1-0005	
6. AUTHOR(S) Chalmers M. Butler, Anthony Q. Martin, A. Kustepeli, and C. Ozzaim					
7. PERFORMING ORGANIZATION NAME(S) AND ADDRESS(ES) Department of Electrical and Computer Engineering 105 Riggs Hall Clemson University Clemson, SC 29634-0915				8. PERFORMING ORGANIZATION REPORT NUMBER	
9. SPONSORING / MONITORING AGENCY NAME(S) AND ADDRESS(ES) Air Force Office of Scientific Research 110 Duncan Avenue, Suite B115 Bolling Air Force Base, DC 20332-0001				10. SPONSORING / MONITORING AGENCY REPORT NUMBER	
11. SUPPLEMENTARY NOTES					
12a. DISTRIBUTION / AVAILABILITY STATEMENT				12b. DISTRIBUTION CODE	
13. ABSTRACT (Maximum 200 Words) A modulated laser beam incident upon a conducting surface can cause electrons to be emitted which in turn causes time harmonic electromagnetic fields. In this two-part report we describe an analysis of the electromagnetic interaction of modulated laser light and selected conducting structures. In Part 1 the interaction of laser-induced electromagnetic fields with conducting surfaces containing narrow slots is investigated. Integral equation methods have been developed to determine the electromagnetic response of such structures to the modulated laser light. Coupling to several slotted structures of interest is investigated. It has been found that for the laser-light excitation, scattering and penetration characteristics result that are markedly different from those expected for more traditional excitations. In Part 2, techniques are described that enable one to compute the voltage at a load impedance terminating a coaxial waveguide whose center conductor protrudes into an open-ended cylindrical tube. The finite-length tube may be empty or it may be partially filled with a dielectric insert. Also, the axial electric field at the focal point of a parabolic reflector is found. Computed results are supported by measurements.					
14. SUBJECT TERMS Electromagnetic coupling, integral equations, apertures, waveguides				15. NUMBER OF PAGES 340	
				16. PRICE CODE	
17. SECURITY CLASSIFICATION OF REPORT	18. SECURITY CLASSIFICATION OF THIS PAGE	19. SECURITY CLASSIFICATION OF ABSTRACT	20. LIMITATION OF ABSTRACT		

A Final Report for

**AFOSR Grant #F49620-96-1-0005**

Entitled

**ELECTROMAGNETIC FIELDS AND CURRENTS  
ON CONDUCTING BODIES EXCITED BY  
MODULATED LASER LIGHT — PART 2**

Submitted by

Chalmers M. Butler, Anthony Q. Martin,  
A. Kustepeli and C. Ozzaim  
Department of Electrical and Computer Engineering  
Clemson University  
Clemson, SC 29634-0915

Submitted to

**AIR FORCE RESEARCH LABORATORY**

through

Department of the Air Force  
Air Force Office of Scientific Research (AFOSR)  
110 Duncan Avenue, Suite B115  
Bolling Air Force Base, DC 20332-0001

25 March 1999

## PREFACE

When a properly modulated laser beam illuminates a conducting surface, it causes electrons to be emitted in such a way that the resulting electromagnetic radiation is closely approximated by that from a distribution of electric dipoles normal to the surface. The electromagnetic response of a conducting object to such an excitation is of interest to The Air Force Research Laboratory of the US Air Force. A major goal of this research has been to develop an understanding of the coupling of electromagnetic energy from the modulated laser to objects and to the medium surrounding the objects. This is part 2 of a final report in which specific attention is focused upon coupling of the laser-induced electromagnetic field to structures which exhibit some of the characteristics of symmetric antennas. A method is presented for computing the signal caused by a modulated laser beam at a load impedance terminating a coaxial waveguide whose center conductor protrudes into a thin-wall cylindrical tube. The tube is open at one end and, on the other, it has a planar bottom through which the coax center conductor protrudes. Two cases are treated: one in which the cavity is empty (free space) and a second in which it is partially filled with a dielectric insert. The excitation is the signal radiated by electrons "kicked off" the conducting surface by an impinging laser beam, modulated in such a way that the electrons at the surface oscillate harmonically in time. The computations are based on a procedure involving the formulation and numerical solution of integral equations plus utilization of the reciprocity theorem. A model was fabricated and experimental data were obtained to corroborate the results obtained from theory and numerical analysis. A similar analysis was conducted in the case of the common parabolic reflector antenna illuminated by the laser-induced dipoles, but no experiments were performed in this case.

## TABLE OF CONTENTS

	Page
Title Page .....	ii
Preface .....	iii
Table of Contents .....	iv
CHAPTER	
0. Introduction .....	1
1. Electric Field Integral Equation for Conducting Bodies of Revolution .....	6
1.1 Introduction .....	6
1.2 Formulation .....	7
1.3 Numerical Scheme .....	10
1.4 Singularity Analysis .....	14
1.5 Excitation .....	16
1.6 Imperfectly Conducting BOR .....	17
1.7 Corroboration .....	18
1.8 References .....	28
2. Magnetic Field Integral Equation for Conducting Bodies of Revolution .....	30
2.1 Formulation .....	30
2.2 Numerical Scheme .....	31
3. Analysis of Bodies Containing Conductors and Dielectrics .....	33
3.1 Introduction .....	33
3.2 A Single Homogeneous Dielectric body .....	37
3.3 Conductor Surrounded by a Dielectric .....	39
3.4 Disjoint Conductor and Dielectric .....	41
3.5 Conductor and Dielectric Intersecting .....	42
3.6 Numerical Solution .....	44
3.7 Results and Discussions .....	46
3.8 Observations .....	48
3.9 References .....	72
4. Coupling to a Probe in a Dielectric-Capped Metal Can by a Laser Induced Field .....	76
4.1 Introduction .....	76
4.2 The Reciprocity Approach .....	78

## Table of Contents (Continued)

	Page
5. Computation of the Near Field .....	85
5.1 Introduction .....	85
5.2 Normal Component of E-Field on the Coax-Fed BOR Antenna .....	85
5.3 Tangential Component of H-Field on the Coax-Fed BOR Antenna .....	88
5.4 Field Distribution .....	89
6. Experimental Apparatus and Measurement .....	93
6.1 Introduction .....	93
6.2 Construction of Can .....	94
6.3 Construction of the Monopole .....	95
6.4 Construction of Probes .....	95
6.5 Probing the Can Wall .....	99
6.6 Probing the Can Wall with Dielectric Loading .....	99
6.7 The Instrumentation and Measurement .....	101
7. Discussion of Results and Corroboration of Theory .....	103
8. Fields at the Focal Point of a Reflector due to Laser Light Induced Field .....	124
8.1 Introduction .....	124
8.2 The Reciprocity Approach .....	125
8.3 Numerical Results and Discussions .....	128
Supplementary References .....	143
Personnel Supported, Publications, and Interactions .....	144

## CHAPTER 0

### INTRODUCTION

This is part 2 of a final technical report of advancements accomplished under AFOSR Grant F49620-96-1-0005, covering the period December 1, 1995, through December 31, 1998. In this part of the report is described a method for computing, and an experimental procedure for verifying, the coupling of a signal, caused by a modulated laser beam, to a load impedance terminating a coaxial waveguide whose center conductor protrudes into a an open-ended cylindrical tube as suggested in Figure 0-1. By a similar procedure, we also propose and implement a method to determine the axial field, caused by the same laser source, at the focal point of a conducting reflector as suggested in Figure 0-2.

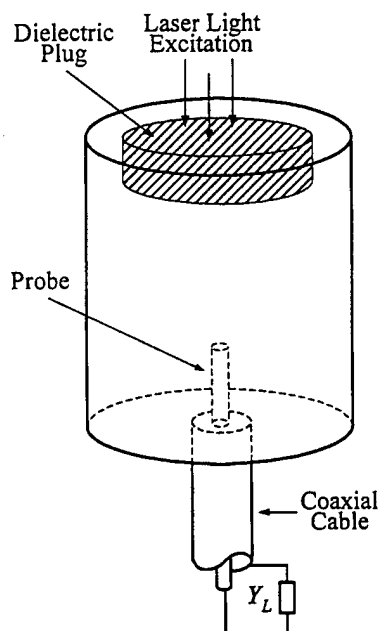


Figure 0-1. Probe in a dielectric capped metal can illuminated by a laser light.

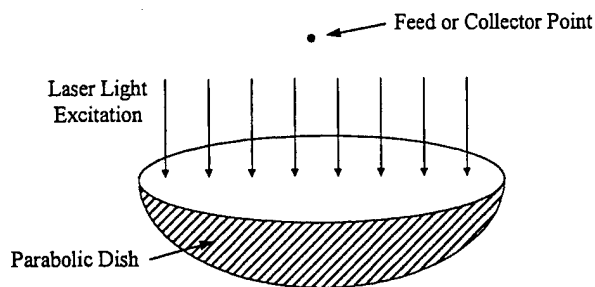


Figure 0-2. Parabolic reflector antenna illuminated by a modulated laser-light.

In Figure 0-1 is illustrated a right circular cylindrical shell or tube with a planar bottom through which protrudes the center conductor of a coax. For convenience, we refer to the structure as a "can" connected to a loaded coaxial monopole. The can wall and bottom are taken to be vanishingly thin perfectly conducting, as are the inner and outer walls of the coaxial waveguide. The coax axis is the same as the cylinder axis and its outer conductor terminates at, and is electrically connected to, the can bottom. We consider one case in which the cavity is empty (free space) and a second case in which it is partially filled with a dielectric insert. The insert is a solid dielectric cylinder whose axis coincides with those of the cylindrical shell and the coax. The excitation is the signal radiated by electrons "kicked off" the conducting surface by an impinging laser beam, modulated in such a way that the electrons escaping the surface oscillate harmonically in time causing them to radiate a coherent signal at an angular frequency  $\omega$ .

The laser excited electrons radiate in the presence of the can and coax and a signal is induced on the load admittance  $Y_L$  terminating the end of the coax remote from the point where it joins the bottom of the can. It is this signal at the load, as a function of the laser beam characteristics, that one wishes to determine. For a vanishingly small spot of laser light on the conducting surface, the radiating source is modeled as an electric dipole normal to and located at the surface. For a larger spot, the source is taken to be an ensemble of normal dipoles whose amplitudes and phases are dictated by the characteristics of the laser light and the spot. The dipoles radiate in the presence of the entire can-coax structure and, therefore, all parts of the can and coax, together with the terminating load, must be accounted for simultaneously in any analysis for determining  $V_L$  the signal at the load  $Y_L$ . In this work only the small-spot case is considered. The extension to the larger spot is trivial.

Of course, one can compute the radiation from the dipoles on the conducting surface of the can and the coupling to the terminating admittance, but one must be aware that doing so is not a simple undertaking. The dipoles radiate in the presence of the entire



can-coax structure and all parts of the can and coax are coupled. Fortunately, since one needs to know the signal only at the load, which electromagnetically speaking occupies a vanishingly small region of space, one can obtain the desired information by solving a radiation problem and employing the reciprocity theorem. This is far simpler than it would be to solve the reception problem directly in which one must allow the laser stimulated dipoles to radiate in the presence of the loaded (load admittance  $Y_L$  in place at the end of the coax) coax-can structure. One might designate this procedure *indirect* but it allows one to obtain the desired signal far more efficiently than would a more direct method necessitating the solution of a vector integral equation rather than the scalar equation of the indirect procedure. The indirect approach, though far less complex than the direct, does not sacrifice rigor.

The solution of the problem of determining the signal induced by a modulated laser beam at the load which terminates the coax of the coax-can structure, has been reduced to two steps: (1) computation of the electric field at points on the coax-can structure where the laser light might fall, caused by TEM excitation at the coax terminus, and (2) application of the reciprocity theorem to obtain the signal at  $Y_L$  caused by the laser light. From knowledge of this electric field, the value of the load admittance, and the value of the impressed source, one can determine the signal induced in the load impedance by invoking the reciprocity theorem.

Since the can, the center-joined coax, and the dielectric insert form a circularly symmetric structure, the field radiated by the structure due to excitation at the coax terminal is circularly symmetric, which property allows for additional simplification in the radiation problems associated with the indirect approach. The effort to determine radiation from the coax-can structure is, itself, partitioned into two phases. The first is the computation of the radiated field when the dielectric plug is absent. The formulation of an integral equation and numerical solution technique needed to solve for the currents induced on the coax-can structure in the absence of dielectric, from which one can find

the radiated field directly, is reported in Chapter 1 (**Electric Field Integral Equation for Conducting Bodies of Revolution**). The second is the computation when the plug is present. When the dielectric plug is introduced into the coax-can structure, the single electric field integral equation (EFIE) technique is inadequate to account for the resulting inhomogeneous-medium problem, owing to the presence of the dielectric which partially fills the can interior. Coupled integral equations sufficient to account for this new feature must be formulated and methods for solving them must be devised. The coupled integral equations developed for this purpose incorporate the operator found in the familiar magnetic field integral equation (MFIE) so a brief discussion of the MFIE applied to the geometry of interest is provided in Chapter 2 (**Magnetic Field Integral Equation for BOR**). Formulations of sets of coupled integral equations for structures comprising inhomogeneous regions made up of different dielectric materials contiguous with conductors are presented in Chapter 3 (**Analysis of Bodies Containing Conductors and Dielectrics**.) This section also contains an outline of a procedure for solving these coupled equations. This section serves two purposes. First, it conveys to the reader some of the type structures or radiators that our integral equation method can be used to analyze. Second, it conveys a sense of confidence in the results obtained by the method. Most of the structures illustrated in the figures in this section come from recent publications in the literature. They are selected on the basis that our method can be used to solve the problem in the literature with which the structure is associated. By comparing our data with that published by others, we corroborate our findings and gain confidence in our method and data. Our analysis has been intentionally made sufficiently general that it can be used to solve, as special cases, a number of problems found in the recent literature.

The procedure employed for computation of the signal caused by the laser beam at the load admittance  $Y_L$ , which terminates the end of the coax remote from the can-coax

junction, is presented in Chapter 4 (**Coupling to a Probe in a Dielectric Capped Metal Can by a Laser-Light**).

An intermediate step in the implementation of the technique for computing the desired signal at the coax load is the determination of the normal component of the electric field at points on the surface of the structure when the coax is excited. The analysis leading to the needed values of normal electric field is described in Chapter 5 (**Computation of the Near Field**). Illustrative data are also presented to support the validity of the computations.

In order to obtain data to enable us to corroborate further the results obtained from theory and numerical analysis, experiments were conducted. Models of the can and coax were fabricated and a set of probes for measuring surface current and charge were designed and built. Admittance, surface current, and surface charge were measured. Detailed descriptions of the fabrication of models and probes are presented in Chapter 6 (**Experimental Apparatus and Measurement**). Instrumentation, probe theory, and experimental procedures are discussed in this section too.

The results of theory and experiment are presented and discussed in Chapter 7 (**Discussion of Results and Corroboration of Theory**). There it is observed that excellent agreement is achieved between computed and measured results in almost all cases. Where the agreement is only "good," explanations are offered.

In chapter 8 (**Fields At The Focal Point Of A Reflector Antenna Due To Laser Light Illumination**), the reciprocity concept is applied, with a minor modification, to determine the axial electric field at the focal point of a reflector antenna due to a laser light induced field.

# CHAPTER 1

## ELECTRIC FIELD INTEGRAL EQUATION FOR CONDUCTING BODIES OF REVOLUTION

### 1.1 Introduction

Since many antennas are rotationally symmetric and fed by coaxial probes through either an infinite or a finite ground plane, it is important to have reliable methods to accurately predict the input impedance of such structures. The coupling between wire antennas and conducting bodies of revolution (bor) has been investigated extensively. Various wire/BOR configurations are depicted in Figures 1-4 and 1-5. These configurations are representative of many practical situations.

For a dipole mounted on a cylinder, a model which depends on the determination of the elements of an array of magnetic ring sources has been developed [1]. The interaction between the radiating portion of the antenna and its feed system has been studied by methods based on coupled integral equations [2]. A thin wire attached to a conducting disk and a conducting BOR and fed at the attachment point has been investigated by various methods [3]-[6]. The thin wire attached to a BOR has also been investigated by a scheme involving the introduction of a special junction basis function [7]-[8]. The electric field integral equation (EFIE) is used with the MoM for treating problems of arbitrary wires attached to arbitrary conducting surface configurations [9]. The coupling between the wire and a conducting BOR has been investigated, including the case where the wire is attached on axis to the BOR [10]-[11]. Thin or thick rotationally symmetric antennas have also been investigated by using an EFIE followed by the MoM [12]-[14]. The coupling between a wire antenna exciting an infinite circular conducting tube has been analyzed by a technique which incorporates an analytically determined Green's function [15]-[16]. The sleeve and top-hat monopole antenna have been studied by modal expansion methods [17]-[19].

In this chapter we study the input impedance and currents of the wire/BOR by formulating an EFIE and solving it numerically. The wire/BOR geometry is restricted to be rotationally symmetric. The coaxial aperture wire/BOR geometry is shorted and the wire and BOR are treated as parts of a whole body of revolution. Either the delta gap or magnetic frill source [20]-[21] is used as the excitation. Data are presented and compared for several geometrical configurations found in the literature in order to verify the accuracy of our solutions. For a special case when the wire probe is mounted at the bottom of a conducting can, the input impedance is measured and computed. Good agreement between measurements and numerical results is obtained.

## 1.2 Formulation

Consider a perfect electrical conductor (pec) body in an infinite homogeneous space. Let  $S$  denote the surface of this body. An electric field  $\mathbf{E}^i$ , defined to be the field due to an impressed source in the absence of the scatterer, is incident on the body and induces a surface current  $\mathbf{J}$  on  $S$ . This current in turn radiates a scattered electric field  $\mathbf{E}^s$ . The scattered electric field  $\mathbf{E}^s$  can be expressed in terms of the magnetic vector potential  $\mathbf{A}$  and the electric scalar potential  $\Phi$  as

$$\mathbf{E}^s = -j\omega\mathbf{A} - \nabla\Phi, \quad (1.1)$$

where

$$\mathbf{A}(\mathbf{r}) = \mu \iint_S \mathbf{J}(\mathbf{r}') G(\mathbf{r}; \mathbf{r}') dS', \quad (1.2)$$

$$\Phi(\mathbf{r}) = \frac{j\eta}{k} \iint_S (\nabla'_s \cdot \mathbf{J}(\mathbf{r}')) G(\mathbf{r}; \mathbf{r}') dS', \quad (1.3)$$

in which the free space Green's function is defined as

$$G(\mathbf{r}, \mathbf{r}') = \frac{e^{-jk|\mathbf{r}-\mathbf{r}'|}}{4\pi|\mathbf{r}-\mathbf{r}'|}, \quad (1.4)$$

$\eta = \sqrt{\mu/\epsilon}$ , and  $k = \omega\sqrt{\mu\epsilon}$ . The total electric field may be viewed as the sum of the incident and scattered fields and must satisfy

$$\left[ \mathbf{E}^s(\mathbf{r}) + \mathbf{E}^i(\mathbf{r}) \right]_{\text{tan}} = 0, \quad \mathbf{r} \in S \quad (1.5)$$

on the conducting surface where “tan” denotes the tangential component of the field on the surface  $S$ . Combining (1.1) through (1.5) one can formulate an electric field integral equation (EFIE) to determine the induced electric current on the scatterer:

$$-j \frac{\eta}{k} \left\{ k^2 \iint_S \mathbf{J}(\mathbf{r}') G(\mathbf{r}, \mathbf{r}') dS' + \nabla \iint_S \nabla_s' \cdot \mathbf{J}(\mathbf{r}') G(\mathbf{r}, \mathbf{r}') dS' \right\}_{\text{tan}} = -\mathbf{E}_{\text{tan}}^i(\mathbf{r}), \quad \mathbf{r} \in S. \quad (1.6)$$

Let  $S$  be the surface of a body of revolution (BOR) where the BOR is formed by rotating a curve, called the ‘generating arc,’ around the  $z$  axis as shown in Figure 1-3.

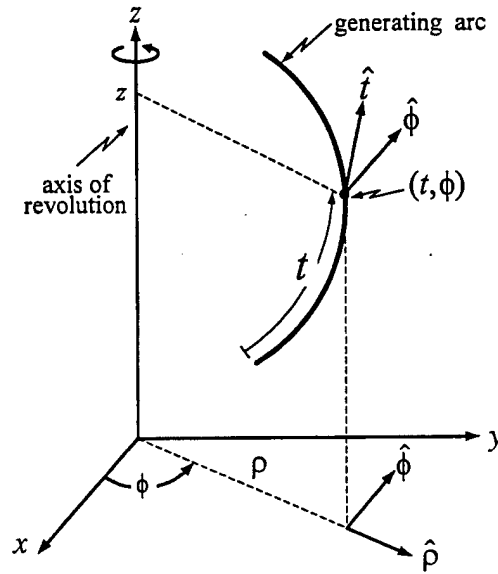


Figure 1-3. The generating arc and unit vectors of BOR.

Assume that the excitation is of the form

$$\mathbf{E}^i = E_\rho^i(\rho, z) \hat{\rho} + E_z^i(\rho, z) \hat{z} \quad (1.7)$$

with  $E_\phi^i = 0$ . Under the condition imposed upon the excitation, the current induced on the BOR has a component only in the  $t$  direction

$$\mathbf{J}(t) = J_t(t) \hat{t} \quad (1.8)$$

and the resulting scattered electric field has no  $\phi$  component. Under these conditions, (1.6) can be written as

$$[\mathbf{E}^i(\mathbf{r}) + \mathbf{E}^s(\mathbf{r})] \cdot \hat{\mathbf{t}} = 0, \quad \mathbf{r} \in S. \quad (1.9)$$

The surface divergence and gradient operators are given by

$$\nabla_s \cdot \mathbf{J} = \frac{1}{\rho} \frac{\partial}{\partial t} (\rho J_t) \quad (1.10)$$

$$\nabla f = \hat{\mathbf{t}} \frac{\partial}{\partial t} f \quad (1.11)$$

on the BOR surface, allowing one to write (1.9) as

$$-\frac{j\eta}{k} \left\{ k^2 \iint_S J_t(\mathbf{r}') \hat{\mathbf{t}} \cdot \hat{\mathbf{t}}' G(\mathbf{r}, \mathbf{r}') dS' + \frac{\partial}{\partial t} \iint_S \frac{\partial}{\partial t} J_t(\mathbf{r}') G(\mathbf{r}, \mathbf{r}') dS' \right\} = -\mathbf{E}_i(\mathbf{r}) \cdot \hat{\mathbf{t}}, \quad \mathbf{r} \in S. \quad (1.12)$$

Since

$$\hat{\mathbf{t}} = \sin \gamma \hat{\rho} + \cos \gamma \hat{\mathbf{z}} \quad (1.13)$$

the dot product  $\hat{\mathbf{t}} \cdot \hat{\mathbf{t}}'$  in (1.12) can be performed and (1.12) becomes

$$\begin{aligned} -j \frac{\eta}{4\pi k} \left\{ k^2 \int_0^T \int_{-\pi}^{\pi} (\rho' J_t(t')) (\sin \gamma \sin \gamma' \cos(\phi - \phi') + \cos \gamma \cos \gamma') \frac{e^{-jkR}}{R} d\phi' dt' \right. \\ \left. + \frac{\partial}{\partial t} \int_0^T \int_{-\pi}^{\pi} \frac{\partial}{\partial t'} (\rho' J_t(t')) \frac{e^{-jkR}}{R} d\phi' dt' \right\} = -E_t^i(t), \quad t \in (0, T) \end{aligned} \quad (1.14)$$

In (1.14),  $T$  is the total arc length of the generating arc and  $\rho$  is the radial displacement, parallel to the  $xy$  or  $\rho\phi$  plane, from the BOR axis ( $z$ -axis) to the general coordinate point  $(t, \phi)$  on the surface of the BOR,  $\gamma$  and  $\gamma'$  are defined as the angles between the BOR axis and the unit vectors  $\hat{\mathbf{t}}$  and  $\hat{\mathbf{t}}'$ , respectively, and  $R$  is the distance between an observation point  $\mathbf{r}$  or  $(\rho, \phi, z)$  and a source point  $\mathbf{r}'$  or  $(\rho', \phi', z')$ . In cylindrical coordinates  $R$  can be computed as

$$R = |\mathbf{r} - \mathbf{r}'| = \sqrt{(\rho - \rho')^2 + (z - z')^2 + 4\rho\rho' \sin^2((\phi - \phi')/2)}. \quad (1.15)$$

Since all of the quantities of interest are independent of  $\phi$ , one can set  $\phi$  equal to some convenient value without affecting the value of the quantity. We select  $\phi = 0$ . In (1.15)  $\mathbf{r}$  and  $\mathbf{r}'$  fall on the surface at  $t$  and  $t'$  so  $\rho = \rho(t)$ ,  $\rho' = \rho'(t')$ ,  $z = z(t)$ , and  $z' = z'(t')$ .

### 1.3 Numerical Scheme

In this section the reader will find an outline of a numerical scheme for solving the integral equation (1.14).

On the generating arc,  $N+2$  points are defined, beginning with  $t_0$  and ending with  $t_{N+1}$ , where the point identified by  $t_n$  is at arc displacement  $t = t_n$ , measured along the arc from the reference at  $t = t_0 = 0$ . We require  $t_0 < t_1 < t_2 \dots t_{N-1} < t_N < t_{N+1}$  in our point identification scheme, which enables one to define positive arc displacement in terms of a progression from lower to higher index number  $n$  of  $t_n$ . A simple piecewise-straight-line approximation to the generating arc is obtained by connecting  $t_0$  to  $t_1$ ,  $t_1$  to  $t_2$ , ...,  $t_n$  to  $t_{n+1}$ , ...,  $t_N$  to  $t_{N+1}$  with line segments as shown in Figure 1-2. The points,  $t_0, \dots, t_n, \dots, t_{N+1}$ , can be defined, respectively, by the coordinate points  $(\rho_0, z_0), \dots, (\rho_n, z_n), \dots, (\rho_{N+1}, z_{N+1})$ . Together with the assumed circular displacement  $\rho\phi$ , for  $\phi \in (-\pi, \pi)$ , the arc displacement  $t_n$ ,  $n = 0, 1, 2, \dots, N+1$ , or the corresponding coordinate values  $(\rho_n, z_n)$ , define a discretized piecewise linear approximation to the surface of the BOR. It is this set of coordinate values  $(\rho_n, z_n)$ ,  $n = 0, 1, 2, \dots, N+1$ , that serves as input of geometrical information to the numerical solution technique. In Figure 1-3 are depicted points  $t_{n-1}$ ,  $t_n$  and  $t_{n+1}$  on the generating arc, plus the  $n^{\text{th}}$  and  $(n+1)^{\text{th}}$  line segments of the polygonal line approximation of the arc. The lengths of these segments joined to  $t_n$  are designated  $\Delta_{n-1/2}$  and  $\Delta_{n+1/2}$  in order to identify them as the lengths of the segments associated with  $t_n$ , and their values are determined from  $(\rho_{n-1}, z_{n-1})$ ,  $(\rho_n, z_n)$ , and  $(\rho_{n+1}, z_{n+1})$ :

$$\Delta_{n\pm 1/2} = \sqrt{(\rho_n - \rho_{n\pm 1})^2 + (z_n - z_{n\pm 1})^2} \quad n = 1, 2, \dots, N+1. \quad (1.16)$$



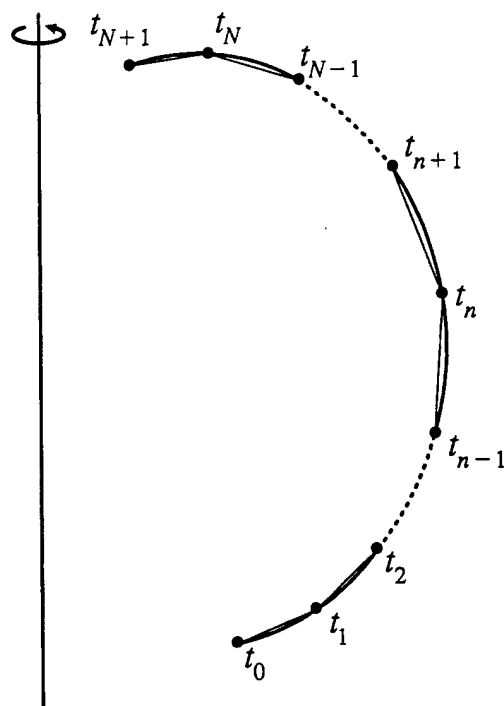


Figure. 1-2. Numbering scheme and polygonal line approximation of the generating arc.

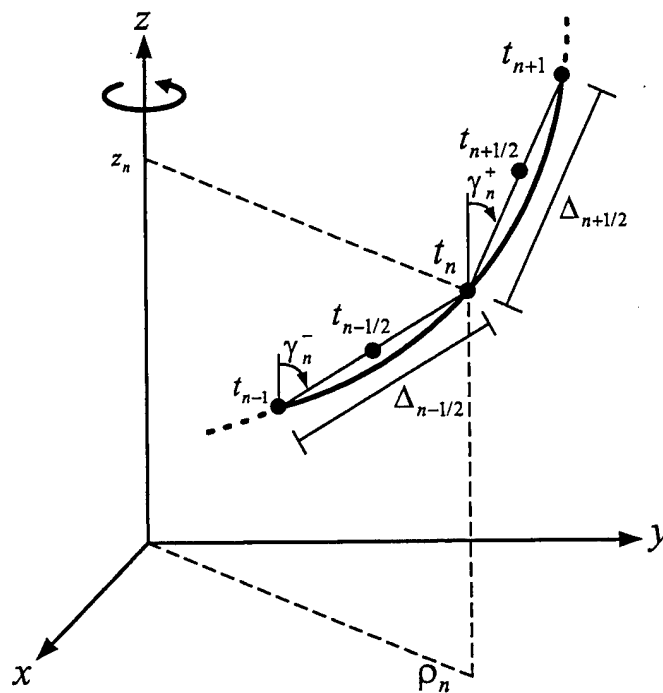


Figure 1-3. Illustration of the points on the generating arc and the line segments, the lengths of the line segments and angles

The midpoints of the  $n^{\text{th}}$  and  $(n+1)^{\text{th}}$  line segments are designated  $t_{n-1/2}$  and  $t_{n+1/2}$ . The coordinates  $(\rho_{n\pm 1/2}, z_{n\pm 1/2})$  corresponding to values of arc displacement  $t_{n\pm 1/2}$  along the discretized generating arc are not among the input data but can be determined from  $\rho_{n\pm 1/2} = (\rho_{n\pm 1} + \rho_n) / 2$  and  $z_{n\pm 1/2} = (z_{n\pm 1} + z_n) / 2$ .

At this point we rewrite (1.14) in terms of kernel functions  $K$  and  $K_1$ , in the form

$$-j \frac{\eta}{4\pi k} \left\{ k^2 \int_0^T I_t(t') [\sin \gamma \sin \gamma' K_1(t; t') + \cos \gamma \cos \gamma' K(t; t')] dt' + \frac{\partial}{\partial t} \int_0^T \frac{\partial}{\partial t'} I_t(t') K(t; t') dt' \right\} = -E_t^i(t), \quad t \in (0, T) \quad (1.17)$$

where  $I_t(t) = 2\pi\rho J_t(t)$ , is the total current and  $K_1$  and  $K$  are defined by

$$K_1(t; t') = \frac{1}{2\pi} \int_{-\pi}^{\pi} \frac{e^{-jkR} \cos \phi'}{R} d\phi', \quad (1.18)$$

$$K(t; t') = \frac{1}{2\pi} \int_{-\pi}^{\pi} \frac{e^{-jkR}}{R} d\phi', \quad (1.19)$$

in which

$$R = \sqrt{(\rho - \rho')^2 + (z - z')^2 + 4\rho\rho' \sin^2(\phi' / 2)}. \quad (1.20)$$

The current  $I_t$  which is the unknown quantity in the integral equation of (1.17), is approximated by a linear combination of  $N$  piecewise linear basis functions

$$I_t(t) \approx \sum_{n=1}^N I_n \Lambda_n(t) \quad (1.21)$$

where  $\{I_n\}$  are the  $N$  unknown coefficients of the finite-series representation of  $I_t(t)$  and where the known  $n^{\text{th}}$  expansion function represented by  $\Lambda_n(t)$  is

$$\Lambda_n(t) = \begin{cases} \frac{t_n - t_{n-1}}{\Delta_{n-1/2}}, & t \in (t_{n-1}, t_n) \\ \frac{t_{n+1} - t_n}{\Delta_{n-1/2}}, & t \in (t_n, t_{n+1}) \\ 0, & \text{otherwise} \end{cases} \quad (1.22)$$

The basis or expansion function  $\Lambda_n(t)$  is commonly referred to as a triangle function or, simply, as a triangle. They not only facilitate computation of the derivative of the current in the equation, but also they lend themselves to enforcement of the condition that the current goes to zero at edges. When (1.21) is substituted into (1.17), one introduces  $N$  unknown coefficients into the latter equation. In order to solve for the  $N$  unknown coefficients, one must have the same number of equations. We accomplish this by testing each equation by a testing function. We multiply (1.17) by pulse functions defined by

$$\Pi_m(t) = \begin{cases} 1, & t \in (t_{m-1/2}, t_{m+1/2}) \\ 0, & \text{otherwise} \end{cases} \quad (1.23)$$

and integrate the result over  $t \in (t_0, t_N)$  for  $m = 1, 2, \dots, N$ . This procedure leads to the following set of linear algebraic equations

$$[Z_{mn}][I_n] = [V_m] \quad (1.24)$$

in which  $[Z_{mn}]$  is a matrix whose elements are

$$\begin{aligned} Z_{mn} = & -j \frac{\eta}{4\pi k} \left\{ \frac{k^2}{2} (\Delta_{m-1/2} \cos \gamma_m^- + \Delta_{m+1/2} \cos \gamma_m^+) \left( \cos \gamma_n^- \int_{t_{n-1/2}}^{t_n} K(t_m; t') dt' + \cos \gamma_n^+ \int_{t_n}^{t_{n+1/2}} K(t_m; t') dt' \right) \right. \\ & + \frac{k^2}{2} (\Delta_{m-1/2} \sin \gamma_m^- + \Delta_{m+1/2} \sin \gamma_m^+) \left( \sin \gamma_n^- \int_{t_{n-1/2}}^{t_n} K_1(t_m; t') dt' + \sin \gamma_n^+ \int_{t_n}^{t_{n+1/2}} K_1(t_m; t') dt' \right) \\ & \left. + \frac{1}{\Delta_{n-1/2}} \int_{t_{n-1}}^{t_n} [K(t_{m+1/2}; t') - K(t_{m-1/2}; t')] dt' - \frac{1}{\Delta_{n+1/2}} \int_{t_n}^{t_{n+1}} [K(t_{m+1/2}; t') - K(t_{m-1/2}; t')] dt' \right\}. \quad (1.25) \end{aligned}$$

The first four integrals of (1.25) result from approximations of the integral of the triangle basis function by an equal-area, unit amplitude pulse function to facilitate the integration, while the remaining integrals reflect the piecewise constant derivative of the triangle basis function employed to represent the current  $I_i(t)$ .  $[V_m]$  is a column vector whose elements are computed from

$$V_m = \int_{t_{m-1/2}}^{t_{m+1/2}} E_i^i(t) dt, \quad m = 1, 2, \dots, N. \quad (1.26)$$

### 1.4 Singularity Analysis

In computing matrix elements from (1.25) one should be aware that the integrals contained therein may possess singularities when the field point  $t_m$  is within the source region. The elements must be computed accurately and efficiently so the singular integrals must be treated carefully. A discussion of these singular integrals is given in this section. We employ the following coordinate parameterization

$$\rho' = \rho_n + l' \sin \gamma_n, \quad (1.27)$$

$$z' = z_n + l' \cos \gamma_n. \quad (1.28)$$

and assume that the observation point is fixed at some point  $t = t_m = (\rho_m, z_m)$  within the source segment of length  $\Delta t$ . For all terms we then have that

$$(z - z') = z_m - z_n - l' \cos \gamma_n, \quad (1.29)$$

$$(\rho - \rho') = \rho_m - \rho_n - l' \sin \gamma_n. \quad (1.30)$$

Consider the integral

$$I = \frac{1}{2\pi} \int_{\Delta t - \pi}^{\pi} \int \cos \phi' \frac{e^{-jkR}}{R} d\phi' dt' \quad (1.31)$$

which occurs in discretized form in (1.25). As  $t \rightarrow t'$  and  $\phi' \rightarrow 0$ ,  $R \rightarrow 0$  which means that the integrand of (1.31) is singular. Adding and subtracting the singular term  $\frac{1}{R}$  to and from the integrand, one obtains

$$I = \frac{1}{2\pi} \int_{\Delta t - \pi}^{\pi} \int \frac{\cos \phi' e^{-jkR} - 1}{R} d\phi' dt' + \frac{1}{2\pi} \int_{\Delta t - \pi}^{\pi} \int \frac{1}{R} d\phi' dt'. \quad (1.32)$$

The first integral in (1.32) has a well behaved integrand and can be integrated numerically with ease. The second integral may be written as

$$\frac{1}{2\pi} \int_{\Delta t - \pi}^{\pi} \int \frac{1}{R} d\phi' dt' = \frac{2}{\pi} \int_{\Delta t} \frac{\kappa(\beta)}{R_2} dt' \quad (1.33)$$

where  $\kappa(\beta)$  is the complete elliptic integral of the first kind defined by

$$\kappa(\beta) = \int_0^{\pi/2} \frac{1}{[1 - \beta^2 \sin^2 \phi]^{1/2}} d\phi \quad (1.34)$$

and

$$\beta = \frac{2\sqrt{\rho\rho'}}{R_2} \quad (1.35)$$

with

$$R_2 = \sqrt{(\rho + \rho')^2 + (z - z')^2} . \quad (1.36)$$

Of course, the integrand of (1.33) now possesses the singularity. However, as  $t \rightarrow t'$ , one can show that

$$\frac{\kappa(\beta)}{R_2} \xrightarrow{t \rightarrow t'} \frac{1}{2\rho} [\ln 4 + \ln|R_2| - \ln|R_1|] \quad (1.37)$$

where

$$R_1 = \sqrt{(\rho - \rho')^2 + (z - z')^2} . \quad (1.38)$$

Only the last term in (1.37) is singular but it can be integrated analytically, so we add it to and subtract it from the integrand of (1.33) to obtain

$$\frac{2}{\pi} \int_{\Delta t} \frac{\kappa(\beta)}{R_2} dt' = \frac{2}{\pi} \int_{\Delta t} \left[ \frac{\kappa(\beta)}{R_2} + \frac{1}{2\rho} \ln|R_1| \right] dt' - \frac{1}{\pi\rho} \int_{\Delta t} \ln|R_1| dt' . \quad (1.39)$$

The first integrand on the right hand side is no longer singular and can be integrated numerically. The second integral has a singular integrand but this integral can be evaluated analytically in cases of interest.

In the computation of matrix elements of (1.25), the observation point is within the source segment when  $m = n$ . In this case the second integral of (1.39), subject to the discretization of the previous section with  $m = n$  is readily evaluated:

$$-\frac{1}{\pi\rho} \int_{l_1}^{l_2} \ln|l'| dl' = \frac{1}{\pi\rho} [(l_2 - l_1) - l_2 \ln|l_2| + l_1 \ln|l_1|] = \frac{(l_2 - l_1)}{\pi\rho} \left[ 1 + \ln \frac{2}{\Delta} \right] \quad (1.40)$$

where  $l_1$  and  $l_2$  represent the local integration limits of the integrals of (1.25). The integral  $I$  can be rewritten in the following forms,

$$I = \frac{(l_2 - l_1)}{\pi \rho} \left[ 1 + \ln \frac{2}{\Delta} \right] + \frac{2}{\pi} \int_{\Delta t} \left[ \frac{\kappa(\beta)}{R_2} + \frac{1}{2\rho} \ln |R_1| \right] dt' + \frac{1}{2\pi} \int_{\Delta t - \pi}^{\pi} \frac{\cos \phi' e^{-jkR} - 1}{R} d\phi' dt', \quad m = n \quad (1.41)$$

and

$$I = \frac{2}{\pi} \int_{\Delta t} \frac{\kappa(\beta)}{R_2} dt' + \frac{1}{2\pi} \int_{\Delta t - \pi}^{\pi} \frac{\cos \phi' e^{-jkR} - 1}{R} d\phi' dt', \quad m \neq n. \quad (1.42)$$

$I$  of (1.41) and (1.42) are to be used as the basis for evaluating the integrals which appear in the matrix element definitions of  $Z_{mn}$  in (1.25). Taking advantage of (1.41) and (1.42), one will find the integrals called for in (1.25) easy to evaluate.

### 1.5 Excitation

The EFIE analysis given above is valid as long as the incident field is rotationally symmetric about the  $z$ -axis and the incident electric field does not contain a  $\phi$  component. One of the sources that creates this kind of field is a  $z$ -directed hertzian dipole located at some point on the  $z$  axis. Another, which is utilized in this study, is the radiation from the annular aperture at the end of a coax, properly located and oriented with respect to the axis of revolution. Coaxial aperture feeds for the probe-fed BOR antenna are modeled as magnetic frill sources in this work. Consider a coaxial aperture terminated in an infinite ground plane. Using the equivalence principle and image theory, we may determine the radiated field as that caused by a magnetic frill. If the TEM mode assumption in the coax is made, the aperture distribution of the coax for a 1-Volt excitation is

$$E_p(\rho) = \frac{1}{2\rho \ln(b/a)} \text{ V/m.} \quad (1.43)$$

The corresponding magnetic current distribution is

$$M_\phi = \frac{-1}{\rho \ln(b/a)} \quad (1.44)$$

and the electric vector potential of this source is

$$F_\phi = -\frac{\epsilon_0}{2\pi \ln(b/a)} \int_a^b \int_0^\pi \cos \phi' \frac{e^{-jkR}}{R} d\phi' d\rho' \quad (1.45)$$

where  $R$  is defined in (1.20). Expressions for the field components are as follows [20]-[21]

$$E_\rho = \frac{1}{2\pi \ln(b/a)} \int_a^b \int_0^\pi \frac{e^{-jkR}}{R^3} (jkR + 1)(z - z') \cos \phi' d\phi' d\rho' \quad (1.46)$$

$$E_z = \frac{-1}{2\pi \ln(b/a)} \int_0^\pi \left[ \frac{e^{-jkR}}{R} \right]_{\rho'=a}^{\rho'=b} d\phi' \quad (1.47)$$

$$H_\phi = \frac{j(k/\eta)}{2\pi \ln(b/a)} \int_a^b \int_0^\pi \frac{e^{-jkR}}{R} \cos \phi' d\phi' d\rho'. \quad (1.48)$$

## 1.6 Imperfectly Conducting BOR

To formulate an integral equation to account for the losses on the imperfectly conducting BOR, the impedance boundary condition is applied on the surface of the structure

$$[\mathbf{E}^s(\mathbf{r}) + \mathbf{E}^i(\mathbf{r})]_{\tan} = \mathbf{J}(\mathbf{r}) Z(\mathbf{r}), \quad \mathbf{r} \in S, \quad (1.49)$$

in which  $Z(\mathbf{r})$  is the surface impedance of the body. The integral equation of (1.17) is modified to account for this modification as

$$\begin{aligned} -j \frac{\eta}{4\pi k} \left\{ k^2 \int_0^T I_t(t') [\sin \gamma \sin \gamma' K_1(t; t') + \cos \gamma \cos \gamma' K(t; t')] dt' \right. \\ \left. + \frac{\partial}{\partial t} \int_0^T \frac{\partial}{\partial t'} I_t(t') K(t; t') dt' \right\} - I_t(t) \frac{Z(t)}{2\pi \rho} = -E_t^i(t), \quad t \in (0, T). \end{aligned} \quad (1.50)$$

This integral equation is solved numerically according to the numerical solution method discussed in an earlier section. Hence, the matrix elements for this case are not given.

### 1.7 Corroboration

In order to ascertain the correctness of the integral equation formulation, the numerical solution technique, and the computer code developed to implement the solution for the current on the coax-can structure of Figure 1-5(d), we have compared our results with those which are available from the recent literature. We have made our solution tool very general so that it would apply to our structure and to a wide class of others of the type illustrated in Figures 1-4 and 1-5. Because of the generality of the techniques reported here, we have been able to solve numerous problems found in the literature that have been solved by other methods. Several structures/problems in this category have been selected as cases against which to test our work. In each case, data from the corresponding solution in the literature are compared with our data and the agreement is found to be very close, lending support to the correctness of our method. However, in view of the effort required to reproduce a large amount of data from the literature in this report, no attempt is made here to present data of other workers in the figures displaying our data. The various examples discussed do reveal the versatility of the solution method reported here and, if one were inclined to compare data, one could do so readily.

Figure 1-6 shows the current induced on the sleeve monopole antenna driven by a delta gap generator [17]. Figure 1-7 shows the input impedance of a biconical antenna made up of two inverted conducting cones mounted on an infinite ground plane. The data compare very favorably with data from [13]- [14]. In Figure 1-8 and 1-9 are illustrated the input impedance and current distribution for a circular top-hat loaded monopole antenna mounted on an infinite ground plane [19]. The current is plotted against displacement from the edge of the circular top-hat to the feed point. In Figure 1-10 is seen



the input impedance of a monopole antenna mounted in the center of a finite circular ground plane [3]. In Figure 1-11 is shown the current distribution of a monopole antenna attached to the bottom of a conducting can. This structure is very similar to one of the configurations of ultimate interest in this project. The current is plotted against arc displacement with the reference at the top of the monopole

Figures 1-12 and 1-13 depict the current induced on the wire and tube walls for a wire antenna residing coaxially inside a conducting tube of infinite extent. Our analysis is capable of solving for the current on such a structure when the frequency of operation is below the cut-off frequency of the infinite conducting tube viewed as a circular waveguide. As seen from the figure, the real part of the current on the wire is zero due to the cut-off condition [15]-[16].

Experimental and theoretical data are compared next, again to enable us to demonstrate the validity of our work. In Figures 1-14 through 1-17 one finds, for the purpose of comparison, measured and computed input admittance of a monopole attached to the bottom of a brass can of Figure 1-5(d). Losses due to the finite conductivity of the brass are accounted for in the analysis by making use of the well known surface impedance approximation. It has been ensured that the thickness of the walls of brass can used in this measurement was at least ten times greater than the skin depth at the frequency of operation. The measured and computed data agree very well.

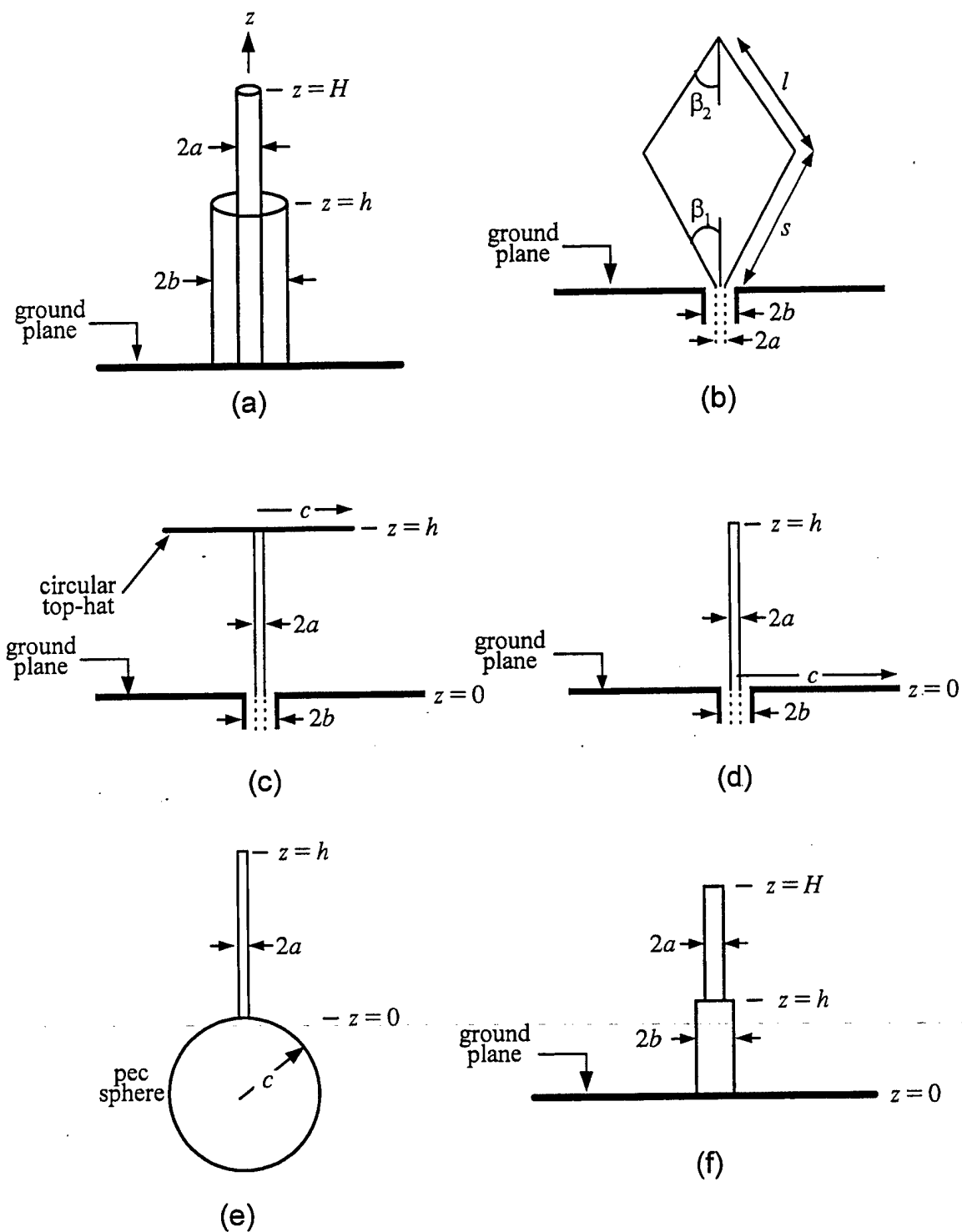


Figure 1-4. Various wire/BOR geometries. (a) sleeve monopole antenna, (b) biconical antenna, (c) top-hat monopole antenna, (d) a monopole antenna over infinite ground plane, (e) wire attached to a conducting sphere, (f) stepped radius monopole antenna.

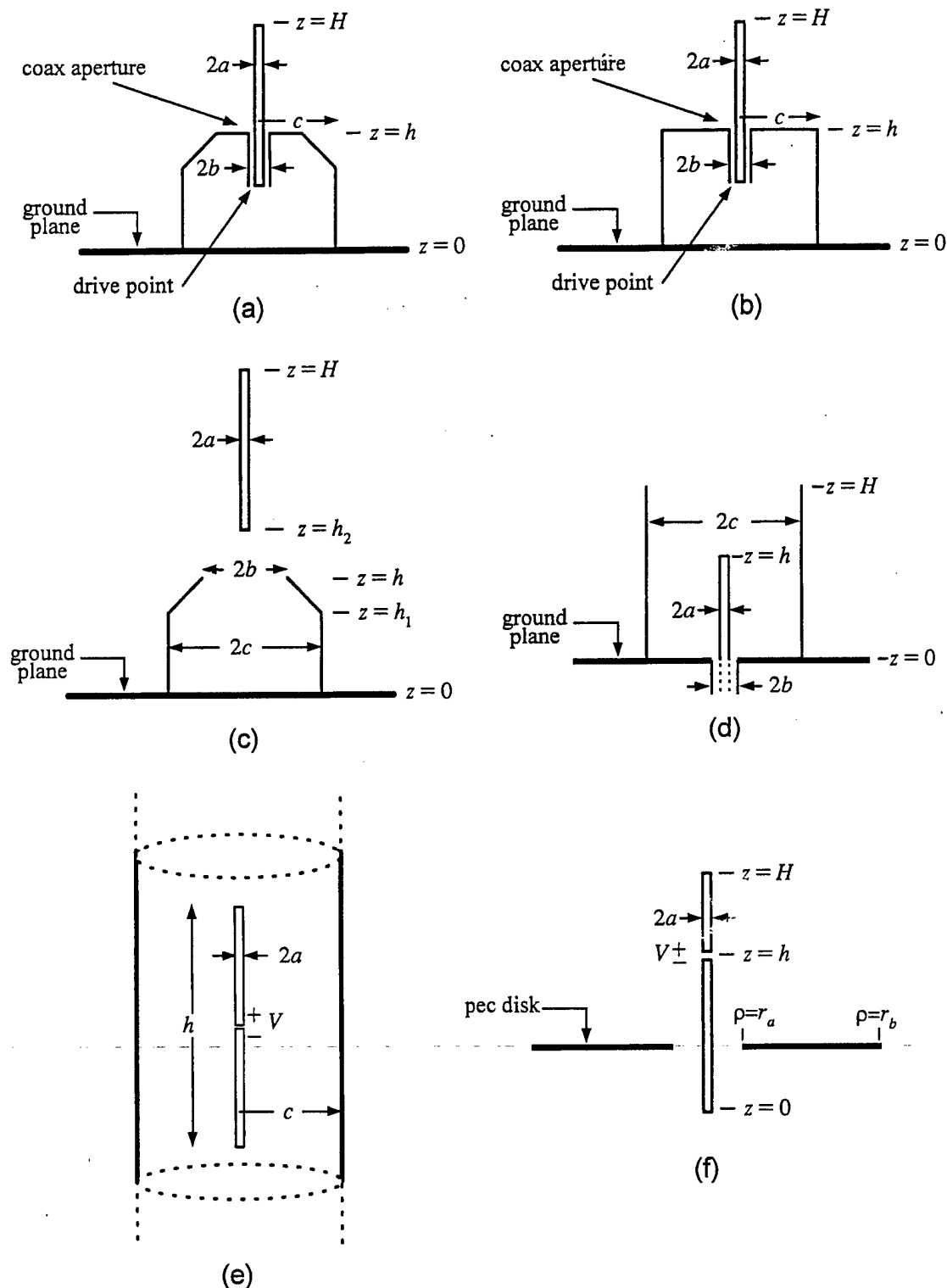


Figure 1-5. Various wire/BOR geometries. (a) and (b) missile like wire BOR geometries, (c) wire in the coupled to open BOR, (d) a conducting can fed by a coax, (e) wire axially located inside a hollow infinite conducting tube, (f) a dipole in the presence of an annular conducting disk.

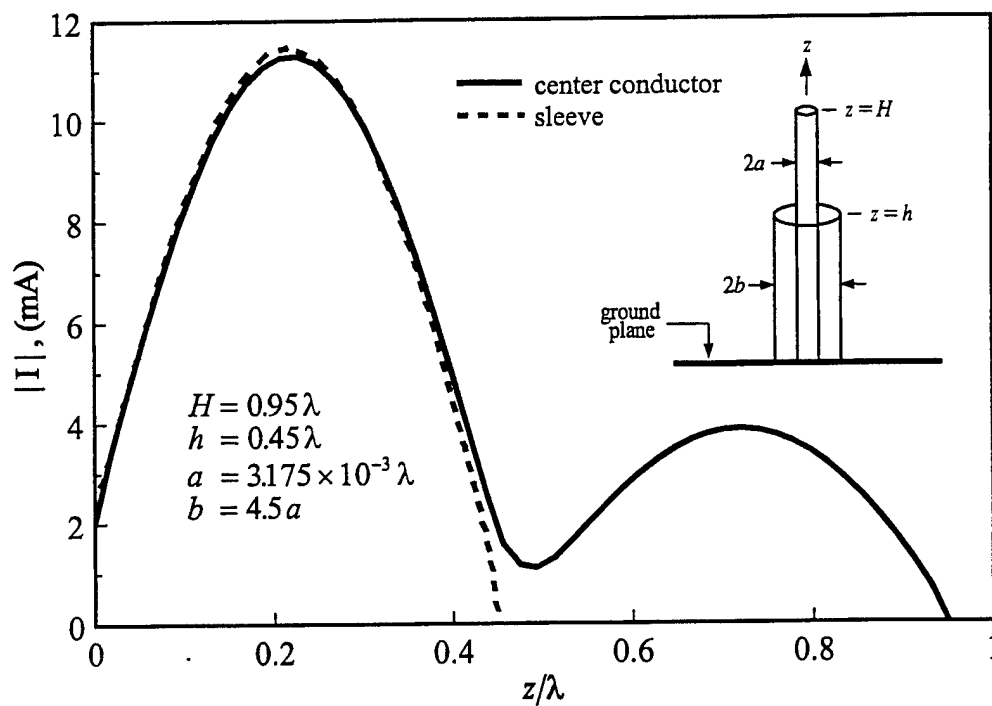


Figure 1-6. Magnitude of current distribution along a sleeve monopole antenna base driven by a one volt delta-gap source.

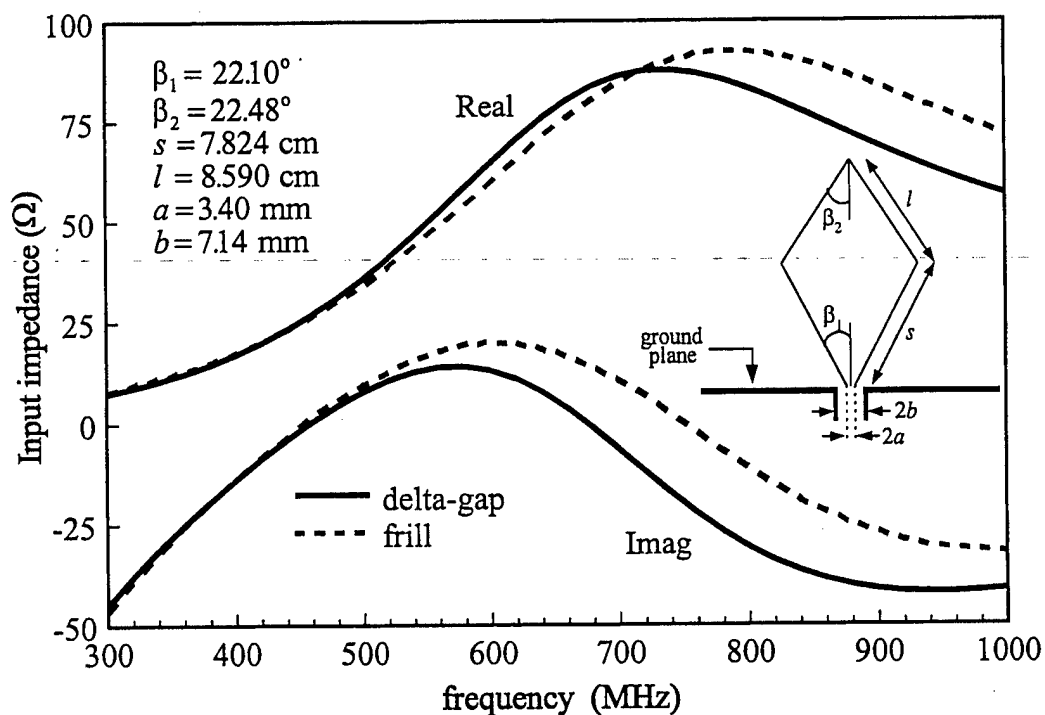


Figure 1-7. Input impedance of a biconical antenna on an infinite ground plane.

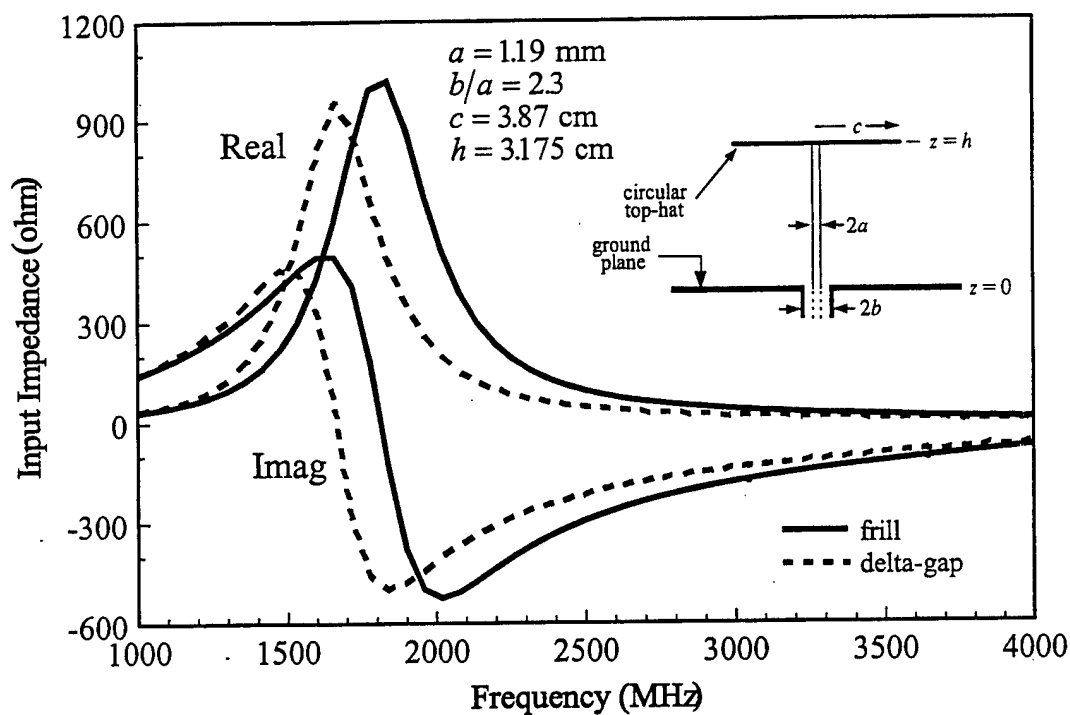


Figure 1-8. Input impedance of a top-hat monopole over an infinite ground plane.

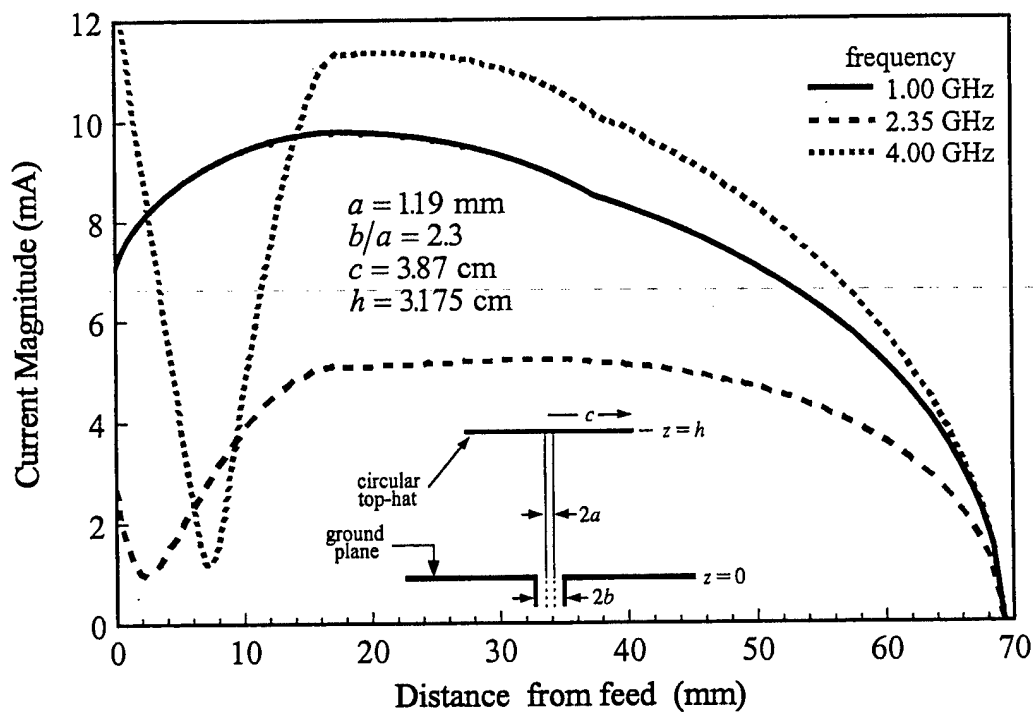


Figure 1-9. Magnitude of current distribution of a top-hat monopole antenna driven by a one delta-gap source.

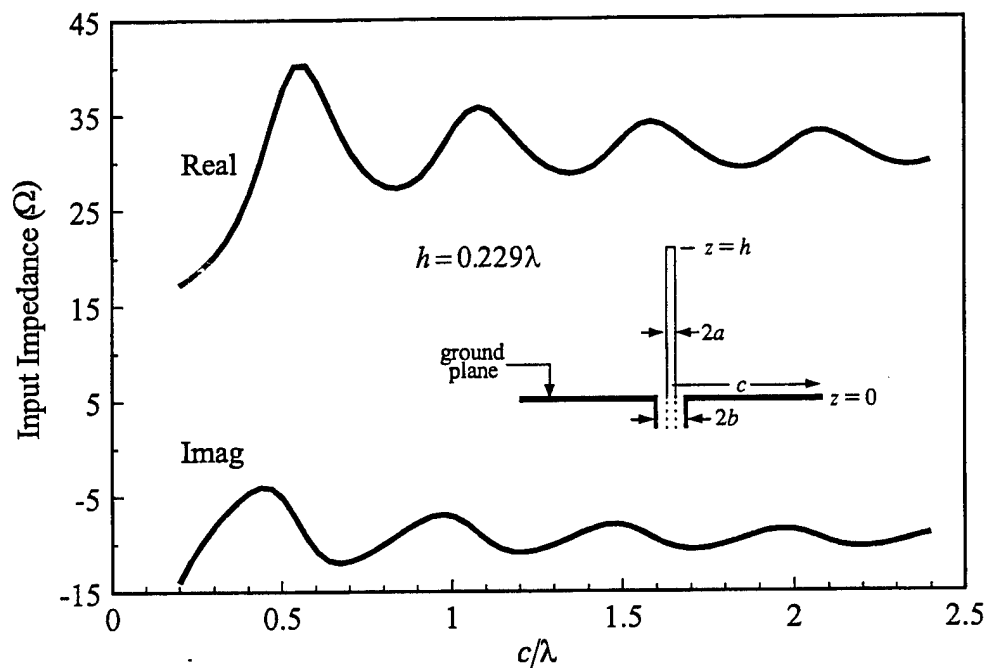


Figure 1-10. Input impedance of a monopole antenna at the center of circular disk.

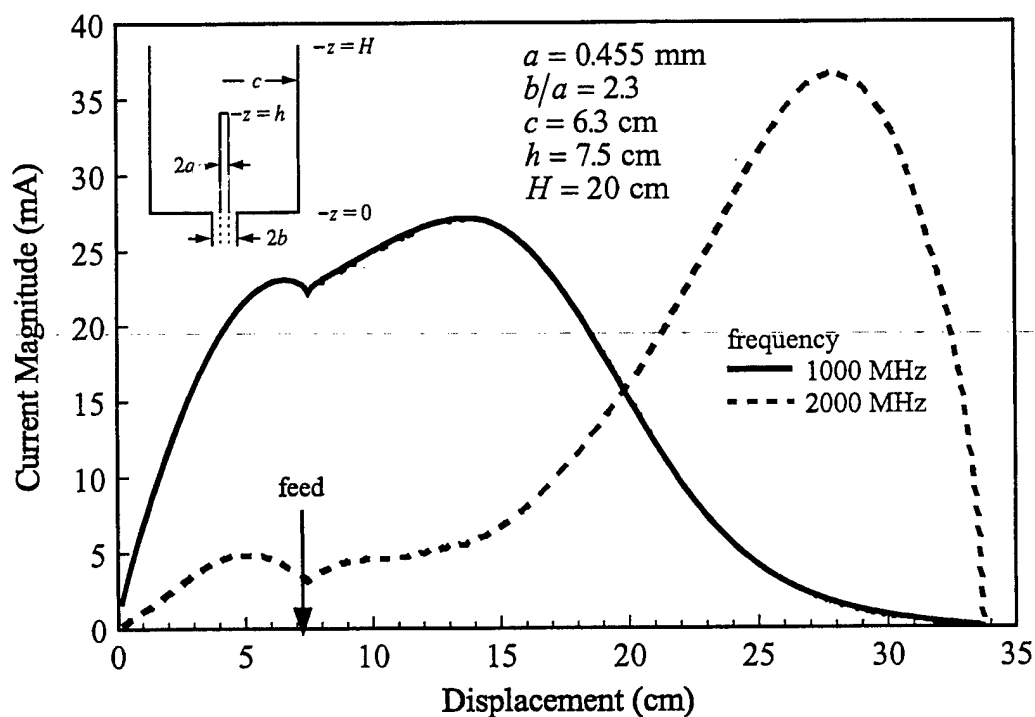


Figure 1-11. Magnitude of current distribution of a monopole attached at the bottom of a conducting can.

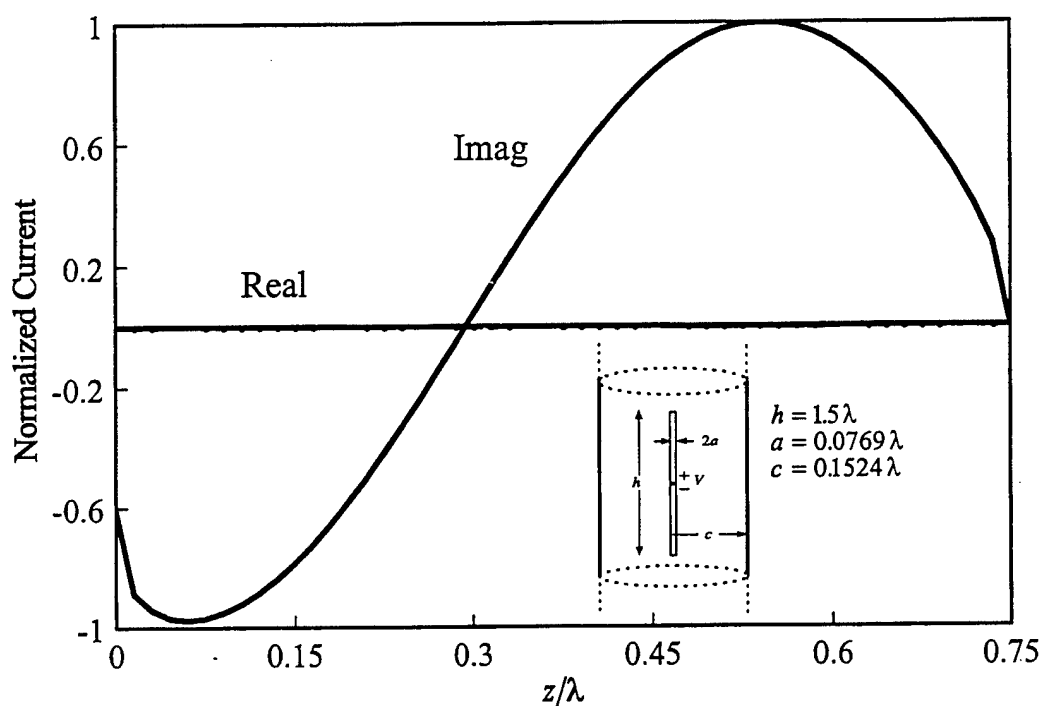


Figure 1-12. Normalized current induced on the dipole antenna residues coaxially inside an infinite conducting tube.

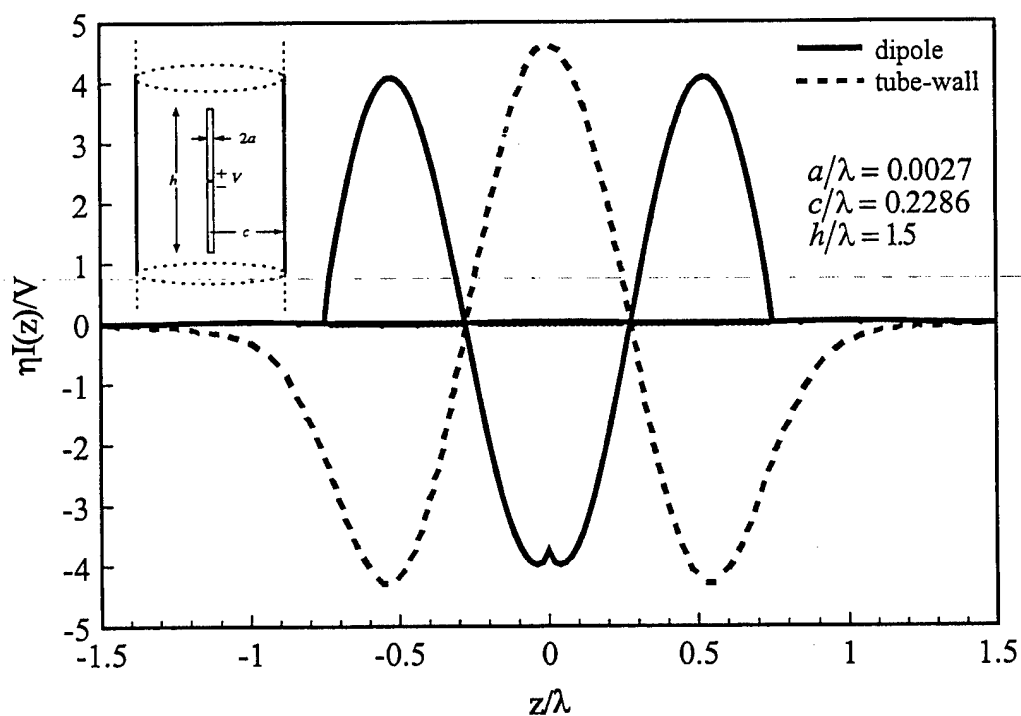


Figure 1-13. Current induced on the dipole and on the tube wall when the dipole antenna resided coaxially inside an infinite conducting tube.

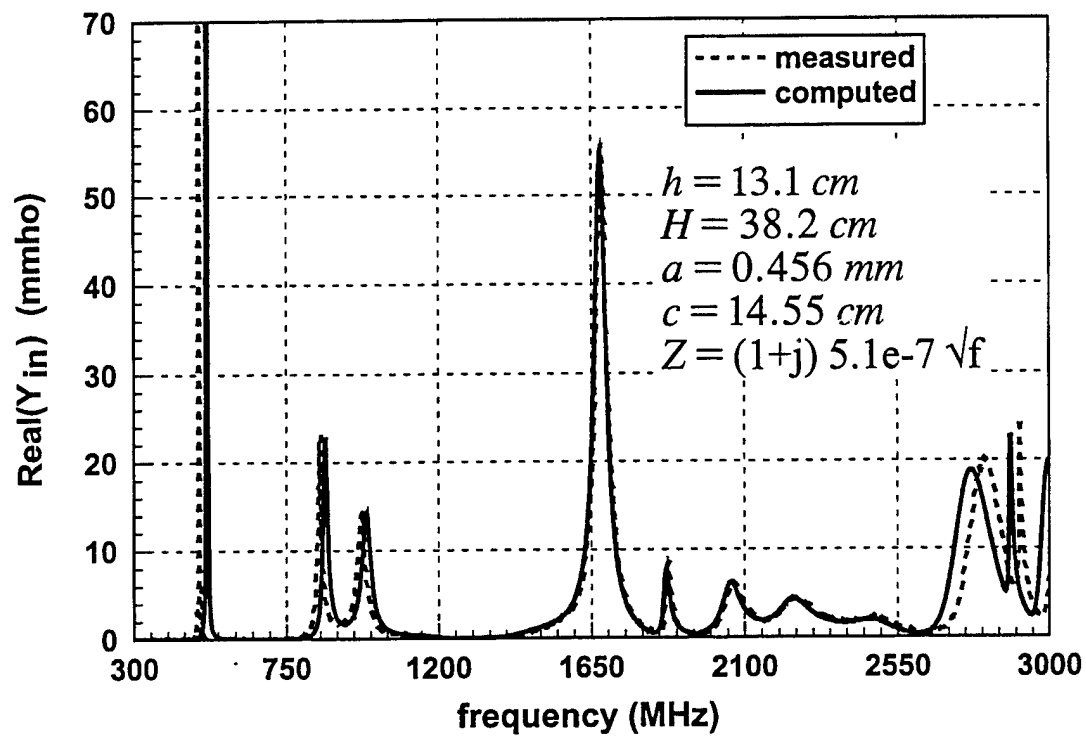


Figure 1-14. Measured and computed input admittance (real part) of the imperfectly conducting coax-fed can.

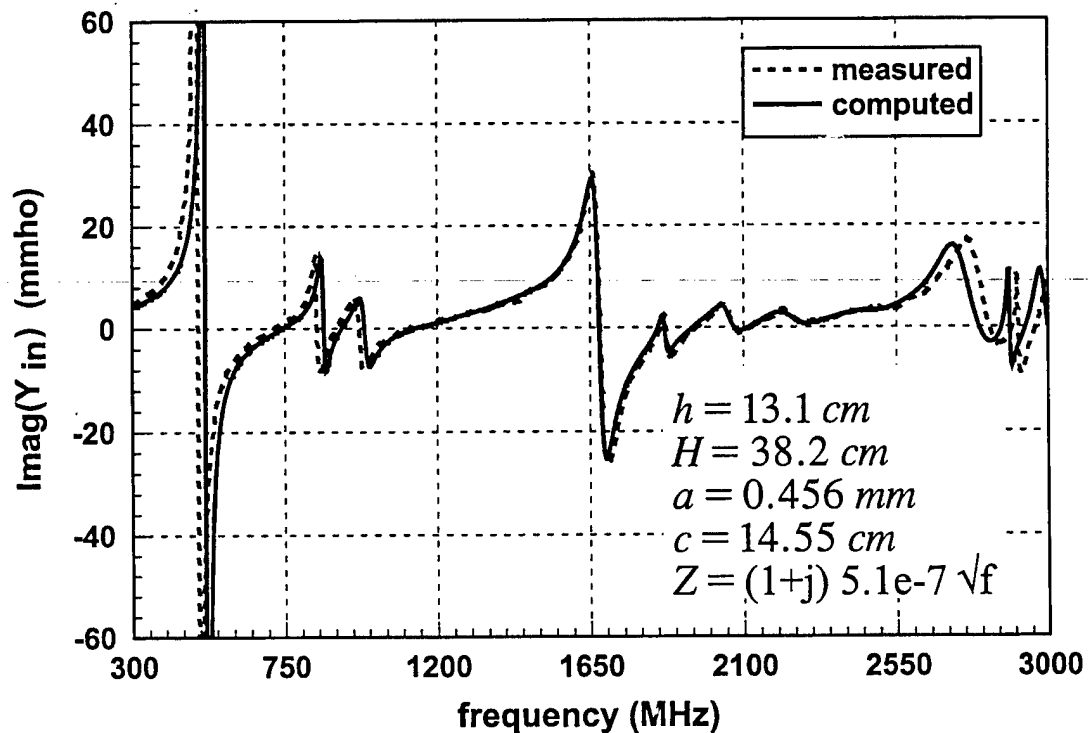


Figure 1-15. Measured and computed input admittance (imaginary part) of the imperfectly conducting coax-fed can.



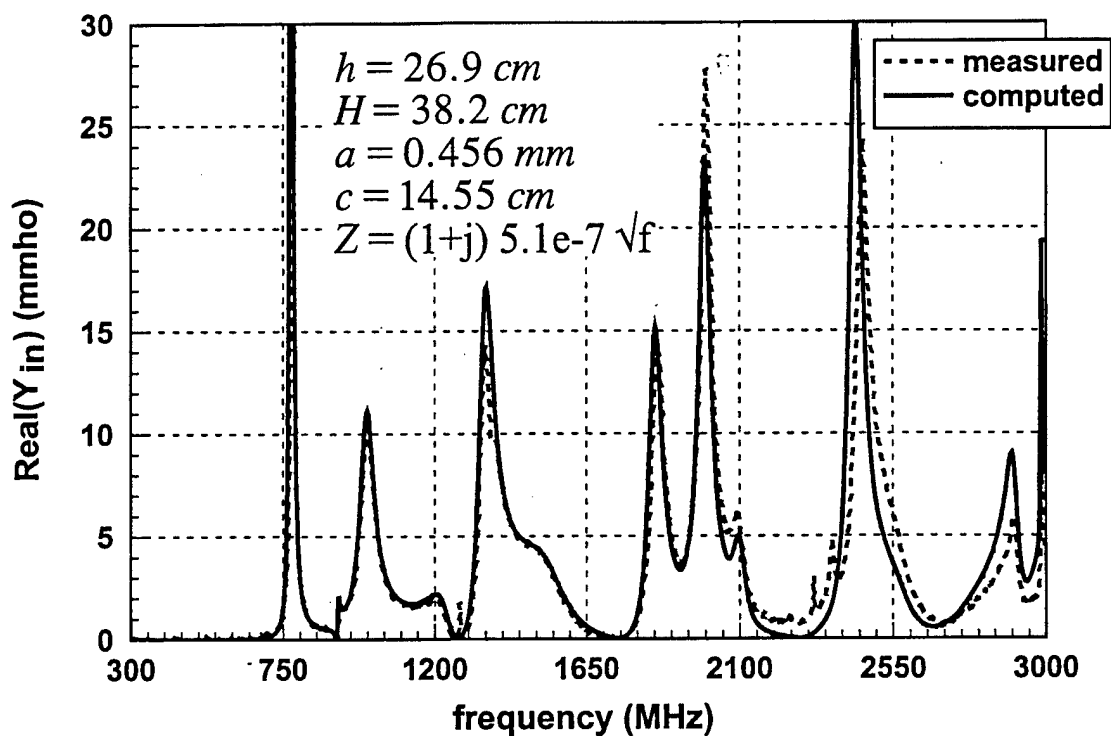


Figure 1-16. Measured and computed input admittance (real part) of the imperfectly conducting coax-fed can.

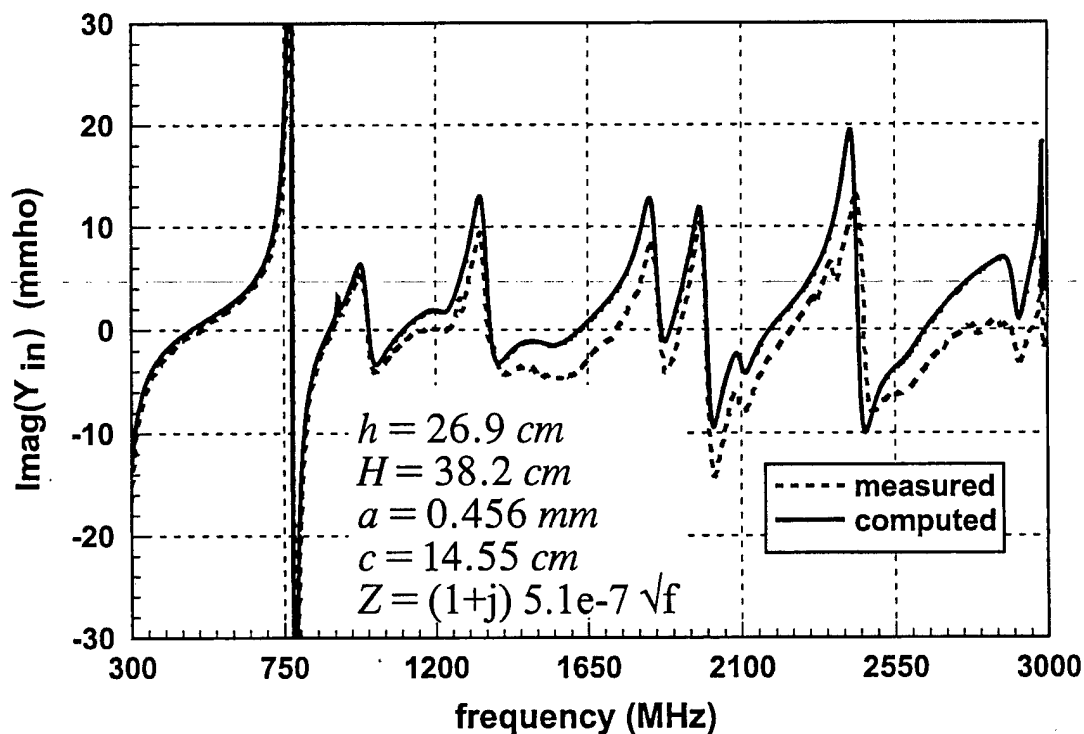


Figure 1-17. Measured and computed input admittance (imaginary part) of the imperfectly conducting coax-fed can.

## 1.8 References

1. L. L. Tsai, "Dipole antenna coaxially mounted on a conducting cylinder," *IEEE Trans. Antennas Propagat.*, pp. 89-94, Jan 1973.
2. E. K. Yung and C. M. Butler, "Coaxial-line driven monopole on an electrically thick conducting cylinder over a ground plane", *IEE Proceedings.*, Part. H, vol. 131, no. 1, pp. 54-60, Feb 1984.
3. J. H. Richmond, "Monopole Antenna on circular disk," *IEEE Trans. Antennas Propagat.*, vol. 42, pp. 1282-1287, Dec 1984.
4. E. J. Rothwell and M. J. Cloud, "A Hallen-type integral equation for symmetric scattering from lossy circular disks," *IEEE Trans. Antennas Propagat.*, vol. 40, no. 8, pp. 920-925, Aug 1992.
5. M. Marin and M. F. Catedra, "A study of a monopole arbitrarily loacted on disk using hybrid MM/GTD techniques," *IEEE Trans. Antennas Propagat.*, vol. 35, no. 3, pp. 1236-1243, Mar 1987.
6. R. Perez-Leal and M. F. Catedra, "Input impedance of wire antennas attached on-axis to conducting bodies of revolution," *IEEE Trans. Antennas Propagat.*, vol. 36, no. 9, pp. 1236-1243, Sep 1988.
7. J. F. Sheaffer, "EM scattering from bodies of revolution with attached wires," *IEEE Trans. Antennas Propagat.*, vol. 30, no. 3, pp. 426-431, Jan 1975.
8. J. F. Sheaffer and L. N. Medgyesi-Mitschang, "Radiation from wire antennas attached to bodies of revolution: the junction problem," *IEEE Trans. Antennas Propagat.*, vol. 29, no. 3, pp. 479-487, May 1981.
9. S. H. Hwu, D. R. Wilton and S. M. Rao, "Electromagnetic scattering and radiation by arbitrary conducting wire/surface configurations," *IEEE AP-S Int. Symp.*, pp. 890-893, July 1997.
10. Z. Qiu and C. M. Butler, "Analysis of a wire in the presence of an open body of revolution," *Progress in Electromagnetic Research PIER 15*, pp.3-26, 1997.
11. Z. Qiu and C. M. Butler, "Analysis of a wire probe mounted on the nose of a missile-like body of revolution," *URSI National Meeting*, pp.11, 1994.
12. H. Kawakami and G. Sato, "Broad-band characteristics of rotationally symmetric antennas and thin wire constructs," *IEEE Trans. Antenn. Propagat.*, vol. 35, no. 1, pp. 26-32, Jan 1987.
13. W. Huang, A. A. Kishk and A. W. Glisson, "Electromagnetic characteristics of a thick monopole antenna with dielectric loading," *IEEE SOUTHEASTCON.*, pp. 314-317, 1992 .
14. W. Huang, A. A. Kishk and A. W. Glisson, "Analysis of a thick monopole antenna loaded with dielectric material," *AEU*, vol. 48, no. 4, pp. 177-183, 1994.

15. A. Q. Martin and C. M. Butler, "Analysis of an axially-directed antenna exciting a conducting tube," *Journal of Electromagnetic Waves and Applications*, vol. 7, no. 8, pp. 1033-1056, 1993.
16. A. Q. Martin and C. M. Butler, "Corroboration of the analysis of an axially directed antenna exciting a conducting tube," *Journal of Electromagnetic Waves and Applications*, vol. 11, pp. 821-858, 1997.
17. A. D. Wunsch, "Fourier series treatment of the sleeve monopole antenna," *IEE Proceedings-H*, vol. 135, no. 4, pp. 217-225, Aug 1988.
18. Z. Shen, and R. H. MacPie, "Rigorous evaluation of the input impedance of a sleeve monopole by model expansion method," *IEEE Trans. Antenn. Propagat.*, vol. 44, no. 12, pp. 1584-1591, December 1996.
19. M. A. Morgan and F. K. Schwering, "Eigenmode analysis of dielectric loaded top-hat monopole antennas," *IEEE Trans. Antenn. Propagat.*, vol. 42, pp. 54-61, Jan 1994.
20. C. M. Butler and L. L. Tsai, "An alternate frill field formulation," *IEEE Trans. Antenn. Propagat.*, vol. 21, no. 1, pp. 115-116, Jan 1973.
21. L. L. Tsai, "A numerical solution for the near and far fields of an annular ring of magnetic current," *IEEE Trans. Antenn. Propagat.*, vol. 20, no. 5, pp. 569-576, Sep 1972.

## CHAPTER 2

### MAGNETIC FIELD INTEGRAL EQUATION FOR BOR

#### 2.1 Formulation

In this section we outline the derivation of the magnetic field integral equation for the zero order body of revolution subject to excitation in which  $E_\phi = 0$ . Let  $S$  denote the surface of a closed PEC scatterer. An incident magnetic field  $\mathbf{H}^i$ , defined in the absence of the scatterer, induces surface currents  $\mathbf{J}$  on  $S$ . The magnetic field integral equation (MFIE) is derived from the requirement

$$\mathbf{J} = \hat{\mathbf{n}} \times (\mathbf{H}^s + \mathbf{H}^i), \text{ on } S^+ \quad (2.1)$$

where  $\hat{\mathbf{n}}$  is an outward unit normal vector to  $S^+$ , the exterior side of the surface  $S$ . Since the tangential magnetic field is discontinuous at an electric surface current,  $\hat{\mathbf{n}} \times \mathbf{H}^s$  is evaluated in the limit as the surface is approached from the exterior as suggested by the superscript “+.” It can be shown by a limiting argument that for observation points  $\mathbf{r}$  not on an edge,

$$\hat{\mathbf{n}} \times \mathbf{H}^s = \lim_{\mathbf{r} \rightarrow \mathbf{r}'} \hat{\mathbf{n}} \times \frac{1}{\mu} \nabla \times \mathbf{A} = \frac{1}{2} \mathbf{J}(\mathbf{r}) + \iint_S \hat{\mathbf{n}}(\mathbf{r}) \times \mathbf{J}(\mathbf{r}') \times \nabla' G(\mathbf{r}, \mathbf{r}') dS', \quad \mathbf{r} \in S, \quad (2.2)$$

in which  $G(\mathbf{r}, \mathbf{r}')$  is the free space Green's function and  $\mathbf{A}$  is the magnetic vector potential. From (2.1) and (2.2), a magnetic field integral equation (MFIE) can be formulated to determine the induced electric current on the scatterer:

$$-\frac{1}{2} \mathbf{J}(\mathbf{r}) + \iint_S \hat{\mathbf{n}}(\mathbf{r}) \times [\mathbf{J}(\mathbf{r}') \times \nabla' G(\mathbf{r}, \mathbf{r}')] dS' = -\hat{\mathbf{n}}(\mathbf{r}) \times \mathbf{H}^i(\mathbf{r}), \quad \mathbf{r} \in S^+. \quad (2.3)$$

The MFIE in (2.3) takes a slightly different form if the observation point is allowed to lie on an edge. It can be shown by a limiting argument that the MFIE in (2.3) takes the following alternate form

$$\frac{\beta}{\pi} \frac{\mathbf{J}(\mathbf{r})}{2} - \hat{\mathbf{n}} \times \iint_S \mathbf{J}(\mathbf{r}') \times \nabla' G(\mathbf{r}, \mathbf{r}') dS' = \hat{\mathbf{n}} \times \mathbf{H}^i, \quad \mathbf{r} \in S, \quad (2.4)$$

where  $\beta$  is the exterior solid angle between the two limiting tangent lines at the point of tangency approached by the observation point. Note that, on a surface with no edge  $\beta = \pi$ , in which case (2.4) is identical to (2.3).

Let  $S$  be the surface of the body of revolution illustrated in Figure 2-1. We assume a rotationally symmetric excitation in which  $E_\phi = 0$ . This excitation induces a  $t$  directed current on the BOR surface. Under this condition (2.4) becomes

$$\begin{aligned} \frac{\beta}{\pi} \frac{I_t(t)}{4\pi\rho} + \frac{1}{8\pi^2} \int_0^T \int_{-\pi}^{\pi} I_t(t') [((\rho - \rho') \cos \gamma' - (z - z') \sin \gamma') \cos \phi' \\ + 2\rho \cos \gamma' \sin^2(\phi' / 2)] [1 + jkR] \frac{e^{-jkR}}{R^3} d\phi' dt' = H_\phi^i(t), \quad t \in S, \end{aligned} \quad (2.5)$$

where  $R$  and  $I_t(t)$  are defined in the previous in Chapter 1.

## 2.2 Numerical Solution

A method for solving (2.5) is now presented. In the following numerical scheme, all indexing and parameterization of the generating arc are the same as those discussed in Chapter 1. Maintaining the same discretization has the advantage that the currents are represented at common arc points and equation enforcement takes place at the same points when the HFIE and the EFIE are used in a common formulation, which is very convenient in the analysis of dielectric bodies.

Since no derivatives of current appear in (2.5) the unknown current is expanded into pulse basis functions as

$$I_t(t) \approx \sum_{n=1}^N I_n \Pi_n(t) \quad (2.6)$$

where  $\Pi_n$  is as defined and the complex constants  $\{I_n\}$  represents the complex value of the current  $I_i(t)$  at the point  $t_n$ . Zero half pulses are placed at  $t_0$  and  $t_{N+1}$  to comply with the boundary condition  $I_i(t_0) = I_i(t_{N+1}) = 0$ . The current representation in (2.6) is next substituted into (2.5) and the equation is enforced at the match points  $t_m$ . The resulting equation can be written in matrix form as

$$[\Gamma_{mn}][I_n] = [H_m] \quad (2.7)$$

where  $[I_n]$  is a column vector containing the unknown current coefficients,  $[H_m]$  is a column vector whose elements are sampled values of the incident field given by  $H_m = H_\phi^i(t_m)$ , and  $[\Gamma_{mn}]$  is a matrix whose complex-valued elements are

$$\Gamma_{mn} = \frac{\beta_m}{\pi} \frac{\delta_{mn}}{4\pi\rho_m} + \frac{1}{8\pi^2} \int_{t_{n-1/2}}^{t_n} \int_{-\pi}^{\pi} K(t_m; t', \phi') d\phi' dt' + \frac{1}{8\pi^2} \int_{t_n}^{t_{n+1/2}} \int_{-\pi}^{\pi} K(t_m; t', \phi') d\phi' dt' \quad (2.8)$$

where

$$K(t; t', \phi') = \left[ ((\rho - \rho') \cos \gamma' - (z - z') \sin \gamma') \cos \phi' + 2\rho \cos \gamma' \sin^2(\phi' / 2) \right] [1 + jkR] \frac{e^{-jkR}}{R^3}, \quad (2.9)$$

$\beta_m$  is the angle defined in Figure 2-1, and  $\delta_{mn}$  is the Kronecker delta defined as

$$\delta_{mn} = \begin{cases} 1, & m = n \\ 0, & \text{otherwise} \end{cases} \quad (2.10)$$

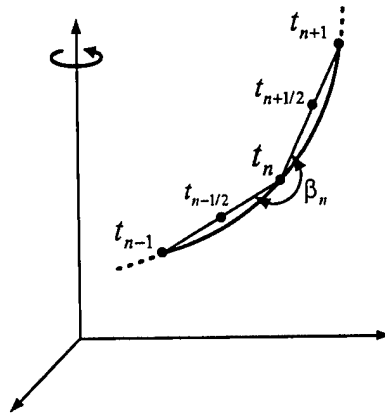


Figure 2-1. Illustration of the solid angle  $\beta_n$ .

# CHAPTER 3

## ANALYSIS OF BODIES CONTAINING CONDUCTORS AND DIELECTRICS

### 3.1 Introduction

Electromagnetic radiation and scattering problems involving combination of conductors and dielectric materials have recently received much attention from researchers since their applications occur in important antenna problems such as the control of radar cross-section, dielectric loaded antenna design, the design of microwave devices and microwave printed circuits, etc. These problems are usually analyzed using surface integral equation methods (SIE), differential equation methods (DE), and hybrid techniques. Other methods employing eigenfunction expansions or Green's functions are suited only to simple structures whose boundaries coincide with a constant coordinate surface in a separable coordinate system. Each of these methods exhibits advantages in particular types of applications. Comparing the DE and SIE approaches, we note that the former has simple formulation, results in more unknowns, but yields a sparse matrix, whereas the latter is rather difficult to formulate for complex media, results in fewer unknowns, but yields full matrices which may be costly to solve when the structure is very large. One advantage of the SIE approach is that the radiation condition is automatically incorporated through the free space Green's functions, whereas the DE approach requires an approximate boundary condition to enforce the radiation condition which may lead to an extremely large number of unknowns. A hybrid approach represents a synthesis of coupled integral and differential equation formulations and may be adopted for problems consisting of both inhomogeneous and homogeneous regions. However, the formulations and especially the numerical implementation of the hybrid techniques usually require extensive effort. We choose to circumvent the major difficulties by employing surface integral equation formulations.

A number of different integral equation formulations for a homogeneous dielectric body have been used by various authors. One may consult [1] for some of these formulations and [2]-[4] for a review of past research using surface integral equation techniques and other methods.

The numerical solution of problems involving both conducting and dielectric bodies have been studied extensively and the literature is voluminous. Different integral equations have been formulated for scattering from bodies of revolution of arbitrary composition [6]-[10] and arbitrary shaped three-dimensional bodies [11]-[14]. The widely applied surface integral equation formulation for coupling to a perfectly conducting body with a dielectric region is the method of Mautz and Harrington [5 Equation (15)-(18)].

TE and TM plane wave scattering from multiple perfectly conducting and homogeneous lossy dielectric cylinders has been studied and different surface integral equation formulations have been utilized [15]-[21]. In these formulations, dielectric and conducting cylinders with intersecting surfaces have been treated as if they were disjoint. A similar solution has been presented for a homogeneous dielectric cylinder partially covered by zero thickness conductors excited by both TE and TM plane waves [22]. In this formulation conducting and dielectric bodies are treated together. A two-dimensional conducting body with a dielectric filled cavity has been analyzed by the same method [23]. Cut-off wavenumbers of partially dielectric filled waveguides of arbitrary cross section have been determined from such techniques [24]. Conducting strips loaded by dielectric cylinders have been investigated by methods incorporating analytically determined Green's functions in integral equation kernels and numerical solution procedures [25]-[30]. Volume and surface integral equations have been formulated and solved numerically for problems of scattering of plane waves by coated and partially coated cylinders [31]-[33]. Some examples of plane wave scattering from composite cylinders employing differential equation methods are found in [34]-[35].



In recent years, dielectric resonator (DR) antennas have been studied at microwave frequencies [36]. A class of axially symmetric dielectric resonators excited by a coaxial probe extending into the dielectric material from below through a ground plane has been extensively investigated by surface integral equation methods [37]-[43]. Electric and magnetic equivalent surface currents are used as a basis to obtain a system of integro-differential equations. These equations are then solved by the MoM. Dyadic Green's function techniques are well suited for the analysis of probe-excited, hemispherical dielectric resonator antennas [44]-[47]. One of the fundamental configurations of the DR antenna is the axially probe-fed cylindrical DR antenna. Input impedance and radiation characteristics of this antenna have been found from solutions of integral equations possessing analytically determined Green's functions [48]-[49]. Other investigators employ methods based on FDTD [50]. The eigenmode expansion method has been used to evaluate the resonant frequency of these antennas [51]. The eigenmode expansion method has also been used for computing the currents on a dielectric loaded top-hat monopole antenna [52]. The null field formulation has been used to analyze rotationally symmetric dielectric coated antennas [53]. Volume and surface integral equations find application for analyzing dielectric coated wire antennas [54].

In all surface integral equation techniques cited above, both electric and magnetic equivalent currents are incorporated in formulations. Approaches adopted in this report are based on integral equations which involve only equivalent electric currents. If two dielectric regions exist in the structure of interest, two equivalent electric currents are employed in equivalent models from which fields appropriate to the two regions are represented. These currents reside on the boundaries separating homogeneous dielectric regions, and each current is used to represent the field on one or the other side of the boundary. Continuity conditions for tangential electric and magnetic fields are then enforced at the dielectric interface. Once these currents are determined all other electromagnetic quantities can be obtained.

Using two equivalent electric currents at the dielectric interface simplifies the numerical formulation and generally improves the conditioning and, hence, the accuracy of the solution. As is true of mixed current formulations, our method suffers the disadvantage that the resulting integral equations may not have a unique solution at the resonant frequencies of the cavity formed by the dielectric boundaries. Of course, any correct formulation can be modified to arrive at equations whose solution is unique but at the expense of additional equation complexity. In the case of the present work, the conditions under which solutions are not unique can be predicted and avoided without loss of information sought. Therefore, rather than facing the additional complexity attendant to equations which do have unique solutions, we choose to implement the simpler and more efficient analysis while avoiding the false resonances at which non uniqueness occurs. Another feature in any surface integral equation solution method developed for structures involving dielectrics is worthy of mention. The equivalent currents obtained by solving the integral equations are not all "physical currents" which can be related to a real quantity such as a surface current on a perfect conductor. These equivalent currents do enable one to compute true fields in all cases.

We consider in this part arbitrary conductors which may be open or closed, may be disjoint, may have intersecting surfaces, may be completely covered by a single homogeneous dielectric material, or may be partially covered by one dielectric and partially by another. Although the method is applicable to multiple conducting and/or dielectric bodies, a one-conducting and a one-dielectric body example will be considered to illustrate the procedure. Selected results for two dimensional bodies and bodies of revolution are obtained from the computations using this method and are compared with data published by others. We present illustrative data for far fields of two dimensional structures and for input impedance and current distribution of antennas which take the form of dielectric-loaded bodies of revolution.

### 3.2 A Single Homogeneous Dielectric Body

Consider the homogeneous dielectric body of Figure 3-1(a) in homogeneous space with bounding surface  $S$ . The surface  $S$  represents the interface between the dielectric-filled region and the exterior space. The incident field  $(\mathbf{E}^i, \mathbf{H}^i)$  is the field produced by external sources in the absence of the scatterer. The properties of the regions exterior and interior to the dielectric body are characterized by the medium parameters  $(\mu_e, \epsilon_e)$  and  $(\mu_d, \epsilon_d)$ , respectively. In Figure 3-1(a), the total field outside the dielectric region is represented by  $(\mathbf{E}^e, \mathbf{H}^e)$  while the field inside is represented by  $(\mathbf{E}^d, \mathbf{H}^d)$ . Both media may be lossless or lossy. Guided by the uniqueness theorem, we develop two models, one of which is electromagnetically equivalent to the original structure and field outside the dielectric body while the other is equivalent inside the body.

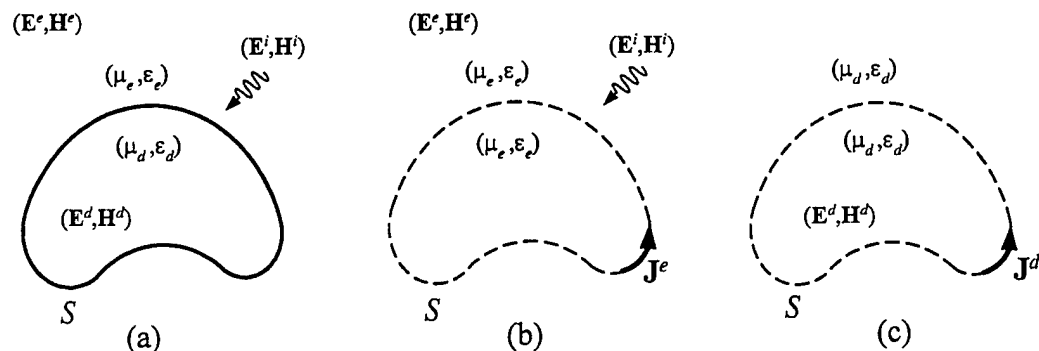


Figure 3-1. A single dielectric body in a homogeneous free space. (a) original problem, (b) exterior equivalence, (c) interior equivalent problem.

A model which can be made equivalent to the original structure and source in the region exterior to  $S$  is shown in Figure 3-1(b). In this model the all space is filled with the homogeneous material  $(\mu_e, \epsilon_e)$  of the external medium, an equivalent electric current  $\mathbf{J}^e$  is placed on an imaginary surface  $S$ , and the original source is restored. The imaginary surface  $S$  is the same as the bounding surface of the body. The total field in the region exterior to the surface  $S$  can be represented as a superposition of the incident field and the field due to  $\mathbf{J}^e$ :

$$\mathbf{E}^e(\mathbf{r}) = \mathbf{E}^i(\mathbf{r}) + \mathcal{E}^e(\mathbf{r}; \mathbf{J}^e) \quad (0.1)$$

$$\mathbf{H}^e(\mathbf{r}) = \mathbf{H}^i(\mathbf{r}) + \mathcal{H}^e(\mathbf{r}; \mathbf{J}^e). \quad (0.2)$$

In the model constructed to be equivalent, ultimately, to the original structure interior to  $S$ , the entire space is filled with the material  $(\mu_d, \epsilon_d)$  of the interior region and on the imaginary surface  $S$  an electric surface current  $\mathbf{J}^d$  is introduced as illustrated in Figure 3-1(c). The total field interior to the surface  $S$  in the model of Figure 3-1(c) is due to  $\mathbf{J}^d$  only

$$\mathbf{E}^d(\mathbf{r}) = \mathcal{E}^d(\mathbf{r}; \mathbf{J}^d) \quad (0.3)$$

$$\mathbf{H}^d(\mathbf{r}) = \mathcal{H}^d(\mathbf{r}; \mathbf{J}^d). \quad (0.4)$$

Enforcing the continuity of tangential components of the total electric and magnetic fields at  $S$ , we obtain two coupled equations in terms of the two unknown surface electric currents as

$$[\mathcal{E}^e(\mathbf{r}; \mathbf{J}^e) - \mathcal{E}^d(\mathbf{r}; \mathbf{J}^d)]_{tan} = -[\mathbf{E}^i(\mathbf{r})]_{tan}, \quad \mathbf{r} \in S \quad (0.5)$$

$$[\mathcal{H}^{e\downarrow}(\mathbf{r}; \mathbf{J}^e) - \mathcal{H}^{d\uparrow}(\mathbf{r}; \mathbf{J}^d)]_{tan} = -[\mathbf{H}^i(\mathbf{r})]_{tan}, \quad \mathbf{r} \in S. \quad (0.6)$$

In (0.6), the superscripts “ $\downarrow$ ” and “ $\uparrow$ ” indicate that the surface  $S$  is approached from the exterior and interior, respectively.

The fields due to the equivalent currents  $\mathbf{J}^e$  and  $\mathbf{J}^d$  are expressed in terms of vector and scalar potentials which incorporate homogeneous space Green's functions appropriate for the medium of each equivalent model. This causes the fields to satisfy Maxwell's equations in the two models and the radiation condition is satisfied by selecting the “outward wave” Green's function for the potentials of the fields in the exterior model. The fields determined as prescribed above satisfy Maxwell's equations and the radiation condition and they approach common values at points on the surface  $S$ . Hence, the conditions of the uniqueness theorem are satisfied implying that the fields of the equivalent models are unique. The fields of the equivalent models satisfy all conditions of the fields in the originally specified structure and sources, so the unique fields of the equivalent models are identical to the unique original fields.

### 3.3 Conductor Surrounded by a Dielectric

In Figure 3-2(a) is illustrated a pec body which is completely surrounded by a homogeneous region containing dielectric material characterized by  $(\mu_d, \epsilon_d)$ . The dielectric-surrounded pec body is in turn embedded in a homogeneous material which extends to infinity and in which resides a source as illustrated in Figure 3-2(a).  $S_c$  denotes the surface of the pec body and  $S_d$  denotes the interface between the exterior-most region and that immediately surrounding the pec body. The dielectric-surrounded conducting body is illuminated by the incident field  $(\mathbf{E}^i, \mathbf{H}^i)$ , which is that field which would exist if the conductor and its surrounding dielectric were removed and the entire space were filled with the material of the outer-most region. We develop two models, one of which is electromagnetically equivalent to the original structure and fields in the region outside  $S_d$  and the other of which is equivalent in the region between  $S_d$  and  $S_c$ .

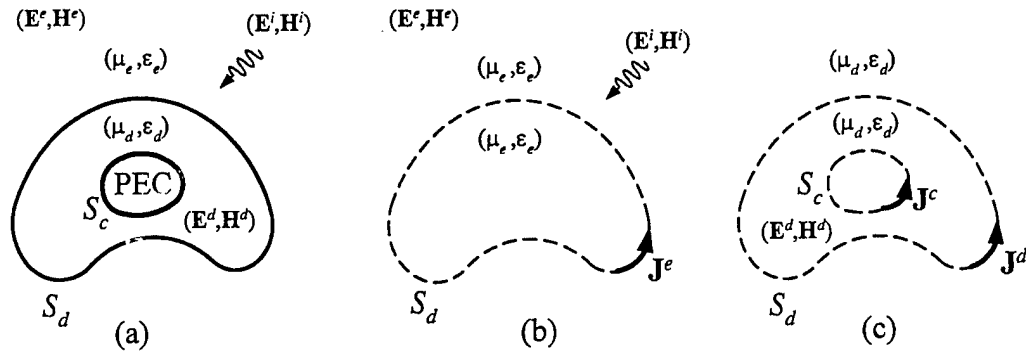


Figure 3-2. A conductor coated by dielectric. (a) original problem, (b) exterior equivalence, (c) interior equivalent problem.

A model equivalent to the original problem in the region exterior to  $S_d$  is shown in Figure 3-2(b). In this model all space is filled with the homogeneous material  $(\mu_e, \epsilon_e)$  of the external medium, the original source is placed in its original position, and an electric surface current  $\mathbf{J}^e$  is impressed on the imaginary surface  $S_d$ . The total field in the region exterior to the surface  $S_d$  of the original structure can be represented as a superposition of the incident field and field due to  $\mathbf{J}^e$  as

$$\mathbf{E}^e(\mathbf{r}) = \mathbf{E}^i(\mathbf{r}) + \mathcal{E}^e(\mathbf{r}; \mathbf{J}^e) \quad (0.7)$$

$$\mathbf{H}^e(\mathbf{r}) = \mathbf{H}^i(\mathbf{r}) + \mathcal{H}^e(\mathbf{r}; \mathbf{J}^e). \quad (3.8)$$

Next, a model is constructed in such a way as to be equivalent to the original structure and field interior to  $S_d$  and exterior to  $S_c$ , the bounding surface of the conductor. All space, including that inside  $S_d$ , is filled with material found in the region surrounding the conductor and characterized by  $(\mu_d, \epsilon_d)$ , as shown in Figure 3-2(c). On the imaginary surfaces  $S_d$  and  $S_c$ , electric surface currents  $\mathbf{J}^d$  and  $\mathbf{J}^c$ , respectively, are introduced. The total field interior to the surface  $S_d$  and outside of  $S_c$  is due to  $\mathbf{J}^d$  and  $\mathbf{J}^c$  radiating in concert and can be expressed in the form

$$\mathbf{E}^d(\mathbf{r}) = \mathcal{E}^d(\mathbf{r}; \mathbf{J}^d) + \mathcal{E}^d(\mathbf{r}; \mathbf{J}^c) \quad (0.8)$$

$$\mathbf{H}^d(\mathbf{r}) = \mathcal{H}^d(\mathbf{r}; \mathbf{J}^d) + \mathcal{H}^d(\mathbf{r}; \mathbf{J}^c). \quad (0.9)$$

Expressing all fields due to currents in terms of potentials, one is ensured that Maxwell's equations are satisfied and, using the "outward wave" form of the homogeneous-space Green's function in the outer-most region, one is ensured that the radiation condition is honored. Enforcing continuity of tangential components of the total electric and magnetic fields at  $S_d$  and the boundary condition that the total tangential component of electric field vanish on  $S_c$ , one adds what is needed to satisfy the conditions of the uniqueness theorem of electromagnetics and arrives at three coupled integral equations in terms of the three unknown surface electric currents with the incident electric and magnetic fields as forcing functions:

$$[\mathcal{E}^e(\mathbf{r}; \mathbf{J}^e) - \mathcal{E}^d(\mathbf{r}; \mathbf{J}^d) - \mathcal{E}^d(\mathbf{r}; \mathbf{J}^c)]_{tan} = -[\mathbf{E}^i(\mathbf{r})]_{tan}, \quad \mathbf{r} \in S_d \quad (0.10)$$

$$[\mathcal{H}^e(\mathbf{r}; \mathbf{J}^e) - \mathcal{H}^d(\mathbf{r}; \mathbf{J}^d) - \mathcal{H}^d(\mathbf{r}; \mathbf{J}^c)]_{tan} = -[\mathbf{H}^i(\mathbf{r})]_{tan}, \quad \mathbf{r} \in S_d \quad (0.11)$$

$$[\mathcal{E}^d(\mathbf{r}; \mathbf{J}^d) + \mathcal{E}^d(\mathbf{r}; \mathbf{J}^c)]_{tan} = 0, \quad \mathbf{r} \in S_c. \quad (0.12)$$

### 3.4 Disjoint Conductor and Dielectric

Figure 3-3(a) illustrates separate dielectric and conducting bodies. If the two bodies are allowed to approach one another, one obtains a partially surrounded conductor or a partially coated conductor. One approach to the problem of a partially coated conductor is to treat the dielectric and conductor as disjoint but allow them to become arbitrarily close, *i.e.*, the distance of separation becomes vanishingly small relative to wavelength. The surfaces may be taken to be in contact or may be thought of as sharing a common surface or interface. In Figure 3-3(a)  $S_c$  and  $S_d$  represent the surfaces of the separate conducting and dielectric bodies. This composite structure is illuminated by the incident field  $(\mathbf{E}^i, \mathbf{H}^i)$ . Again making use of equivalent currents, one can postulate two models for this structure, one valid inside the dielectric and the other outside.

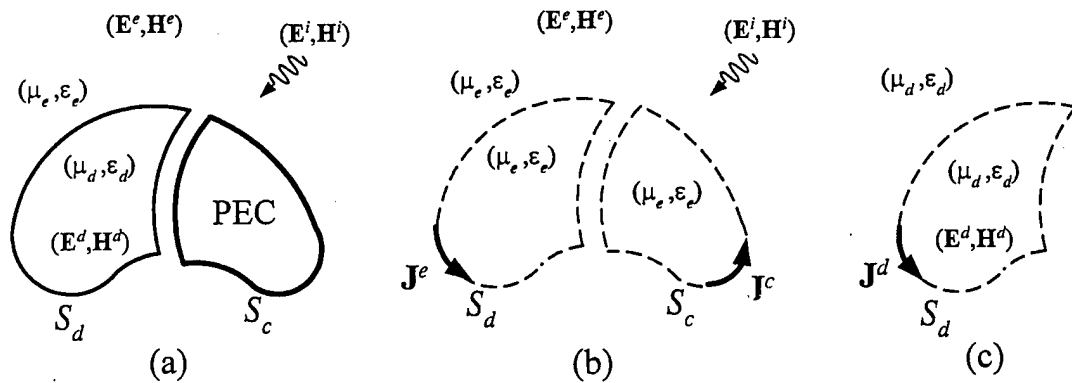


Figure 3-3. Disjoint conductor and dielectric. (a) original problem, (b) exterior equivalence, (c) interior equivalent problem.

A model equivalent to the original problem in the region exterior to  $S_d$  and  $S_c$  is shown in Figure 3-3(b). In this model the dielectric and conducting bodies are replaced by imaginary surfaces  $S_d$  and  $S_c$ , respectively, and the entire region is filled with the homogeneous material  $(\mu_e, \epsilon_e)$  of the exterior medium. Surface electric current  $\mathbf{J}^e$  and  $\mathbf{J}^c$  are impressed on  $S_d$  and  $S_c$ , respectively. The total field in the region exterior to both surfaces  $S_d$  and  $S_c$  can be expressed as the sum of the incident field and the fields radiated by the currents  $\mathbf{J}^e$  and  $\mathbf{J}^c$ :

$$\mathbf{E}^e(\mathbf{r}) = \mathbf{E}^i(\mathbf{r}) + \mathcal{E}^e(\mathbf{r}; \mathbf{J}^e) + \mathcal{E}^e(\mathbf{r}; \mathbf{J}^c) \quad (0.13)$$

$$\mathbf{H}^e(\mathbf{r}) = \mathbf{H}^i(\mathbf{r}) + \mathcal{H}^e(\mathbf{r}; \mathbf{J}^e) + \mathcal{H}^e(\mathbf{r}; \mathbf{J}^c). \quad (0.14)$$

In the model constructed to be equivalent to the original structure interior to  $S_d$ , all space is filled with the material of the dielectric medium  $(\mu_d, \epsilon_d)$  as illustrated in Figure 3-3(c). On the imaginary surface  $S_d$ , a surface electric current  $\mathbf{J}^d$  is introduced. Note that the field interior to the surface  $S_d$  is due to  $\mathbf{J}^d$  only:

$$\mathbf{E}^d(\mathbf{r}) = \mathcal{E}^d(\mathbf{r}; \mathbf{J}^d) \quad (0.15)$$

$$\mathbf{H}^d(\mathbf{r}) = \mathcal{H}^d(\mathbf{r}; \mathbf{J}^d) \quad (0.16)$$

Requiring continuity of tangential electric and magnetic fields at the surface  $S_d$  and forcing the tangential component of the electric field to be zero on  $S_c$  leads to

$$\left[ \mathbf{E}^e(\mathbf{r}; \mathbf{J}^e) - \mathbf{E}^d(\mathbf{r}; \mathbf{J}^d) + \mathbf{E}^e(\mathbf{r}; \mathbf{J}^c) \right]_{tan} = -\left[ \mathbf{E}^i(\mathbf{r}) \right]_{tan}, \quad \mathbf{r} \in S_d \quad (0.17)$$

$$\left[ \mathcal{H}^{e\downarrow}(\mathbf{r}; \mathbf{J}^e) - \mathcal{H}^{d\uparrow}(\mathbf{r}; \mathbf{J}^d) + \mathcal{H}^{e\downarrow}(\mathbf{r}; \mathbf{J}^c) \right]_{tan} = -\left[ \mathbf{H}^i(\mathbf{r}) \right]_{tan}, \quad \mathbf{r} \in S_d \quad (0.18)$$

$$\left[ \mathcal{E}^e(\mathbf{r}; \mathbf{J}^e) + \mathcal{E}^e(\mathbf{r}; \mathbf{J}^c) \right]_{tan} = -\left[ \mathbf{E}^i(\mathbf{r}) \right]_{tan}, \quad \mathbf{r} \in S_c. \quad (0.19)$$

### 3.5 Conductor and Dielectric Intersecting

Figure 3-4(a) shows a conducting body partially covered by a dielectric object. The surfaces  $S_{ce}$ ,  $S_{cd}$  and  $S_{de}$  refer to the boundaries between the conductor and the exterior region, the conductor and the dielectric region, and the dielectric and the exterior region, respectively. The dielectric region is filled with a homogeneous material characterized by  $(\mu_d, \epsilon_d)$  and is bounded by two surfaces  $S_{cd}$  and  $S_{de}$ . The exterior region is characterized by  $(\mu_e, \epsilon_e)$  and have an interface with the surfaces  $S_{ce}$  and  $S_{de}$ . The sources are provided in the exterior region only. The total field vectors within the dielectric and the exterior region are represented by  $(\mathbf{E}^d, \mathbf{H}^d)$  and  $(\mathbf{E}^e, \mathbf{H}^e)$ , respectively. This composite structure is illuminated by the incident field  $(\mathbf{E}^i, \mathbf{H}^i)$ . According to the field equivalence principle one can postulate two models for this structure, one is valid inside the dielectric and the other outside.



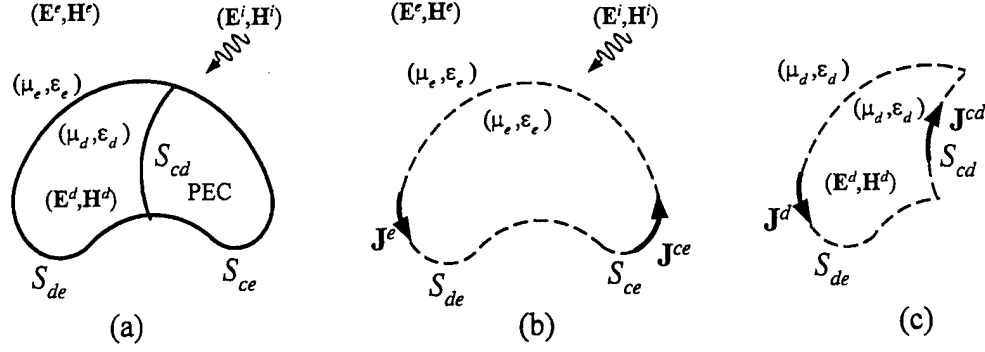


Figure 3-4. Conductor and dielectric intersecting. (a) original problem, (b) exterior equivalence, (c) interior equivalent problem.

A model equivalent to the original problem in the region exterior to  $S_{de}$  and  $S_{ce}$  is shown in Figure 3-4(b). In this model the entire region is filled with the homogeneous material  $(\mu_e, \epsilon_e)$  of the exterior medium. Surface electric currents  $J^e$  and  $J^{ce}$  are impressed on  $S_{de}$  and  $S_{ce}$ , respectively. The total field in this region can be expressed as the sum of the incident field and the fields radiated by the currents  $J^e$  and  $J^{ce}$ :

$$E^e(r) = E^i(r) + \mathcal{E}^e(r; J^e) + \mathcal{E}^e(r; J^{ce}) \quad (0.20)$$

$$H^e(r) = H^i(r) + \mathcal{H}^e(r; J^e) + \mathcal{H}^e(r; J^{ce}). \quad (0.21)$$

In the model constructed to be equivalent to the original structure interior to  $S_{de}$  and  $S_{cd}$ , all space is filled with the material of the dielectric medium  $(\mu_d, \epsilon_d)$  as shown in Figure 3-4(c). On  $S_{de}$  and  $S_{cd}$ , surface electric currents  $J^d$  and  $J^{cd}$  are introduced, respectively. The total field in the dielectric region is due to  $J^d$  and  $J^{cd}$ :

$$E^d(r) = \mathcal{E}^d(r; J^d) + \mathcal{E}^d(r; J^{cd}) \quad (0.22)$$

$$H^d(r) = \mathcal{H}^d(r; J^d) + \mathcal{H}^d(r; J^{cd}). \quad (0.23)$$

Enforcing the following boundary conditions

$$E_{\tan}^d = 0 \quad \text{on } S_{cd}, \quad (0.24)$$

$$E_{\tan}^e = 0 \quad \text{on } S_{ce}, \quad (0.25)$$

$$E_{\tan}^d = E_{\tan}^e \quad \text{on } S_{ce}, \quad (0.26)$$

$$H_{\tan}^{d\uparrow} = H_{\tan}^{e\downarrow} \quad \text{on } S_{ce}, \quad (0.27)$$

we obtain the following integral equations written in an operator form in terms of the equivalent currents as

$$\left[ \mathcal{E}^d(\mathbf{r}; \mathbf{J}^d) + \mathcal{E}^d(\mathbf{r}; \mathbf{J}^{cd}) \right]_{\tan} = 0 \quad \text{on } S_{cd} \quad (0.28)$$

$$\left[ \mathcal{E}^e(\mathbf{r}; \mathbf{J}^e) + \mathcal{E}^e(\mathbf{r}; \mathbf{J}^{ce}) \right]_{\tan} = -\mathbf{E}_{\tan}^i(\mathbf{r}) \quad \text{on } S_{ce} \quad (0.29)$$

$$\left[ \mathcal{E}^e(\mathbf{r}; \mathbf{J}^e) + \mathcal{E}^e(\mathbf{r}; \mathbf{J}^e) - \mathcal{E}^d(\mathbf{r}; \mathbf{J}^d) - \mathcal{E}^d(\mathbf{r}; \mathbf{J}^{cd}) \right]_{\tan} = -\mathbf{E}_{\tan}^i(\mathbf{r}) \quad \text{on } S_{de} \quad (0.30)$$

$$\left[ \mathcal{H}^{e\downarrow}(\mathbf{r}; \mathbf{J}^e) + \mathcal{H}^{e\downarrow}(\mathbf{r}; \mathbf{J}^{ce}) - \mathcal{H}^{d\uparrow}(\mathbf{r}; \mathbf{J}^d) - \mathcal{H}^{d\uparrow}(\mathbf{r}; \mathbf{J}^{cd}) \right]_{\tan} = -\mathbf{H}_{\tan}^i(\mathbf{r}) \quad \text{on } S_{de} \quad (0.31)$$

The operator equations from (0.1) through (0.31) are computed from

$$\mathcal{E}^{e,d}(\mathbf{r}; \mathbf{J}^{e,d}) = -j\omega \mathbf{A}^{e,d} - \nabla \Phi^{e,d} \quad (0.32)$$

$$\mathcal{H}^{e,d}(\mathbf{r}; \mathbf{J}^{e,d}) = \frac{1}{\mu_{e,d}} \nabla \times \mathbf{A}^{e,d} \quad (0.33)$$

### 3.6 Numerical Solution

Having formulated the E-field and H-field operator equations for the induced currents on the surface of pec bodies, we can now determine the interaction of sources with dielectric bodies or with bodies comprising part dielectric and part conductor. The operators in the EFIE and the HFIE analysis are exactly those needed for the numerical solution of homogeneous dielectric bodies, conductors surrounded by dielectric regions, and conducting bodies partially surrounded by dielectrics.

**Dielectric Body.** The currents  $\mathbf{J}^e$  and  $\mathbf{J}^d$  in equation (0.5) are expanded in series of triangle basis functions and the equations are tested with pulse functions as is outlined in the description of the method employed to solve the EFIE. Similarly, the currents  $\mathbf{J}^e$  and  $\mathbf{J}^d$  in equation (0.6) are expanded in linear combinations of pulse basis functions and the equations are point matched as discussed in the section on the HFIE analysis. The matrix equation for the expansion coefficients for the equivalent currents needed to determine coupling to a dielectric body can be expressed in the simple form below:

$$\begin{bmatrix} [Z_{mn}^e]_{N_d \times N_d} & [-Z_{mn}^d]_{N_d \times N_d} \\ [\Gamma_{mn}^{e\downarrow}]_{N_d \times N_d} & [-\Gamma_{mn}^{d\uparrow}]_{N_d \times N_d} \end{bmatrix} \begin{bmatrix} [I_n^e]_{N_d \times 1} \\ [I_n^d]_{N_d \times 1} \end{bmatrix} = \begin{bmatrix} [V_m^i]_{N_d \times 1} \\ [I_m^i]_{N_d \times 1} \end{bmatrix}. \quad (0.34)$$

Solution of (0.34) yields the column vectors  $[I_n^e]$  and  $[I_n^d]$  which are the coefficients of the basis function expansions of the unknown currents. With these current known, one can determine all quantities of interest.

**Conductor Surrounded by a Dielectric.** In the case of a conductor surrounded by a dielectric, the currents  $\mathbf{J}^e$ ,  $\mathbf{J}^d$  and  $\mathbf{J}^c$  in (0.10) and (0.12) are expanded in triangle basis functions and the equations are tested with pulse functions. Similarly, the currents  $\mathbf{J}^e$ ,  $\mathbf{J}^d$  and  $\mathbf{J}^c$  in the HFIE of (0.11) are expanded in pulse basis functions and the equation is point matched. The matrix equation for a dielectric coated pec body becomes

$$\begin{bmatrix} [Z_{mn}^e]_{N_d \times N_d} & [-Z_{mn}^d]_{N_d \times N_d} & [Z_{mn}^e]_{N_d \times N_c} \\ [\Gamma_{mn}^{e\downarrow}]_{N_d \times N_d} & [-\Gamma_{mn}^{d\uparrow}]_{N_d \times N_d} & [\Gamma_{mn}^{e\downarrow}]_{N_d \times N_c} \\ [0]_{N_c \times N_d} & [Z_{mn}^d]_{N_c \times N_d} & [Z_{mn}^d]_{N_c \times N_c} \end{bmatrix} \begin{bmatrix} [I_n^e]_{N_d \times 1} \\ [I_n^d]_{N_d \times 1} \\ [I_n^c]_{N_c \times 1} \end{bmatrix} = \begin{bmatrix} [V_m^i]_{N_d \times 1} \\ [I_m^i]_{N_d \times 1} \\ [V_m^i]_{N_c \times 1} \end{bmatrix}. \quad (0.35)$$

**Disjoint Conductor and Dielectric.** Similarly, the matrix equation for the expansion coefficients associated with a partially coated pec body can be expressed in the form

$$\begin{bmatrix} [Z_{mn}^e]_{N_d \times N_d} & [-Z_{mn}^d]_{N_d \times N_d} & [Z_{mn}^e]_{N_d \times N_c} \\ [\Gamma_{mn}^{e\downarrow}]_{N_d \times N_d} & [-\Gamma_{mn}^{d\uparrow}]_{N_d \times N_d} & [\Gamma_{mn}^{e\downarrow}]_{N_d \times N_c} \\ [Z_{mn}^e]_{N_c \times N_d} & [0]_{N_c \times N_d} & [Z_{mn}^e]_{N_c \times N_c} \end{bmatrix} \begin{bmatrix} [I_n^e]_{N_d \times 1} \\ [I_n^d]_{N_d \times 1} \\ [I_n^c]_{N_c \times 1} \end{bmatrix} = \begin{bmatrix} [V_m^i]_{N_d \times 1} \\ [I_m^i]_{N_d \times 1} \\ [V_m^i]_{N_c \times 1} \end{bmatrix}. \quad (0.36)$$

It may be noted that the matrix elements of  $[Z_{mn}^e]_{N_d \times N_d}$ ,  $[-Z_{mn}^d]_{N_d \times N_d}$ , and  $[Z_{mn}^e]_{N_d \times N_c}$  in (0.36) represent the tangential component of the scattered electric field, produced by the

individual basis functions that represent the currents  $\mathbf{J}^e$ ,  $\mathbf{J}^d$ , and  $\mathbf{J}^c$  and tested on the surface  $S_d$ . Techniques for evaluation of these of these matrix elements are presented in the EFIE analysis and hence are not repeated here. The matrix elements of  $[\Gamma_{mn}^{e\downarrow}]_{N_d \times N_d}$ ,  $[-\Gamma_{mn}^{d\uparrow}]_{N_d \times N_d}$ , and  $[\Gamma_{mn}^{e\downarrow}]_{N_d \times N_c}$  represent the tangential components of the scattered magnetic field produced by the basis functions that represent  $\mathbf{J}^e$ ,  $\mathbf{J}^d$ , and  $\mathbf{J}^c$  and tested on the surface  $S_d$ . And the matrix elements of  $[Z_{mn}^e]_{N_c \times N_d}$  and  $[Z_{mn}^e]_{N_c \times N_c}$  represent the tangential component of the scattered electric field produced by the basis function for  $\mathbf{J}^e$  and  $\mathbf{J}^c$  and tested on  $S_d$ . The some elements of one of the submatrices are zero since, in the equivalent model described here, the currents located on the conductor do not interact with the inner medium of the dielectric object.  $N_c$  and  $N_d$  are the numbers of unknown expansion coefficients on the conducting and dielectric surface, respectively. The matrix elements of (0.34) and (0.35) are interpreted accordingly. The numerical solution of (0.28) through (0.31) is performed as in other cases, hence is not given in this section.

From (0.34) to (0.36), the submatrix  $[Z_{mn}^i]$  in which  $i$  implies the characteristics of the medium, is computed in a way similar to that employed to compute the impedance matrix elements of the EFIE analysis. The submatrix  $[\Gamma_{mn}^{i\downarrow\uparrow}]$  is computed in a way analogous to the method for computing the matrix elements of an HFIE analysis. The “ $\uparrow\downarrow$ ” signs indicate from which side a point on a surface is approached.

### 3.7 Results and Discussions

In order to ascertain the correctness of the computer code developed to implement the integral equation formulation and numerical analysis for the coax-can structure of Figure 3-8(d), the equations and analysis have been made general, they have been applied to a number of structures appearing recently in the literature, and the resulting data

obtained have been compared with data available in the literature. Because of the generality of the techniques reported here, a number of problems in the literature that have been solved by other methods can be solved by our method. Several structures/problems in this category have been selected as cases against which to test our work. Several are enumerated below and data are presented. In each case, data from the corresponding solution in the literature are compared and the agreement is found to be very close, lending support to the correctness of our method. However, no attempt is made here to present data of other workers for comparison. The various examples discussed do reveal the versatility of the solution method reported here.

The following are representative structures which can be analyzed by our method to show the interaction of fields in/on conducting and dielectric bodies of arbitrary shape. Figure 3-5 to 3-8 illustrate examples of typical physical structures which the numerical methods presented in this report can be used to analyze. Selected computational results are included in this section to demonstrate the validity of the above integral equations and numerical procedure. All data are validated by analyzing a vacuum coating which, of course, should reduce to the case of a single conductor in open space. The two dimensional operators utilized in this chapter and their numerical solutions are exactly those found in [55]. The operators for bodies of revolution and their numerical solutions are those derived in Chapter 1 and Chapter 2.

Figure 3-9 shows the induced currents on the conducting strip covered by a circular dielectric cylinder [29]. In Figure 3-10 is illustrated the scattered far field pattern of the same structure [28]. Figure 3-11 shows results of TM plane wave scattering from a circular conducting cylinder covered by a circular dielectric cylinder [16] while Figure 3-12 shows data from scattering from a square conducting cylinder covered by square dielectric cylinder [18]. Figure 3-13 depicts scattered far field patterns due to a TM plane wave incident on a square dielectric cylinder backed by a conducting strip [15]. In Figure 3-14 one see data illustrating the magnitude of electric current induced on a metal

backing applied to a portion of the surface of a circular dielectric cylinder excited by a TM plane wave [29]. In Figures 3-15 to 3-20 are presented electric currents induced on conducting strips and the corresponding scattered far field data for the problem of a rectangular dielectric cylinder partially clad by zero thickness conductors and illuminated by TE and TM plane waves [21]-[22]. The current induced on the pec portion of a composite circular cylinder comprising a pec "hemi-cylinder" contiguous with dielectric "hemi-cylinder" illuminated by a TM plane wave is presented in Figure 3-21 [35].

Current induced on a conducting strip partially covered by a circular dielectric cylinder and excited by a TE and TM plane wave is displayed in Figures 3-22 and 3-23 [25]-[26]. The data in Figure 3-24 correspond to the case when the strip just touches the dielectric cylinder. In Figure 3-25 is seen data from which one can study the bistatic scattering cross-section of disjoint circular conducting and circular dielectric cylinders excited by a TE plane wave [21].

In Figure 3-26 is illustrated the input impedance of a circular top-hat monopole antenna loaded by a dielectric "plug" and fed by a coax through an infinite ground plane [52]. The input conductance of a conducting sphere coated by a dielectric layer, plotted against the thickness of the dielectric layer, is given in Figure 3-27 [53]. Input impedance of a hemispherical dielectric resonator antenna, which is a monopole embedded in a hemispherical dielectric material, is presented in Figure 3-28 [45]-[47]. In Figure 3-29 and 3-30 are given the current and input impedance of a monopole antenna in a finite height dielectric cylinder driven by a coaxial line through an infinite ground plane [38].

### 3.8 Observations

We considered structures in this chapter involving a conductor and a dielectric that may be disjoint from each other or may have common surface. A conductor partially surrounded by, and in contact with, a dielectric is obtained by letting the separation be arbitrarily close. The analysis remains valid even if the conductor and dielectric are in

contact or share a common interface. For partially coated and partially clad structures, it is recommended that the interface or surface between the conducting body and dielectric body should be partitioned by the same discretization scheme. Using the same discretization scheme for these common surfaces does not produce a singular moment matrix because the effects of the different bodies are accounted for by different equivalent currents used to represent the fields on the conductor and on opposite sides of a material boundary.

The electromagnetic scattering from a dielectric body partially covered by vanishingly thin conductors is important in designing microwave printed circuits. Partially clad structures can be treated in two different ways: (1) equations are formulated with the conductor completely inside the dielectric body (coated body formulation) or (2) with dielectric and conductor treated as if disjoint. The partially clad case can then be obtained by letting the conductors approach the surface of the dielectric from inside or outside. An important point to note is that the dielectric and conductor are treated no differently when physically separated from the way they are treated when in contact. Distinct expansion functions are used for the current on both the models for the conductor and for the dielectric interface.

The computed results are in excellent agreement with published data available in the literature. One of the advantages of the present method is that it can generate accurate results for high dielectric constants. The algorithm developed can easily be extended to other general cases, such as a body consisting of several piecewise homogeneous material regions, multiple disjoint bodies, and conducting bodies with multi-layered coating. Finally, all the effects of surface waves, wedge diffraction, and the interaction between various dielectric and conducting parts of the system are automatically accounted for in the analysis. However, the method presented here has several limitations. One practical limitation is that it cannot be used for very large structures due to excessive computer time and storage requirements. But this is true of any standard moment method technique.

Reasonably large structures can be handled with the computer facilities available today. Theoretical limitations of this model are its failure at certain resonant frequencies. To circumvent the problem of interior resonance, electric and magnetic equivalent currents must be used at the dielectric interface and boundary conditions on both tangential electric and magnetic field must be satisfied [1].



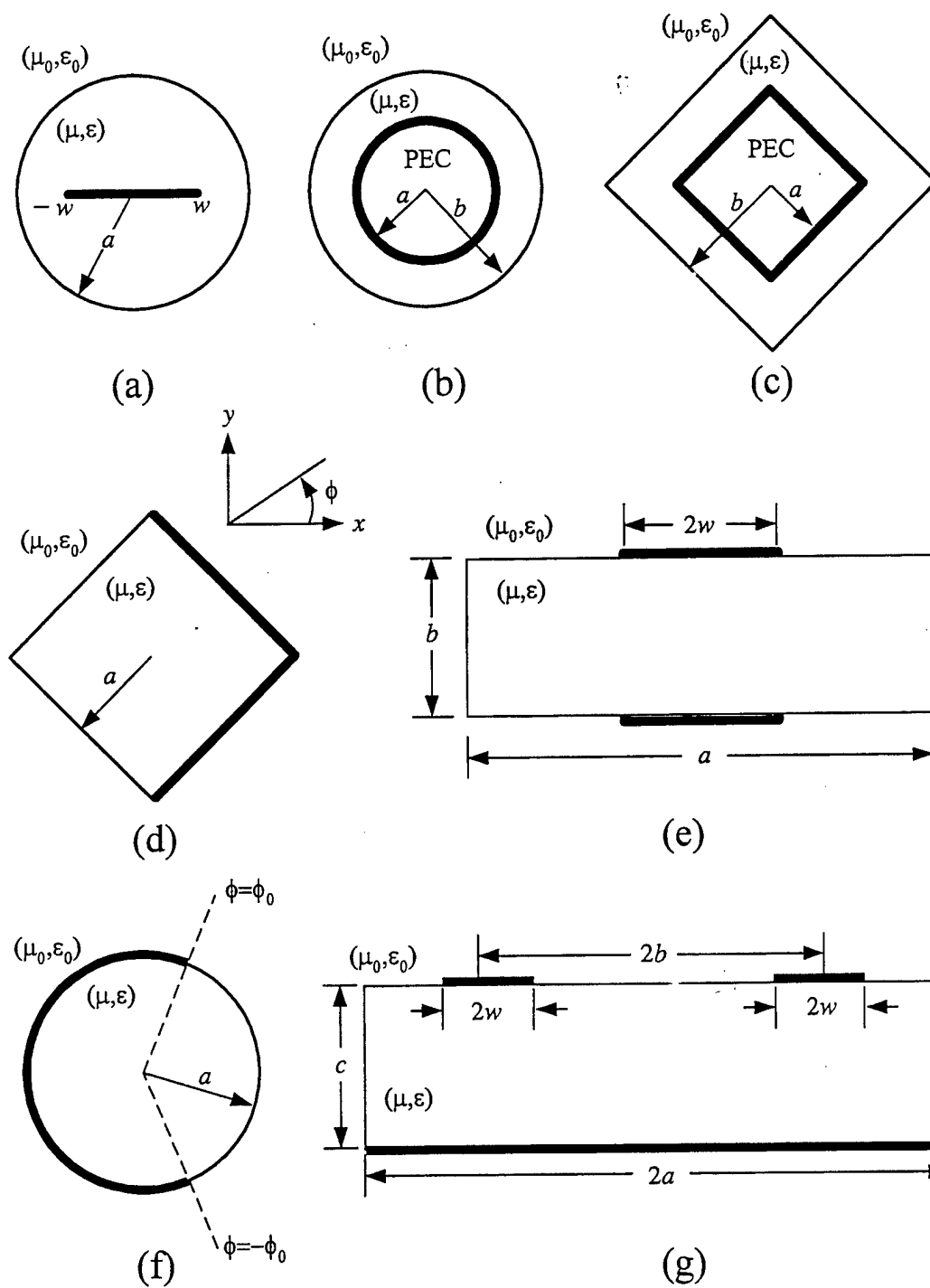


Figure 3-5. Dielectric loaded conducting cylinders. (a), (b) and (c) dielectric coated conducting cylinders, (d), (e), (f), and (g) dielectric cylinders partially clad by zero-thickness conductors.

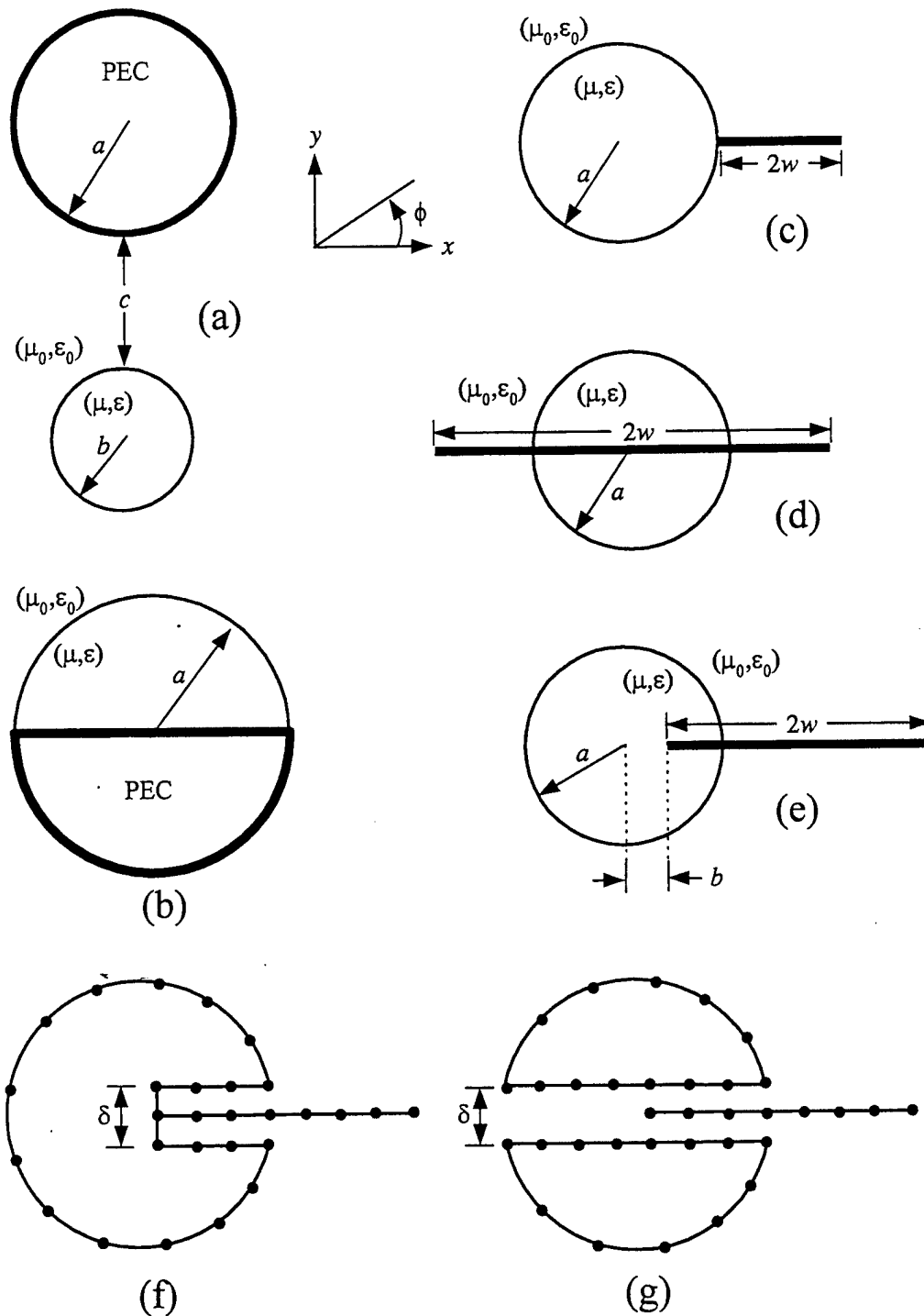


Figure 3-6. (a) and (b) Disjoint conductor and dielectric cylinders. (c), (d), and (e) circular dielectric cylinders loaded by conducting strips, (f) and (g) approaches to solve problem (e).

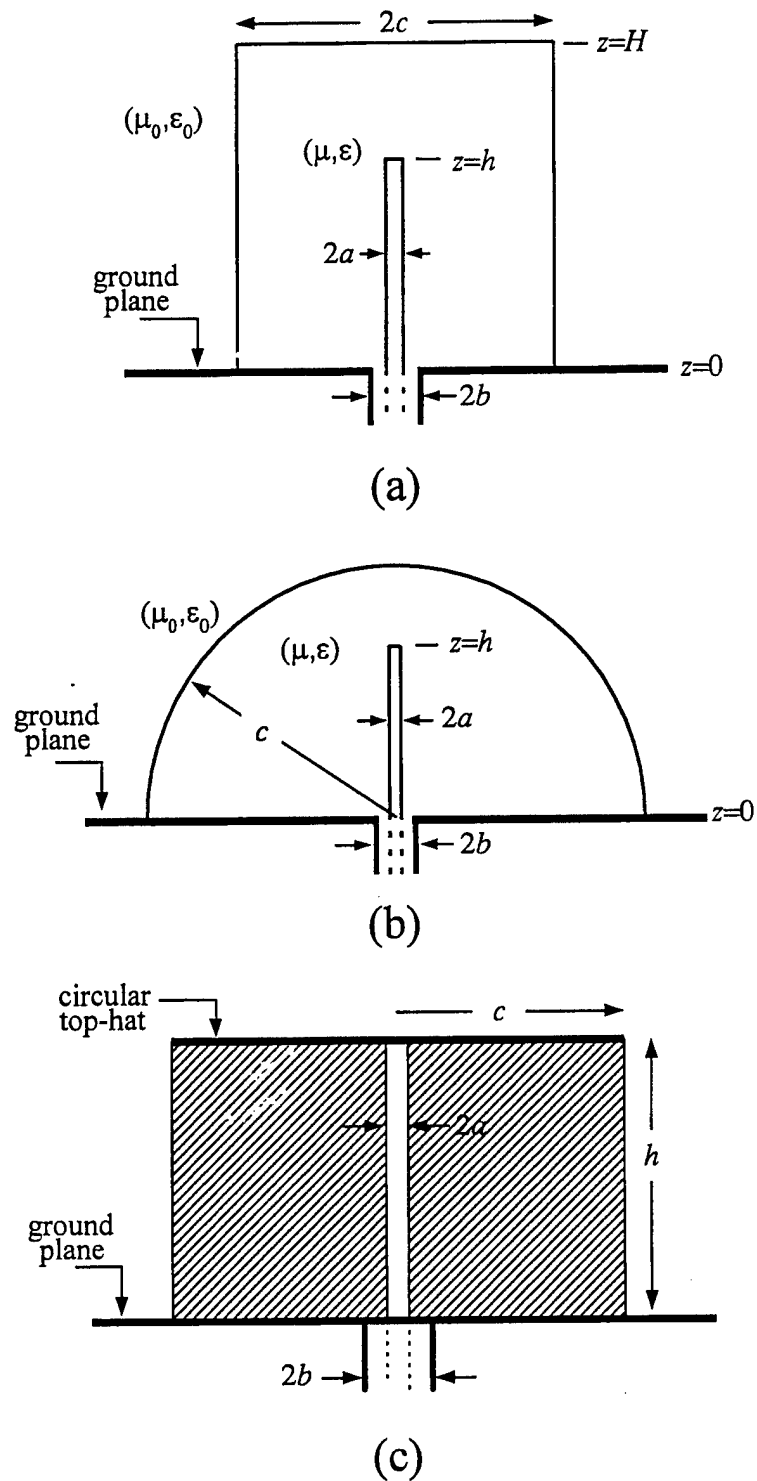


Figure 3-7. Axially symmetric dielectric loaded antennas. (a) cylindrical (b) hemispherical dielectric resonator antennas excited by a coaxial probe extending into the dielectric material through the bottom of the ground plane, (c) dielectric loaded top-hat monopole antenna.

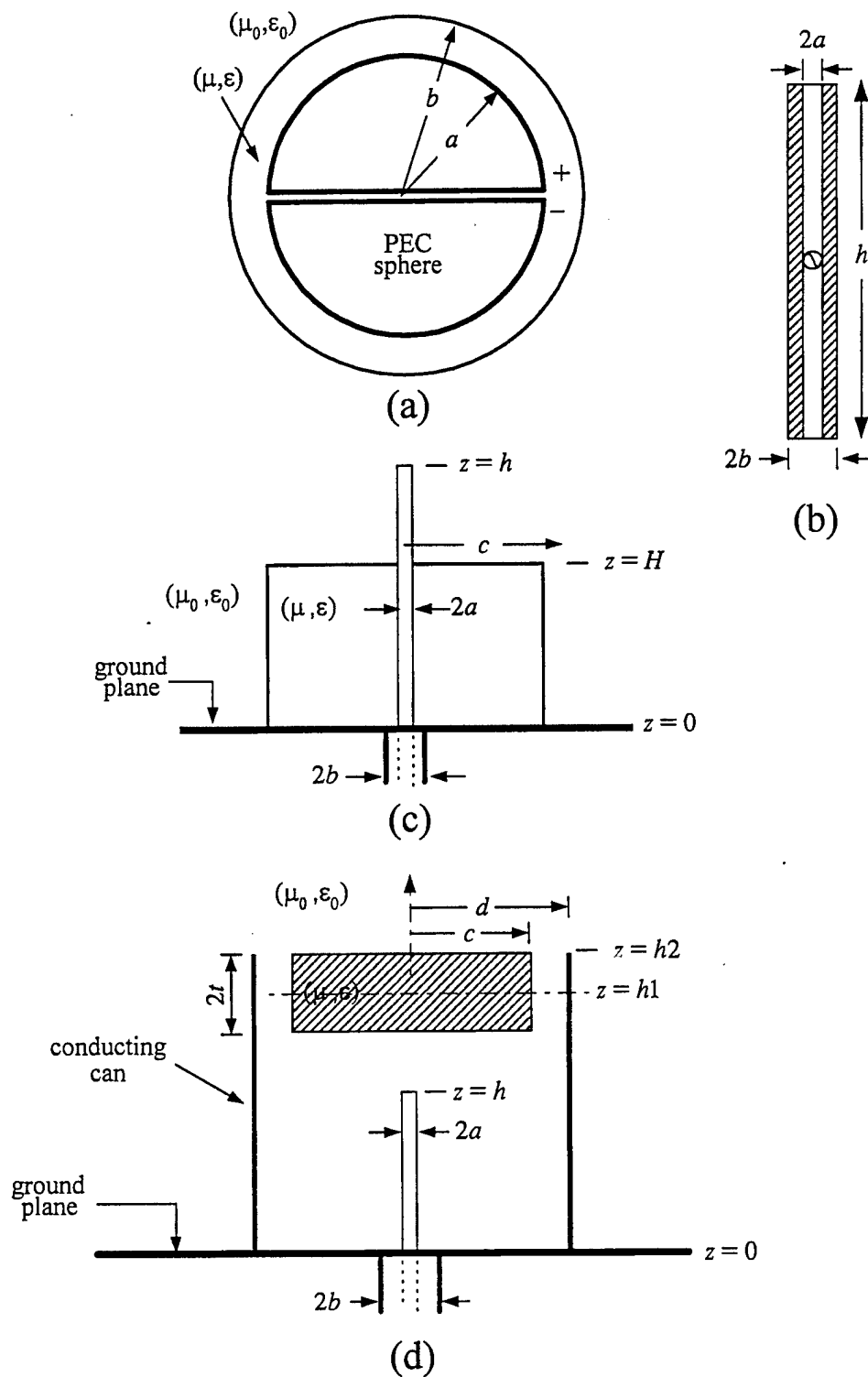


Figure 3-8. Axially symmetric dielectric loaded antennas. (a) dielectric coated conducting sphere (b) wire, (c) monopole protrudes into dielectric BOR through ground plane, (d) monopole in a can loaded by a dielectric BOR over ground plane.

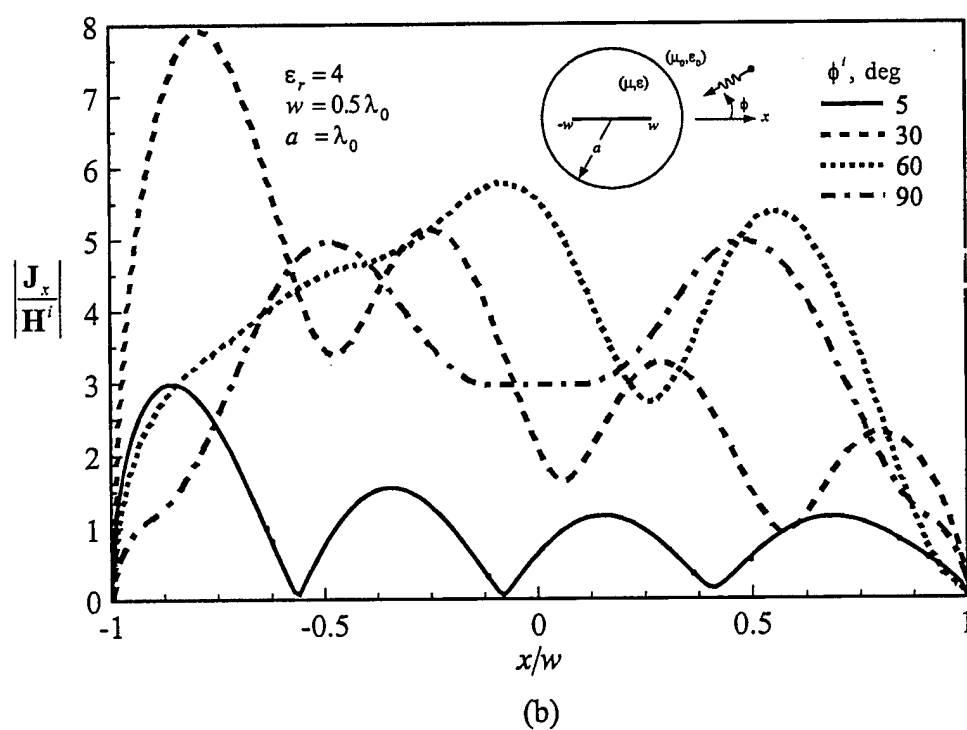
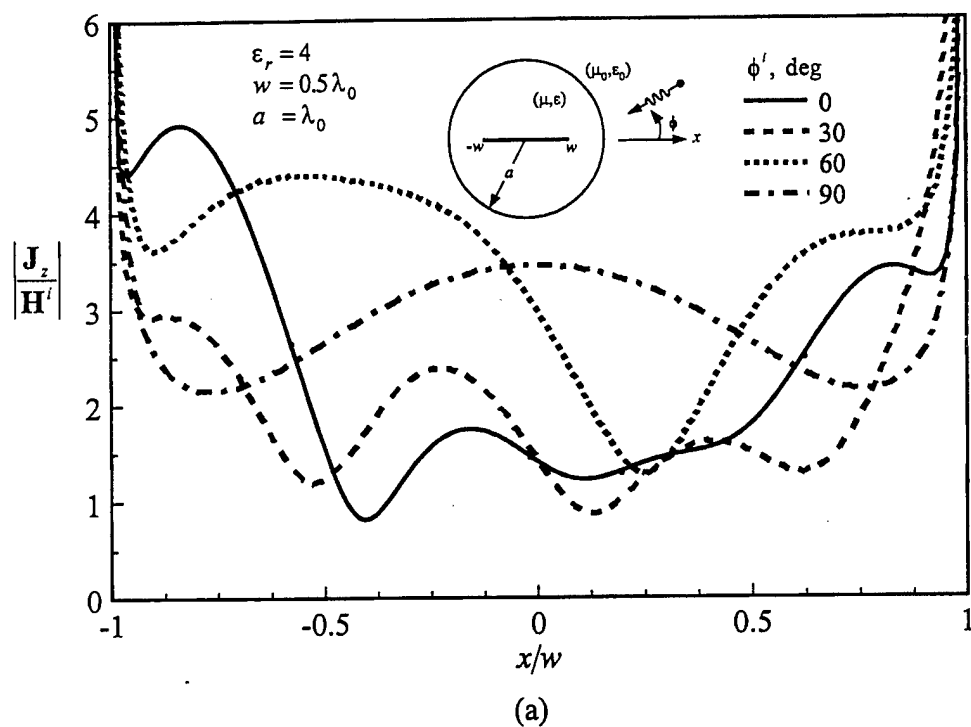


Figure 3-9. Magnitude of current induced on the conducting strip covered by a circular dielectric cylinder. (a) TM case, (b) TE case.

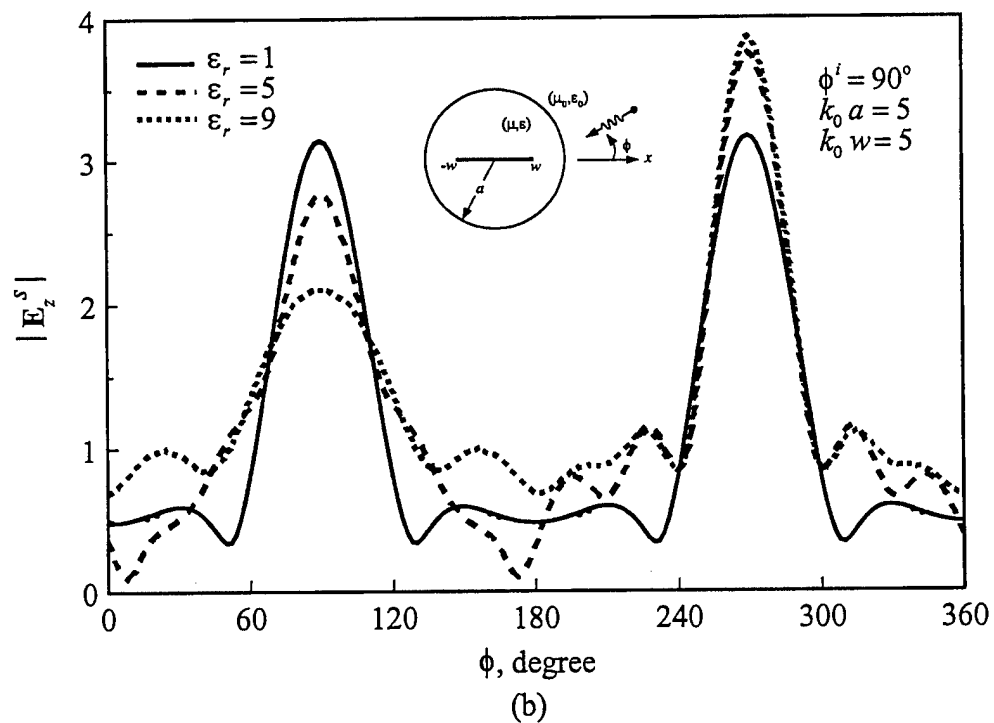
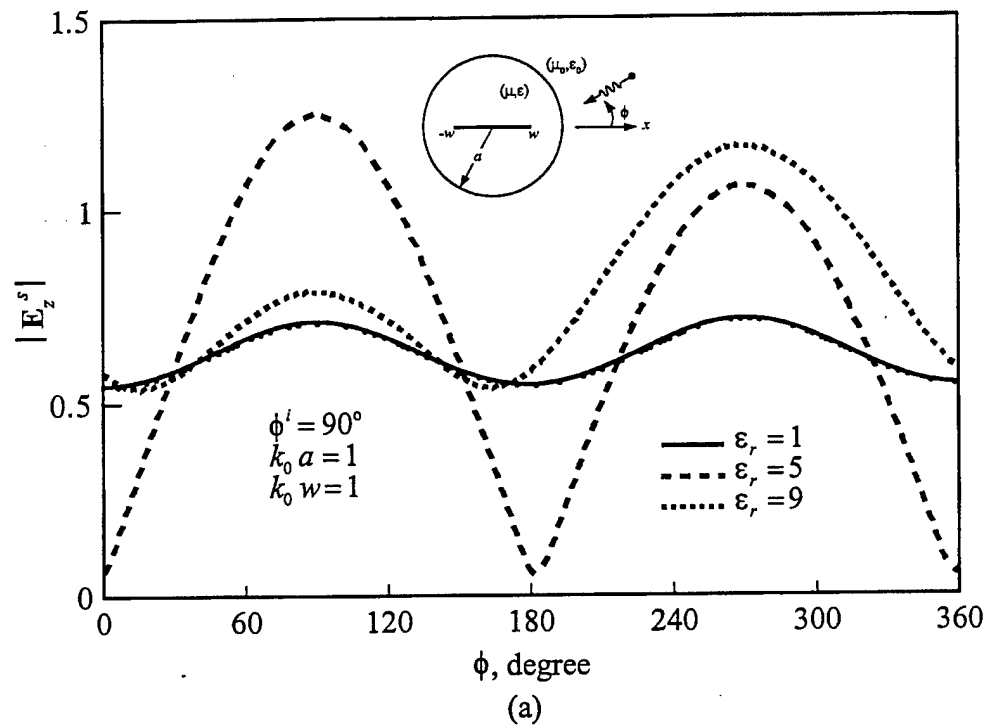


Figure 3-10. Scattered far field pattern due to TM plane wave incident on the conducting strip covered by a circular dielectric cylinder. (a)  $k_0 a = k_0 w = 1$ , (b)  $k_0 a = k_0 w = 5$ .

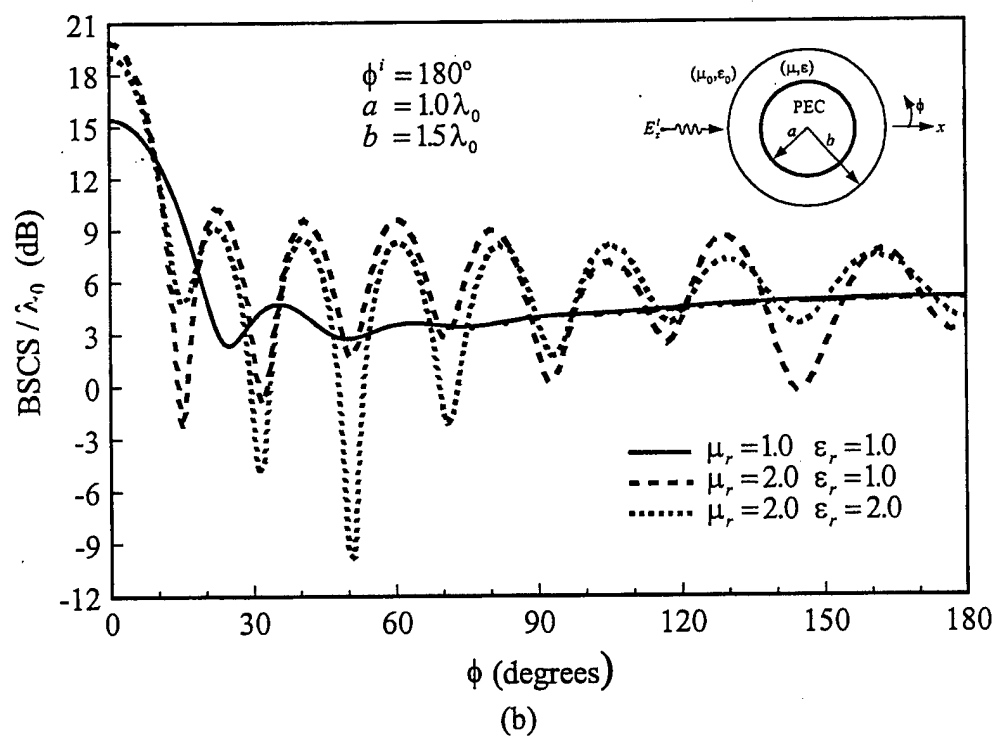
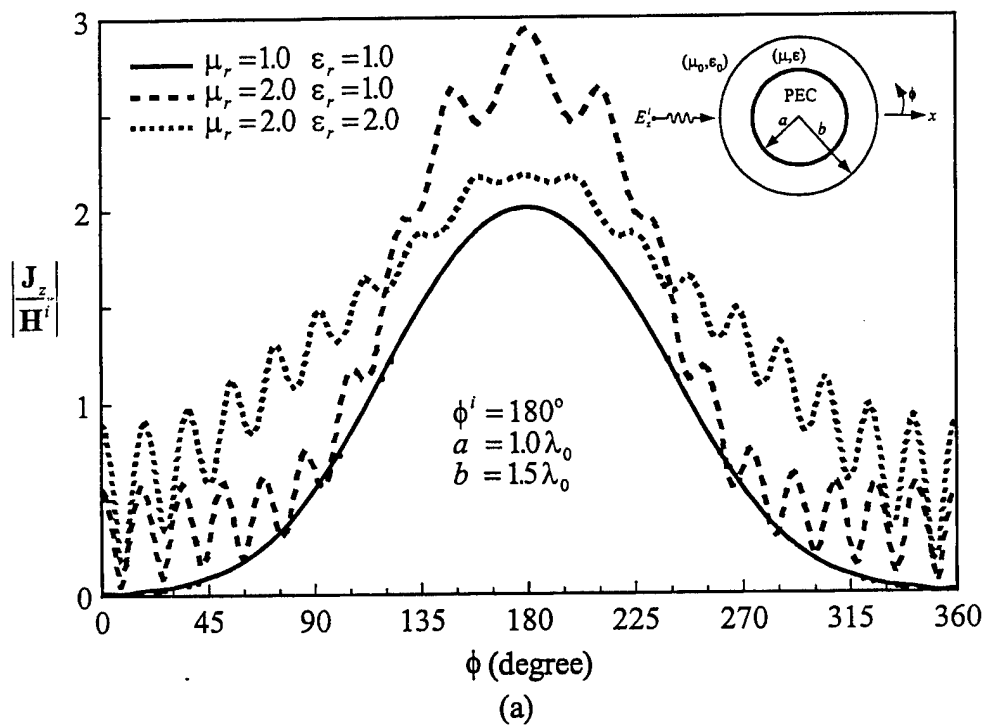


Figure 3-11. TM plane wave scattering from circular conducting cylinder covered by a circular dielectric cylinder. (a) magnitude of current induced on the conducting cylinder, (b) Bistatic radar cross section.

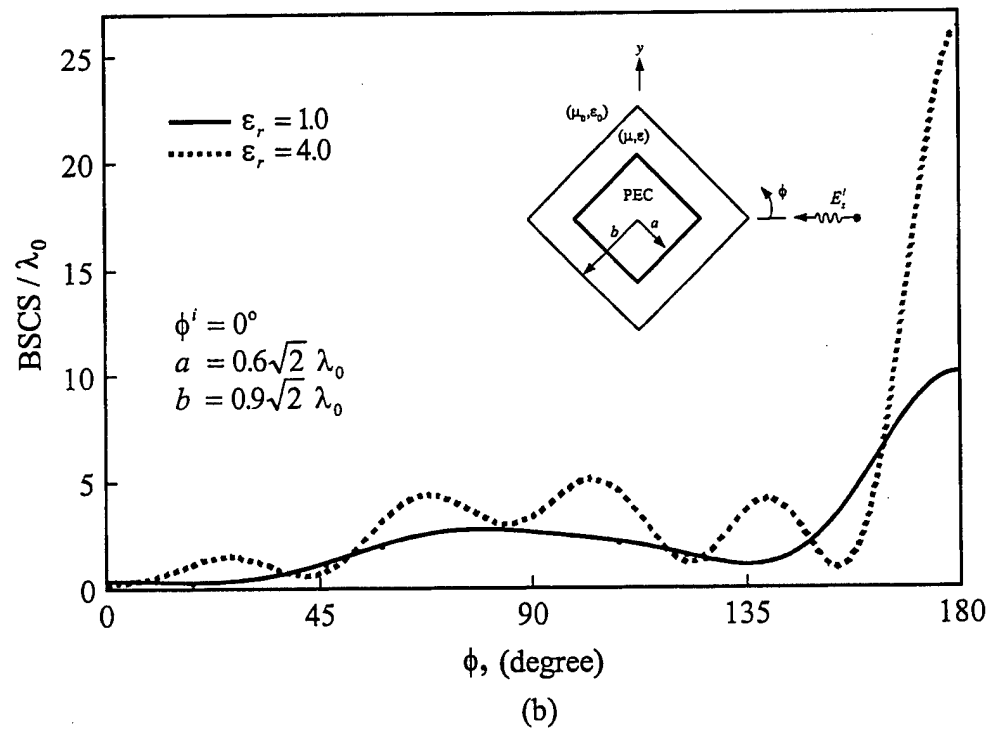
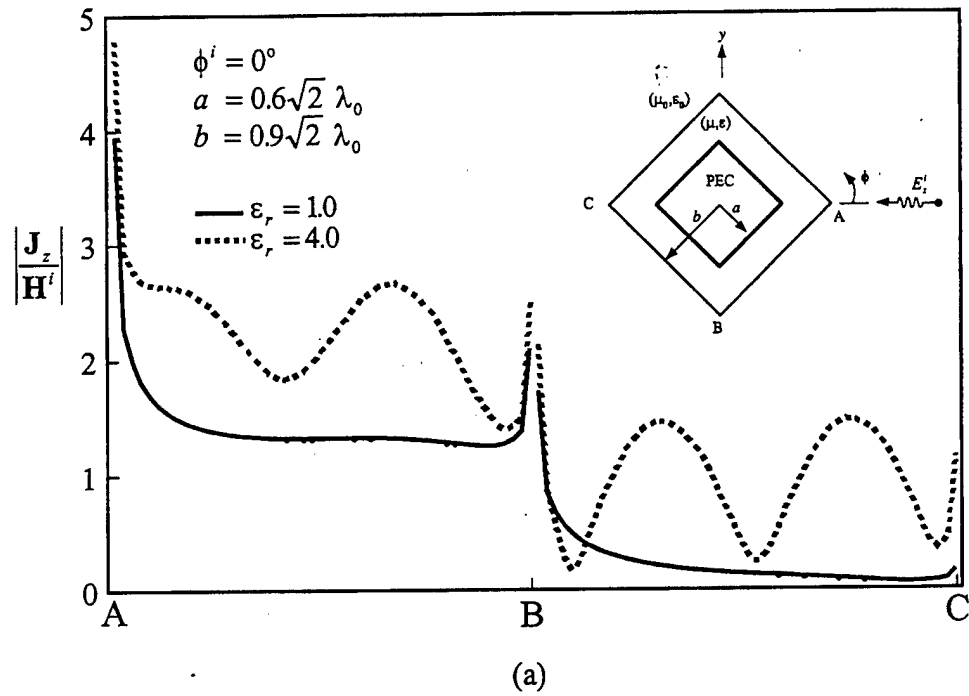


Figure 3-12. TM plane wave scattering from a square conducting cylinder covered by square dielectric cylinder. (a) magnitude of current induced on the conducting cylinder, (b) bistatic scattering cross section



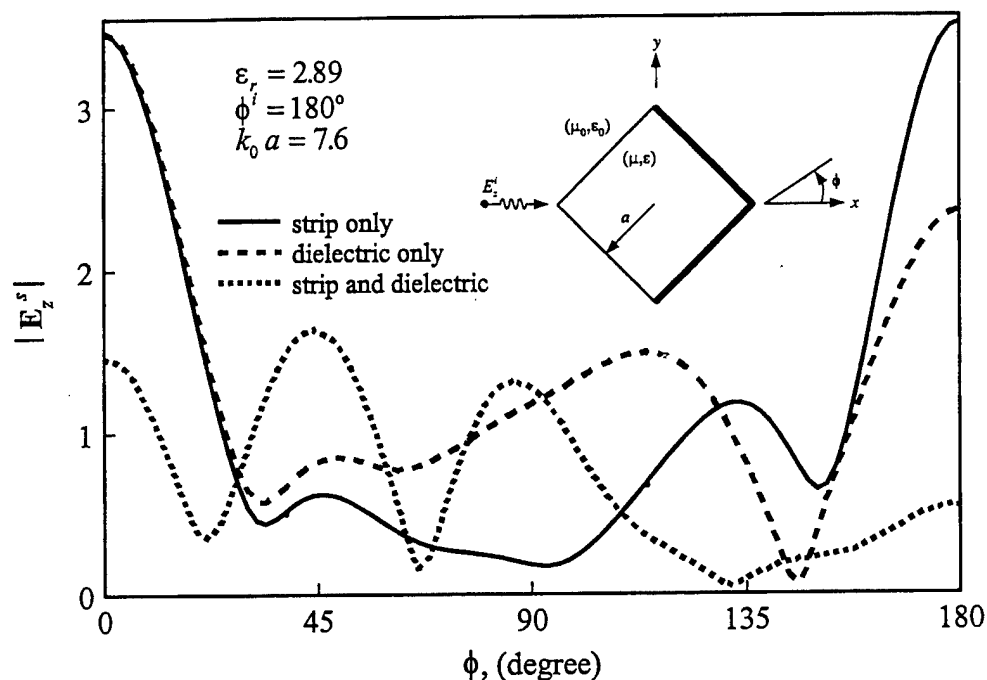


Figure 3-13. Scattered far field pattern due to TM plane wave incident on a square dielectric cylinder backed by a conducting strip.

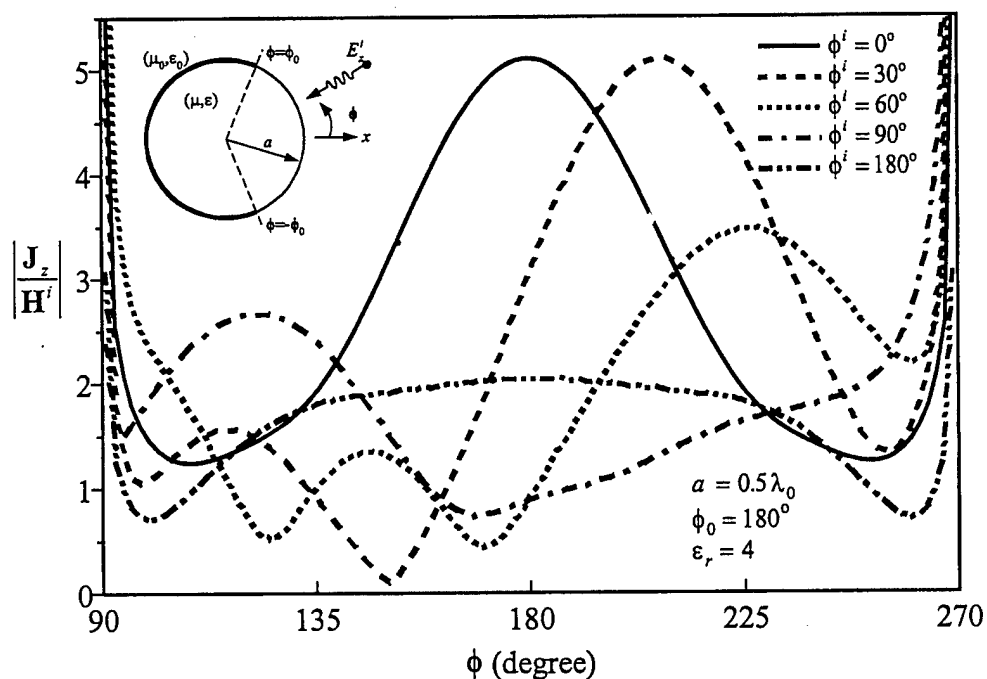


Figure 3-14. Magnitude of electric current induced on the conducting strip right on the surface of a circular dielectric cylinder (TM case).

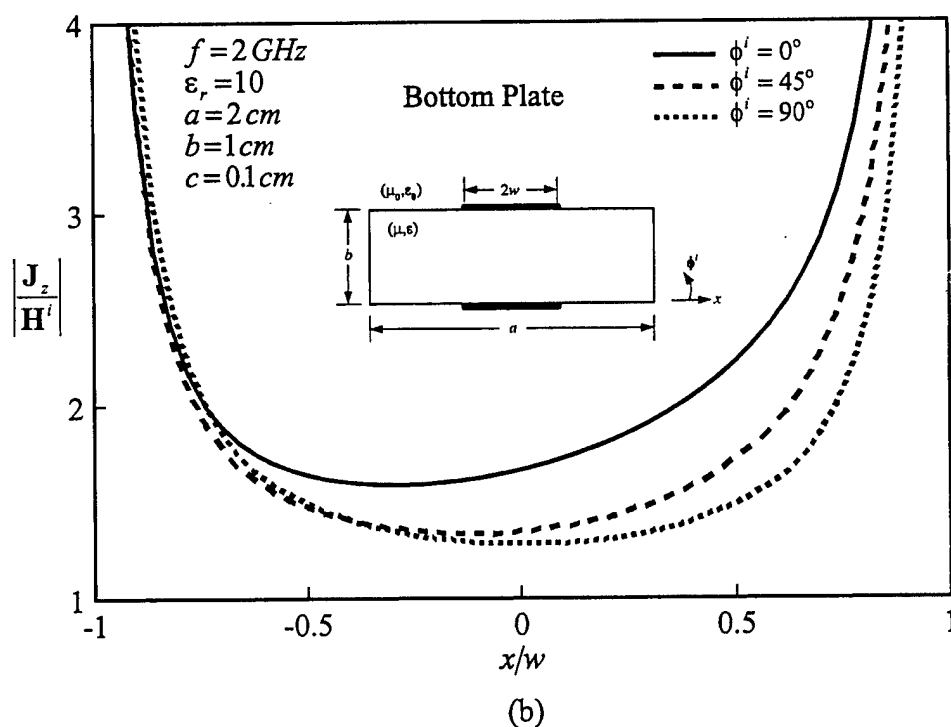
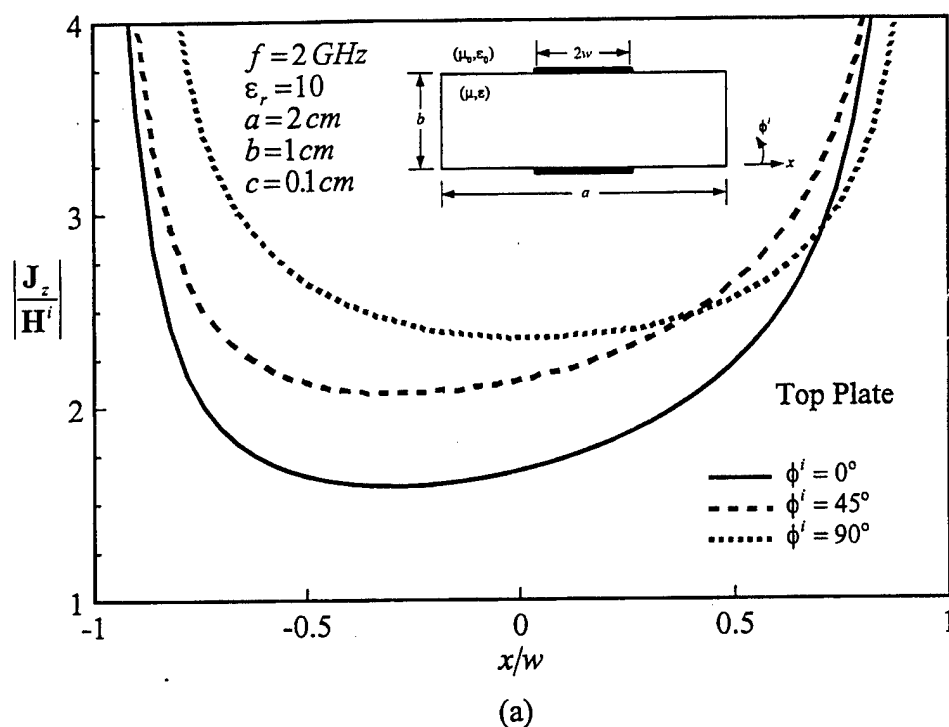


Figure 3-15. Magnitude of electric currents induced on the conducting strips right on top and bottom of a rectangular dielectric cylinder illuminated by a TM plane wave. (a) current on the top plate, (b) current on the bottom plate.

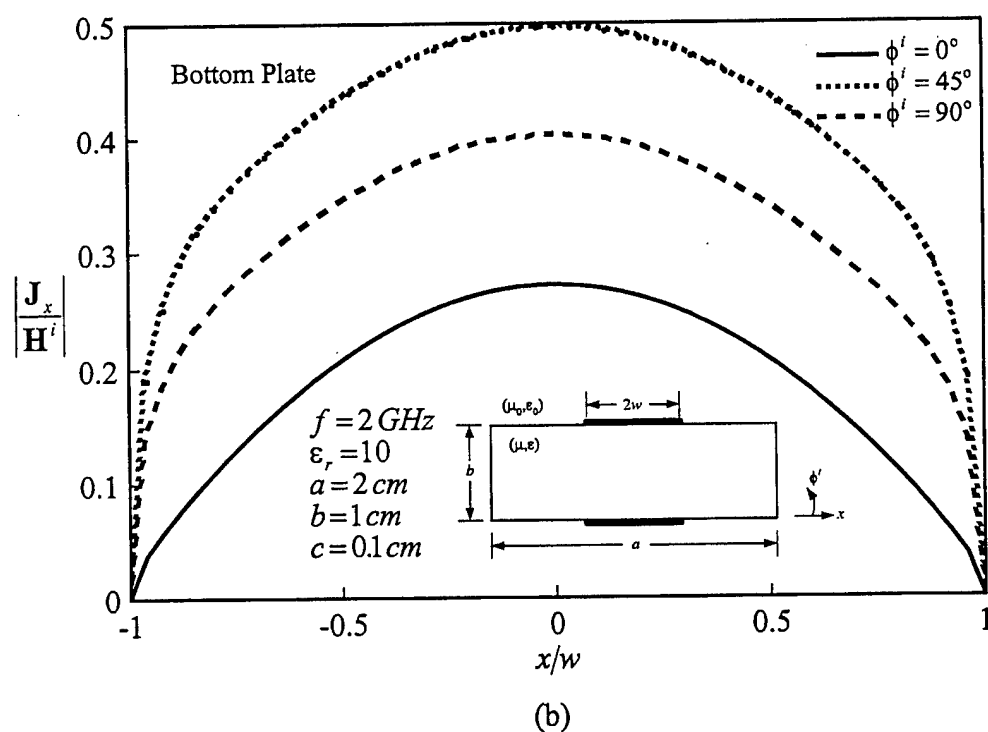
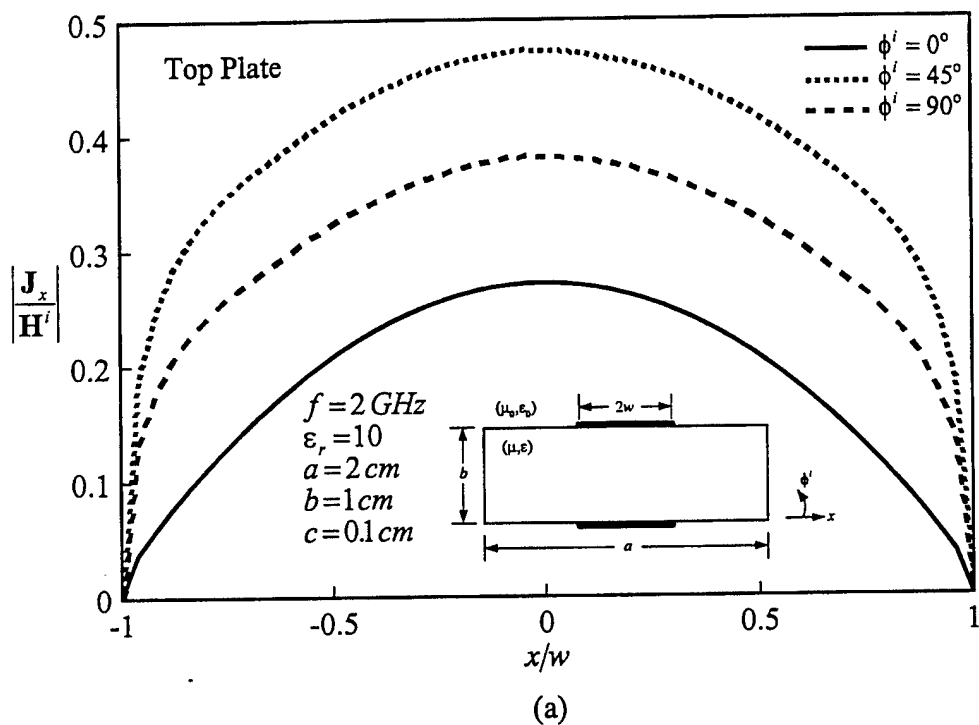


Figure 3-16. Magnitude of electric currents induced on the conducting strips right on top and bottom of a rectangular dielectric cylinder illuminated by a TE plane wave. (a) current on the top plate, (b) current on the bottom plate.

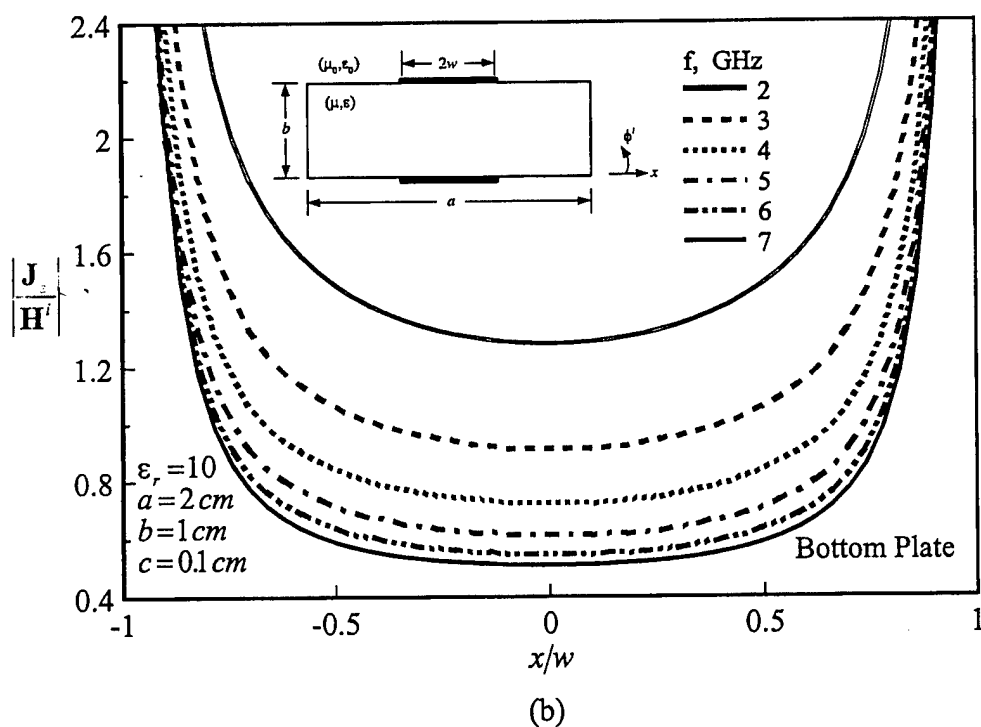
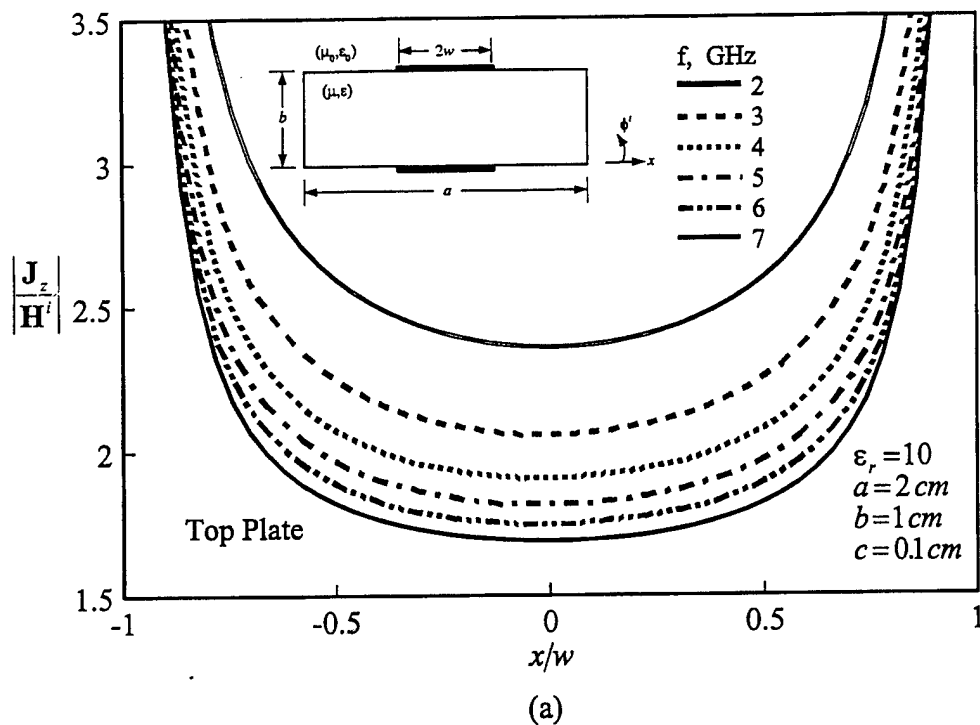


Figure 3-17. Magnitude of electric currents induced on the conducting strips right on top and bottom of a rectangular dielectric cylinder illuminated by a TM plane wave. (a) current on the top plate, (b) current on the bottom plate.

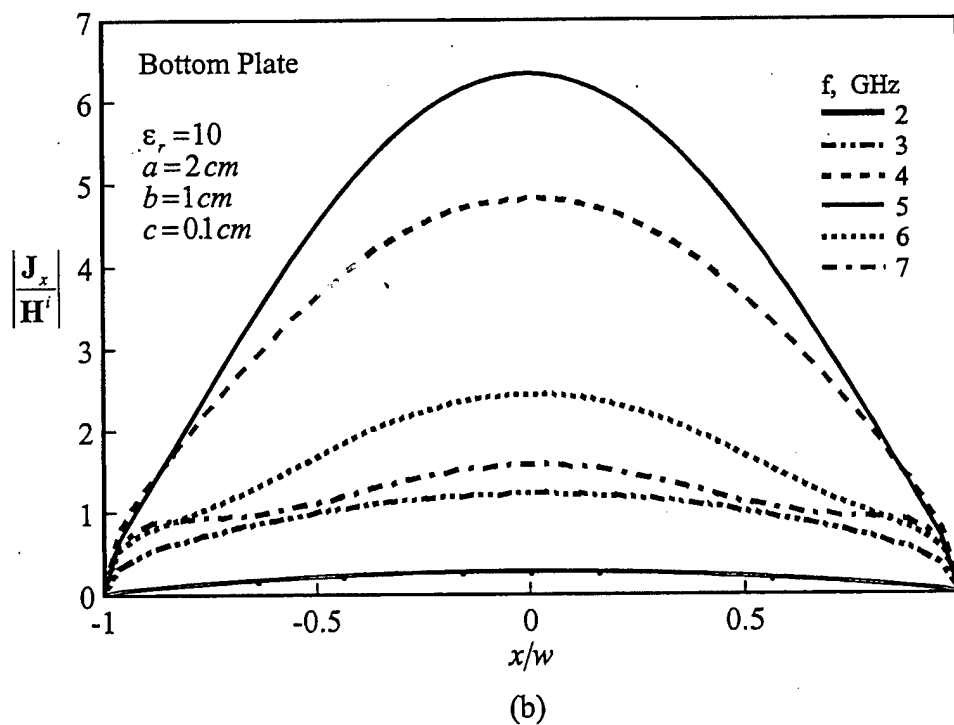
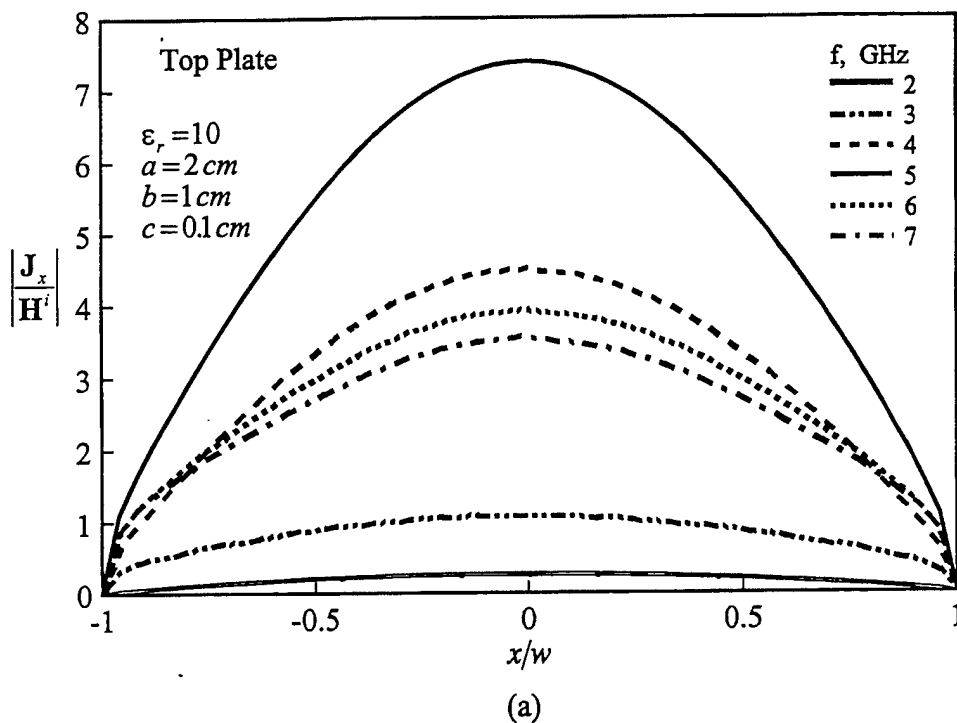


Figure 3-18. Magnitude of electric currents induced on the conducting strips right on top and bottom of a rectangular dielectric cylinder illuminated by a TE plane wave. (a) current on the top plate, (b) current on the bottom plate.

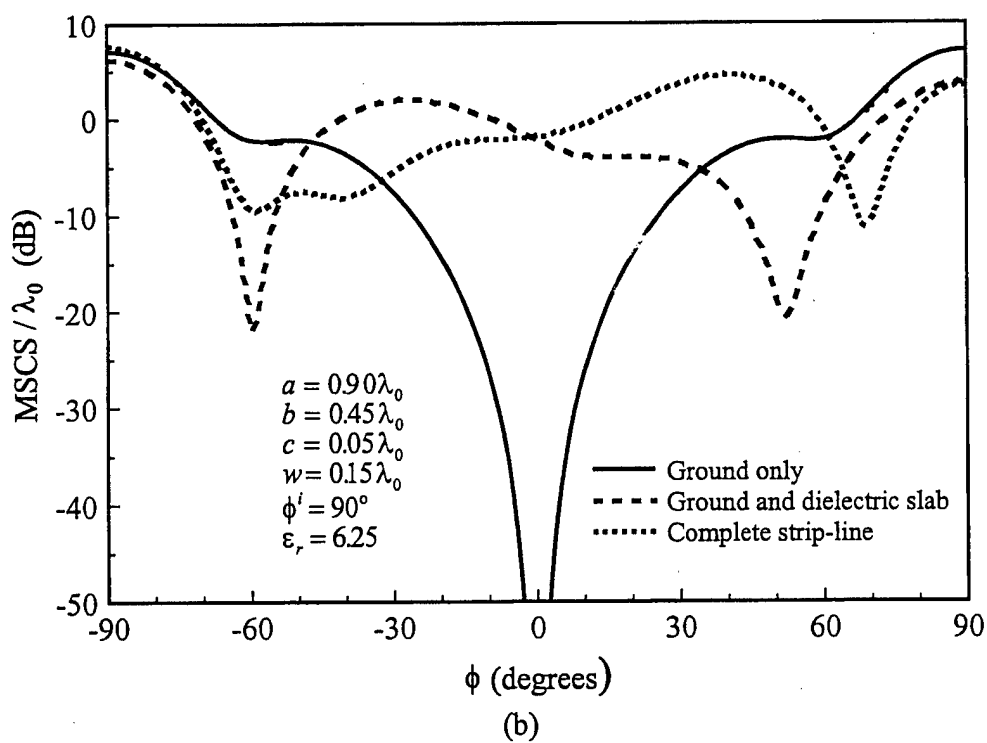
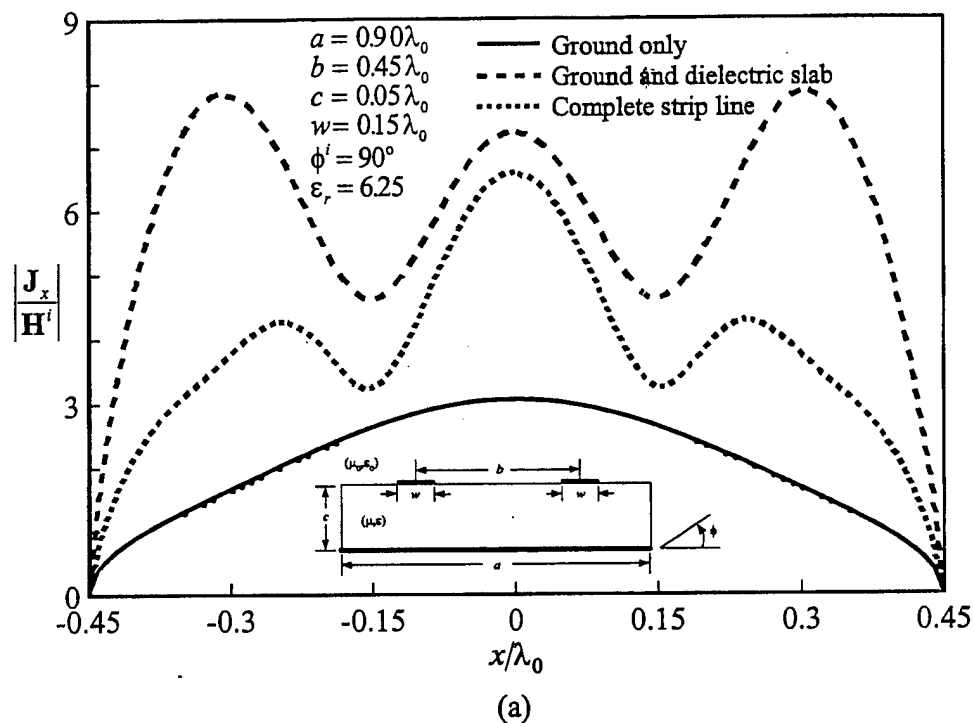


Figure 3-19. TE plane wave incident on the microstrip transmission line. (a) magnitude of electric current induced on the ground strip, (b) monostatic scattering cross-section.

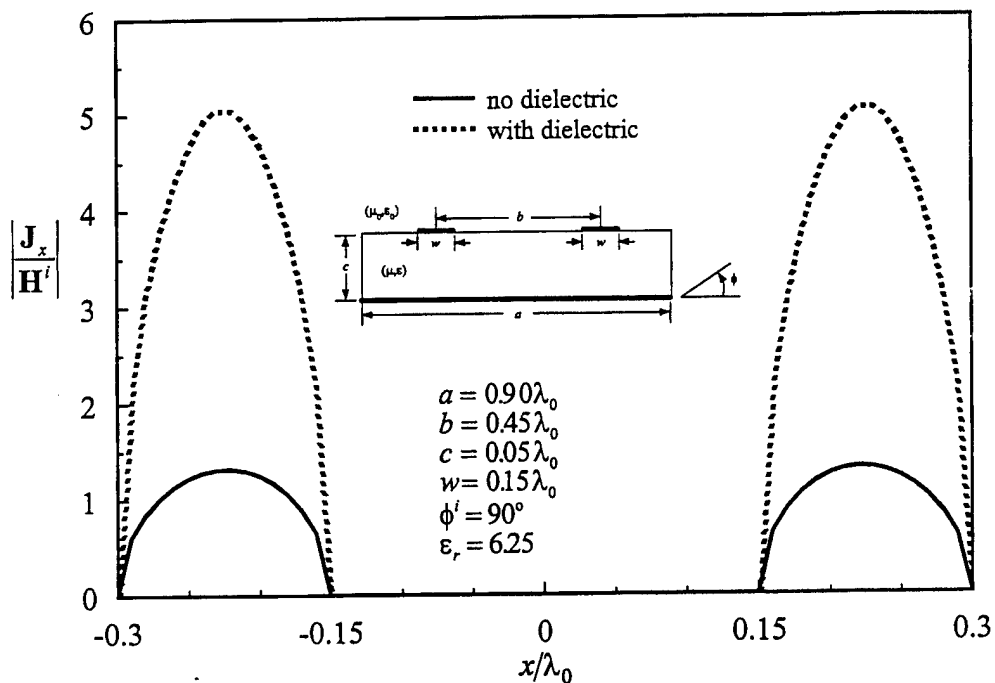


Figure 3-20. Magnitude of current induced on the narrow strips of the transmission line excited by a TE plane wave.

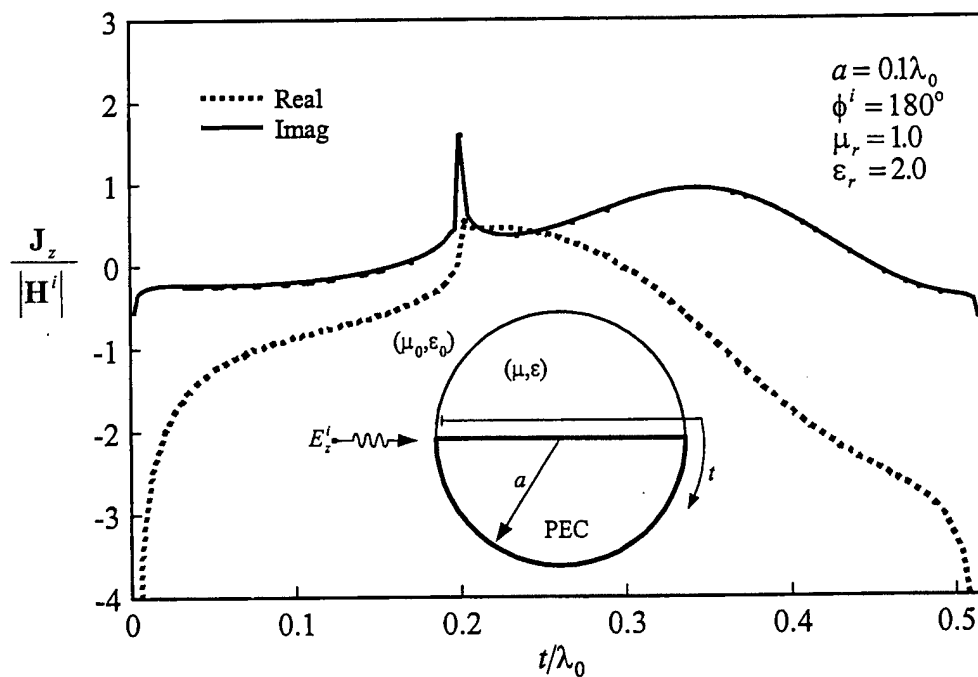


Figure 3-21. The real and imaginary parts of the current induced on the pec portion of the body comprising half-dielectric half-pec circular cylinders intersecting one another.

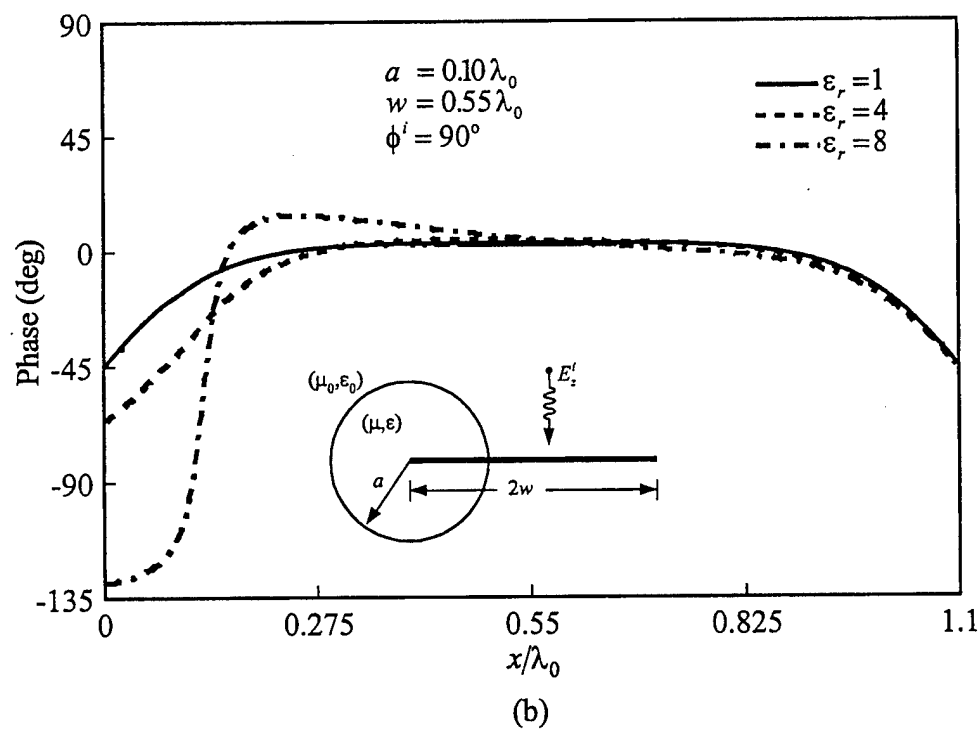
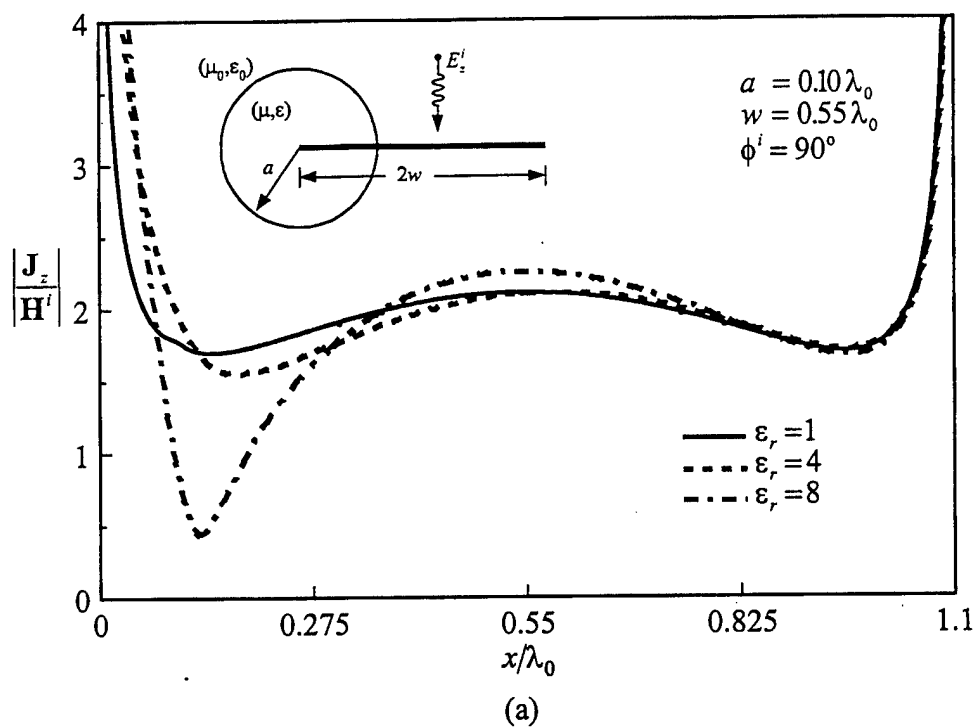


Figure 3-22. Current induced on the conducting strip penetrating into a circular dielectric cylinder excited by a TM plane wave. (a) magnitude, (b) phase.



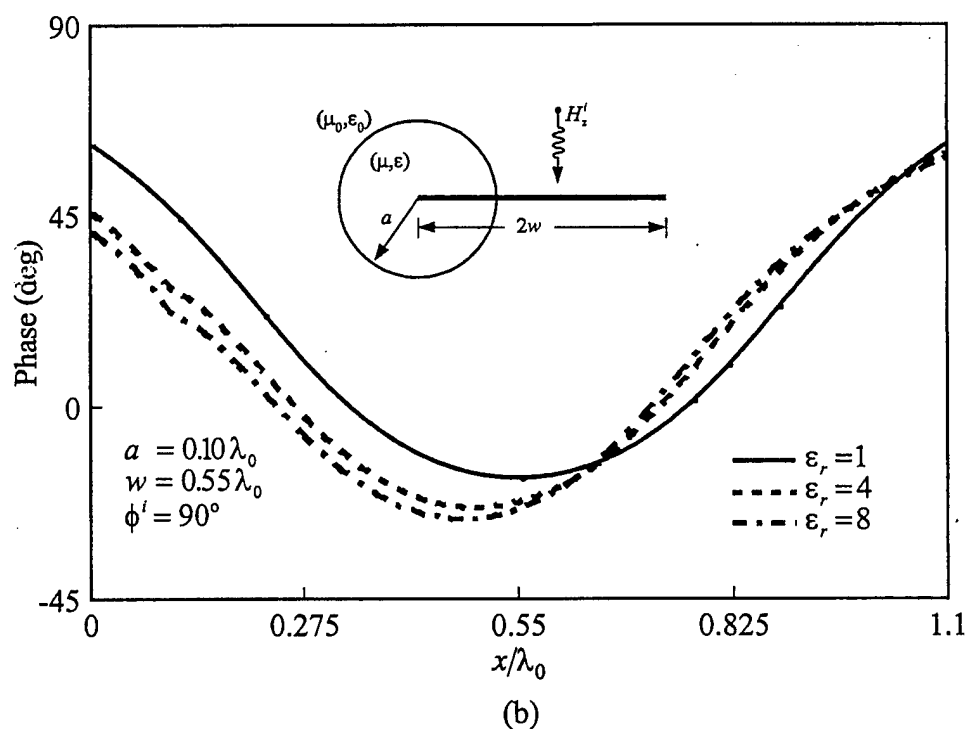
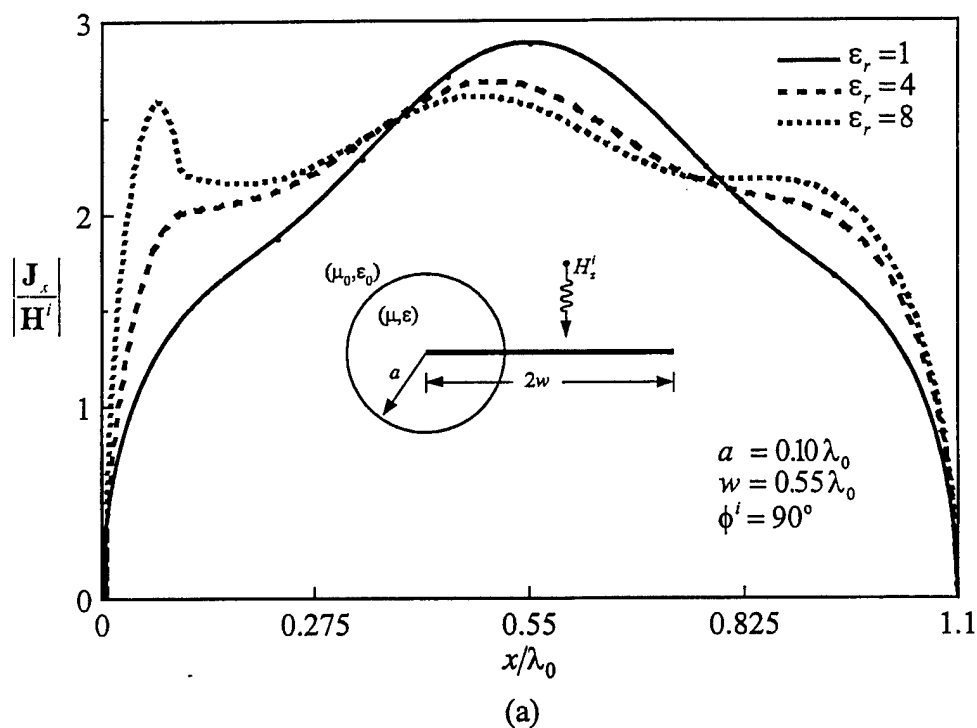


Figure 3-23. Current induced on the conducting strip penetrating into a circular dielectric cylinder excited by a TE plane wave. (a) magnitude, (b) phase.

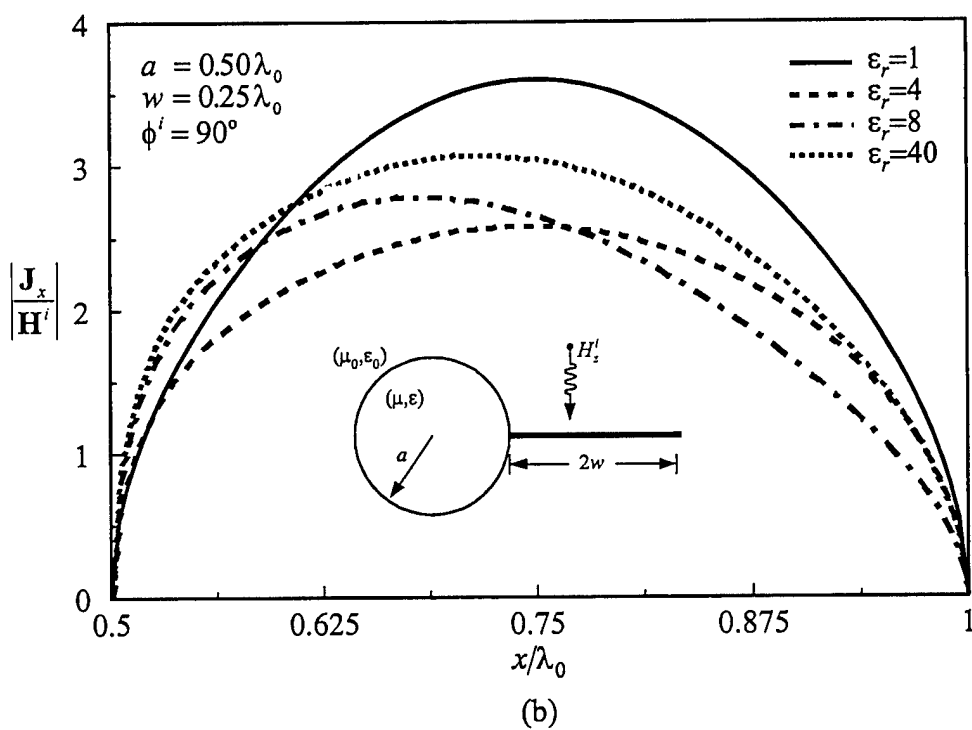
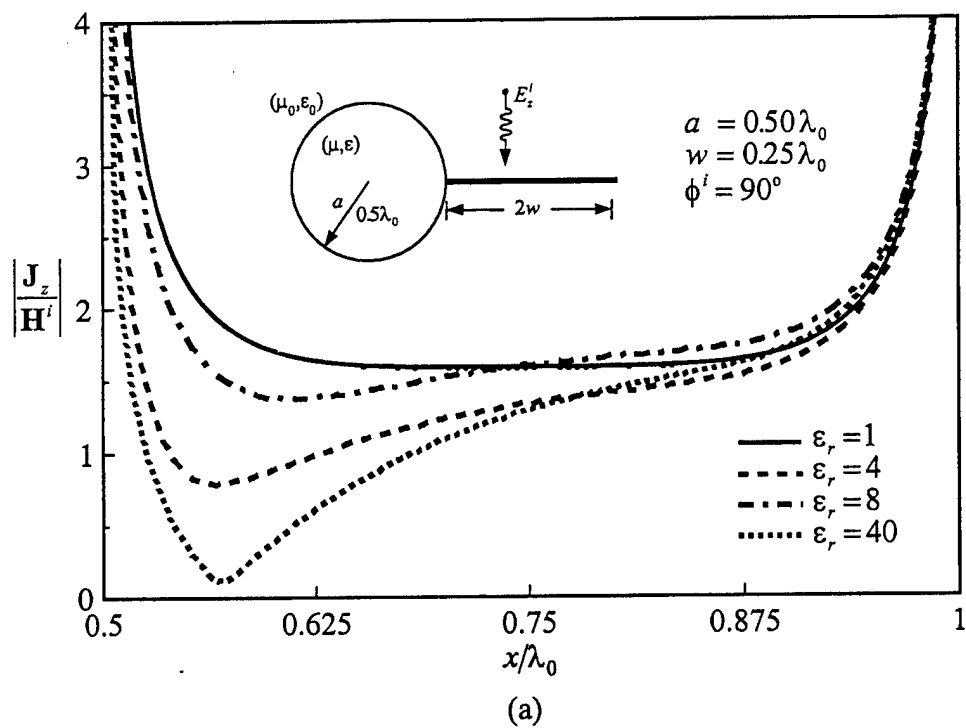


Figure 3-24. Magnitude of current induced on the conducting strip loaded by a circular dielectric cylinder excited by a plane wave. (a) TM case, (b) TE case.

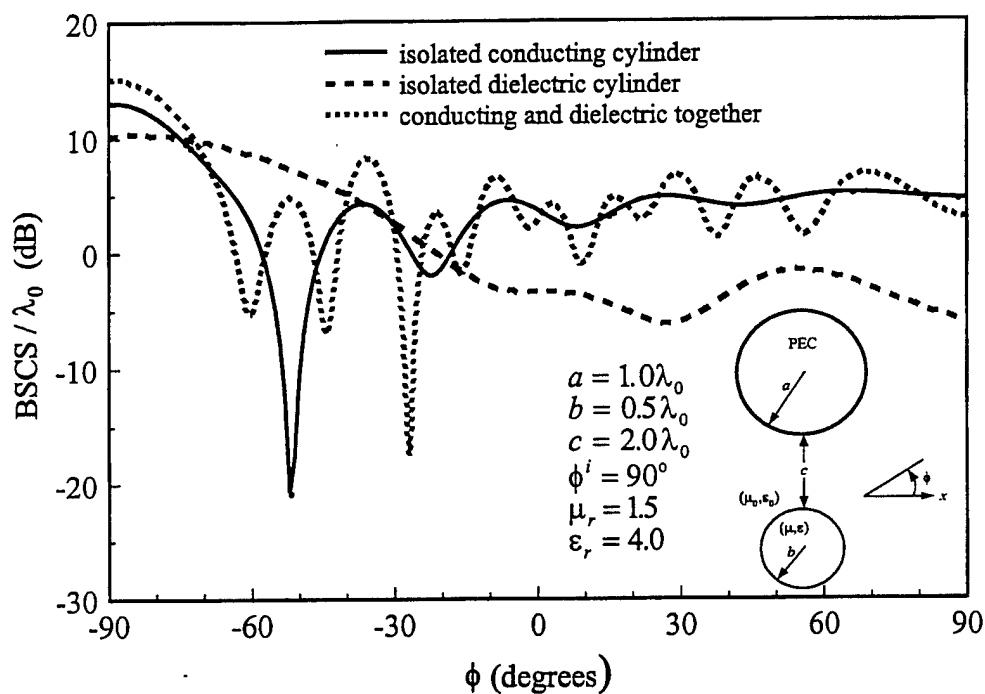


Figure 3-25. Bistatic scattering cross-section of disjoint circular conducting and dielectric cylinders excited by a TE plane wave.

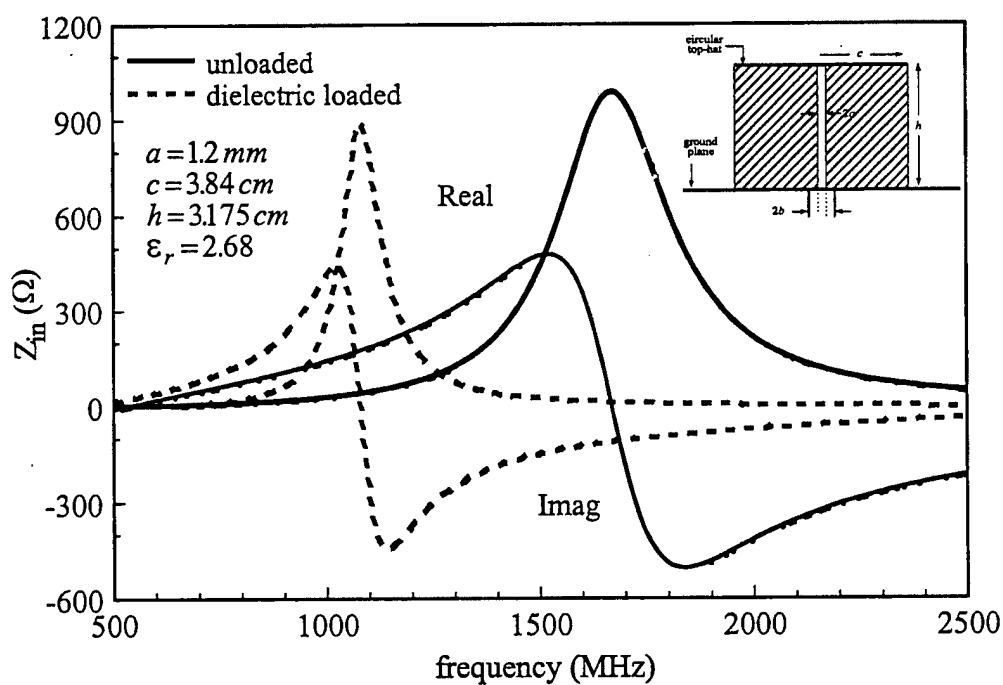


Figure 3-26. Input impedance of dielectric loaded top-hat monopole antenna over an infinite ground plane.

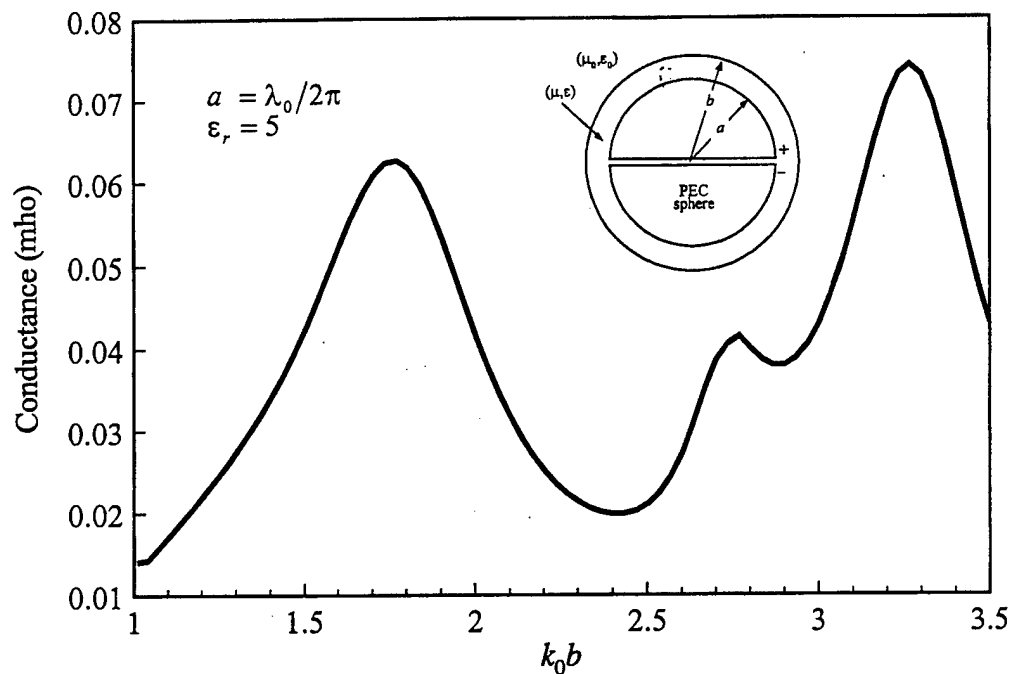


Figure 3-27. Input conductance of a conducting sphere coated by a dielectric layer.

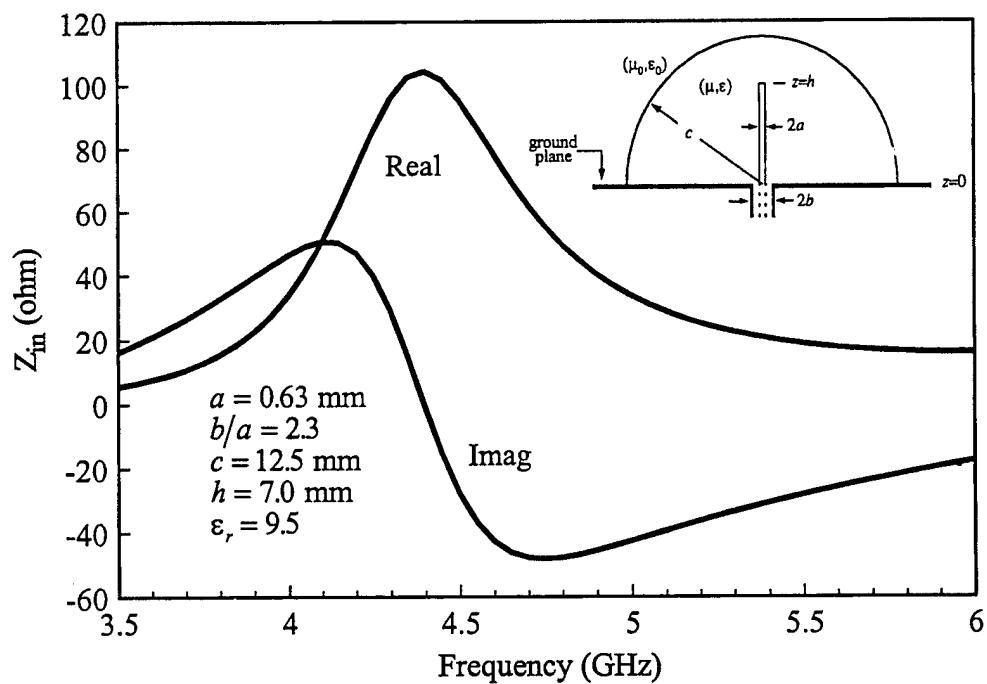


Figure 3-28. Input impedance of a hemispherical dielectric resonator antenna excited by a coaxial probe through an infinite ground plane.

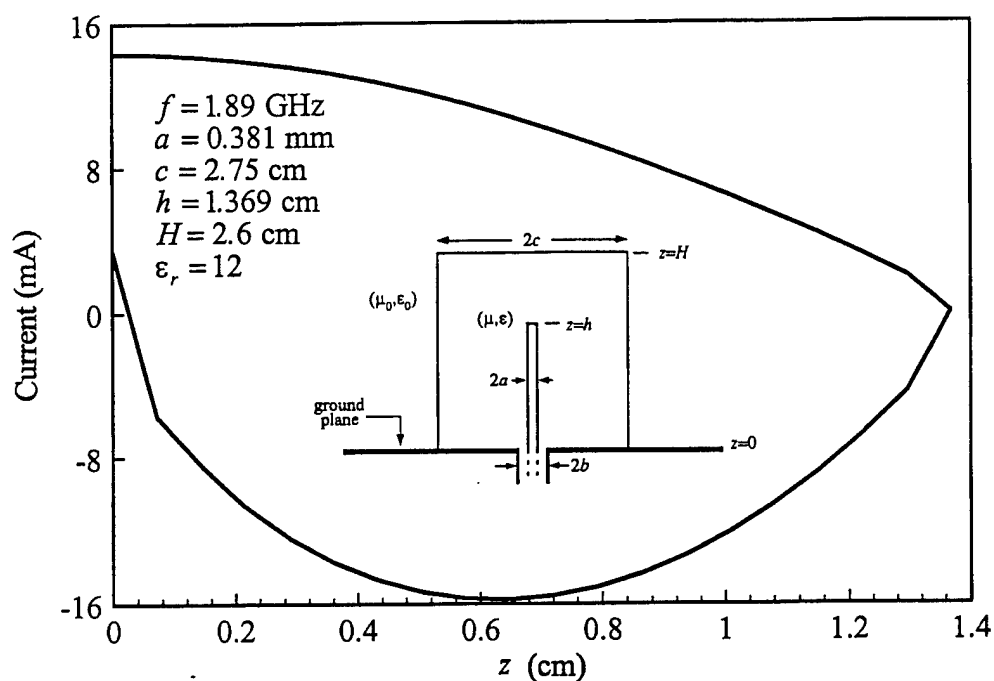


Figure 3-29. The real and imaginary parts of the current induced on the monopole antenna excited by a delta-gap source and covered by a finite height dielectric cylinder.

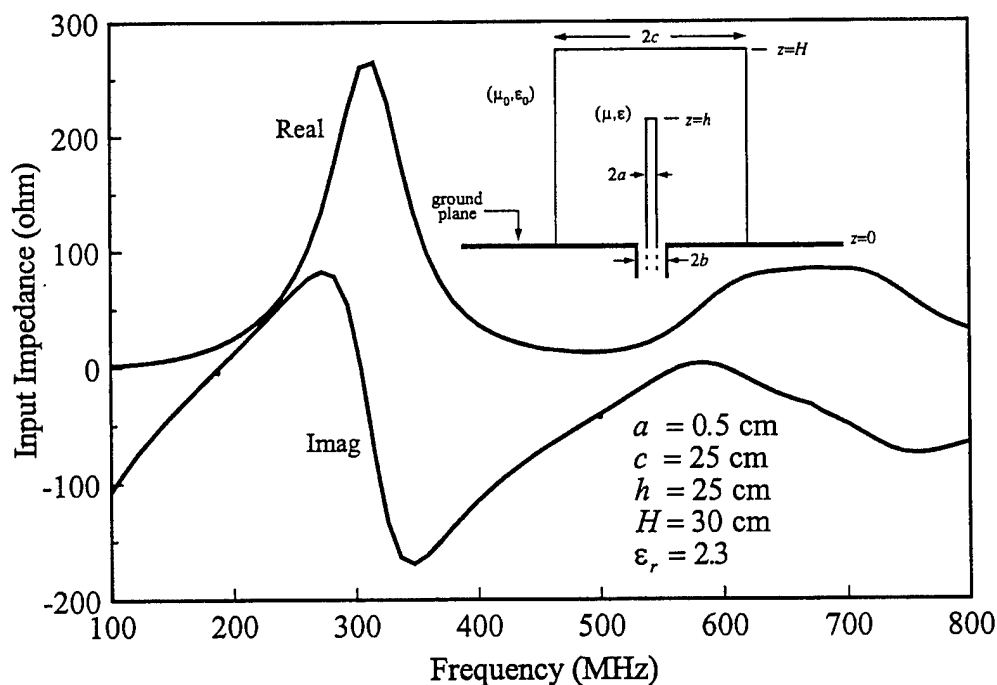


Figure 3-30. Input impedance of monopole antenna covered by a finite height dielectric cylinder.

## 3.9 References

1. R. F. Harrington, "Boundary integral formulations for homogeneous material bodies", JEMWA, vol. 3, no. 1, pp. 1-15, 1989.
2. K. Umashankar, A. Taflove and S. M. Rao, "Electromagnetic scattering by arbitrary shaped three-dimensional homogeneous lossy dielectric objects", IEEE Trans. Antennas and Propagat., vol. 34, no. 6, pp. 758-765, May 1986.
3. S. M. Rao and D. R. Wilton, "E-field, H-field, and combined field solution for arbitrarily shaped three-dimensional dielectric bodies", Electromagnetics, vol. 10, pp. 257-308, 1990.
4. A. A. Kishk, Y. M. M. Antar, L. Shafai and L. E. Allan, "Electromagnetic scattering from dielectric bodies of revolution: theoretical and experimental results", Electromagnetics, pp. 51-60, 1987.
5. J. R. Mautz and R. F. Harrington, "Boundary formulations for aperture coupling problems", Arch. Elek. Ubertragung, vol. 34, pp. 377-384, 1980.
6. J. R. Mautz and R. F. Harrington, "Electromagnetic coupling to a conducting body of revolution with a homogeneous material region", Electromagnetics, vol. 2, no. 4, pp. 257-308, 1982.
7. A. A. Kishk and L. Shafai, "Different formulations for numerical solution of single or multibodies of revolution with mixed boundary conditions", IEEE Trans. Antennas and Propagat., vol. AP-34, no.5, pp. 666-673, May 1986.
8. A. A. Kishk and L. Shafai, "Numerical solution of scattering from coated bodies revolution using different integral equation formulations", IEE Proceedings, vol. 133, Pt. H, no. 3, pp. 227-232, June 1986.
9. Y. M.M. Antar, A. A. Kishk, L. Shafai and L. E. Allan, "Radar backscattering from partially coated targets with axial symmetry", IEEE Trans. Antennas and Propagat., vol. 37, no. 5, pp. 564-574, May 1989.
10. A. A. Kishk, G. E. Bridges, A. Sebak, and L. Shafai, "Integral equation solution of scattering from partially coated bodies of revolution", IEEE Trans. on Magnetism, vol. 27, no. 5, pp. 4283-4286, September 1991.
11. S. M. Rao, Chung-Chi Cha, R.L. Cravey, and D.L. Wilkes, "Electromagnetic scattering from arbitrary shaped conducting bodies coated with lossy materials of arbitrary thickness," IEEE Trans. Antennas Propagat., vol. 39, no. 5, pp. 627-631, May 1991.
12. S. M. Rao, T. K. Sarkar, P. Midya, A. R. Djordevic "Electromagnetic radiation and scattering from finite conducting and dielectric structures: surface /surface formulation," IEEE Trans. Antennas Propagat., vol. 39, no.7, pp. 1034-1037, July 1991.
13. Q. Chen, "Electromagnetic modeling of three-dimensional piecewise homogeneous material bodies of arbitrary composition and geometry", Ph.D. Dissertation, University of Houston, May 1990.

14. L. Shafai, H. Moheb and A. A. Kishk, "Multiple formulations for solution verification in numerical handling of antenna analysis and design problems", IEEE Antennas and Prop. Magazine, vol. 33, no. 2, pp. 7-15, April 1991.
15. E. Arvas, S. M. Rao, and T. K. Sarkar, "E-field solution of TM-scattering from multiple perfectly conducting and lossy dielectric cylinders of arbitrary cross-section", IEE Proceedings, vol. 133, Pt. H, no. 2, pp. 115-121, April 1986.
16. E. Arvas, T. K. Sarkar, "RCS of two-dimensional structures consisting of both dielectrics and conductors of arbitrary cross-section," IEEE Trans. Antennas Propagat., vol. 37, no. 5, pp. 546-554, May 1989.
17. S. M. Rao, E. Arvas and T. K. Sarkar, "Combined Field solution for TM scattering from multiple Conducting and Dielectric Cylinders of Arbitrary Cross-Section," Trans. Antennas Propagat., vol. 35, no. 4, pp. 447-451, April 1987.
18. E. Arvas, M. Ross, Y. Qian, "TM scattering from a conducting cylinder of arbitrary cross-section covered by multiple layers of lossy dielectrics," IEE Proceedings, vol. 135, Pt. H, no. 4, pp. 226-230, August 1988.
19. E. Arvas, Y. Qian, T. K. Sarkar, F. Aslan, "TE scattering from a conducting cylinder of arbitrary cross-section covered by multiple layers of lossy dielectrics," IEE Proceedings, vol. 136, Pt. H, no. 6, pp. 425-430, Dec 1989.
20. E. Arvas, A. Rahval-Arabi, and A. Sadigh and S. M. Rao "Scattering from multiple conducting and dielectric bodies of arbitrary shape," IEEE Antennas and Propagation Magazine, vol. 33, no. 2, pp. 29-36, April 1991.
21. E. Arvas, Y. Qian, A. Sadigh, and T. K. Sarkar, "E-Field and H-Field Solutions of TE Scattering from multiple Conducting and Dielectric Cylinders of Arbitrary Cross-section," JEMWA, vol. 3, no. 6, pp. 513-530, 1989.
22. X. Yuan, R. F. Harrington, S. S. Lee, "Electromagnetic scattering by a dielectric cylinder partially covered by conductors," JEMWA, pp. 21-44, 1988.
23. P. M. Goggans, T. H. Shumpert, "CFIE MM solution for TE and TM incidence on a 2-D conducting body with dielectric filled cavity," IEEE Trans. Antennas Propagat., vol. 38, no. 10, pp. 1645-1649, October 1990.
24. S. Shu, P. M. Goggans, and A. A. Kishk, "Computation of cut-off wavenumbers for partially filled waveguides of arbitrary cross section using surface integral formulations and the MoM", IEEE Trans. Antennas Propagat., vol. 41, no. 6/7, pp. 1111-1118, June/July 1993.
25. M. D. G. Karunaratne, K. A. Michalski, C. M. Butler, "TM scattering from a conducting strip loaded by a dielectric cylinder," IEE Proceedings, vol. 132, Pt. H, no. 2, pp. 115-122, April 1985.
26. M. D. G. Karunaratne, K. A. Michalski, C. M. Butler, "TE scattering from a conducting strip loaded by a dielectric cylinder," IEE Proceedings, vol. 132, Pt. H, no. 6, pp. 375-383, October 1985.
27. M. A. Kolbehdari, "Scattering from a dielectric cylinder partially clad by a perfect electric conductor," IEE Proceedings, vol. 141, Pt. H, No. 6, pp. 536-544, December 1994.

28. A. Z. Elsherbeni, M. Hamid, "Scattering by a perfectly conducting strip loaded with a dielectric cylinder (TM case)," IEE Proceedings, vol.136, Pt. H, no. 3, pp. 185-190, June 1989.
29. J. L. Tsalamengas, "Direct singular integral equation methods in scattering from strip-loaded dielectric cylinders," JEMWA, vol. 10, pp. 1331-1358, 1996.
30. J. L. Tsalamengas, I. O. Vardiamnasis and J. G. Fikioris, "Plane-wave scattering by strip loaded circular dielectric cylinders in the case of oblique incidence and arbitrary polarization," IEEE Trans. Antennas Propagat., vol. 43, no. 10, pp. 1099-1108, October 1995.
31. J. M. Jin and V.V. Liepa, "Simple moment method program for computing scattering from complex cylindrical obstacles," IEE Proceedings, vol. 136, Pt. H, no. 4, pp. 321-329, August 1989.
32. T. K. Sarkar, S. M. Rao and A. R. Djordevic "Electromagnetic scattering and radiation from finite microstrip structures," IEEE Trans. Microwave Theory and Tech., vol. 38, no. 11, pp. 1568-1575, November 1990.
33. S. U. Hwu, D. R. Wilton, "Electromagnetic scattering from arbitrary cylinders with thin-material coatings," IEEE Int. AP-S Proc., pp. 1112-1115, 1989.
34. K. L. Wu, G. Y. Delisle and D. G. Fang, "EM scattering of an arbitrary multiple dielectric coated conducting cylinder by coupled finite boundary element," IEE Proceedings, vol. 137, Pt. H, no. 1, pp. 1-4, February 1990.
35. G. K. Gothard, S. M. Rao, D. R. Wilton "Application of finite integral technique to electromagnetic scattering by two-dimensional cylinders: Transverse magnetic case," Radio Science, vol. 32, no. 2, pp. 317-328, March-April 1997.
36. S. A. Long, M. W. McAllister and L. C. Shen "The resonant cylindrical dielectric cavity antenna," IEEE Trans. Antennas Propagat., vol. 31, no. 3, pp. 406-412, May 1983.
37. G. P. Junker, A. A. Kishk and A. W. Glisson, "MoM solution of wire radiators coupled to dielectric bodies of revolution", IEEE AP-S Int. Symp. pp. 40-43, 1993.
38. G. P. Junker, "Analysis of a dielectric resonator antennas excited by a coaxial probe or narrow slot aperture," Ph.D. Disst., University of Mississippi, 1994.
39. G. P. Junker, A. A. Kishk and A. W. Glisson, "Input impedance of dielectric resonator antennas excited by a coaxial probe," IEEE Trans. Antennas Propagat., vol. 41, no. 7, pp. 960-966, July 1994.
40. G. P. Junker, A. A. Kishk, A. W. Glisson and D. Kajfez, "Effect of fabrication imperfections for ground-plane backed dielectric-resonator antennas", IEEE Antennas and Propagation Magazine., vol. 37, no. 1, pp. 40-45, Feb. 1995.
41. W. Huang, A. A. Kishk and A. W. Glisson, "Analysis of a thick monopole antenna loaded with dielectric material," AEU, vol. 48, no. 4, pp. 177-183, 1994.



42. W. Huang, A. A. Kishk and A. W. Glisson, "Electromagnetic characteristics of a thick monopole antenna with dielectric loading," IEEE SOUTHEASTCON., pp. 314-317, 1992 .
43. G. P. Junker, A. A. Kishk, A. W. Glisson and D. Kajfez, "Effect of air gap on cylindrical dielectric resonator antenna operating in  $TM_{01}$  mode", Electronic Letters., vol. 30, no. 2, pp. 97-98, Jan 1994.
44. A. H. Ghods and Y. Rahmat-Samii, "Electromagnetic properties of an insulated dipole antenna immersed in an arbitrary medium," IEE Proceedings-H, vol. 138, no. 6, pp. 497-503, December 1991.
45. A. A. Kishk, G. Zhou and A. W. Glisson, "Analysis of dielectric resonator antennas with emphasis on hemispherical structures", IEEE Antennas and Propagation Magazine., vol. 36, no. 2, pp. 20-31, Apr 1994.
46. K. W. Leung, K. M Luk, K. Y. A. Lai and D. Lin, "Theory and Experiment of a coaxial probe fed hemispherical resonator antenna," IEEE Trans. Antennas Propagat., vol. 41, no. 10, pp. 1390-1398, October 1993.
47. K. W. Leung, K. W. Ng, K. M. Luk and Edward K. N. Yung, "On the efficient calculation of the axially probe fed hemispherical dielectric resonator antenna," IEEE AP-S Int. Symp., pp. 2084-2087, July 1997.
48. D. I. Kaklamani, C. N. Capsalis and N. K. Uzunoglu, "Radiation from a monopole antenna covered by a finite height dielectric cylinder,". Electromagnetics, pp.185-216, 1994.
49. D. I. Kaklamani and N. K. Uzunoglu, "Analysis of dielectrically loaded radiators using entire-domain galerkin technique", IEEE Antennas and Propagation Magazine., vol. 39, no. 5, pp. 30-53, Oct 1997.
50. S. M. Shum and K. M. Luk, "Numerical study of a cylindrical dielectric-resonator antenna coated with a dielectric layer," IEE Proceedings-H, vol.142, no.2, pp.189-191, April 1995.
51. Z. N. Chen, K. W. Leung, K. M. Luk and E. K. N. Yung, "Evaluation of resonant frequency of a cylindrical probe-fed DR antenna", Int. J. Electronics, vol.84, no.5, pp.529-537, 1998.
52. M. A. Morgan and F. K. Schwing, "Eigenmode analysis of dielectric loaded top-hat monopole antennas," IEEE Trans. Antenn. Propagat., vol. 42, pp. 54-61, Jan 1994.
53. K. Aydin, A. Altintas and A. Hizal "Null field formulations for dielectric coated antennas,". Radio Science, vol. 18, No. 6, pp. 1225-1242, Nov-Dec 1983.
54. J. H. Richmond and E. H. Newman, "Dielectric coated wire antennas," Radio Science, vol. 11, no. 1, pp. 13-20, Jan 1976.
55. J. D. Shumpert and C. M. Butler, "Penetration through slots in conducting cylinders " IEEE Trans. Antenn. Propagat., vol. 46, pp. 1612-1628, Nov 1998.

CHAPTER 4

COUPLING TO A PROBE IN A DIELECTRIC-CAPPED METAL CAN  
BY A LASER-LIGHT INDUCED FIELD

4.1 Introduction

In this part we describe a method to compute the coupling of a signal, caused by a modulated laser beam, to a load impedance terminating a coaxial guide whose center conductor protrudes into a conducting can, as suggested in Figure 4-1. The can is a right circular cylindrical shell with a flat bottom through which protrudes the coax center conductor. The coax axis is the same as the cylinder axis and its outer conductor terminates at, and is electrically connected to, the can bottom. The can wall and bottom are taken to be vanishingly thin and they are perfect conductors, as are the inner and outer walls of the coaxial waveguide. We consider one case in which the can is empty and a second case in which there is a dielectric "plug" in the can. The plug is a solid dielectric cylinder whose axis coincides with those of the cylindrical shell and the coax.

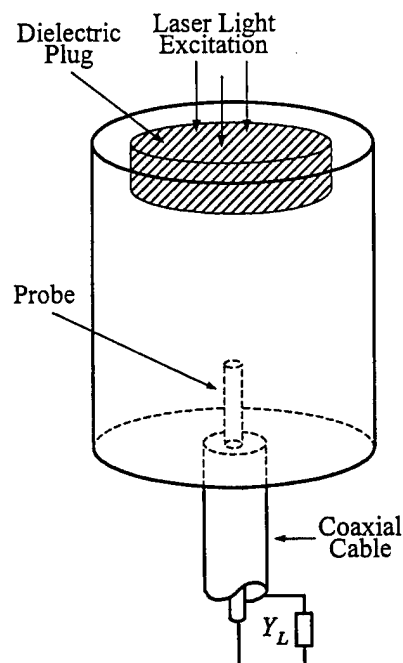


Figure 4-1. Probe in a dielectric capped metal can illuminated by a laser light.

The excitation is the signal radiated by electrons "kicked off" the conducting surface by an impinging laser beam. The laser is modulated in such a way that the electrons escaping the surface oscillate harmonically in time causing them to radiate a coherent signal at an angular frequency  $\omega$ . For a vanishingly small spot of laser light on the conducting surface, the radiating source is modeled as an electric dipole normal to and located at the surface. For a larger spot, the source is taken to be an ensemble of normal dipoles whose amplitude and phase are dictated by the characteristics of the laser light and the spot. The laser excited dipoles radiate in the presence of the can and coax and a signal is induced on the load admittance  $Y_L$  terminating the end of the coax remote from the point where it joins the bottom of the can. It is this signal at the load, as a function of the laser beam characteristics, that one wishes to determine.

Of course, one can compute the radiation from the dipoles on the conducting surface of the can and the coupling to the terminating admittance, but one must be aware that doing so is not a simple undertaking. The dipoles radiate in the presence of the entire can-coax structure and, therefore, all parts of the can and coax, together with the terminating load, must be accounted for simultaneously in any analysis for determining  $V_L$ , the signal at the load  $Y_L$ . In other words, all parts of the structure are coupled and each influences the current induced on all surfaces. Fortunately, since one needs to know the signal only at the load, which electromagnetically speaking occupies a vanishingly small region of space, one can obtain the desired information by solving a radiation problem and employing the reciprocity theorem. This is far simpler than it would be to solve the reception problem directly in which one must allow the laser stimulated dipoles to radiate in the presence of the loaded (load admittance  $Y_L$  in place at the end of the coax) coax-can structure. Since the can and center-joined coax form a circularly symmetric structure, the field radiated by the structure due to excitation at the coax terminal is circularly symmetric, which property allows for simplification in the radiation problem in addition to what would be true of the reception problem.

This indirect but less complex technique for determining the signal at the load due to the laser is carried out in two steps. First, a source is impressed at the location of the load admittance  $Y_L$  at the terminus of the coax and the radiation due to this source is determined. In particular, one computes the electric field normal to the can-coax surface at the point where the laser-light-induced dipole resides. From knowledge of this electric field, the value of the load impedance, and the value of the impressed dipole source, one can determine the signal induced in the load impedance by invoking the reciprocity theorem. This technique, though simpler than the more direct method, is completely rigorous and involves no approximations not employed in the direct procedure.

The solution of the problem of determining the signal induced by a modulated laser beam at the load admittance  $Y_L$ , which terminates the coax of the coax-can structure, has been reduced to two steps: (1) computation of the electric field at points on the coax-can structure where the laser light might fall, caused by TEM excitation at the coax terminus, and (2) application of the reciprocity theorem to obtain the signal at  $Y_L$  caused by the laser light. The effort to determine radiation from the coax-can structure is, itself, partitioned into two phases: the first is the computation of the radiated field when the dielectric plug (Figure 4-2) is absent and the second is the computation when the plug is present. Data are presented to illustrate the result of these analyses.

#### 4.2 The Reciprocity Approach

The end goal is to compute, at the end of the coax remote from the monopole, the voltage and power delivered to the terminal admittance  $Y_L$  caused there by an elementary electric dipole on some part of the surface of the can and monopole structure. To perform this computation directly is very difficult so we resort to a method that allows us to realize significant savings with no loss in generality. In principle, the approach developed to solve this problem is exact and rigorous. Of course, approximations are made but only when the resulting error is very small.

The direct approach to solving this problem would be to determine the radiation due to the elementary dipole on the surface and employ the electric field of this radiation as the excitation of an integral equation for the current on the can and the monopole. The integral equation must account for the load at the terminal end of the coax and its effect at the annular aperture formed where the coax joins the can bottom. And the coupling into the coax must be computed in order to arrive at a full account of the coax and its terminal load. The current induced on the can and the monopole surfaces would be a vector surface density so the integral equation must be a vector equation. The indirect approach adopted here takes advantage of the reciprocity theorem and allows one to determine the signal at the coax terminal load from knowledge of the field radiated by the monopole-can structure under the condition that the excitation results from a current generator impressed at the terminal end of the coax. This scheme necessitates the formulation and solution of a simpler integral equation. It is simpler for two reasons. First, the integral equation is not a vector equation as it would be if the direct procedure were followed and, second, the equation and its unknown possess rotational symmetry.

In Figure 4-2 is illustrated the coax-fed monopole mounted in the can, together with an elementary dipole of current moment  $I \delta(\mathbf{r} - \mathbf{r}_d) \hat{\mathbf{r}}_d$  located at point  $\mathbf{r}_d$  in space. An admittance  $Y_L$  terminates the end of the coax remote from the monopole and can. The desired end result, as mentioned above, is the signal induced in the terminating admittance due to the dipole when the dipole resides on, and is normal to, the can surface. The dipole radiates a field which couples with the can and the monopole terminated in the loaded coax, ultimately causing a signal to appear across  $Y_L$ . In order to set the stage for the use of the reciprocity theorem, we now consider a second source and resulting radiated field. This source is an ideal current generator of  $I_g$  amperes impressed at the terminal end of the coax. This current generator, located very close to admittance  $Y_L$ , produces a signal in the coax which, in turn, excites the monopole and can and gives rise to a radiated field which we call  $\mathbf{E}^g$  (Figure 4-3). A possible structural form that this

generator and  $Y_L$  may take is illustrated in Figure 4-4, while the transmission line model of this structure and its equivalent circuit are shown in Figure 4-5 and Figure 4-6, respectively. We let the generator current be a volume current of density

$$\mathbf{J}^g = -\delta(z - z_g) \left[ I^g / 2\pi\rho \right] \hat{\rho} \quad (4.1)$$

impressed at the end of the coax immediately adjacent to the admittance fabricated in annular form. The current generator is impressed at position  $z = z_g$  along the coax. The negative sign on the current simply implies that the current is directed radially inward.

To apply reciprocity, it is instructive to think of two situations or two experiment. In the first, the impressed generator current  $I_g$  is turned off (leaving an open circuit) and the remote dipole radiates a field causing a voltage  $\mathcal{V}$  to appear across the coax at the location of the generator and load admittance  $Y_L$  as seen in Figure 4-2. Next, the dipole is removed and the current generator turned on as in Figure 4-3. It excites the coax fed monopole and can and causes a field to be radiated, whose electric field is designated  $\mathbf{E}^g$ . The reciprocity theorem applied to these sources and fields can be stated in the form

$$\iiint_V (\mathbf{E}^g \cdot \mathbf{J} - \mathbf{E} \cdot \mathbf{J}^g) dV = \oint_S (\mathbf{E}^g \times \mathbf{H} - \mathbf{E} \times \mathbf{H}^g) \cdot \hat{\mathbf{n}} dS \quad (4.2)$$

where  $V$  is the region in which the theorem applies and  $S$  is the closed surface bounding this region.  $\mathbf{J}^g$  and  $\mathbf{J}$  are sources which acting alone produce fields  $(\mathbf{E}^g, \mathbf{H}^g)$  and  $(\mathbf{E}, \mathbf{H})$ , respectively. For our case,  $V$  is defined to be the volume inside the coax, the body of the can, outside the wire probe (and the center conductor of coax), and inside the (imaginary) sphere at infinity. Let  $S = S_\infty + S_{pec}$ , where  $S_\infty$  is the sphere at infinity and  $S_{pec}$  is the remainder of  $S$ . Since this antenna structure is a perfect conductor, the surface integral over its surface  $S_{pec}$  is zero, and, due to the radiation condition, the integral over the sphere at infinity  $S_\infty$  is zero too. Hence, the surface integral of (4.2) is zero and one has remaining

$$\iiint_V (\mathbf{E}^g \cdot \mathbf{J} - \mathbf{E} \cdot \mathbf{J}^g) dV = 0 \quad (4.3)$$

where  $\mathbf{E}$  is the electric field caused (everywhere) by the elementary dipole  $\mathbf{J} = I \delta(\mathbf{r} - \mathbf{r}_d) \hat{\mathbf{l}}$  radiating in the presence of the structure and  $\mathbf{J}^g$  is given by (4.1). Next we Evaluate the integrals of (4.3). Since the dipole is a delta function, the first term of (4.3) is evaluated as

$$\iiint_V \mathbf{E}^g \cdot \mathbf{J} dV = \iiint_V \mathbf{E}^g \cdot I [\hat{\mathbf{l}} \delta(\mathbf{r} - \mathbf{r}_d)] dV = I \hat{\mathbf{l}} \cdot \mathbf{E}^g(\mathbf{r}_d). \quad (4.4)$$

The coax is operated in its typical way in which all higher order modes are below cutoff. Thus, the fields and currents in the coax are circularly symmetric which implies that  $\mathbf{E}$  is independent of  $\phi$ . Since  $\mathbf{J}^g$  is an annular current concentrated at  $z = z_g$ , the second term of (4.3) simplifies immediately to

$$\begin{aligned} \iiint_V \mathbf{E} \cdot \mathbf{J}^g dV &= -I_g \int_{-\pi}^{\pi} \int_a^b \frac{1}{2\pi\rho} \hat{\rho} \cdot \mathbf{E}(\rho, z_g) \rho d\rho d\phi \\ &= -I_g \int_{-\pi}^{\pi} \int_a^b \frac{1}{2\pi} E_\rho(\rho, z_g) d\rho d\phi = -I_g \mathcal{V} \end{aligned} \quad (4.5)$$

where  $\mathcal{V}$  is the potential of the coax center conductor relative to that of the outer conductor:

$$-\mathcal{V} = -\int_a^b E_\rho(\rho, z_g) d\rho. \quad (4.6)$$

From (4.4) and (4.5) it is clear that one can obtain  $\mathcal{V}$ , the voltage created across the coax by the dipole with the current generator off, from knowledge of the laser-induced dipole and the electric field  $\mathbf{E}^g$  which results from the current generator applied at the coax terminus. Finally we apply reciprocity by replacing the integrals of (4.3) by their equivalent expressions from (4.4) and (4.5) to obtain

$$\mathcal{V} = -I \hat{\mathbf{l}} \cdot \mathbf{E}^g(\mathbf{r}_d) / I_g. \quad (4.7)$$

The procedure for using reciprocity for computing the signal at  $Y_L$  due to a dipole induced on the surface of the can or on the monopole is outlined below. First, one

assumes a voltage  $V_A = 1$  volt across the coaxial aperture and computes the current on the monopole and can. From knowledge of this current, driven by a one-volt generator ( $V_A = 1$  volt), one can compute the driving point or input admittance  $Y_A$  at the base of the monopole. Since the monopole is driven by the coax,  $Y_A$  serves as the terminating admittance of the end of the coax where its center conductor becomes the monopole. Second, one determines the currents on the monopole and can and the field radiated by the structure under the condition that it is excited by the current generator through the coaxial transmission line as illustrated in Figures 4-4 and 4-5. From transmission line theory, it is obvious that the current generator of Figure 4-5 causes the voltage  $V_A$  in the coaxial aperture at the base of the monopole to be

$$V_A = \frac{1 + \Gamma_A}{(Y_L + Y_A)(1 + \Gamma_A e^{-j2\beta L})} e^{-j\beta L} I_g \quad (4.8)$$

in which  $\beta$  is the propagation factor of the transmission line.  $\Gamma_A$  is the reflection coefficient at the monopole base

$$\Gamma_A = \frac{Y_0 - Y_A}{Y_0 + Y_A} \quad (4.9)$$

and  $Y_0$  is the characteristic admittance of the line.  $V_A$  of (4.8) is the actual voltage driving the monopole so one can now compute the actual currents on the structure and, subsequently, the radiated field caused by the current generator in the coax illustrated in Figure 4-4. This is done by the procedure used to compute the currents with  $V_A = 1$  volt or one can simply scale all current and field values by the ratio  $V_A:1$ . The last step is to compute the voltage  $\mathcal{V}$  across the load  $Y_L$  from (4.7). The value computed for  $\mathcal{V}$  depends on the dipole moment  $\Pi \hat{\mathbf{i}}$  of the dipole induced on the structure surface at  $\mathbf{r}_d$  and the current  $I_g$  of the current generator employed in the reciprocity procedure. Recall that  $\mathbf{E}^s(\mathbf{r}_d)$  is the electric field radiated by the structure when the monopole is driven by the current generator through the coaxial transmission line.



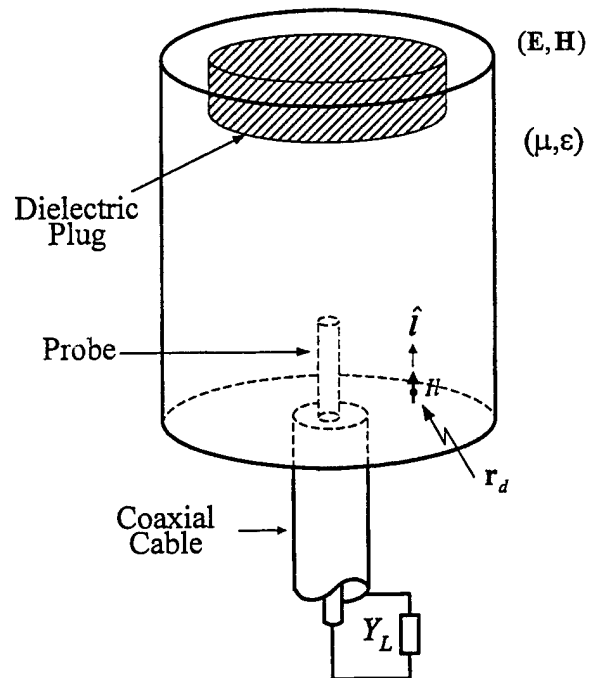


Figure 4-2. The reception problem where a dipole is normal to and located at the surface of the conducting can.

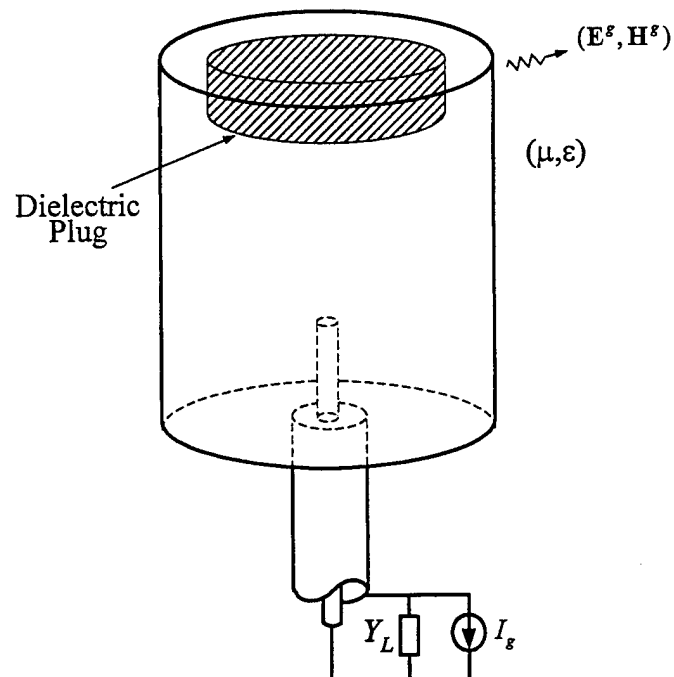


Figure 4-3. The radiation problem where the conducting can is excited through a coaxial probe at the bottom of the can.

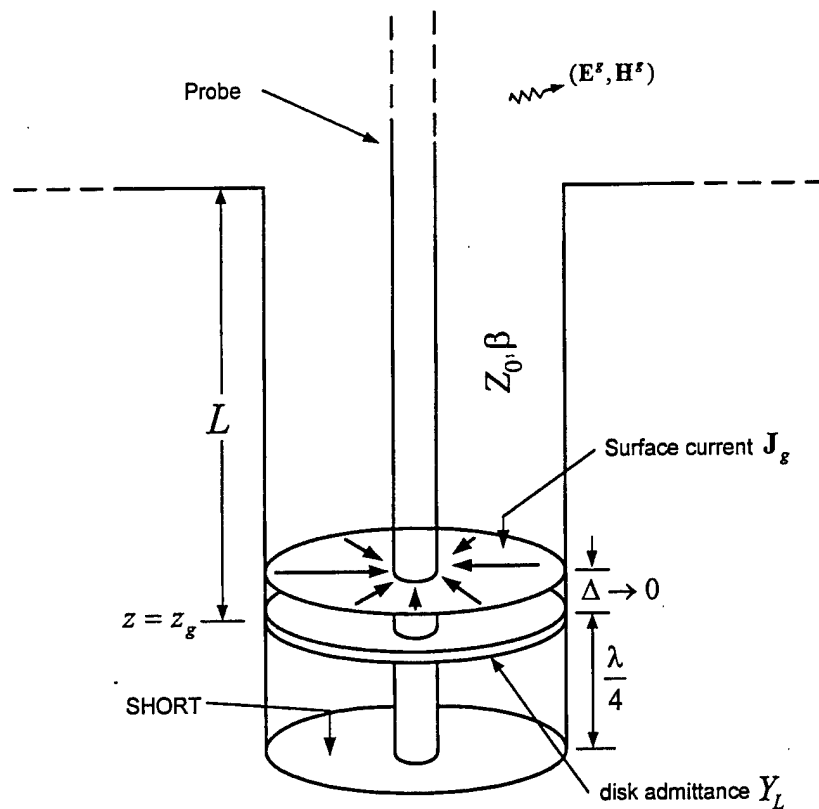


Figure 4-4. The possible form of generator and transmission line.

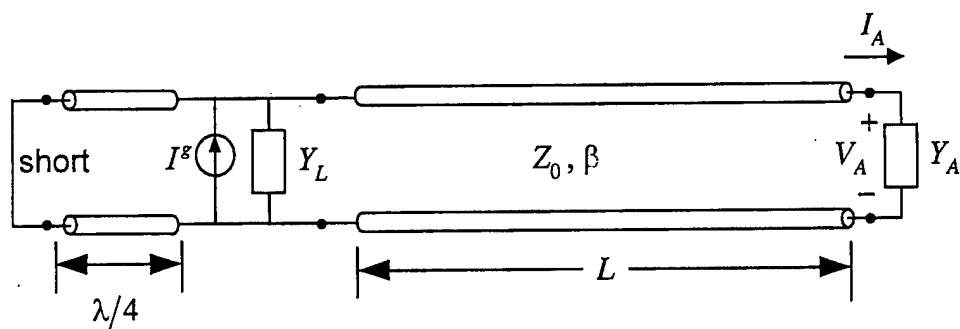


Figure 4-5. The transmission line model of the coax, the generator, and the admittance  $Y_L$  are illustrated.

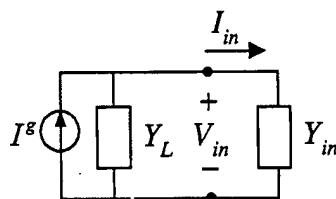


Figure 4-6. The equivalent circuit.

## CHAPTER 5

### COMPUTATION OF THE NEAR FIELD

#### 5.1 Introduction

In this section we present a method for computing the field in the near vicinity of an antenna structure. In particular, we present a method to compute the normal component of the scattered electric field and the tangential component of magnetic field in the near vicinity and immediately on the antenna structure. Our motivation for computing this field is the following. Knowledge of the field on the antenna structure provides a direct means of ascertaining the accuracy of the integral equation solution since surface quantities can be measured. For instance, if a rotationally symmetric antenna is excited by a rotationally symmetric source, the total field everywhere is rotationally symmetric. In this case it is possible to probe the antenna surface without significantly affecting the field structure. So one can probe relative field strength at different locations on the antenna surface through a slot oriented in such a way that its presence does not modify the field from the slotless case. The current and charge densities induced on the antenna surfaces can be related to components of electric and magnetic field. These components can, in principle, be computed once the current and charge on the antenna are known.

#### 5.2 Normal Component of E-Field on the Coax-Fed BOR Antenna

For rotationally symmetric antennas which are excited by a coaxial probe at the center of the structure, the incident field is the field in the coax aperture. This field can be modeled by a magnetic frill source [1]-[2]. The total field is the sum of the incident and scattered fields. The incident field is that due to the magnetic frill source while the scattered field is due to the induced currents and charges on the conducting BOR surface. We may express the normal component of the total electric field as

$$\mathbf{E} \cdot \hat{\mathbf{n}} = (\mathbf{E}^i + \mathbf{E}^s) \cdot \hat{\mathbf{n}} \quad (2.1)$$

where the scattered electric field may be computed from

$$\mathbf{E}^s = -j\omega\mathbf{A} - \nabla\Phi \quad (2.2)$$

in which  $\mathbf{A}$  and  $\Phi$  are vector and scalar potentials. In the limit as the current bearing surface is approached from either side, the normal component of the scattered electric field may be written in terms of current and charge as

$$\mathbf{E}^s \cdot \hat{\mathbf{n}} = -j\eta k \iint_S \mathbf{J}(\mathbf{r}') \cdot \hat{\mathbf{n}} G(\mathbf{r}, \mathbf{r}') dS' + \frac{q(\mathbf{r})}{2\epsilon} - \frac{1}{\epsilon} \iint_S q(\mathbf{r}') \frac{\partial G(\mathbf{r}, \mathbf{r}')}{\partial n} dS', \quad \mathbf{r} \in S \quad (2.3)$$

where  $\frac{\partial G}{\partial n} = \hat{\mathbf{n}} \cdot \nabla G$  is the normal derivative and  $\hat{\mathbf{n}}$  is the unit normal vector on the surface.  $\mathbf{E}^s \cdot \hat{\mathbf{n}}$  is the component of  $\mathbf{E}^s$  normal to the surface on the side of the surface facing the region into which  $\hat{\mathbf{n}}$  is directed in the above since  $\mathbf{E}^s \cdot \hat{\mathbf{n}}$  is a limiting value. Since the induced current has only a  $t$  directed component,

$$\mathbf{J}(\mathbf{r}') = J_t(t') \hat{\mathbf{t}}', \quad (2.4)$$

Equation (2.3) may now be written as

$$E_n^s(t) = -j\eta k \iint_S J_t(t') \hat{\mathbf{t}}' \cdot \hat{\mathbf{n}} G(\mathbf{r}, \mathbf{r}') dS' + \frac{q(t)}{2\epsilon} - \frac{1}{\epsilon} \iint_S q(t') \frac{\partial G(\mathbf{r}, \mathbf{r}')}{\partial n} dS', \quad \mathbf{r} \in S. \quad (2.5)$$

The unit vectors are determined to be

$$\hat{\mathbf{n}} = \hat{\phi} \times \hat{\mathbf{t}} = \cos \gamma \hat{\rho} - \sin \gamma \hat{\mathbf{z}}, \quad (2.6)$$

$$\hat{\mathbf{t}} = \sin \gamma \hat{\rho} + \cos \gamma \hat{\mathbf{z}}. \quad (2.7)$$

Performing the dot product and the normal derivative in (2.5), one finds that

$$\begin{aligned} E_n^s(t) = & -j \frac{\eta k}{4\pi} \int_0^T \int_{-\pi}^{\pi} J_t(t') [\sin \gamma' \cos \gamma \cos \phi' - \sin \gamma \cos \gamma'] \frac{e^{-jkR}}{R} \rho' d\phi' dt' \\ & + \frac{q(t)}{2\epsilon} + \frac{1}{4\pi\epsilon} \int_0^T \int_{-\pi}^{\pi} q(t') \{ [(\rho - \rho') \cos \gamma - (z - z') \sin \gamma] \\ & + 2\rho' \cos \gamma \sin^2(\phi'/2) \} (1 + jkR) \frac{e^{-jkR}}{R^3} \rho' d\phi' dt', \quad t \in (0, T). \quad (2.8) \end{aligned}$$

In (2.8),  $T$  is the total arc length of the generating arc and  $\rho$  is the radial displacement parallel to the  $xy$  or  $\rho\phi$  plane from the BOR axis ( $z$  axis) to the general coordinate point  $(t, \phi)$  on the surface of the BOR. It must be remembered that  $E_n^s(t)$  is a quantity resulting from taking a limit.

The current in (2.8) is approximated by using the triangle basis functions as

$$2\pi\rho J_t(t) \approx \sum_{n=1}^N I_n \Lambda_n(t) \quad (2.9)$$

where  $\Lambda_n(t)$  is defined in Chapter 1. The  $I_n$ 's are the known current coefficients computed in Chapter 1. The charge density at the points  $t$  on the generating arc can be computed from the current coefficients as

$$q(t) \approx \frac{j}{2\pi\omega\rho} \sum_{n=1}^{N+1} \frac{I_n - I_{n-1}}{\Delta_{n-1/2}} \Pi_{n-1/2}(t), \quad (2.10)$$

in which  $\omega$  is the operating angular frequency. The pulse basis function  $\Pi_{n-1/2}(t)$  is also defined in Chapter 1. Using the same indexing and parameterization scheme of the geometry of the generating arc as in Chapter 1, we are able to compute the normal component of the scattered electric field along the generating arc from the current expansion coefficient as

$$\begin{aligned} E_n^s(t_{m-1/2}) = & -j \frac{\eta k}{4\pi} \sum_{n=1}^N I_n \left\{ \int_{t_{n-1/2}}^{t_n} \int_{-\pi}^{\pi} [\sin \gamma_n^- \cos \gamma_m^- \cos \phi' - \sin \gamma_m^- \cos \gamma_n^-] \frac{e^{-jkR}}{2\pi R} d\phi' dt' \right. \\ & + \int_{t_n}^{t_{n+1/2}} \int_{-\pi}^{\pi} [\sin \gamma_n^+ \cos \gamma_m^- \cos \phi' - \sin \gamma_m^- \cos \gamma_n^+] \frac{e^{-jkR}}{2\pi R} d\phi' dt' \left. \right\} + j \frac{\eta}{4\pi k} \frac{\delta(t - t_{m-1/2})}{\rho_{m-1/2}} \frac{I_m - I_{m-1}}{\Delta_{m-1/2}} \\ & + j \frac{\eta}{8\pi^2 k} \sum_{n=1}^{N+1} \frac{I_n - I_{n-1}}{\Delta_{n-1/2}} \int_{t_{n-1}}^{t_n} \int_{-\pi}^{\pi} \{ [(\rho_{m-1/2} - \rho') \cos \gamma_m^- - (z_{m-1/2} - z') \sin \gamma_m^-] \\ & + 2\rho' \cos \gamma_m^- \sin^2(\phi'/2) \} [1 + jkR] \frac{e^{-jkR}}{R^3} d\phi' dt', \quad m=1, \dots, N+1 \quad (2.11) \end{aligned}$$

where

$$R = \sqrt{(\rho - \rho')^2 + (z - z')^2 + 4\rho\rho' \sin^2(\phi' / 2)}. \quad (2.12)$$

The normal component of the incident electric field may be computed from

$$\hat{\mathbf{n}} \cdot \mathbf{E}^i = E_\rho^i(\rho, z) \cos \gamma - E_z^i(\rho, z) \sin \gamma. \quad (2.13)$$

### 5.3 Tangential Component of H-Field on the Coax-Fed BOR Antenna

The scattered magnetic field in terms of induced current may expressed as

$$\mathbf{H}^s = \frac{1}{\mu} \nabla \times \mathbf{A}. \quad (2.14)$$

In the limit as the current bearing surface is approached from either side, the tangential component of the scattered magnetic field may be written as [4]

$$\hat{\mathbf{n}} \times \mathbf{H}^s = \frac{1}{2} \mathbf{J}(\mathbf{r}) + \iint_S \hat{\mathbf{n}} \times \mathbf{J}(\mathbf{r}') \times \nabla' G(\mathbf{r}, \mathbf{r}') dS', \quad \mathbf{r} \in S. \quad (2.15)$$

For the same current distribution in (2.9), (2.15) takes the following form

$$H_\phi^s(t) = \frac{J_t(t)}{2} + \frac{1}{4\pi} \int_0^T \int_{-\pi}^{\pi} (\rho' J_t(t')) [((\rho - \rho') \cos \gamma' - (z - z') \sin \gamma') \cos \phi' + 2\rho \cos \gamma' \sin^2(\phi' / 2)] [1 + jkR] \frac{e^{-jkR}}{R^3} d\phi' dt', \quad t \in S. \quad (2.16)$$

Approximating the current as in (2.9), one may compute the scattered magnetic field from

$$H_\phi^s(t) = \frac{I_m \delta(t - t_{m-1/2})}{4\pi\rho_{m-1/2}} + \sum_{n=1}^N I_n \left\{ \frac{1}{8\pi^2} \int_{t_{n-1/2}}^{t_n} \int_{-\pi}^{\pi} K(t_{m-1/2}; t', \phi') d\phi' dt' + \frac{1}{8\pi^2} \int_{t_n}^{t_{n+1/2}} \int_{-\pi}^{\pi} K(t_{m-1/2}; t', \phi') d\phi' dt' \right\} \quad (2.17)$$

where

$$K(t; t', \phi') = [((\rho - \rho') \cos \gamma' - (z - z') \sin \gamma') \cos \phi' + 2\rho \cos \gamma' \sin^2(\phi' / 2)] [1 + jkR] \frac{e^{-jkR}}{R^3}. \quad (2.18)$$

### 5.4 Field Distributions

Computer programs were developed to implement the formulations discussed in this part of the report. Data are generated from these programs for selected cases of interest. In Figure 5-1 is illustrated the can excited by a coaxial monopole. And shown in Figures 5-2 and 5-3 are values of the field components  $H_\phi(\rho, 0)$  and  $E_z(\rho, 0)$ , computed at the interior bottom of the can surface, along a radial line from the location of the monopole to the can inner wall. For this example, the operating frequency is below cut-off frequency of the  $TM_{01}$  mode of the corresponding circular waveguide. Since the can behaves as an infinite circular wave guide below cutoff, the wave impedance is purely reactive and only reactive energy is contained in the fields of the can [5]-[6]. In Figures 5-4 and 5-5 are found plots of the field components  $H_\phi(\rho, 0)$  and  $E_z(\rho, 0)$  as functions of normalized displacement, when the operating frequency of the can is above cut-off frequency of  $TM_{01}$  mode of the corresponding circular waveguide. In Figures 5-6 and 5-7 are seen the field components  $H_\phi(c, z)$  and  $E_\rho(c, z)$ , computed at the interior wall the can surface. For this example, the operating frequency is above cut-off frequency of the  $TM_{01}$  mode of the corresponding circular waveguide.

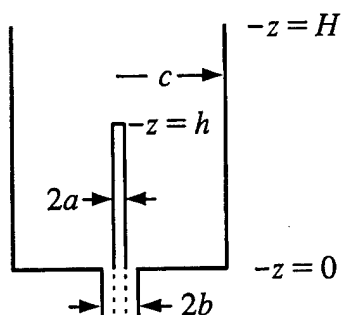


Figure 5-1. Can excited by a coaxial monopole.

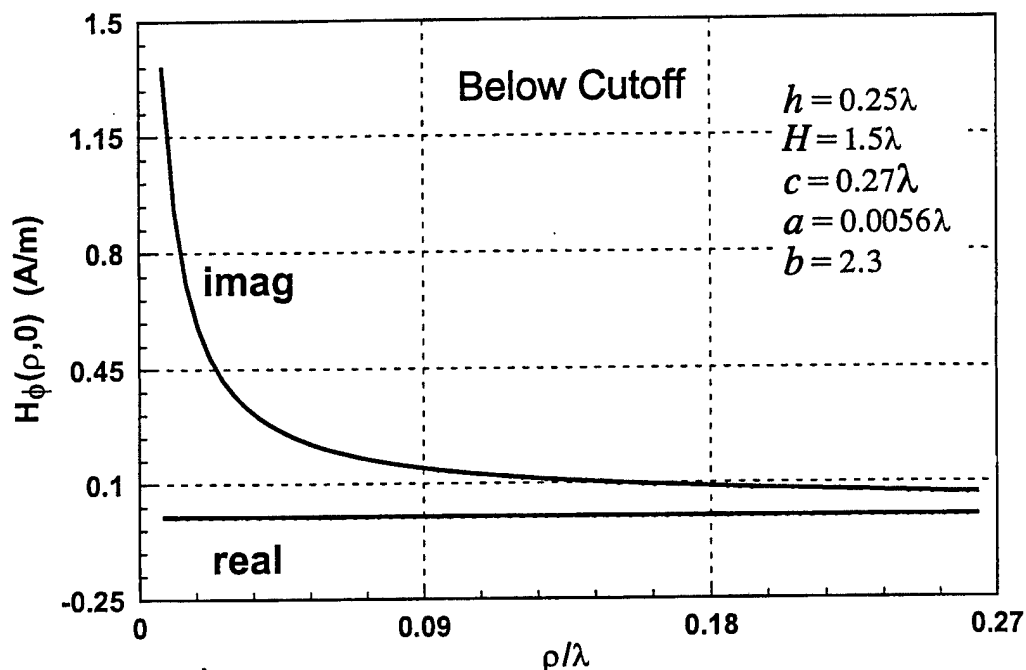


Figure 5-2. The  $\phi$ -directed magnetic field computed at the bottom surface of the can along a line from the monopole, at  $\rho=a$ , to the can wall, at  $\rho=c$  (below cutoff).

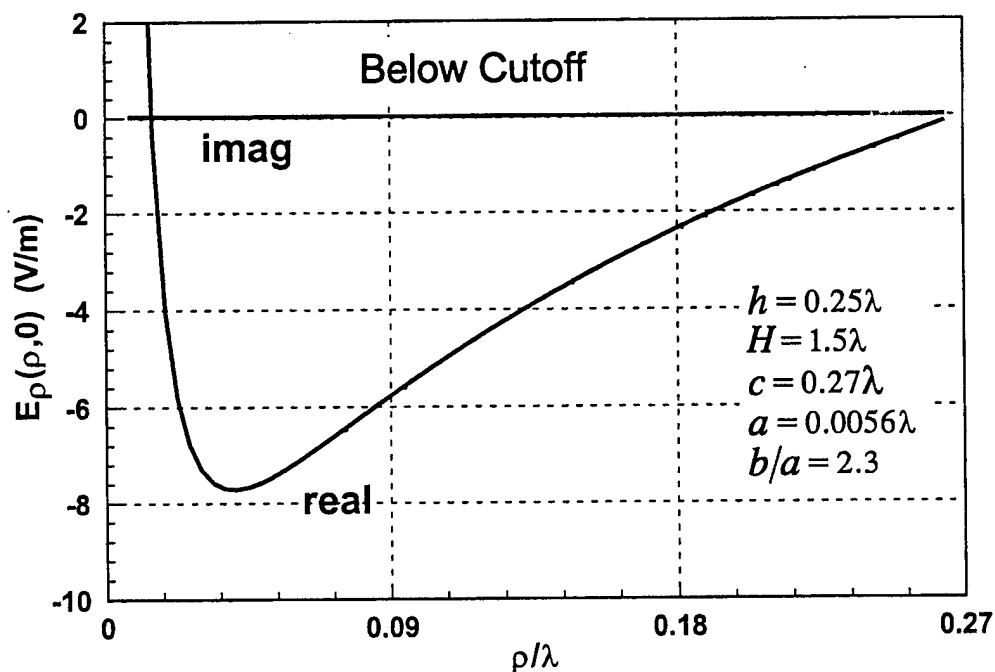


Figure 5-3. The  $z$ -directed electric field computed at the bottom surface of the can along a line from the monopole, at  $\rho=a$ , to the can wall, at  $\rho=c$  (below cutoff).



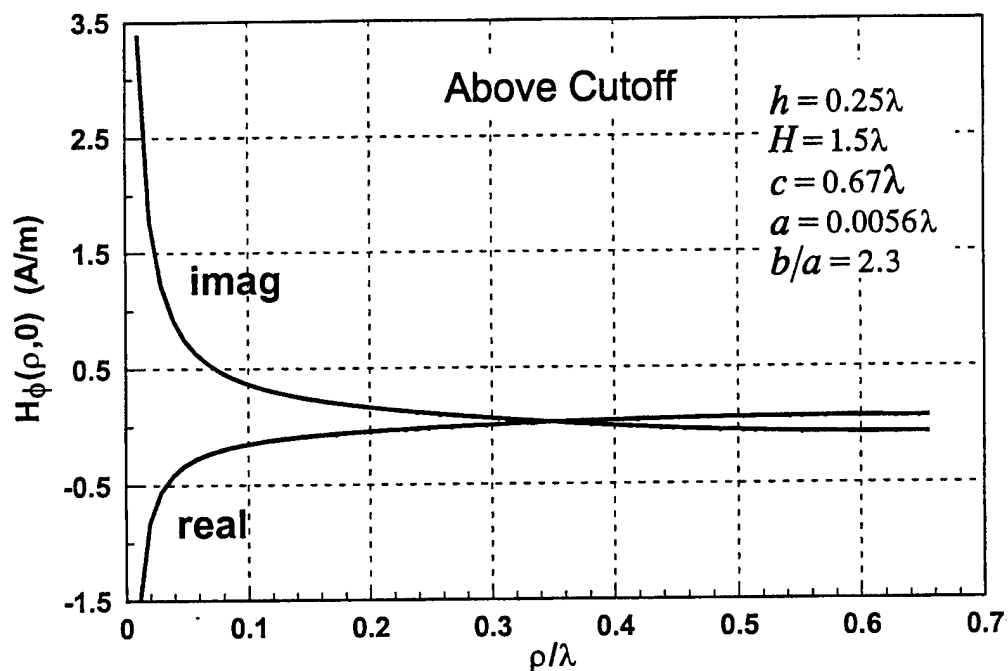


Figure 5-4. The  $\phi$ -directed magnetic field computed at the bottom surface of the can along a line from the monopole, at  $\rho=a$ , to the can wall, at  $\rho=c$  (above cutoff).

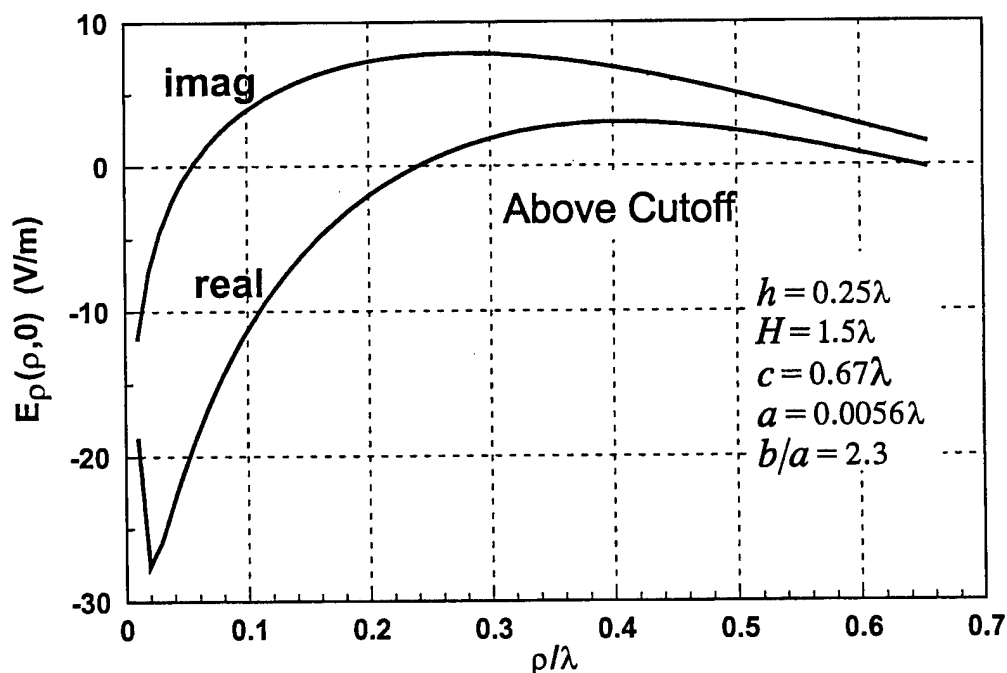


Figure 5-5. The  $z$ -directed electric field computed at the bottom surface of the can along a line from the monopole, at  $\rho=a$ , to the can wall, at  $\rho=c$  (above cutoff).

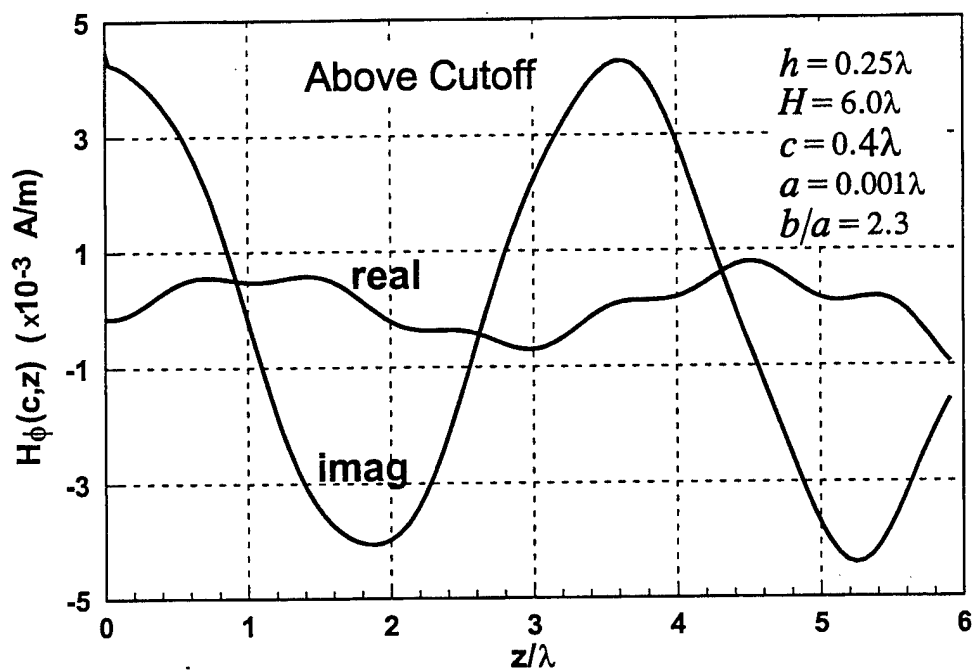


Figure 5-6. The  $\phi$ -directed magnetic field computed at the interior wall of the can at  $\rho = c$  (above cutoff).

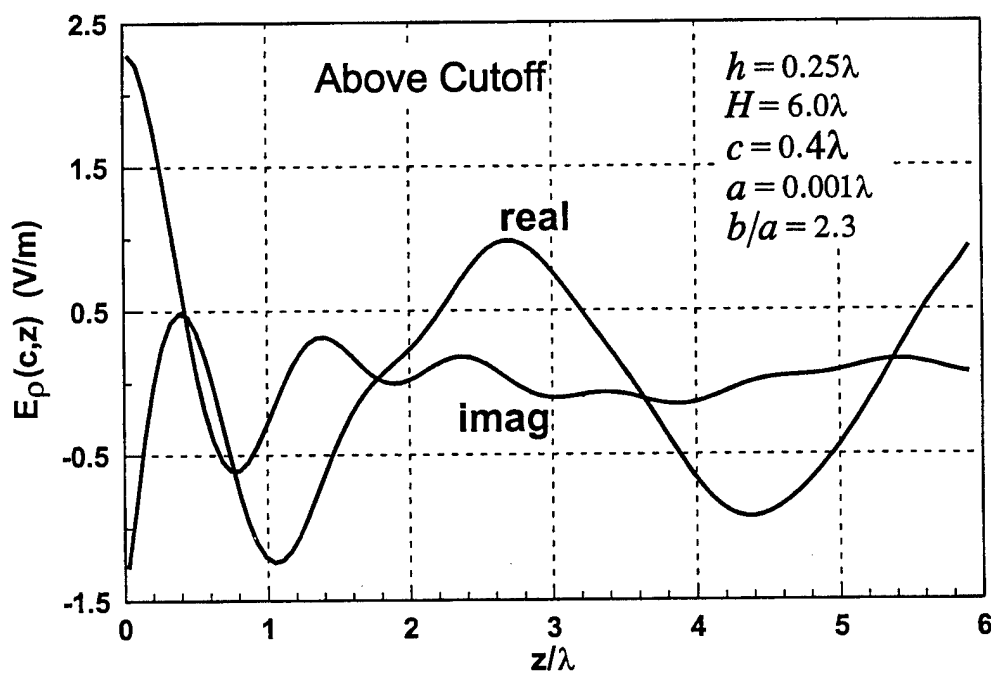


Figure 5-7. The  $\rho$ -directed electric field computed at the interior wall of the can, at  $\rho = c$  (above cutoff).

## CHAPTER 6

### EXPERIMENTAL APPARATUS AND MEASUREMENT

#### 6.1 Introduction

In this section we discuss the apparatus and procedures used to measure current and charge on structures of interest. The experimental data are used to corroborate the theoretical data. The measured data discussed in this section are of two forms. One is the antenna driving-point admittance. Relative measurements are made of the current (magnetic field) and charge (electric field) induced on the interior surface of the can bottom and wall. The admittance and the relative electric and magnetic field are measured subject to the can being excited by a coaxial monopole. These data allow direct comparison with the data obtained from solutions of the integral equation for the zero order BOR.

It is very difficult to conduct useful measurements when the coaxial-monopole-driven can structure resides in open space, since the instrumentation needed to perform these measurements would disturb the field to be determined. Hence, measured data must be taken when the coax-can structure is mounted on a ground plane which provides isolation of the device under test (DUT) from the instrumentation. In this case one can "access" the interior region of the can bottom through the ground plane without disturbing the original field structure. The ground plane and can configuration allows one to employ image theory in the comparison of measured and computed data.

Measurements for the coax-can structure can be readily done without mounting the can on the ground plane when the operating frequency of the can is sufficiently below the cut-off frequency of the corresponding circular waveguide formed by the can. Because the interior fields decay sufficiently below cut-off, as a function of axial displacement toward the can end, the field that escapes the can is very small and does not

couple significantly with exterior objects surrounding this experimental model. For this case one can access the interior region of the can-wall through a short section of an axially directed thin slot cut in the can-wall without disturbing the field.

In the following sub-sections are found discussions of the apparatus and instrumentation used to perform the measurements. The measurement probes used and their construction details are presented and the procedures employed to perform the measurements are outlined.

## 6.2 Construction of Can

In Figure 6-2 is shown a tapered edge circular brass disk of thickness  $3/8$  inch. This disk serves as the can bottom and is machined to fit the mating receptacle in the ground plane in the Computational Electromagnetics Laboratory.

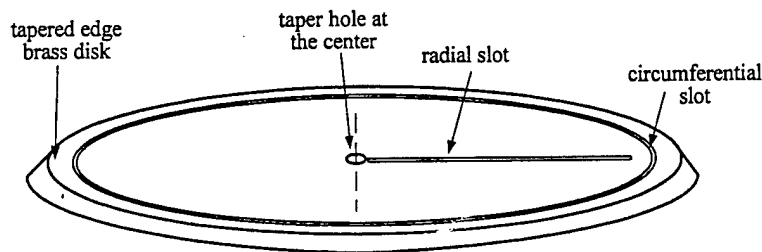


Figure 6-1. A circular brass disk used to construct the can bottom.

A tapered hole is drilled at the center of this circular disk for insertion of the of coaxial monopole. A circumferential slot, approximately  $1/8$  inch deep and 14.55 cm inner diameter, is cut in the disk to receive the can wall. This slot was made slightly thicker than the thickness of the can wall to ensure a snug fit. Along a radial line from a point close to the hole at the center to a point very close to the can wall, a  $1/16$  inch radial slot was cut in the disk to allow access to the interior can bottom. Since the source (monopole) field inside the can is rotationally invariant, the current in the can bottom is radially directed and  $\phi$  invariant. This allows one to cut a thin radially directed slot in the

can bottom (disk) with no resulting disturbance to the disk current. Access to the can's interior region for probing the field can be gained through this radially directed thin slot, which does not significantly alter the field structure. The  $\rho$ -directed slot does not interfere with the  $\rho$ -directed current on the can interior bottom.

A rectangular brass sheet of thickness 1/16 inch is rolled to construct the cylindrical can wall of inner radius 14.55 cm and approximate height of 15 inch. This cylindrical can wall is then inserted in the circumferential slot of the circular brass disk and soldered (Figure 6-2). The can wall is then soldered along the vertical joint with a copper strip applied for mechanical strength. The whole structure is then mounted on the ground plane as schematically suggested in Figure 6-3. The parameters of this experimental configuration are  $H=38.2\text{ cm}$ ,  $a=0.456\text{ mm}$ ,  $c=14.55\text{ cm}$  and  $b/a=2.3$  for the use in computation. This structure is excited by a coaxial monopole as illustrated.

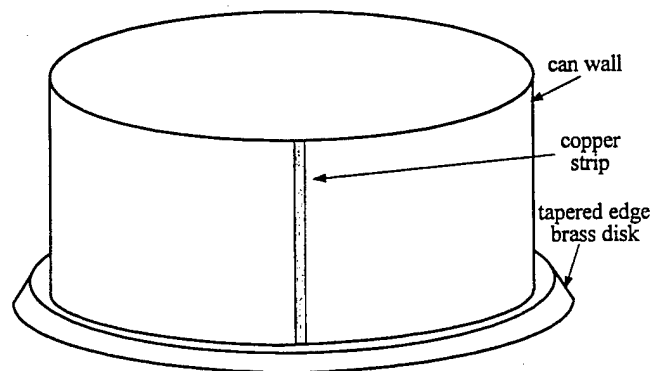


Figure 6-2. The disk and the brass sheet used to construct the can-wall.

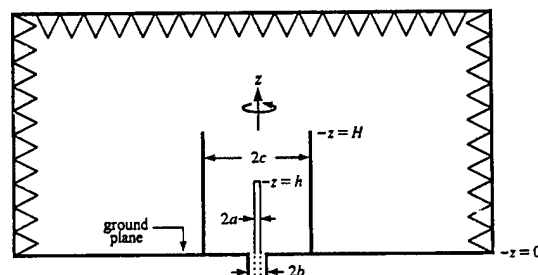


Figure 6-3. The can excited by a coaxial monopole on the ground plane.

### 6.3 Construction of the Monopole

Illustrated in Figure 6-4 are the details of the monopole antennas used in the measurements. They are constructed from low-loss semi rigid 141 mil coaxial cable. To construct the monopole antenna, the outer conductor and dielectric material are removed from a section of the coaxial cable. The exposed center conductor of the coaxial line then serves as the monopole antenna. The feed point is the point where the center conductor exits the coax. To fit the antenna to the tapered hole at the center of the circular disk plate (bottom of can), a tapered brass plug is machined to fit over the outer conductor of the coaxial cable. This plug is soldered to the outer conductor of the coax. The tapered end of the plug is positioned at the feed point of the antenna as shown in Figure 6-4.

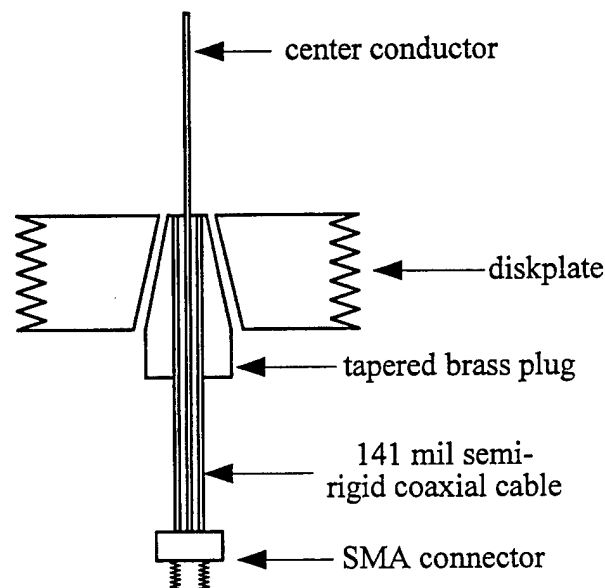


Figure 6-4. Construction of monopole antenna (cross-sectional view).

### 6.4 Construction of Probes

Two types of probes were designed and constructed for this work. One type is for measuring the charge (or electric field normal to the surface,  $E_p$  and  $E_z$ ) while the other type is for measuring the current (or tangential magnetic field,  $H_\phi$ ). Since the charge probe must couple to the normal electric field, it is simply a very short monopole type

probing element. The charge probe may also be viewed as a normal electric dipole exciting the conducting can. The current probe, on the other hand, must couple to a  $\phi$ -directed magnetic field on the disk surface. Hence, its construction consists of a loop-antenna type probing element.

Shown in Figure 6-5 is an illustration of a charge or electric field probe [5]. One charge probe is constructed from a section of 85 mil semi-rigid coaxial cable. As seen, the outer conductor and dielectric material were removed from a section of the cable to expose the center conductor. That section is inserted through a hole in a piece of machined brass stock (1 inch long, 1/2 inch wide, 1/2 inch thick) and the cable is soldered to the brass stock on the side opposite to the surface through which the monopole extends. The brass stock was machined so as to have a ridge of approximately 1/16 inch in width of height slightly greater than 3/8 inch. The ridge was designed to ensure that the probe resides on a surface contiguous with that on which the charge was measured. It also serves as a guide to ensure that the entire probe assembly can be moved along the slot with precision.

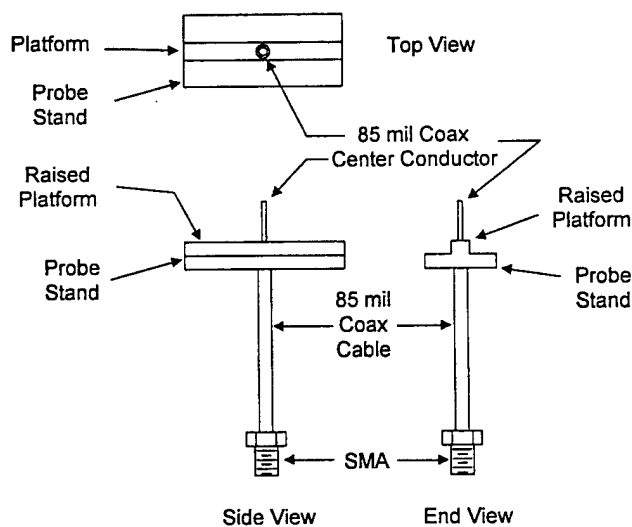


Figure 6-5. Construction of a charge probe.

Shown in Figure 6-6 is an illustration of a current probe [5]. The design and construction of the current probe is more complicated than that of charge probe. For the current probe shown, a similar piece of brass stock is machined as discussed above. However, two holes are drilled through the stock in the ridge along its center line. The diameter of the holes is slightly larger than that of the 20 mil semi-rigid used for fabricating the probe. As indicated in Figure 6-6, a small gap in the outer conductor of the 20 mil coax is cut in the loop. Away from the gap, the outer conductor is retained and soldered to the brass stock at the hole. Further, the end of the center conductor of the 20 mil coax is also soldered to the brass stock. The purpose of this so-called shielded loop with the gap in the outer conductor of the 20 mil cable at the center of the loop is to allow coupling only to the  $\phi$ -directed magnetic field but to reject any coupling to the derivative of the normal electric field. The presence of the probe outer conductor serves as a shield to minimize charge coupling while allowing current coupling. To physically support the structure, a small diameter brass tubing is soldered at one end to the underside of the brass ridge. The 20 mil cable was inserted through the tube. The resulting structure was finally connected to a right-angle SMA connector as indicated in Figure 6-6.

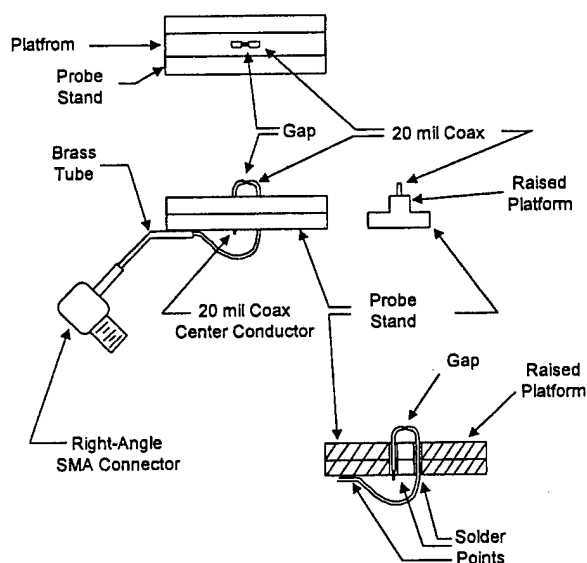


Figure 6-6. Construction of current probe.



### 6.5 Probing the Can Wall

For measuring the charge and current on the interior can wall below cut-off, the finite cylindrical brass tube (can), the monopole, and the probes of [5] are assembled into an experimental model. Along the wall of this can a short thin slot has been cut parallel to the axis of the can ( $z$ -axis) to allow access to the interior can wall. Since the source (monopole) field inside the can is rotationally invariant the current in the can wall is axially directed and  $\phi$  invariant. This allows one to cut a thin  $z$ -directed slot in the can wall with no resulting disturbance to the wall current. Access to the can's interior region for probing the field can be gained through this  $z$ -directed thin slot, which does not significantly alter the field structure since the probe and  $z$ -directed slot do not interfere with the  $z$ -directed current on the can interior wall. The parameters for this configuration are  $H=50\text{ cm}$ ,  $a=0.456\text{ mm}$ ,  $c=635\text{ cm}$  and  $b/a=2.3$  (see Figure 6-3). This structure is excited by a coaxial monopole of height  $h=12.6\text{ cm}$ .

### 6.6 Probing the Can Wall with Dielectric Loading

The can described in [5] and illustrated in Figure 6-7 is used for measuring wall charge and current when dielectric loading is present. Again, the operating frequency is below the cut-off frequency of the corresponding circular waveguide loaded with the same dielectric material. Dielectric loading of the can be obtained by immersing the can into a container filled with a liquid dielectric material as shown in Figure 6-7. The dielectric material used in this measurement should be of liquid type since it allows us to vary the height of the dielectric/air interface easily. Also measuring probes can move freely through this liquid dielectric material. Other than the introduction of the dielectric material, the equipment and apparatus used in this measurement are exactly the same as those discussed in [5]. Isopropanol is used in this experiment as the dielectric material because it has a relatively well understood dielectric constant and loss tangent. The dielectric constant of Isopropanol is less than 20 depending on the operating frequency. It

has also frequency dependent loss. Therefore, one must take the known frequency dependent electrical characteristics of Isopropanol into account when obtaining computed or measured data.

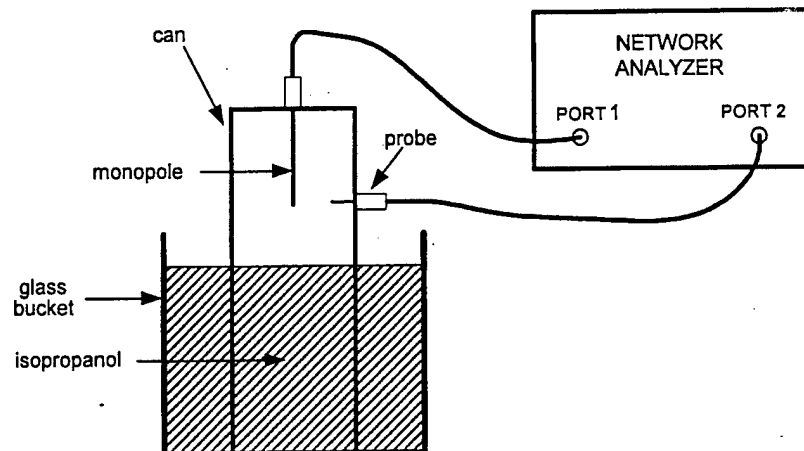


Figure 6-7. Can-wall probing with dielectric loading.

The equivalent parameters corresponding to the experimental set-up of Figure 6-7 are shown in Figure 6-8 for use in the computations. The parameters are as follows:  $H=50\text{ cm}$ ,  $a=0.456\text{ mm}$ ,  $c=6.35\text{ cm}$ ,  $d=10\text{ cm}$  and  $b/a=2.3$  (Figure 6-8). This structure is excited by a coaxial probe of height  $h=12.6\text{ cm}$ .

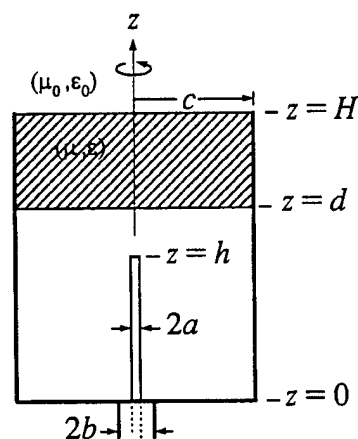


Figure 6-8. Can-coax structure loaded with dielectric material.

## 6.7 The Instrumentation and Measurements

The basic instrumentation utilized to perform the measurements is schematically shown in Figure 6-9. As illustrated, the system consists of a HP Vector Microwave network analyzer, a PC-AT computer controller and the device under test (DUT). The analyzer is connected to a PC having a general-purpose-interface-bus (HPIB). The PC computer is used as a controller to command the network analyzer to take appropriate measurements and to send the measured data over the HPIB for further manipulation on the computer. The network analyzer system is used to make swept frequency measurements over frequency ranges prescribed by the user. The schematic for probing charge and current on the can bottom is illustrated in Figure 6-10(a) while Figure 6-10(b) shows the schematic for can wall probing.

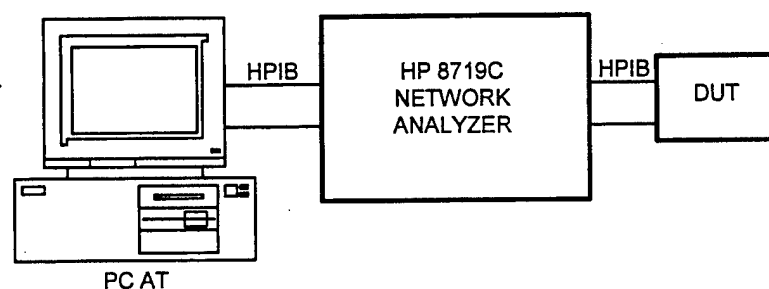


Figure 6-9. Block diagram showing measurement apparatus.

The monopole antenna admittance is measured over the frequency range from 300 MHz to 3000 MHz for the can mounted in the ground plane (Figures 6-2 and 6-3). The cut-off frequency of this structure occurs around 790 MHz. However, the admittance measurement is performed over the frequency range from 100 MHz to 1000 MHz for the can below cut-off [5] of Figure 6-7. The cut-off frequency of this can occurs around 1800 MHz. It has been observed that the fields inside decays rapidly beyond the point at which the monopole ends.

For the field measurements, data have been taken over the frequency ranges of interest at increments of 0.5 cm along the radial slot at the can bottom while the data are

taken at 1 cm increments along the axial slot. Since the absolute response of the specifically designed and constructed field probes is not known, the measured data were normalized by a complex constant at a specified frequency to facilitate comparison against the computed data. Since we don't know the phase reference when measuring the relative fields, to match the phase reference of the computed data, the measured data is normalized by a complex constant at the point where the maximum or local maximum response occurred.

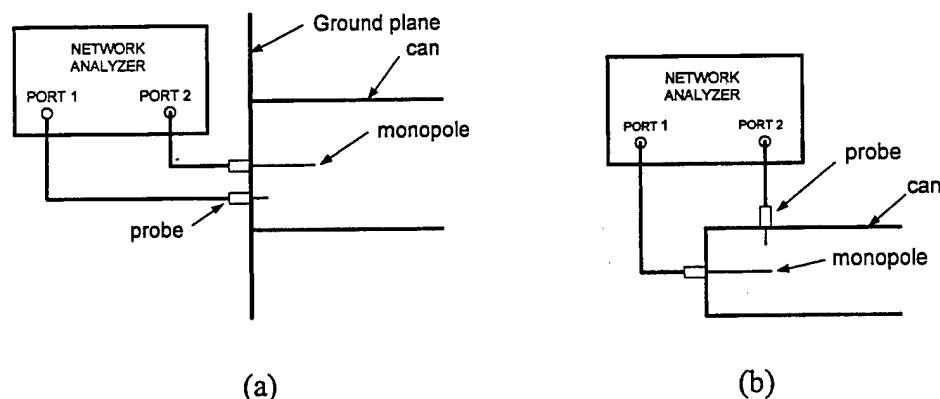


Figure 6-10. Apparatus/setup used for probing the fields (a) at the can-bottom (b).at the can wall.

The magnitude and phase of the scattering parameters  $S_{11}$  and  $S_{12}$  or ( $S_{21}$  and  $S_{22}$ ) are measured in this set-up. From the measured data of  $S_{11}$ , the input impedance of the structures were calculated according to the method described in [5]. The  $S_{12}$  measured data is used for determining the relative current and charge. Measurements along the thin slots were made for a variety of antenna configurations and different monopole lengths. Thin wire antenna length of  $h = 12.6 \text{ cm}$  is used for the below cut-off measurements, while thin wire antennas of lengths  $h = 13.1 \text{ cm}$  and  $h = 26.9 \text{ cm}$  are used for ground plane measurements.

## CHAPTER 7

### DISCUSSION OF RESULTS AND CORROBORATION OF THEORY

For the purpose of corroborating the accuracy of the data obtained from the theoretical analysis set forth in this report, we present and discuss comparisons of computed and measured data. The computed data presented are obtained from numerical solutions of the integral equation formulated in this report. The measured data presented were obtained from experiments as described in section 6. As discussed previously, two types of comparative data are presented to lend plausibility to the validity of the theoretical and numerical aspects of this work. The first set of data is of driving point admittance. The next data are of the values of relative field strength (referred to in the plots as the normalized electric and magnetic fields) on the interior can bottom and can wall. The comparative data presented in this section confirm the accuracy of the numerical solutions obtained in this report.

Shown in Figures 7-1 and 7-2 are real and imaginary parts of the measured (dashed lines) and computed (solid lines) driving point admittance for a 13.1 cm long monopole antenna exciting the can over the frequency range from 300 MHz to 3000 MHz. The data of Figure 7-3 and 7-4 show the real and imaginary parts of the measured and computed driving point admittance when the can is excited by a 29.6 cm long monopole antenna. While the measured data for the 13.1 cm long monopole antenna shows excellent agreement with the computed, the measured data for the 29.6 cm long monopole antenna follow the general trends of the theoretical data closely but the agreement can only be claimed to be "good." The discrepancies at certain frequencies are attributed to faulty orientation of the 29.6 cm monopole antenna. That is, complete rotational symmetry is not obtained because the very long monopole is slightly bent. (When the exciting antenna is curved rotationally symmetry of the fields is

compromised.) In this case, a  $\phi$  - directed current is induced on the experimental structure and is not accounted for in the theoretical model. The monopoles were formed by removing the outer conductor and dielectric of a section of semi-rigid coaxial cable. We simply were not able to keep the center conductor straight when more than about 15 cm of outer conductor and dielectric were removed.

The can is below cut-off when operated below 790 MHz. Because the can is operated below cutoff frequency of the  $TM_{01}$  mode of corresponding the circular waveguide, power cannot be delivered to the can by the monopole and the real part of the driving point admittance is zero (at least for the computed part since loss effects are not modeled). So, since power cannot escape the can structure excited by the monopole antenna operating below cutoff, the monopole must present a purely reactive load to the generator. Thus driving point admittance of the antenna should exhibit the characteristics described in [5] for a lossless structure.

The measured real part of input admittance in a very narrow band about 469 MHz is very large relative to that at other frequencies, even though this frequency is below the cut-off frequency of 790 MHz. The computed value of this real input admittance is very very small and is quite different from the measured. Since this operating frequency is below cut-off, no energy should leak from the can, which observation appears inconsistent with the significant value of real  $Y_{in}$ , which implies that power is being supplied to the monopole. At 469 MHz, the monopole and its image effectively form a straight segment which is  $3/2 \lambda$  long. Under this condition the monopole is resonant and its current is very large. This very large current strongly excites the can and, hence, the losses in the monopole and can are much much greater than at other non-resonant frequencies. The large real  $Y_{in}$  is, indeed, consistent with significant power delivered through the monopole to supply the losses experienced in the finitely-conducting material from which the can and monopole are fabricated. The computed values of real  $Y_{in}$  do not

exhibit this behavior because the integral equation is formulated on the basis of the assumption that the monopole and can are perfect conductors and, therefore, are lossless. This divergence of measured and computed values is expected and explicable.

Figure 4.5 and 4.6 show the relative magnitudes of computed electric field strength at the bottom of the can along a line from the location of the coax center to the can wall. In Figures 7-7 to 7-11 are depicted real and imaginary parts of the measured and computed normalized z-directed electric field strengths at the inner surface of the can bottom for the 13.1 cm long monopole antenna exciting the can at selected frequencies. The measured data shown in these figures are normalized by a complex constant at a selected position along the radial slot, so as to be equal to the computed data at this position. The measured data show excellent agreement with the computed results. This normalization is done to aid the reader who wishes to compare measured and computed data. It is not feasible to calibrate the charge and current probes for absolute magnitude and phase. The basis of the normalization is that one assumes the measured and calculated values to be equal at a single point and then compares the two sets of data at other points along the range (displacement) of measurements.

Figures 7-12 to 7-17 illustrate real and imaginary parts of the measured and computed z-directed electric field strengths at the inner surface of the can bottom for the 26.9 cm long monopole antenna exciting the can at selected frequencies. The agreement between computed and measured data in this case, while excellent at low frequencies, is not as good as the agreement of the data shown for the 13.1 cm long monopole antenna at higher frequencies. The poorer agreement is due to unintended curvature of the 26.9 cm long monopole antenna and to the noisy measured data at some frequencies at which the physical parameters cause the input impedance to be high and, hence, the coupling from the signal generator to the structure to be very weak. Under these conditions the measured signal is weak and not sufficiently above the noise for reliable data. In addition, at

higher frequencies the wavelength is shorter and, hence, the deviation of the curved monopole from a straight line is greater relative to wavelength. As a result the curvature of the monopole has a more dramatic effect on the measurements.

Figures 7-18 to 7-24 show real and imaginary parts of the measured and computed relative magnetic field strengths at the can bottom for the 13.1 cm long monopole antenna exciting the can at selected frequencies. Figures 7-21 and 7-22 show the same data for the 26.9 cm long monopole antenna exciting the can. The agreement between computed and measured data in this case is very good for both monopole lengths. However, for the data of the 29.6 cm long monopole antenna, there are discrepancies at certain frequencies attributable to failure of the monopole to be straight and to the weak signal relative to the noise floor. In Figures 7-23 to 7-26 are shown of real and imaginary parts of the measured and computed normalized  $\rho$ -directed electric field strengths at the inner surface of the can wall for the 12.6 cm long monopole antenna exciting the can at selected frequencies. The measured data shown in these figures are normalized so as to match the computed data at one point along the slot. The measured data show excellent agreement with the computed results. Notice that, since the can is operated below cut-off (1800 MHz), the actual data for the  $z$ -directed electric field should have zero imaginary part as suggested in Figures 7-23 to 3-25.

In Figures 7-27 to 7-29 are illustrated real and imaginary parts of the measured and computed normalized  $\phi$ -directed magnetic field strengths on the inner surface of the can wall. The measured data show excellent agreement with the computed results. In this case, since the can is operated below cut-off (1800 MHz), the data for the magnetic field should have zero real part as predicted by the Figures 7-27 and 7-28.

In Figure 7-30 is illustrated the measured radially directed electric field at the can wall when the can is loaded by isopropanol. In Figure 7-31 and 7-32 are illustrated computed and measured data for dielectric loaded (isopropanol) can. The measured and



computed data agree reasonably well. The discrepancies between the measured and computed data are attributed to approximate representation of the dielectric constant of isopropanol in the computation and to the weak coupling of field during the measurement.

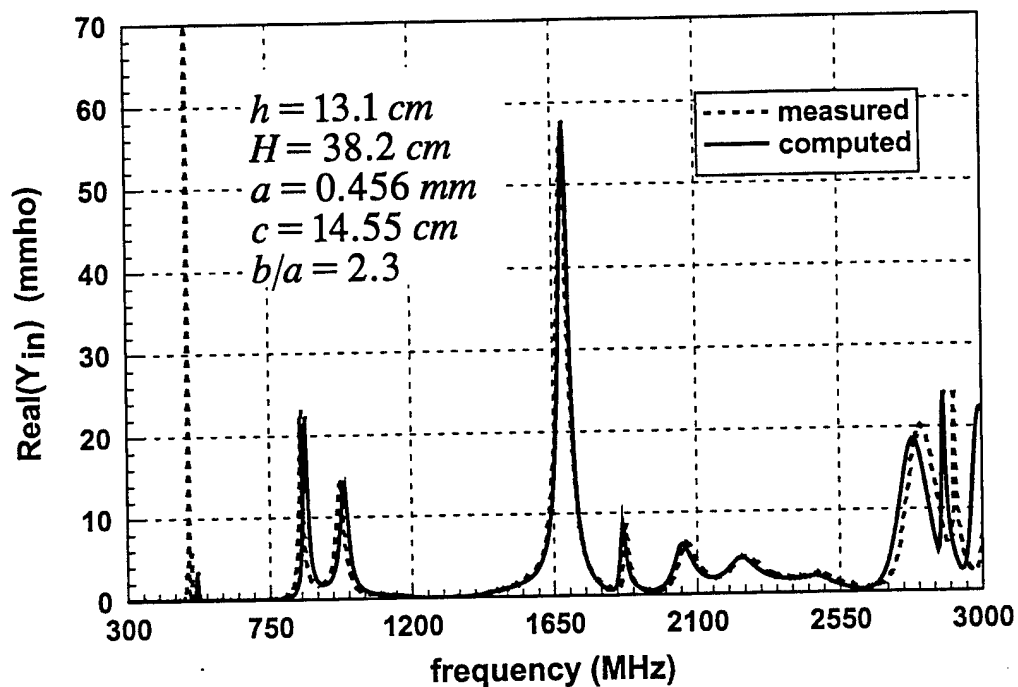


Figure 7-1. Measured and computed input admittance (real part) of coax-fed can for  $h = 13.1 \text{ cm}$ .

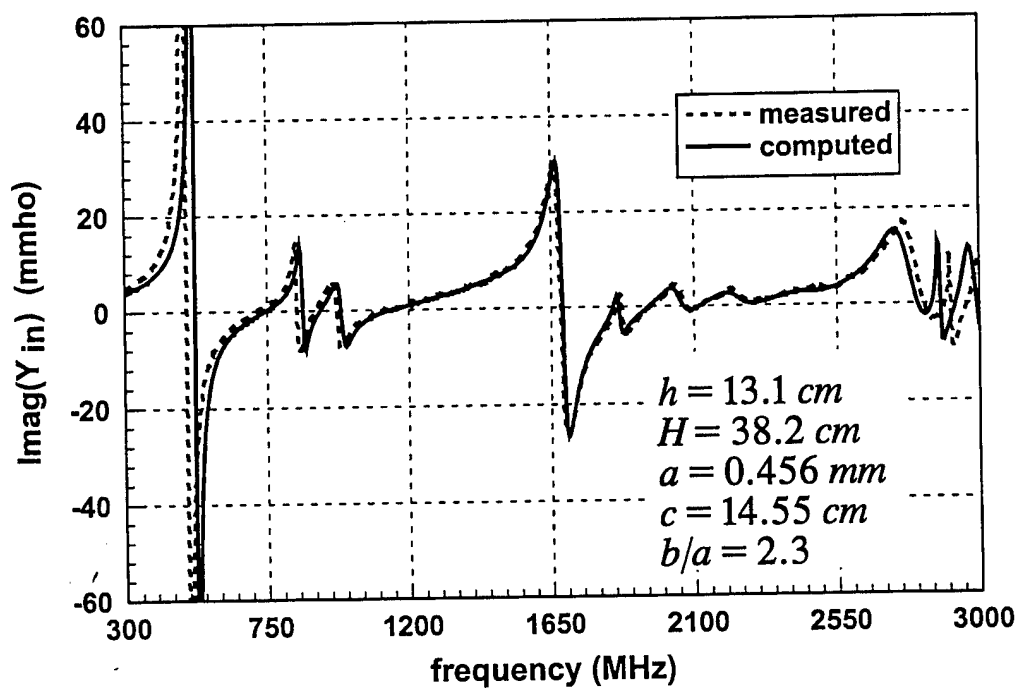


Figure 7-2. Measured and computed input admittance (imaginary part) of coax-fed can for  $h = 13.1 \text{ cm}$ .

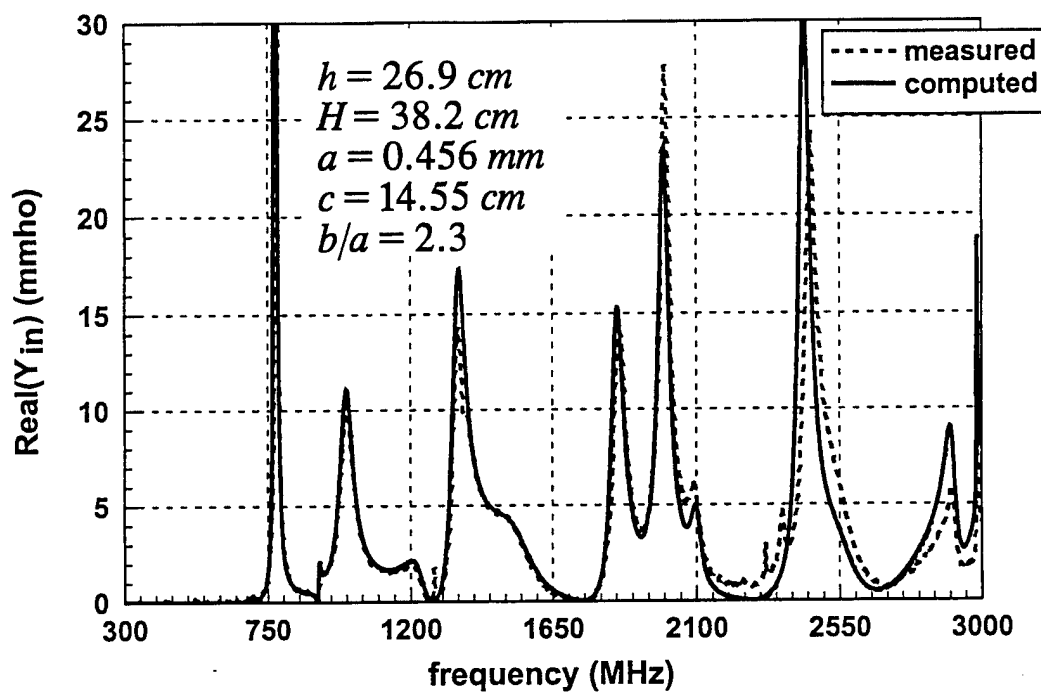


Figure 7-3. Measured and computed input admittance (imaginary part) of coax-fed can for  $h = 26.9 \text{ cm}$ .

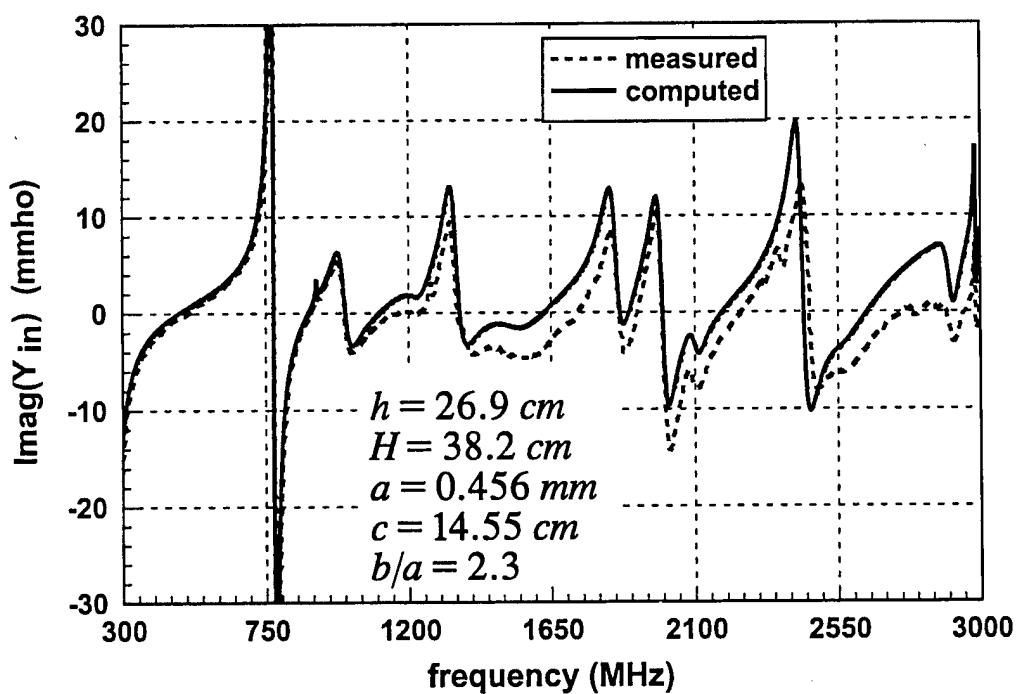


Figure 7-4. Measured and computed input admittance (imaginary part) of coax-fed can for  $h = 26.9 \text{ cm}$ .

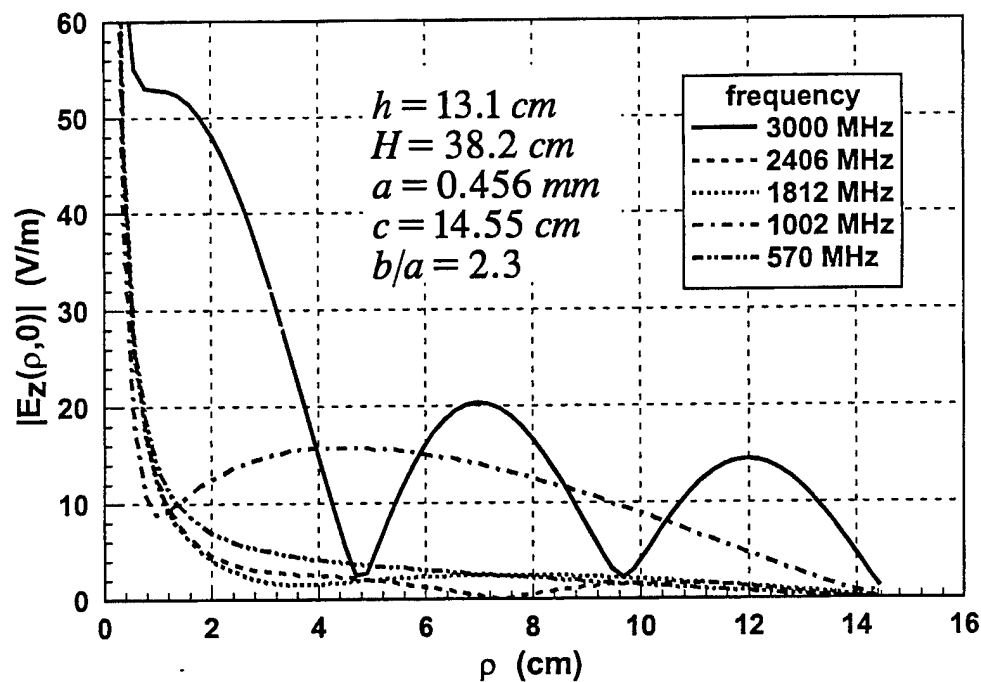


Figure 7-5. The magnitude of z-directed electric field (charge density) at the base of the can computed along a line from the monopole surface, at  $\rho = a$ , to the can wall, at  $\rho = c$  for  $h = 13.1 \text{ cm}$ .

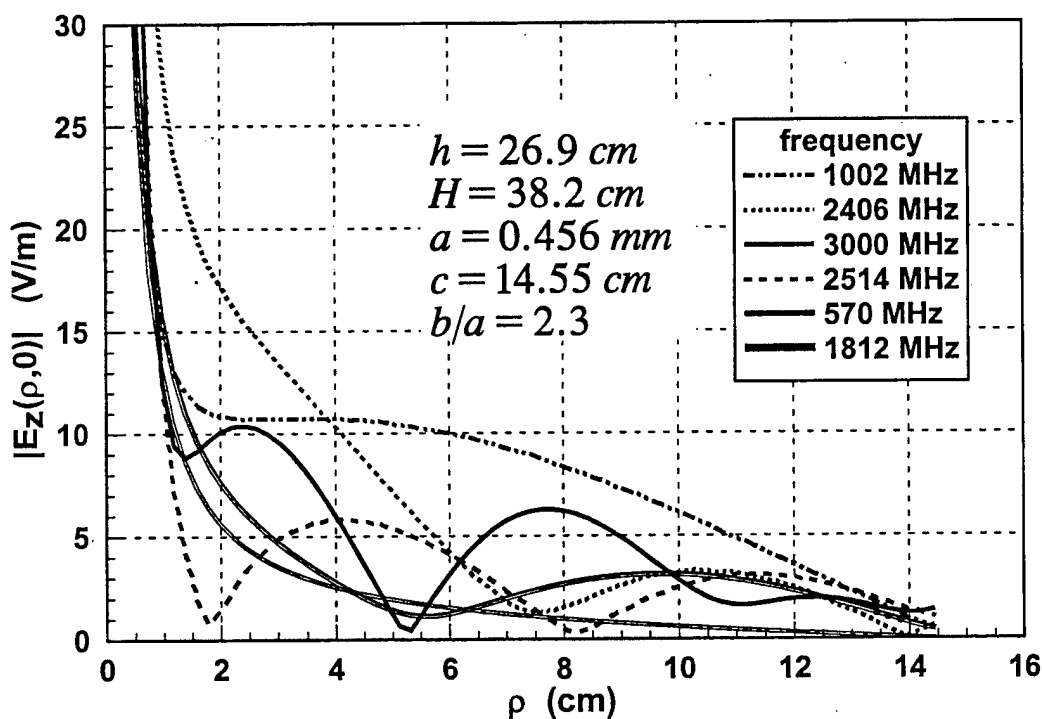


Figure 7-6. The magnitude of z-directed electric field (charge density) at the base of the can computed along a line from the monopole surface, at  $\rho = a$ , to the can wall, at  $\rho = c$  for  $h = 26.9 \text{ cm}$ .

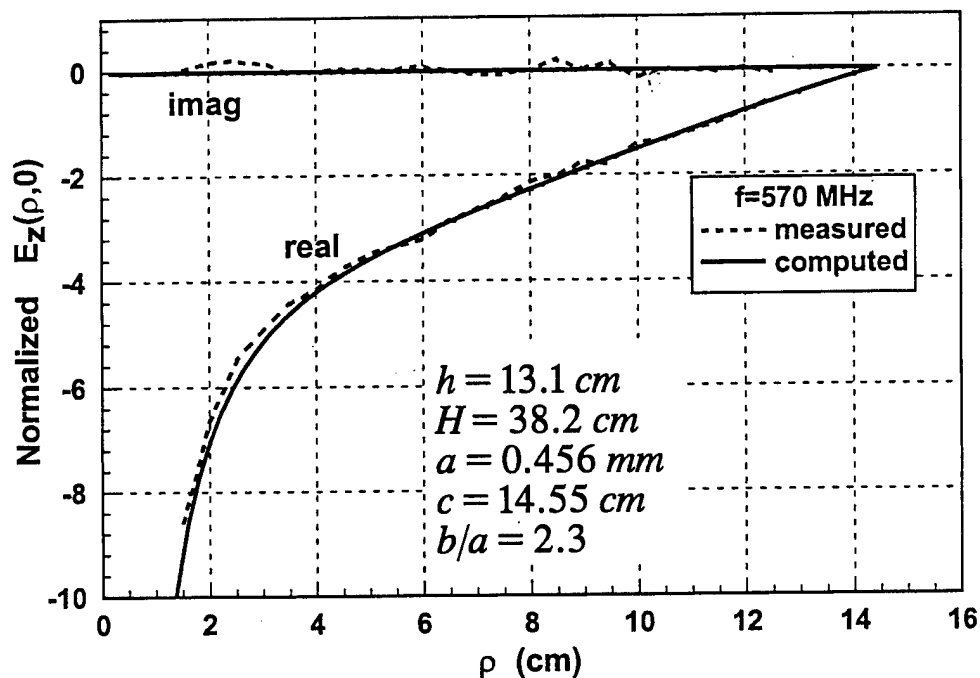


Figure 7-7. Measured and computed data of z-directed electric field at the bottom of the can at 570 MHz for  $h = 13.1 \text{ cm}$ .

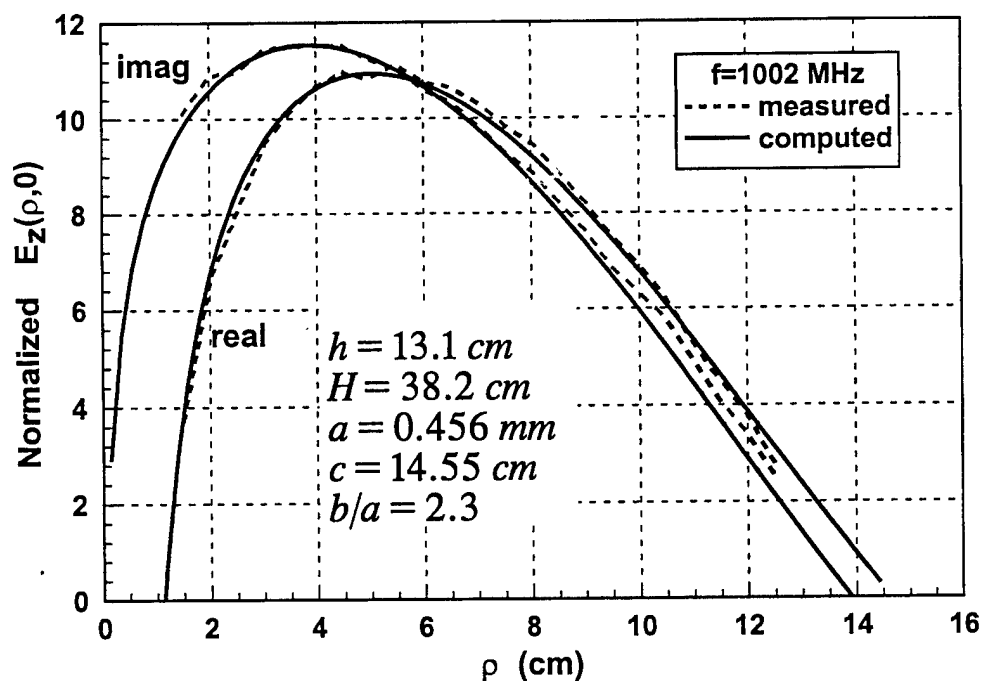


Figure 7-8. Measured and computed data of z-directed electric field at the bottom of the can at 1002 MHz for  $h = 13.1 \text{ cm}$ .

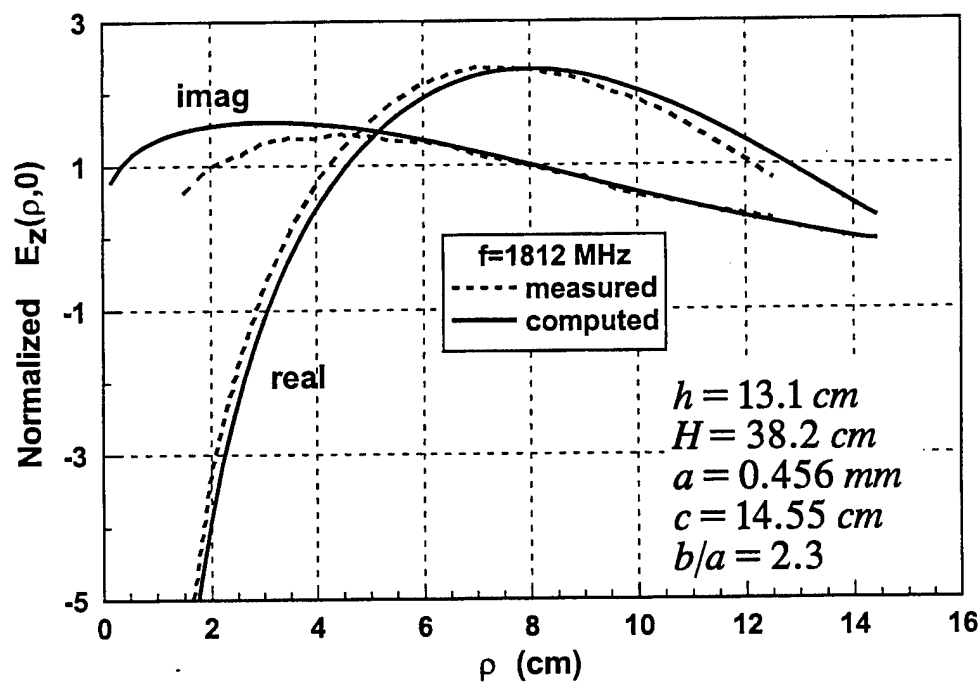


Figure 7-9. Measured and computed data of z-directed electric field at the bottom of the can at 1812 MHz for  $h = 13.1$  cm .

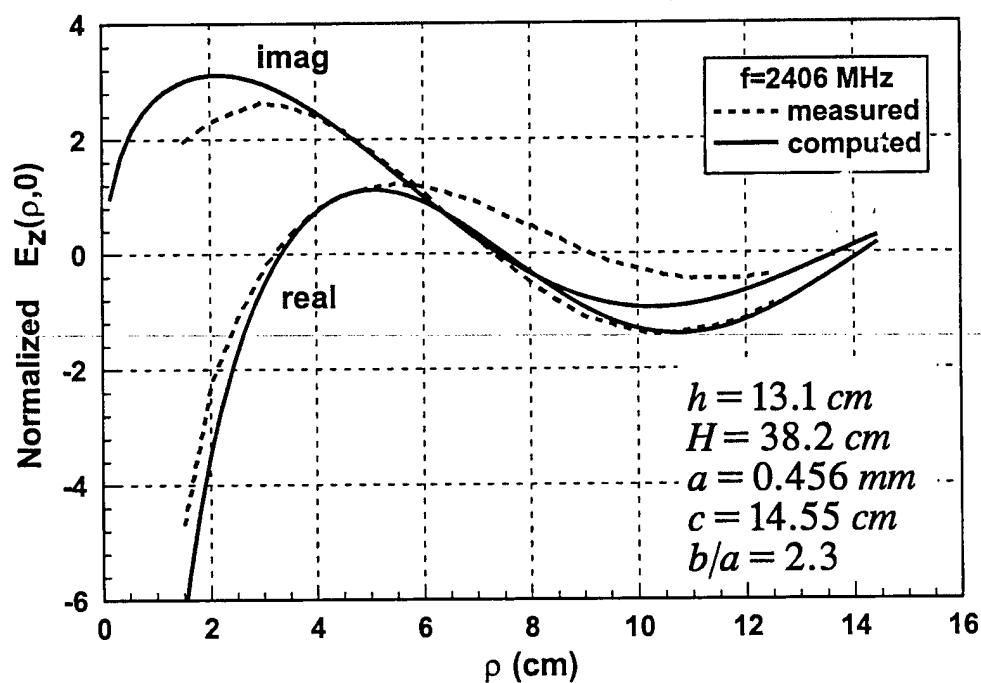


Figure 7-10. Measured and computed data of z-directed electric field at the bottom of the can at 2406 MHz for  $h = 13.1$  cm .

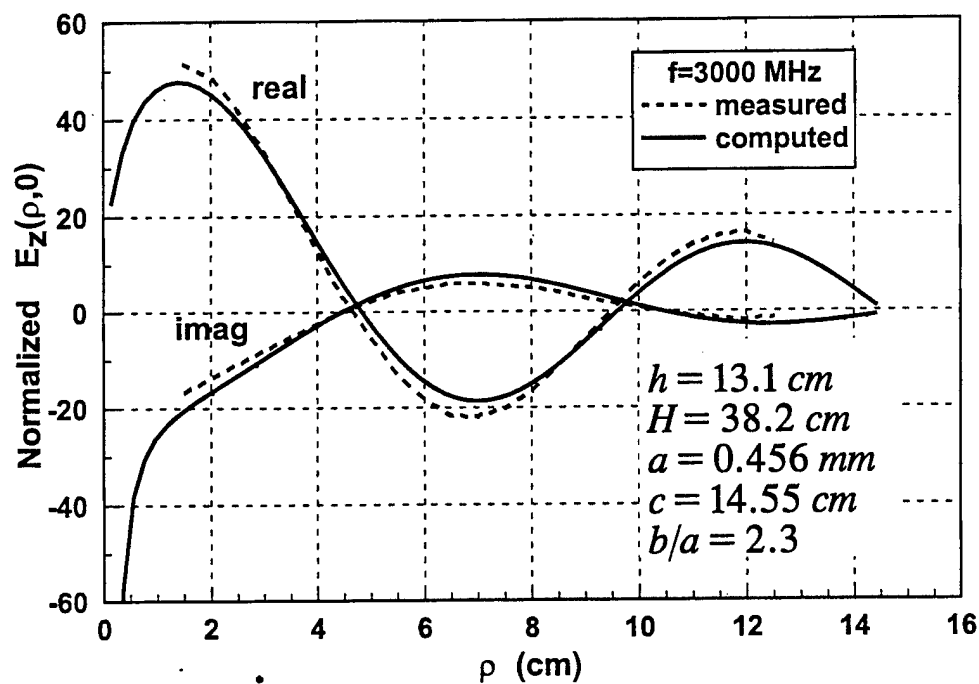


Figure 7-11. Measured and computed data of z-directed electric field at the bottom of the can at 3000 MHz for  $h=13.1$  cm .

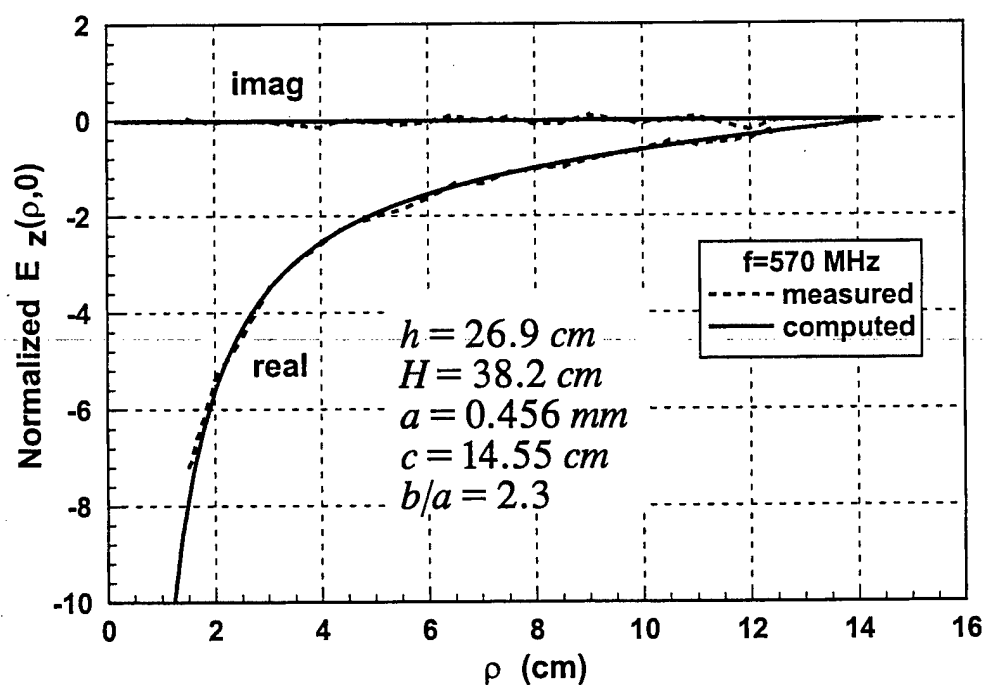


Figure 7-12. Measured and computed data of z-directed electric field at the bottom of the can at 570 MHz for  $h=26.9$  cm .

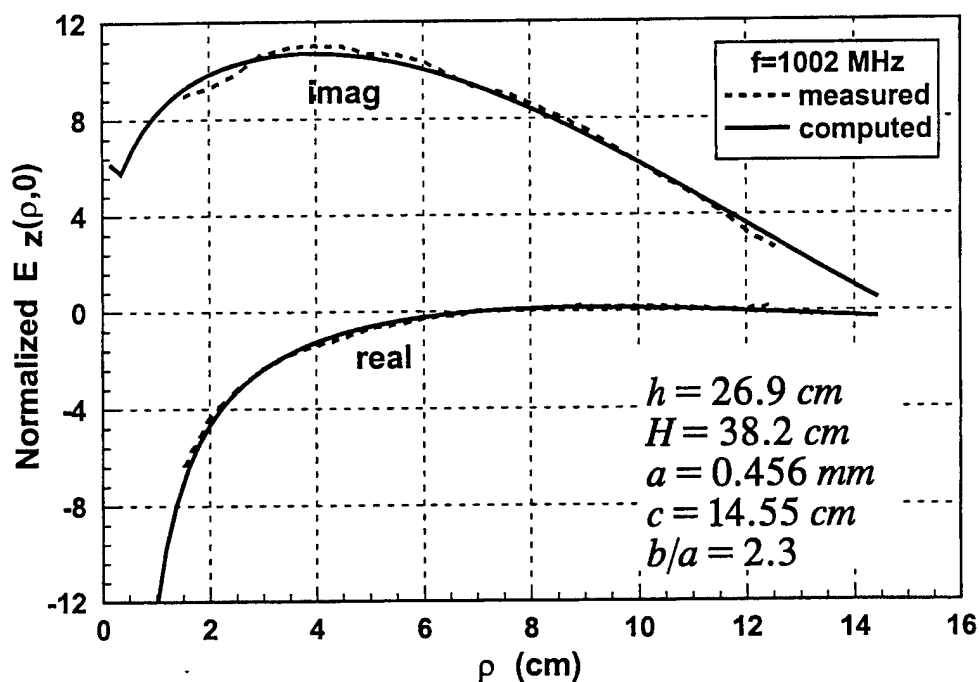


Figure 7-13. Measured and computed data of z-directed electric field at the bottom of the can at 1002 MHz for  $h = 26.9$  cm.

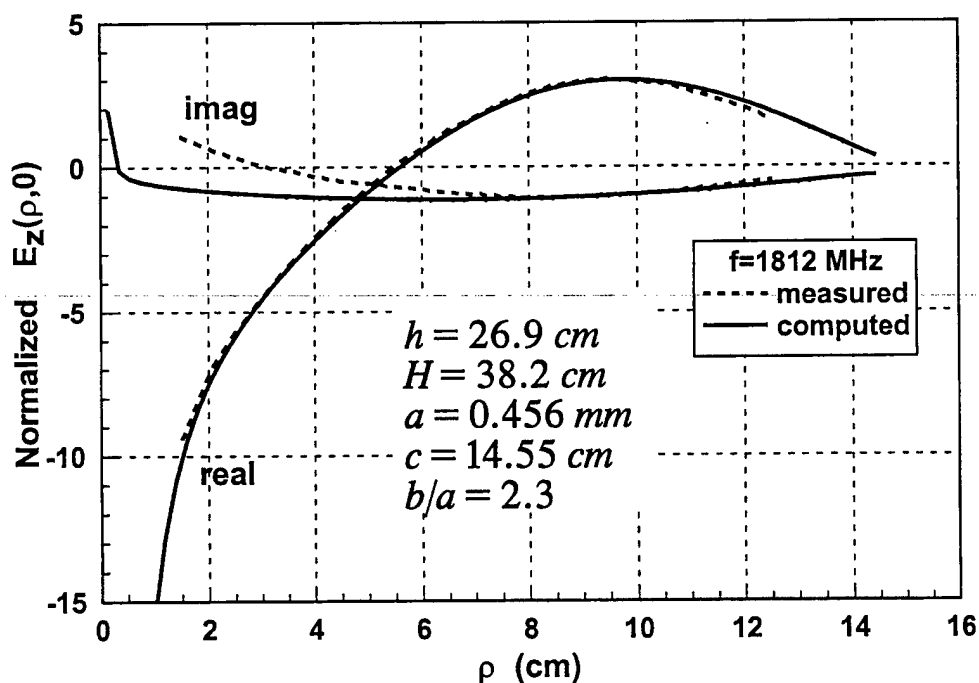


Figure 7-14. Measured and computed data of z-directed electric field at the bottom of the can at 1812 MHz for  $h = 26.9$  cm.



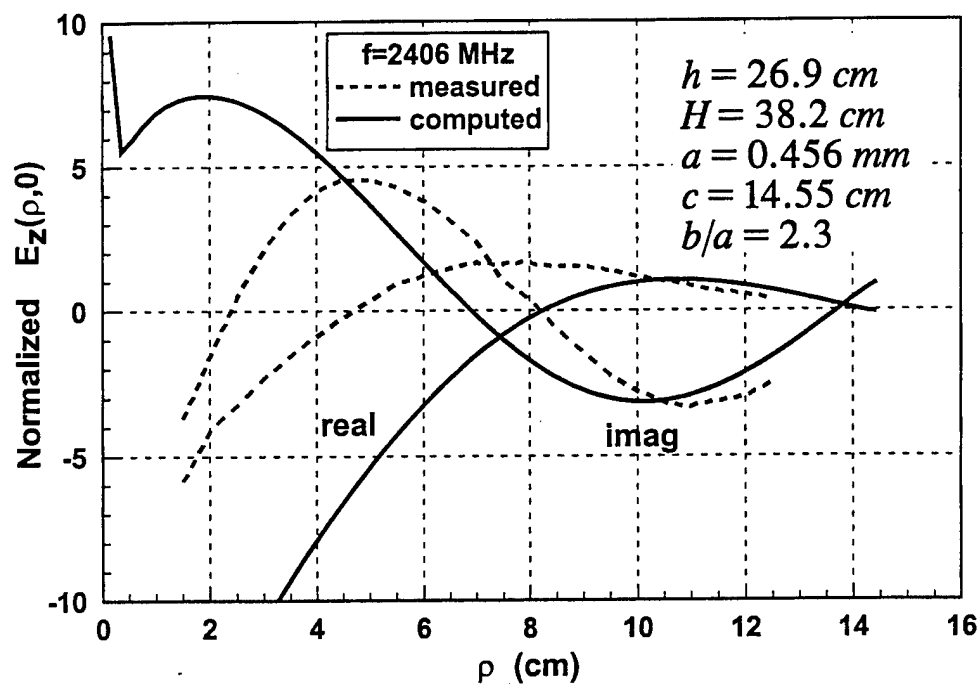


Figure 7-15. Measured and computed data of z-directed electric field at the bottom of the can at 2406 MHz for  $h = 26.9$  cm.

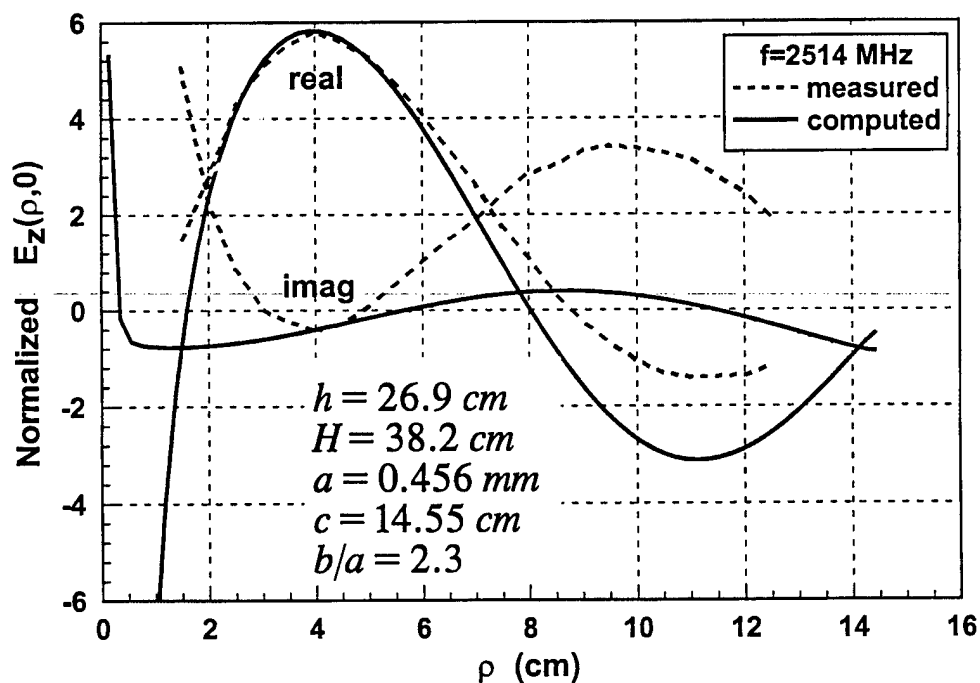


Figure 7-16. Measured and computed data of z-directed electric field at the bottom of the can at 2514 MHz for  $h = 26.9$  cm.

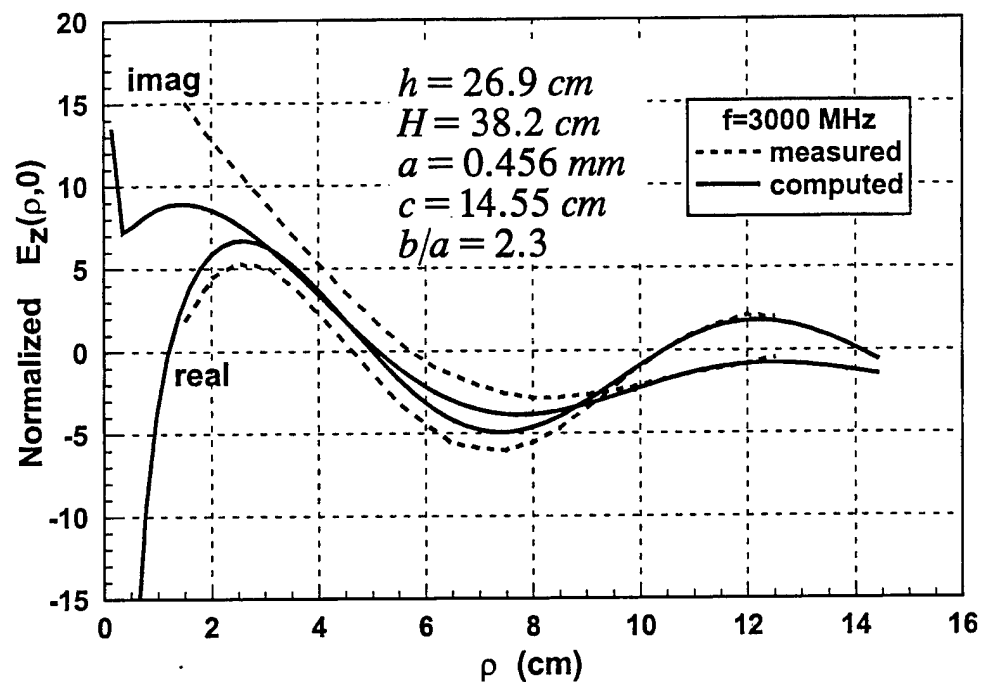


Figure 7-17. Measured and computed data of z-directed electric field at the bottom of the can at 3000 MHz for  $h = 26.9$  cm.

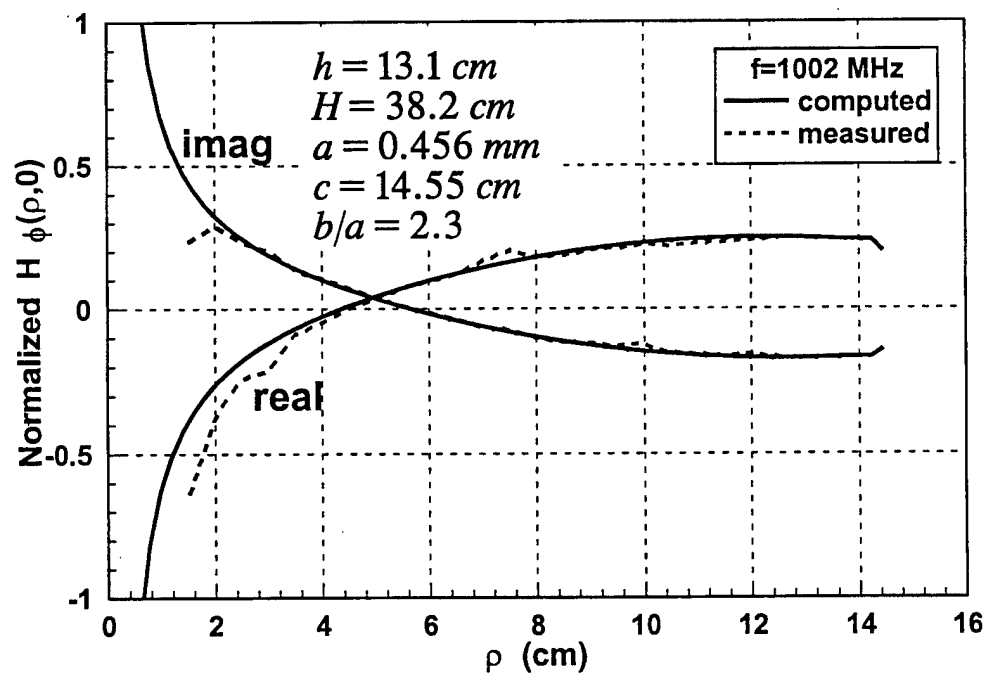


Figure 7-18. Measured and computed data of  $\phi$ -directed magnetic field at the bottom of the can at 1002 MHz for  $h = 13.1$  cm.

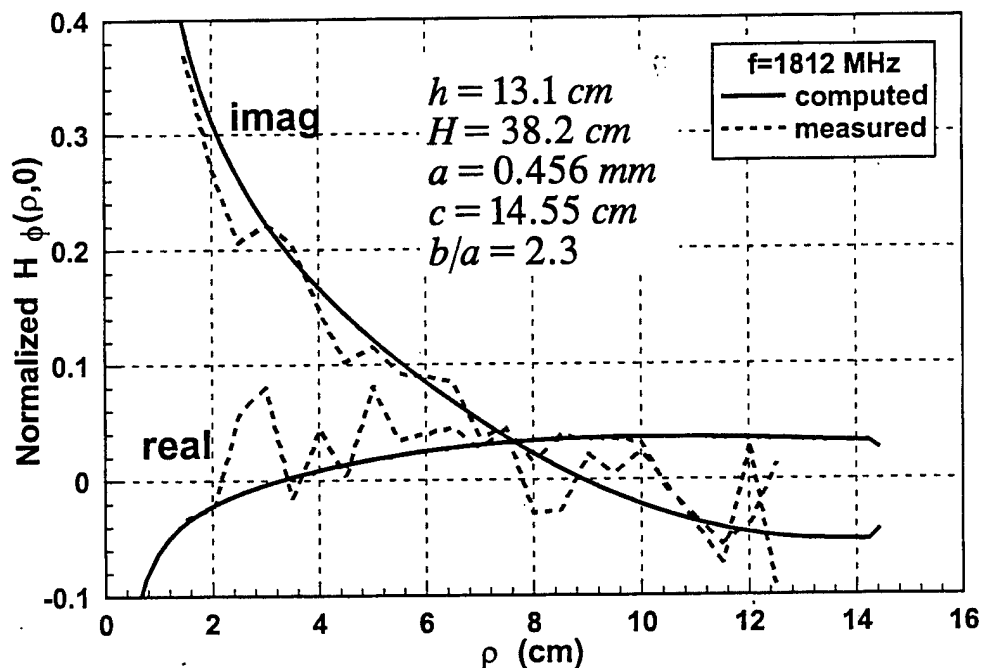


Figure 7-19. Measured and computed data of  $\phi$ -directed magnetic field at the bottom of the can at 1812 MHz for  $h = 13.1$  cm.

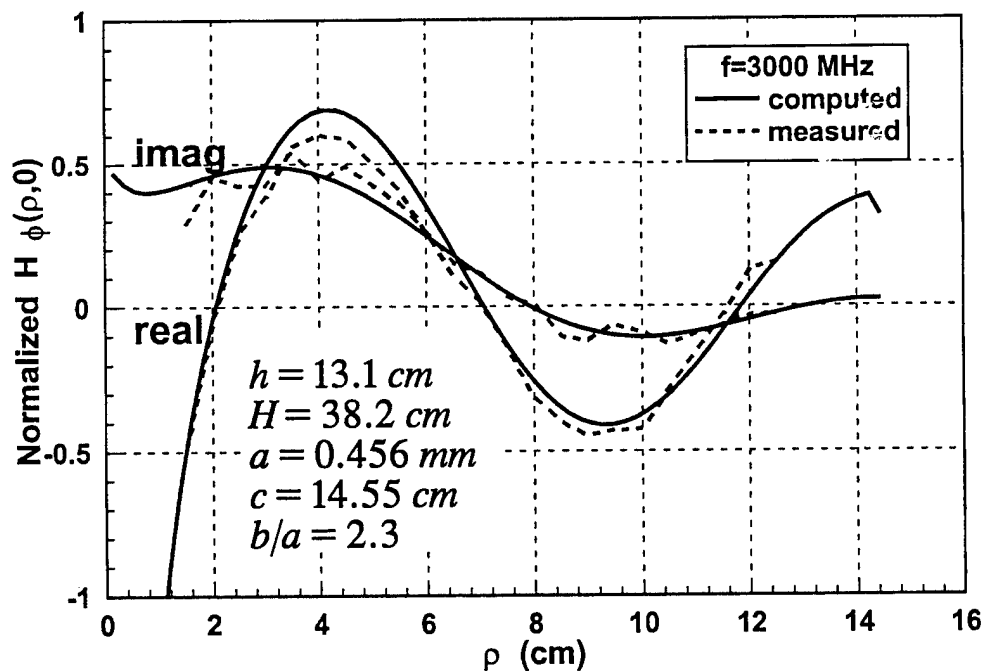


Figure 7-20. Measured and computed data of  $\phi$ -directed magnetic field at the bottom of the can at 3000 MHz for  $h = 13.1$  cm.

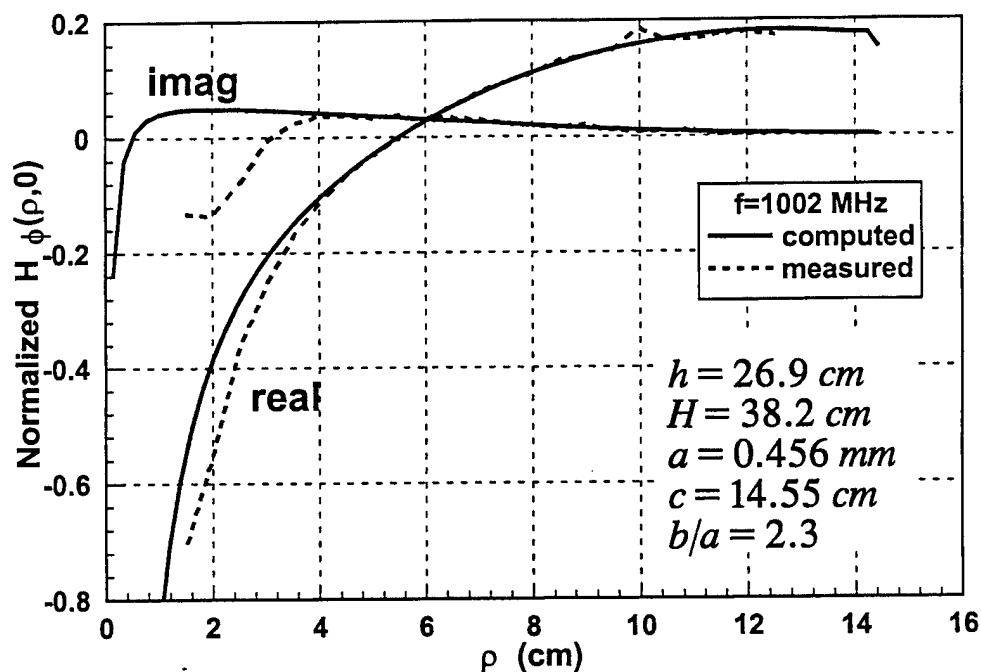


Figure 7-21. Measured and computed data of  $\phi$ -directed magnetic field at the bottom of the can at 1002 MHz for  $h = 26.9$  cm.

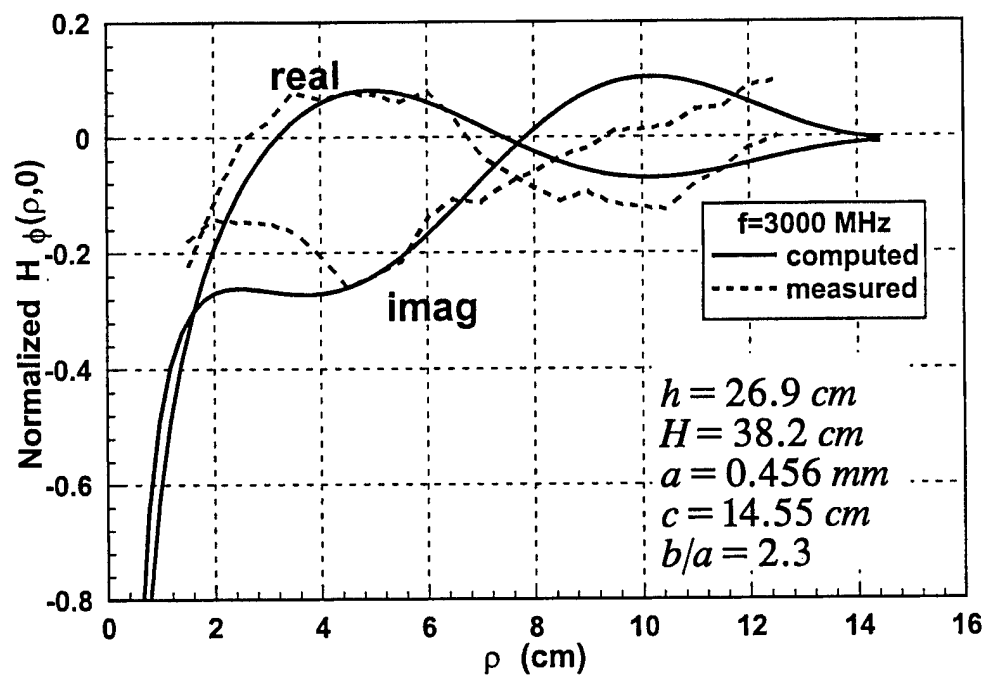


Figure 7-22. Measured and computed data of  $\rho$ -directed magnetic field at the bottom of the can at 3000 MHz for  $h = 26.9$  cm.

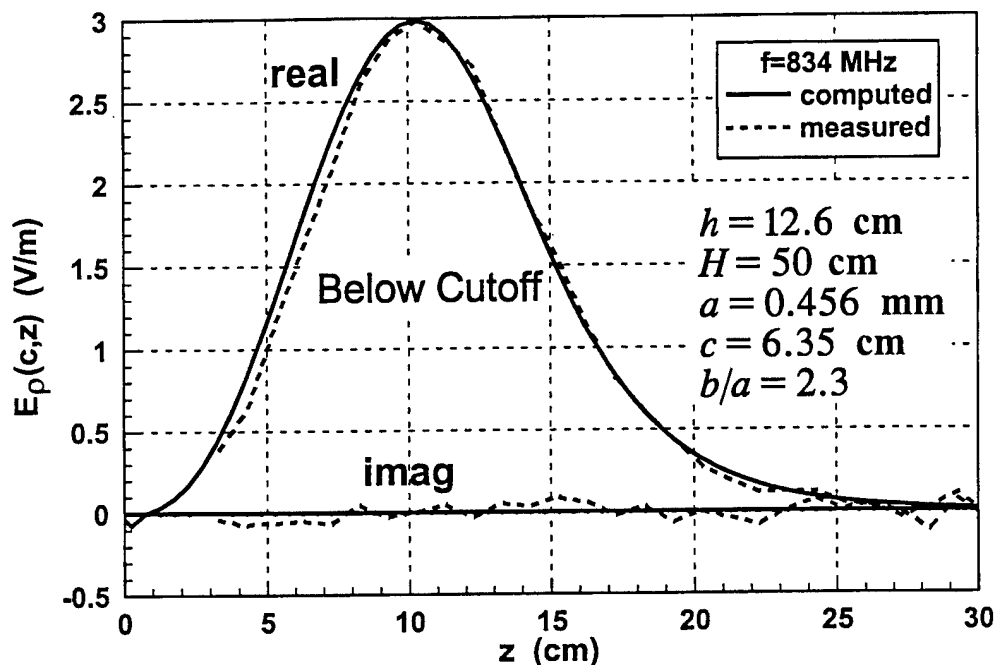


Figure 7-23. Measured and computed data of  $\rho$ -directed electric field at the can wall at 834 MHz.

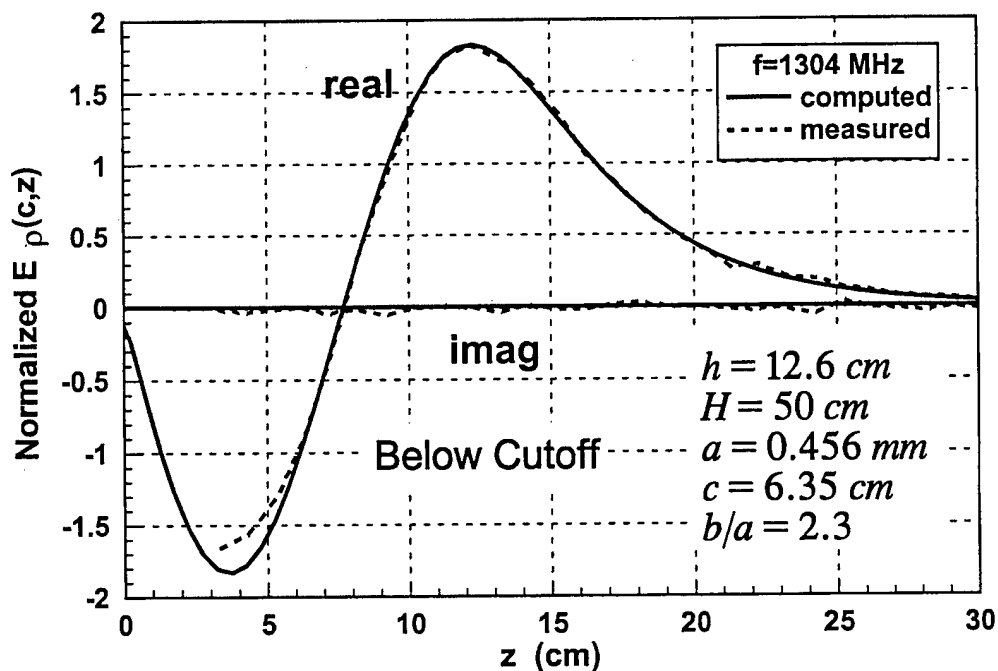


Figure 7-24. Measured and computed data of  $\rho$ -directed electric field at the can wall at 1304 MHz.

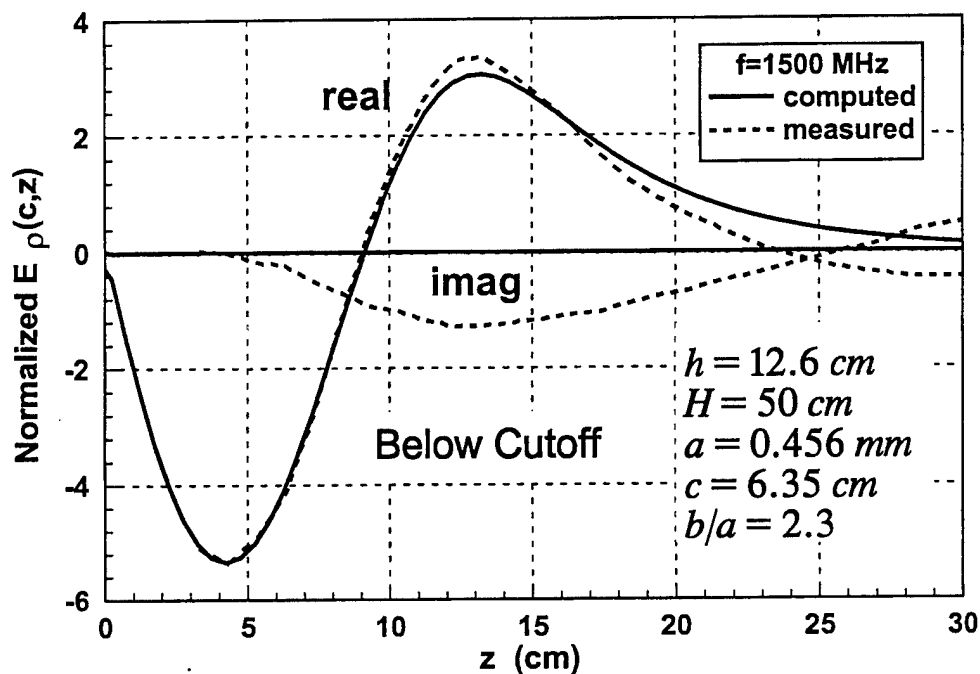


Figure 7-25. Measured and computed data of  $\rho$ -directed electric field at the can wall at 1500 MHz.

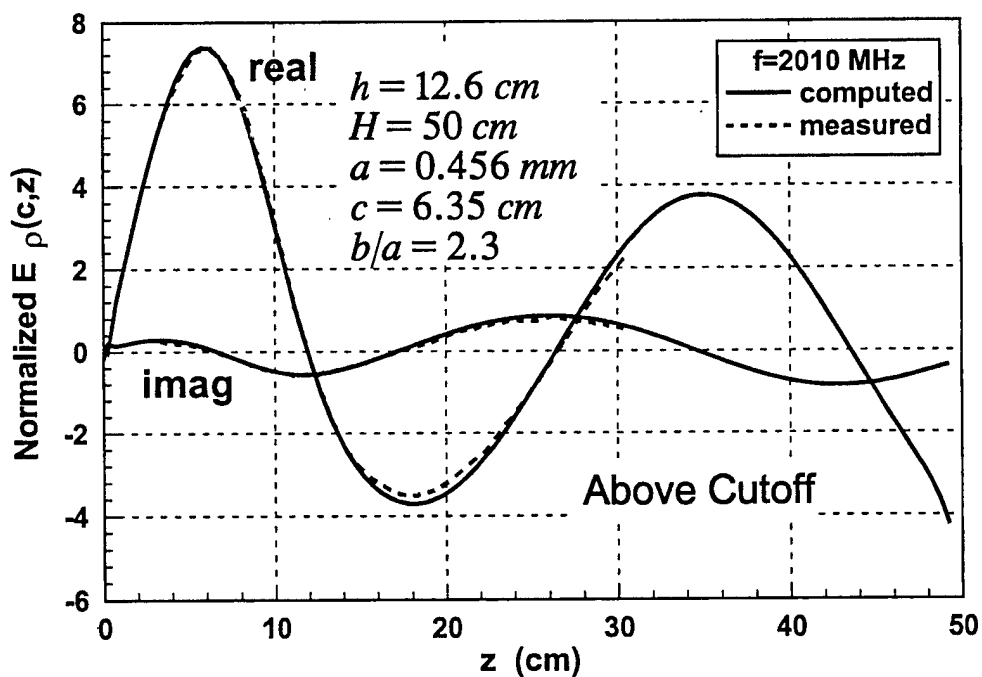


Figure 7-26. Measured and computed data of  $\rho$ -directed electric field at the can wall at 2010 MHz.

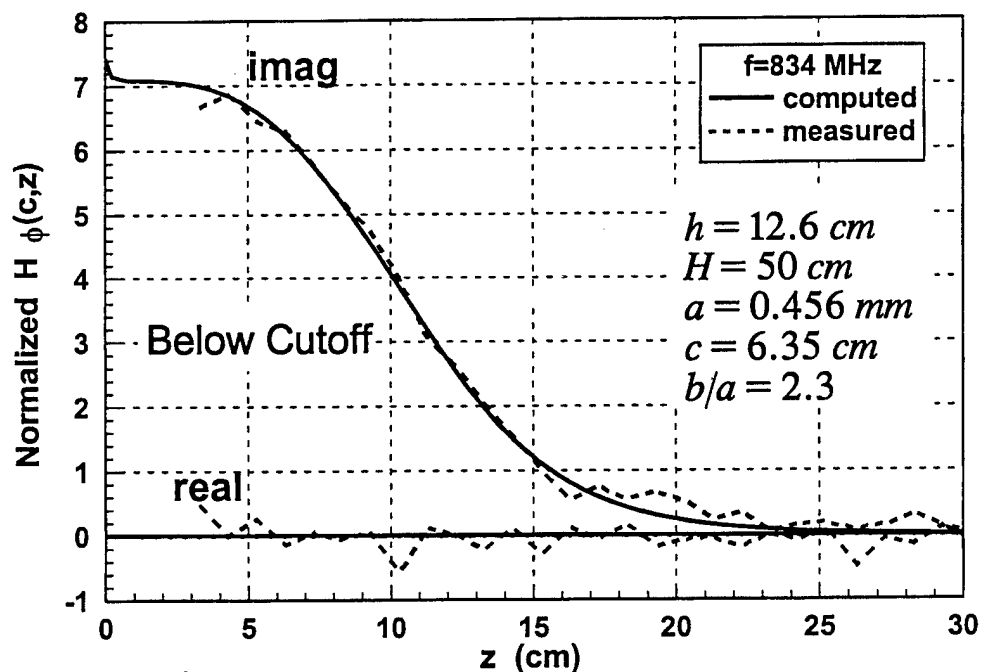


Figure 7-27. Measured and computed data of  $\phi$ -directed magnetic field at the can wall at 834 MHz.

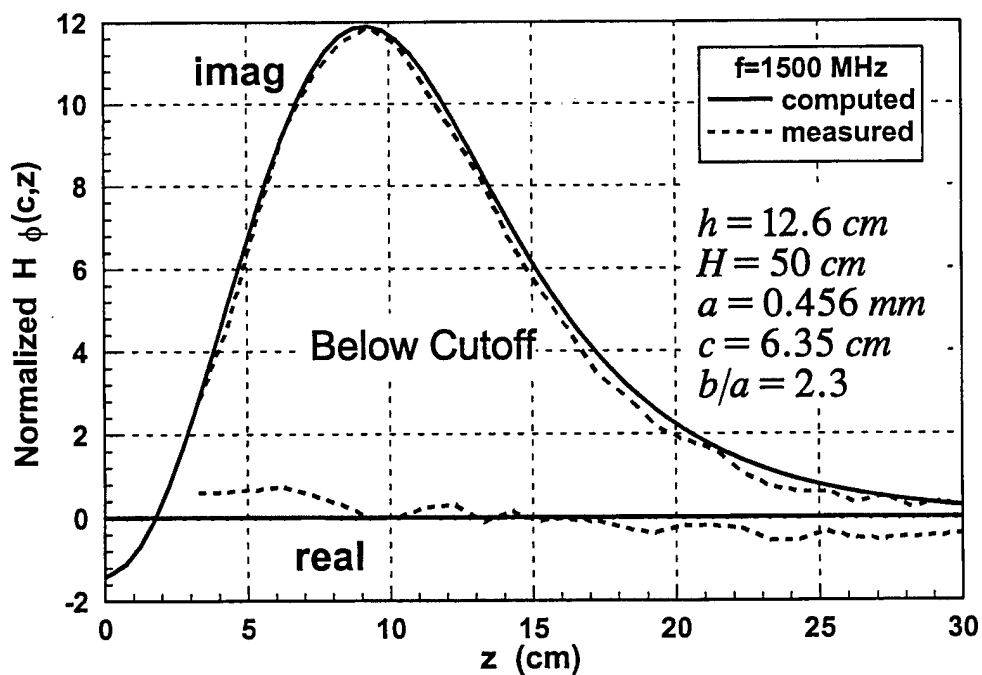


Figure 7-28. Measured and computed data of  $\phi$ -directed magnetic field at the can wall at 1500 MHz.

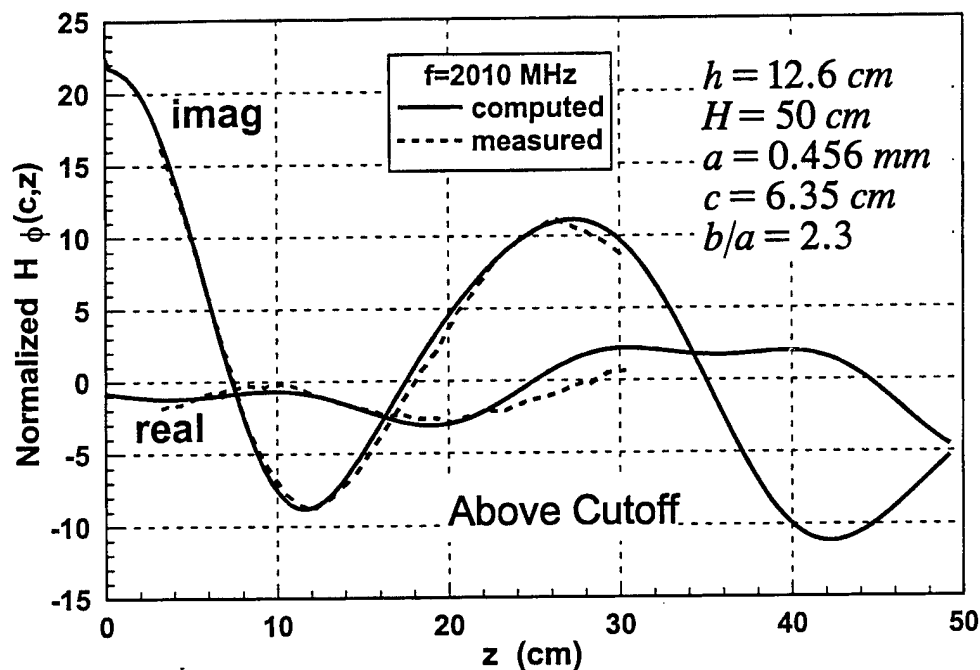


Figure 7-29. Measured and computed data of  $\phi$ -directed magnetic field at the can wall at 2010 MHz.

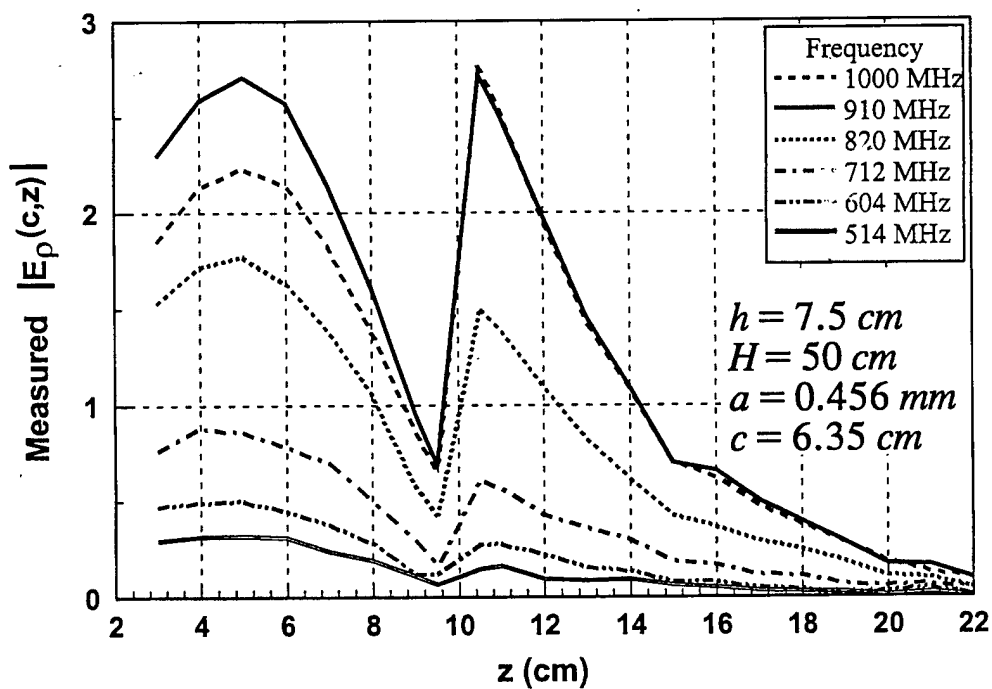


Figure 7-30. Measured data of radially directed electric field at the can wall loaded by isopropanol.



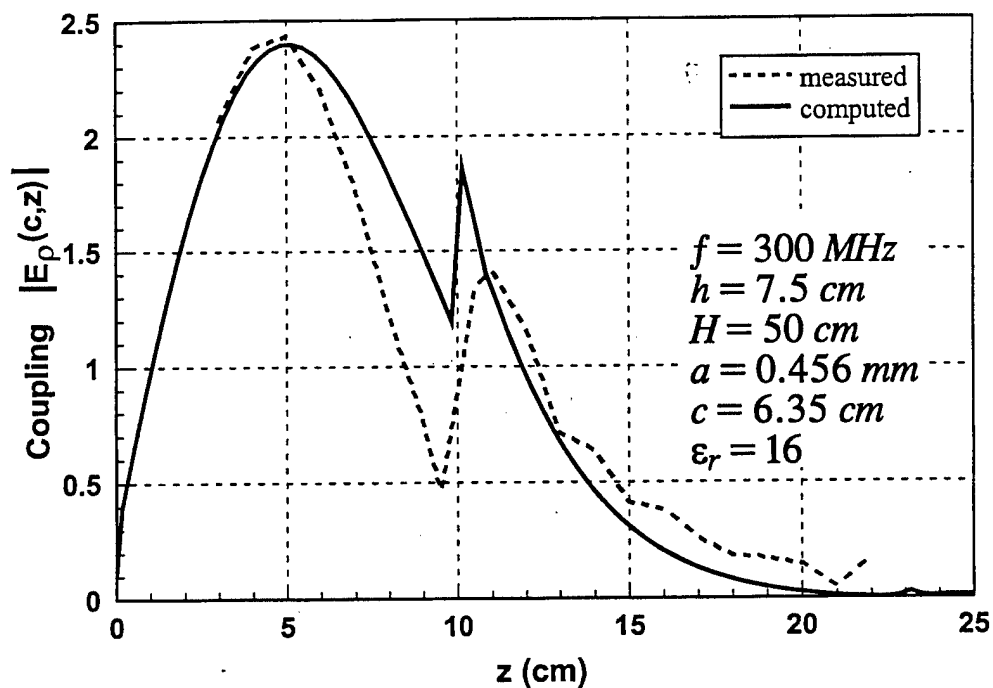


Figure 7-31. Measured and computed data of radially directed electric fields at the dielectric loaded can wall at 300 MHz.

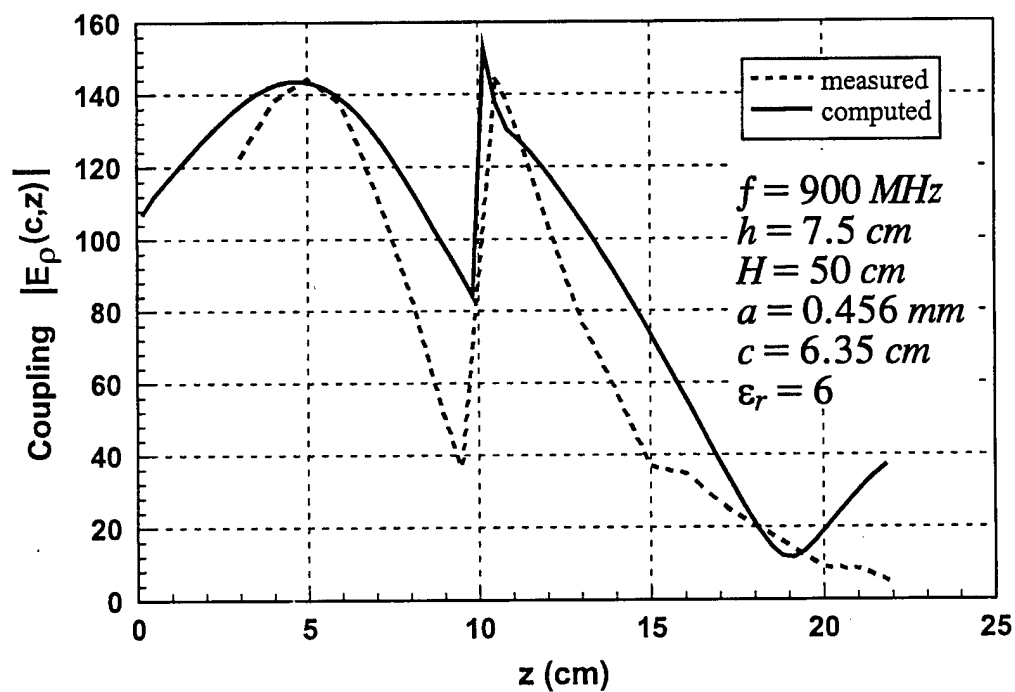


Figure 7-32. Measured and computed data of radially directed electric fields at the dielectric loaded can wall at 900 MHz.

## CHAPTER 8

### FIELDS AT THE FOCAL POINT OF A REFLECTOR ANTENNA DUE TO LASER LIGHT ILLUMINATION

#### 8.1 Introduction

In this section we describe a method to compute the field that would be created at the focal point of a reflector antenna due to illumination by the light of a modulated laser. A conducting parabolic reflector, illuminated by a modulated laser-light, is illustrated in Figure 8-1. The reflector surface is assumed to be vanishingly thin. With the addition of a feed or collector at the focal point of the paraboloid, one has a standard reflector antenna. The excitation is the signal radiated by electrons “kicked off” the conducting surface by an impinging laser beam. The laser excited dipoles radiate in the presence of reflector. It is the signal at the focal point of the reflector antenna, as a function of the laser beam characteristics, that one wishes to determine. This is accomplished by a procedure similar to that described in Chapter 4. Fortunately, since one needs to know the signal only at the focal point, which electromagnetically speaking occupies a vanishingly small region of space, one can obtain the desired information by solving a radiation problem and employing the reciprocity theorem.

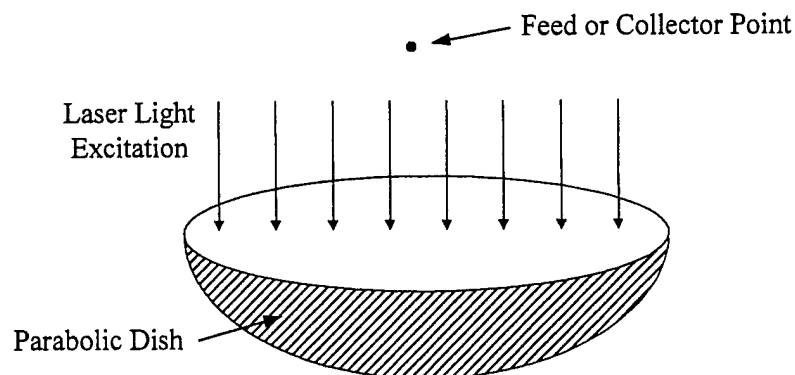


Figure 8-1. Parabolic reflector antenna illuminated by a modulated laser-light.

## 8.2 The Reciprocity Approach

The end goal is to compute the field that would be created at the focal point of a reflector antenna due to the excitation caused by an elementary electric dipole normal to and located at the surface of the reflector. To perform this computation directly is very difficult so we resort to a method that allows us to realize significant savings with no loss in generality. The approach developed to solve this problem is exact and rigorous.

The direct approach to solving this problem would be to determine the radiation due to the elementary dipole on the surface and employ the electric field of this radiation as the excitation of an integral equation for the current on the reflector antenna. The integral equation must also account for the collector or feed placed at the focal point. And the coupling with the collector must be computed in order to take full account of the reflector and its feed structure. The current induced on the reflector-feed surface would be a vector surface density so the desired integral equation must be a vector equation.

The indirect approach adopted here takes advantage of the reciprocity theorem and allows one to determine the signal received at the focal point from knowledge of the field radiated by the reflector antenna under the condition that the excitation results from a z-directed elementary dipole impressed at the focal point. This scheme allows the formulation and solution of a simpler integral equation. It is simpler for two reasons. First, the integral equation is not a vector equation as would be necessary if the direct procedure were followed and, second, the equation and its unknown possess rotational symmetry.

The solution of the problem of determining the signal by a modulated laser beam at the focal point, is reduced to two steps: (1) computation of the electric field at points on the reflector where the laser light might fall, caused by an axially directed dipole excitation at the focal point, and (2) application of the reciprocity theorem to obtain the

signal at the focal point caused by the laser light. Data are presented to illustrate the result of these analyses.

Reciprocity can be used to determine transmitting or receiving properties of a feed-reflector combination from the transmitting properties of the feed by itself or the receiving properties of the reflector by itself for a point-source feed. In theory, the transmitting problem for a feed-reflector combination is easier to solve than is the receiving problem for the same combination. Therefore the transmitting boundary value problem should be solved first in order to determine the transmitting properties of the feed-reflector combination. The receiving properties can then be obtained from the reciprocity theorem.

In Figure 8-2 is illustrated in cross-section a reflector antenna, together with an elementary dipole of current moment  $\delta(\mathbf{r} - \mathbf{r}_0) \hat{\mathbf{n}}$  located at point  $\mathbf{r}_0$  and normal to the surface. The desired end result, as mentioned above, is the signal at the focal point due to the dipole when the dipole resides on, and is normal to, the reflector surface. The dipole radiates a field which may couple with a collector antenna at the focal point. In order to set the stage for the use of the reciprocity theorem, we now consider a second source and its resulting radiated field. This source is a  $z$ -directed elementary dipole impressed at the focal point. This dipole at the focal point produces a radiated electric field which we call  $\mathbf{E}^s$ .

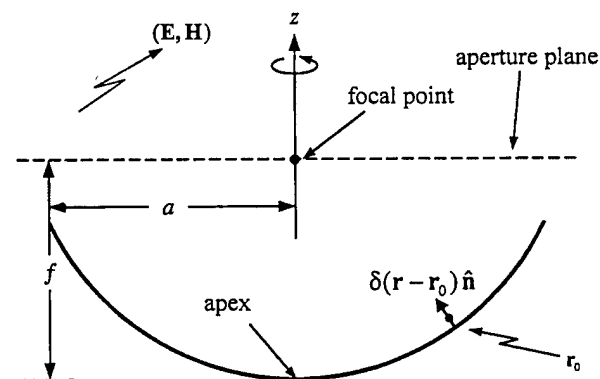


Figure 8-2. A cross sectional view of a conducting parabolic reflector antenna excited by an elementary electric dipole located on and normal to its surface.

It is instructive to think of two situations or two experiments. In the first, the normal dipole on the surface  $\mathbf{J} = \delta(\mathbf{r} - \mathbf{r}_0) \hat{\mathbf{n}}$  radiates a field causing an electric field  $\mathbf{E}$  to appear at the focal point. This field is sought. Next, the dipole is removed and the a  $z$ -directed electric dipole of current moment  $\delta(\mathbf{r} - z_0 \hat{\mathbf{z}}) \hat{\mathbf{z}}$  is placed at the focal point as seen in Figure 8-3.

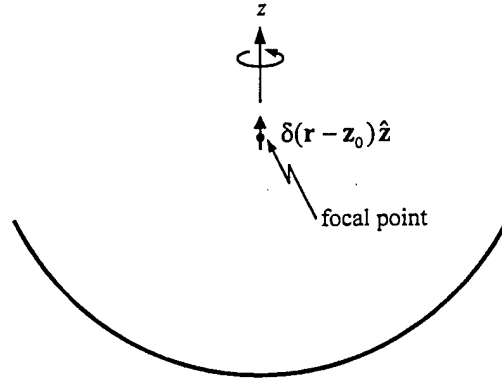


Figure 8-3. The reflector excited by a  $z$ -directed electric dipole at the focal point.

This electric dipole excites the antenna and causes a field to be radiated, whose electric field is designated  $\mathbf{E}^s$ . The reciprocity theorem applied to these sources and fields can be stated in the form

$$\iiint_V (\mathbf{E}^s \cdot \mathbf{J} - \mathbf{E} \cdot \mathbf{J}^s) dV = 0 \quad (8.1)$$

where  $\mathbf{E}$  is the electric field caused (everywhere) by the elementary dipole  $\mathbf{J} = \delta(\mathbf{r} - \mathbf{r}_0) \hat{\mathbf{n}}$  at the surface radiating in the presence of the structure. The current  $\mathbf{J}^s = \delta(\mathbf{r} - z_0 \hat{\mathbf{z}}) \hat{\mathbf{z}}$  is the impressed current at the focal point. We then evaluate the integrals of (8.1) as

$$\iiint_V \mathbf{E} \cdot \mathbf{J}^s dV = \iiint_V \mathbf{E} \cdot \delta(\mathbf{r} - z_0 \hat{\mathbf{z}}) \hat{\mathbf{z}} dV = \mathbf{E}(z_0 \hat{\mathbf{z}}) \cdot \hat{\mathbf{z}} \quad (8.2)$$

$$\iiint_V \mathbf{E}^s \cdot \mathbf{J} dV = \iiint_V \mathbf{E}^s \cdot \hat{\mathbf{n}} \delta(\mathbf{r} - \mathbf{r}_0) dV = \hat{\mathbf{n}} \cdot \mathbf{E}^s(\mathbf{r}_0). \quad (8.3)$$

Equating the integrals of (8.2) and (8.3), we obtain

$$E_z(z_0) = E_n^s(\mathbf{r}_0). \quad (8.4)$$

$E_z(z_0)$  is the z-component of electric field at the focal point that would be created by the dipole on the surface of the antenna.  $E_z(z_0)$  is the quantity of interest.

### 8.3 Results and Discussion

We first perform the computations for a conducting disk instead of a conducting reflector. Since a conducting disk with large radius compared to wavelength approximates a ground plane, we can use image theory to check the computed results. In Figures 8-4 and 8-5 are illustrated the current density and the total current for a conducting disk of radius  $a = 3\lambda$  illuminated by an electric dipole at different heights. In Figures 8-6 and 8-7 are illustrated the current density and the total current for conducting disk of different radii, illuminated by an electric dipole at  $h = 3\lambda$ . In Figure 8-8 is offered a comparison of computed data of the current density on the disk with data determined from image theory subject to the approximation that the disk is a ground plane of infinite extent. The data of Figure 8-8 suggest that the computations are accurate.

Figure 8-9 to 8-13 show computed z-directed electric field on the disk of radius  $a = 3\lambda$  together with values approximated by image theory. Observe that the closer the dipole is to the surface of the conducting disk the better comparison with the data of image theory. The results of Figures 8-9 to 8-13 lend support to the claim that the computation procedure is correct and accurate.

Figures 8-14 to 8-17 show the total current induced on the surface of the reflector antenna due to a dipole at the focal point. The plots are provided for various reflector sizes. The parabolic reflector surface is defined by

$$z = \frac{\rho^2}{4f}, \quad \rho \leq a \quad (8.5)$$

where  $\rho$  is the radial displacement from the apex,  $f$  is the focal distance (distance from apex to the focal point) and  $a$  is the radius of the reflector as suggested in Figure 8-2.

Figures 8-18 to 8-23 show the normal electric field on the surface of the reflector antenna due to a dipole at the focal point for various reflector sizes. It is observed that, for a fixed radius reflector, the electric field intensity increases all along the reflector surface as the focal length is reduced. This is consistent with one's intuition. Reciprocity allows us to interpret this result in another way. For a fixed radius, the electric field intensity at the focal point increases as the focal length is reduced for all dipole locations all along the reflector surface. It is also observed that, for a fixed focal length, the electric field intensity is not strongly effected. The variation in electric field is due only to the operating frequency of the dipole.

The normal electric field at a point  $r_0$  on the parabola due to a z-directed dipole of unity strength at the focal point is the same as the desired z-directed electric field at the focus due to a unity strength dipole normal to the surface at  $r_0$ . This is the meaning of equation (8.4). Hence the data of Figure 8-18 to 8-23 can be interpreted as z-directed electric field at the focus due to a unity strength dipole normal to the surface at  $r_0$ . For the convenience of the reader these data are presented again in Figures 8-24 to 8-29 but with labels which suggest that  $E_z(z_0)$  at the focus is created by a normal dipole of unity strength on the reflector surface at distance  $p$  from the parabola axis.

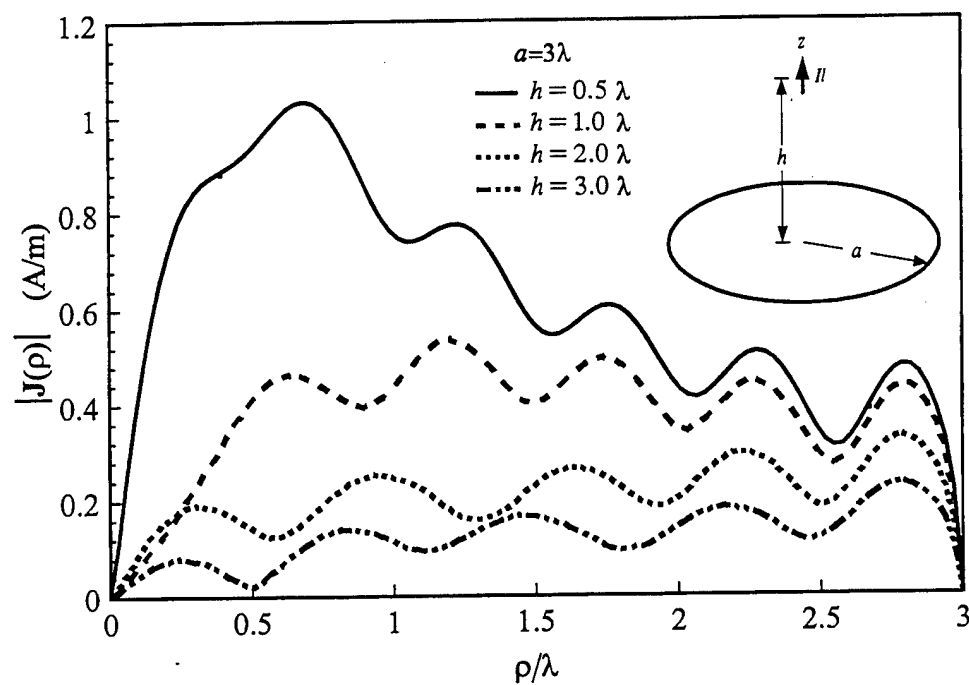


Figure 8-4. Current density on the disk for  $a = 3\lambda$ .

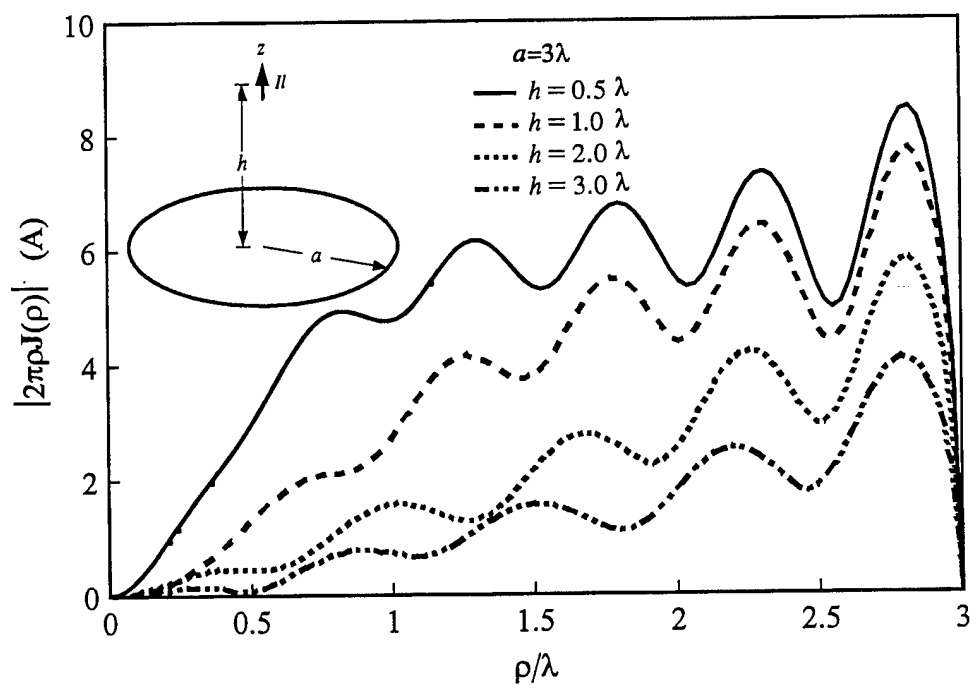


Figure 8-8. Total current on the disk for  $a = 3\lambda$ .



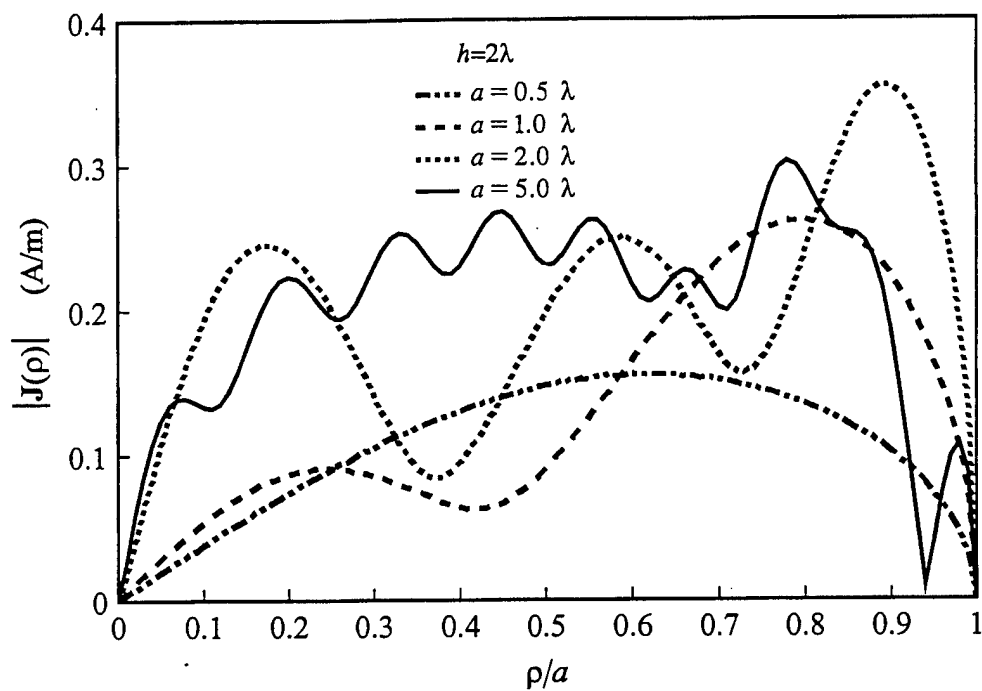


Figure 8-6. Current density on the disk for  $h = 2\lambda$ .

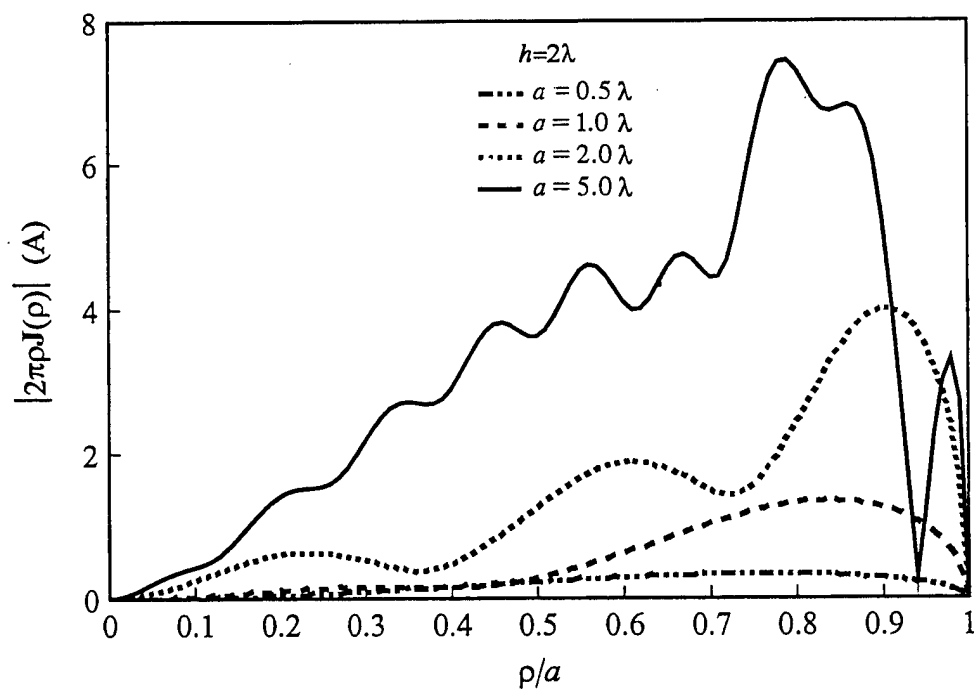


Figure 8-7. Total current on the disk for  $h = 2\lambda$ .

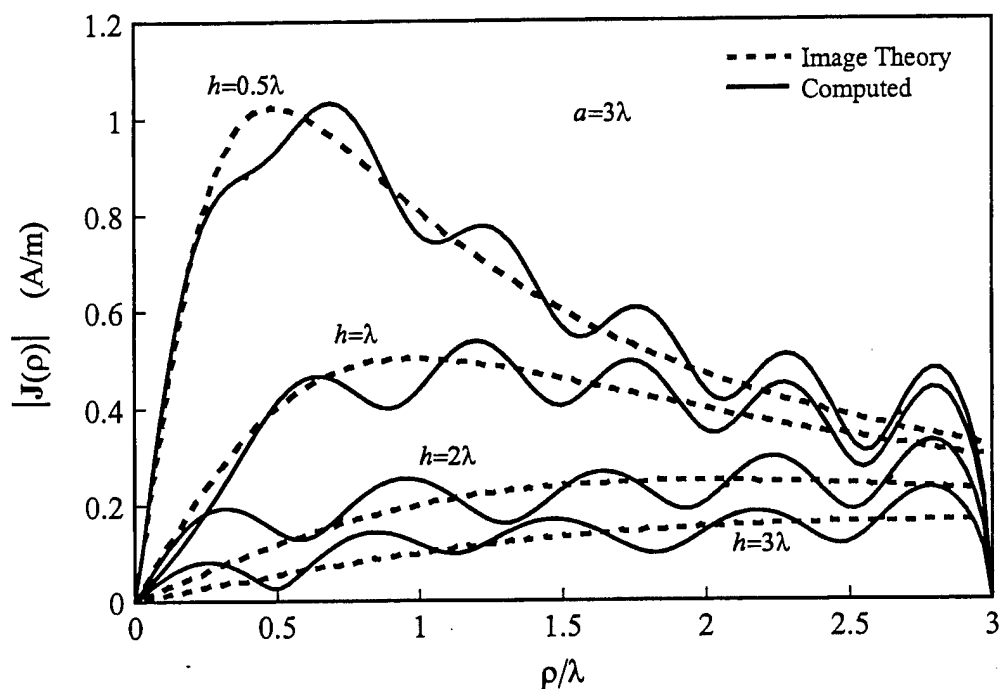


Figure 8-8. Computed current density on the disk compared with image theory.

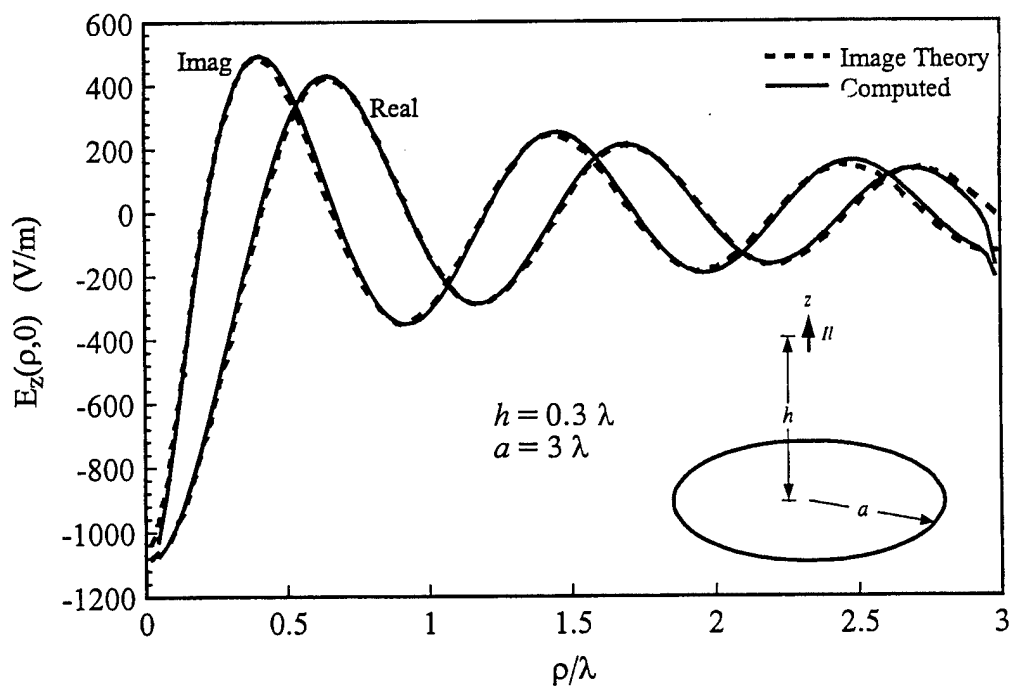


Figure 8-9. A comparison of computed and image theory data of  $z$ -directed electric field on the disk for  $h = 0.3\lambda$ .

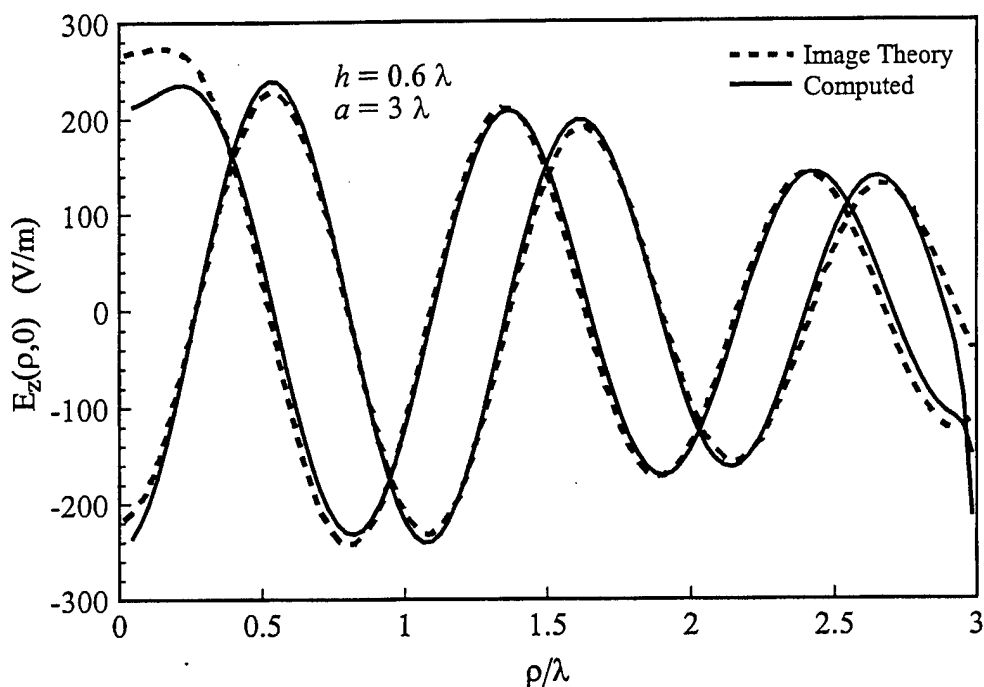


Figure 8-10. A comparison of computed and image theory data of z-directed electric field on the disk for  $h = 0.6\lambda$ .

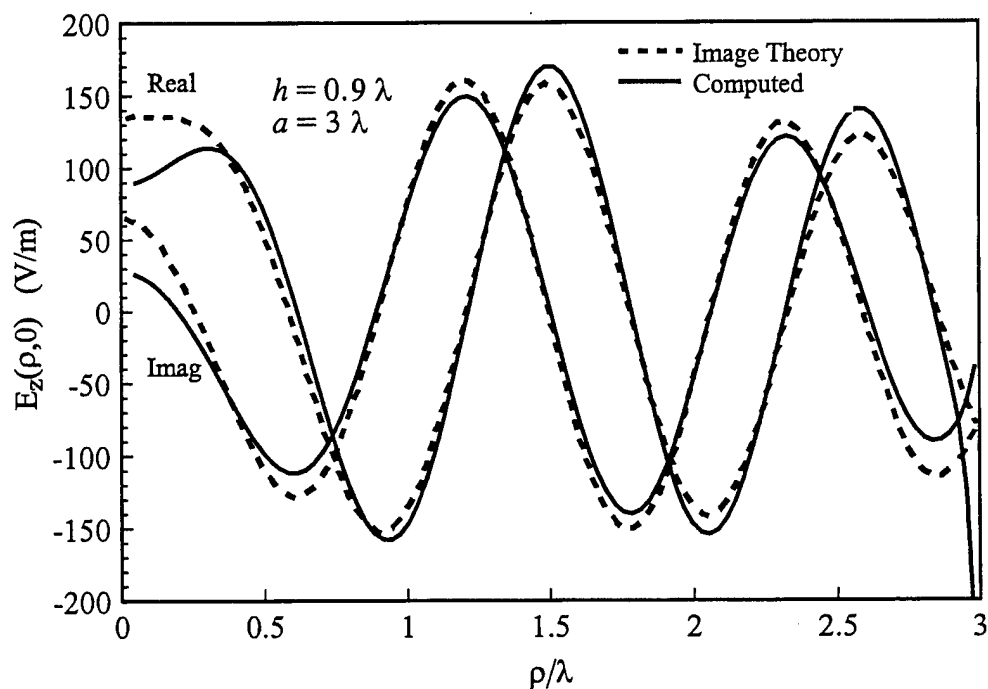


Figure 8-11. A comparison of computed and image theory data of z-directed electric field on the disk for  $h = 0.9\lambda$ .

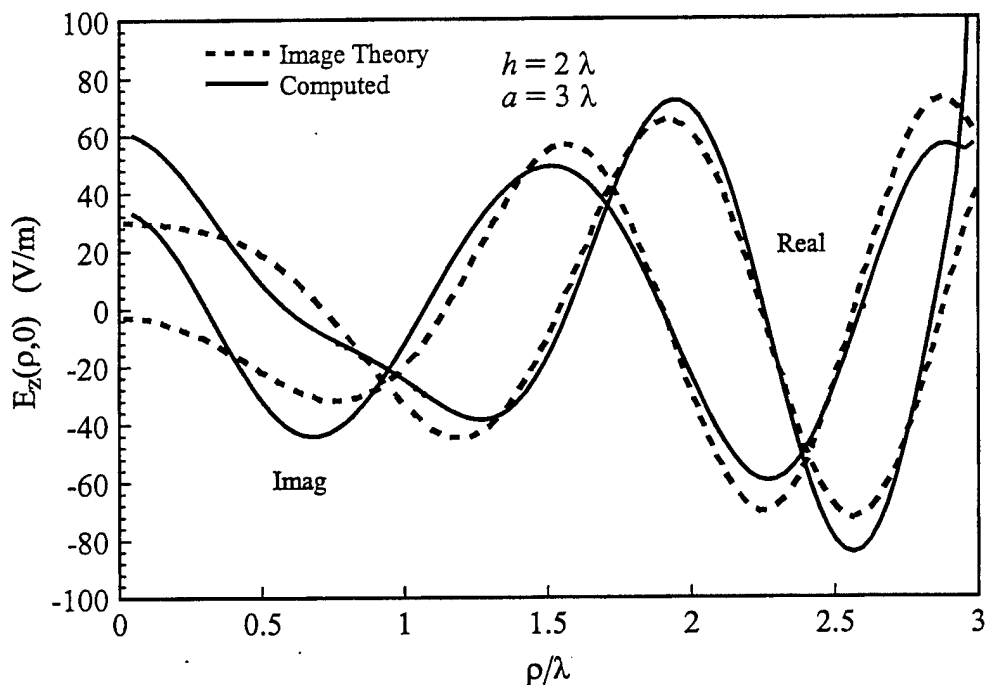


Figure 8-12. A comparison of computed and image theory data of z-directed electric field on the disk for  $h = 2\lambda$ .

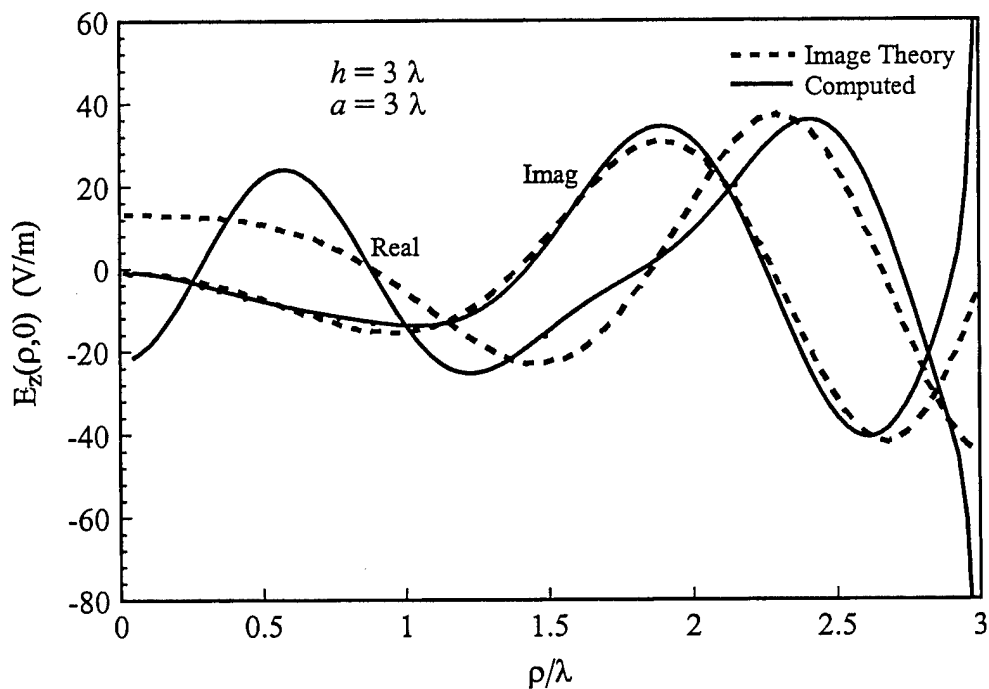


Figure 8-13. A comparison of computed and image theory data of z-directed electric field on the disk for  $h = 3\lambda$ .

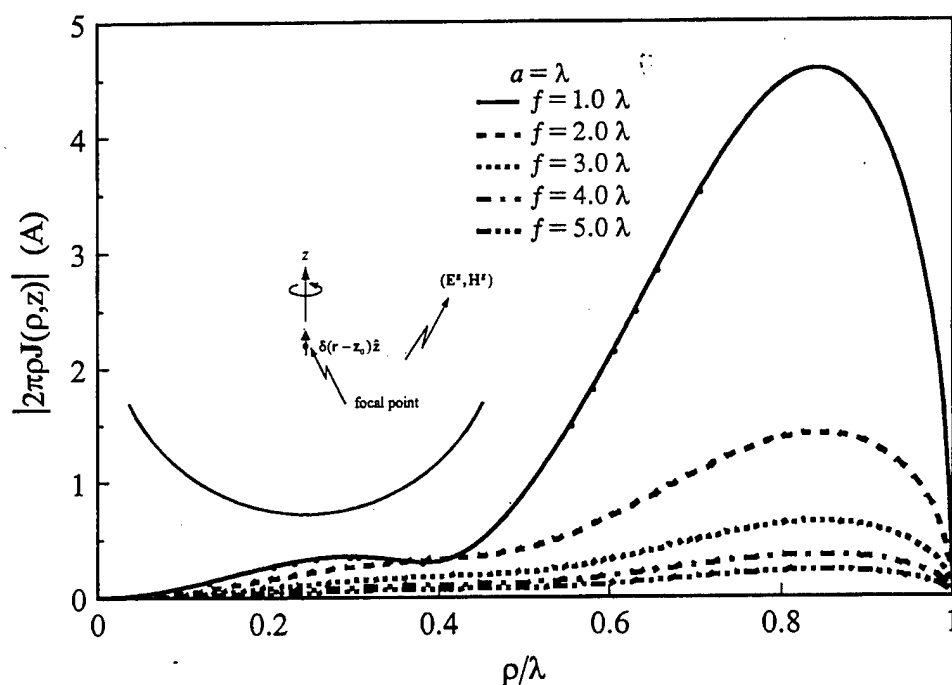


Figure 8-14. Current on the surface of the reflector antenna due to dipole excitation for  $a = \lambda$ .

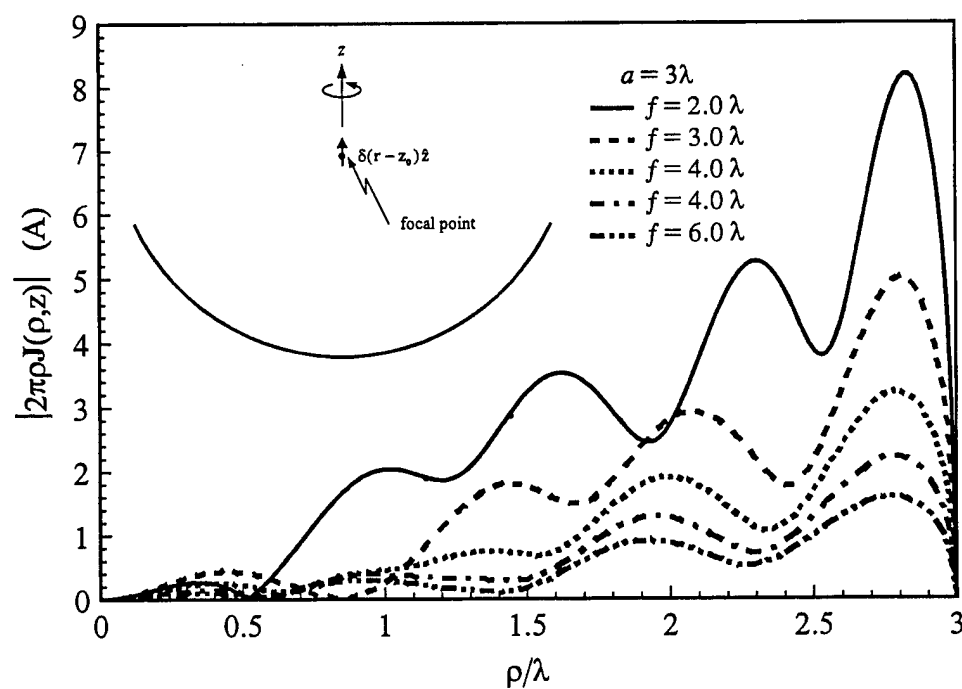


Figure 8-18. Current on the surface of the reflector antenna due to dipole excitation for  $a = 3\lambda$ .

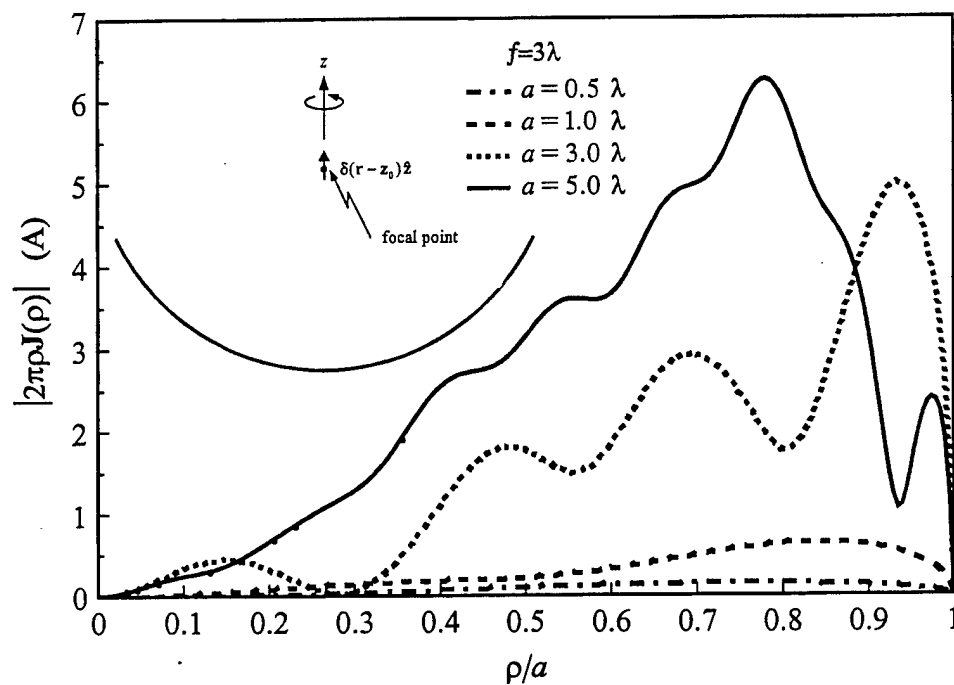


Figure 8-16. Current on the surface of the reflector due to dipole excitation for  $f = 3\lambda$ .

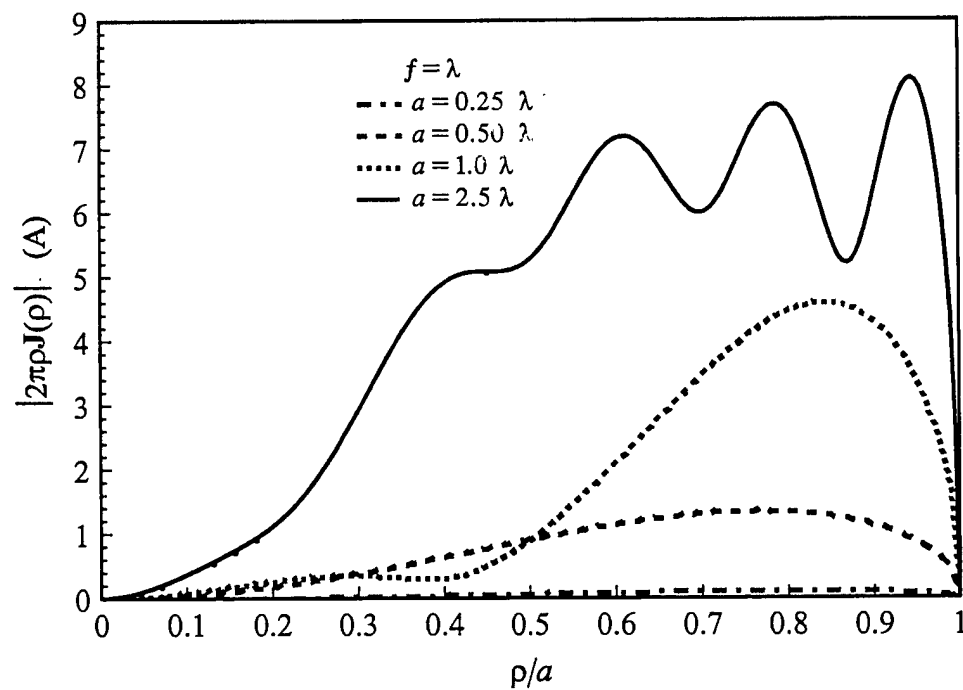


Figure 8-17. Current on the surface of the reflector due to dipole excitation for  $f = \lambda$ .

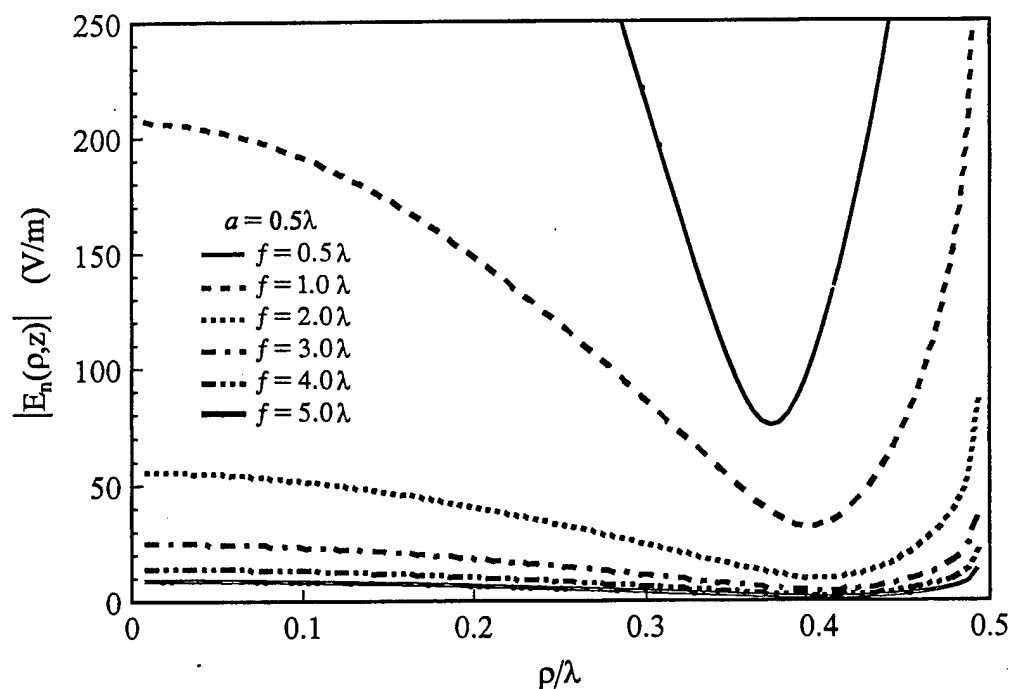


Figure 8-18. Normal electric field on the surface of the reflector antenna for  $a = 0.5\lambda$ .

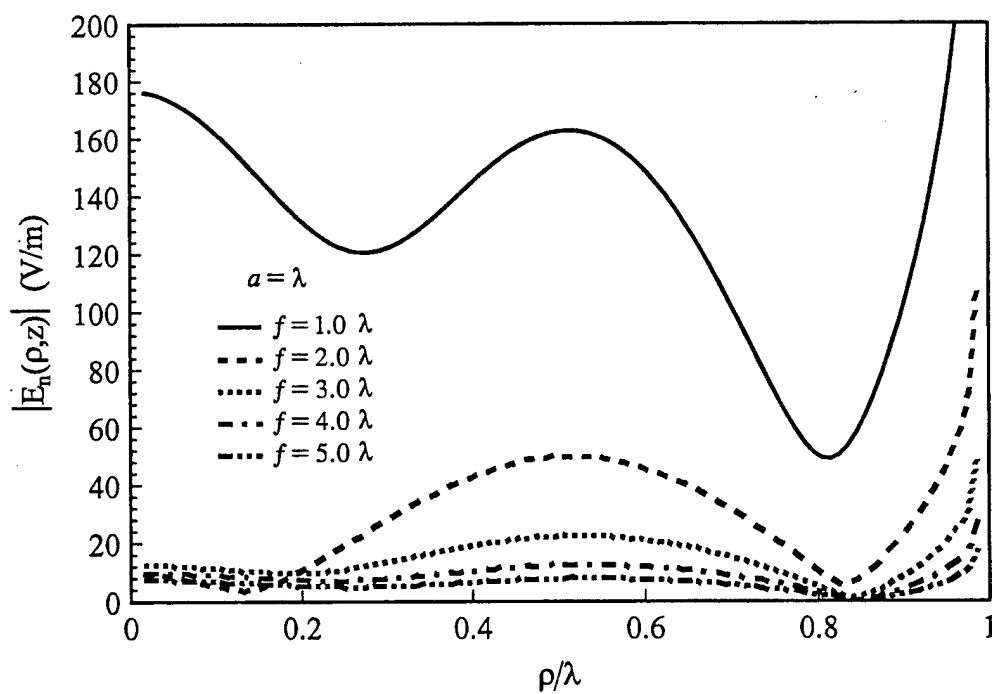


Figure 8-19. Normal electric field on the surface of the reflector antenna for  $a = \lambda$ .

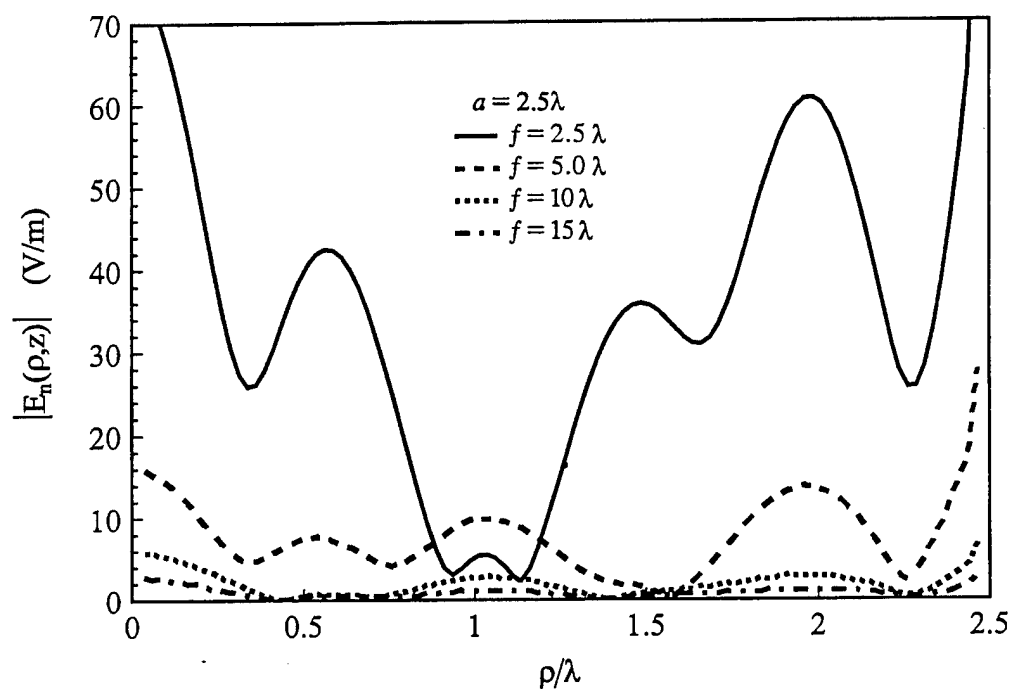


Figure 8-20. Normal electric field on the surface of the reflector antenna for  $a = 2.5\lambda$ .

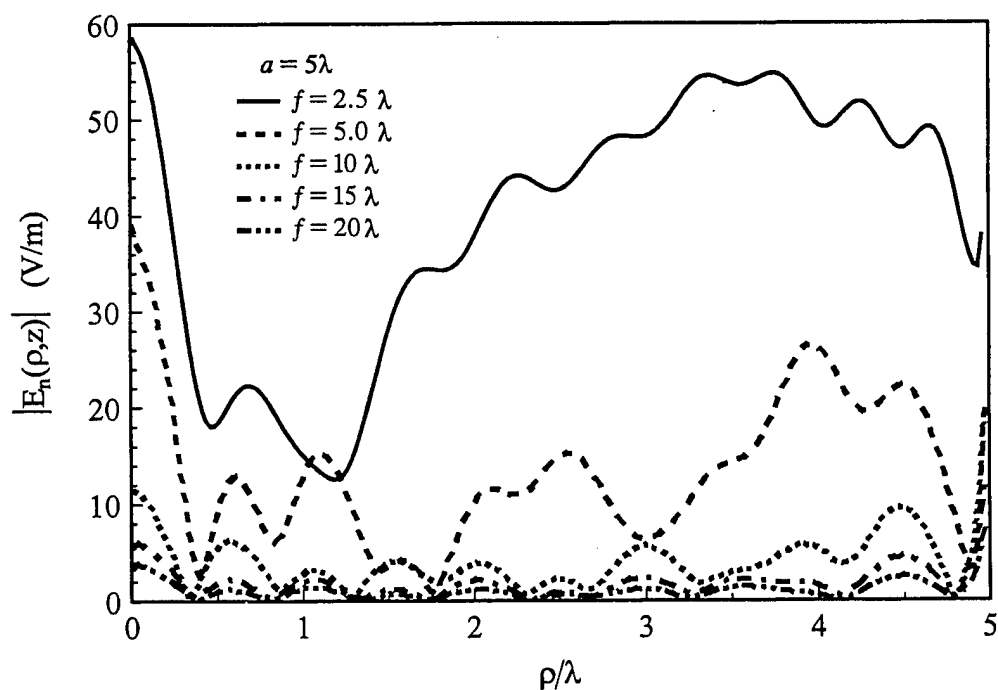


Figure 8-21. Normal electric field on the surface of the reflector antenna for  $a = 5\lambda$ .



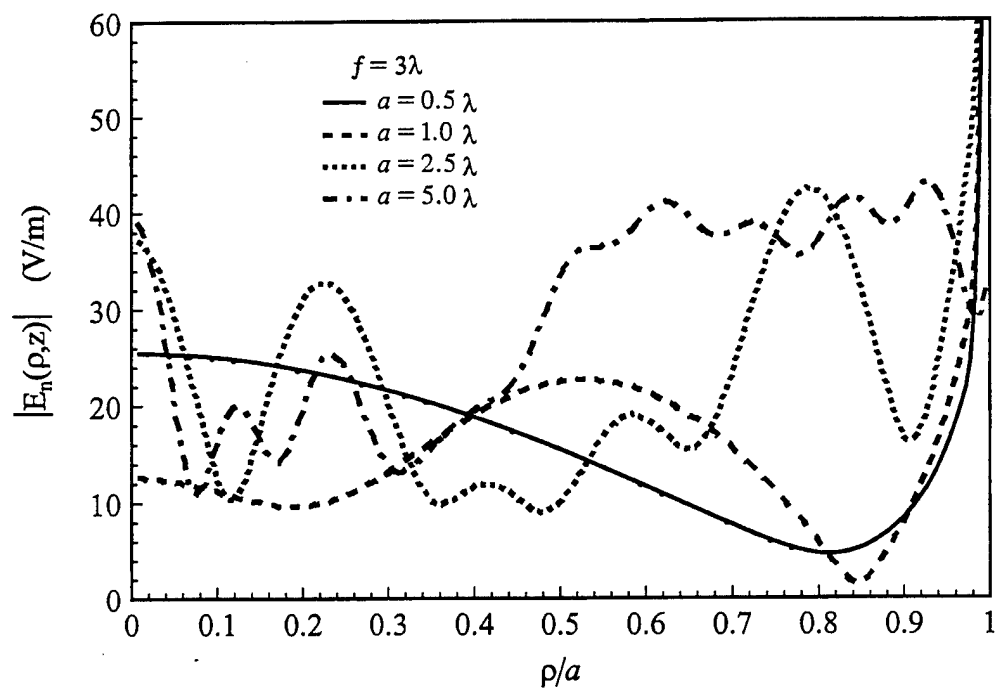


Figure 8-22. Normal electric field on the surface of the reflector antenna for  $f = 3\lambda$ .

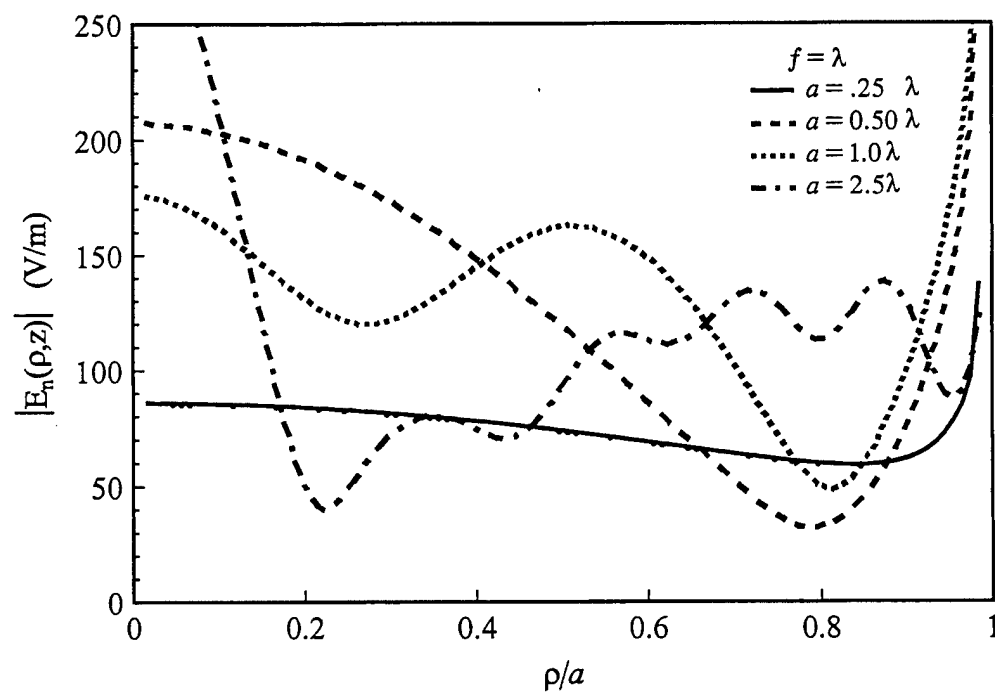


Figure 8-23. Normal electric field on the surface of the reflector antenna for  $f = \lambda$ .

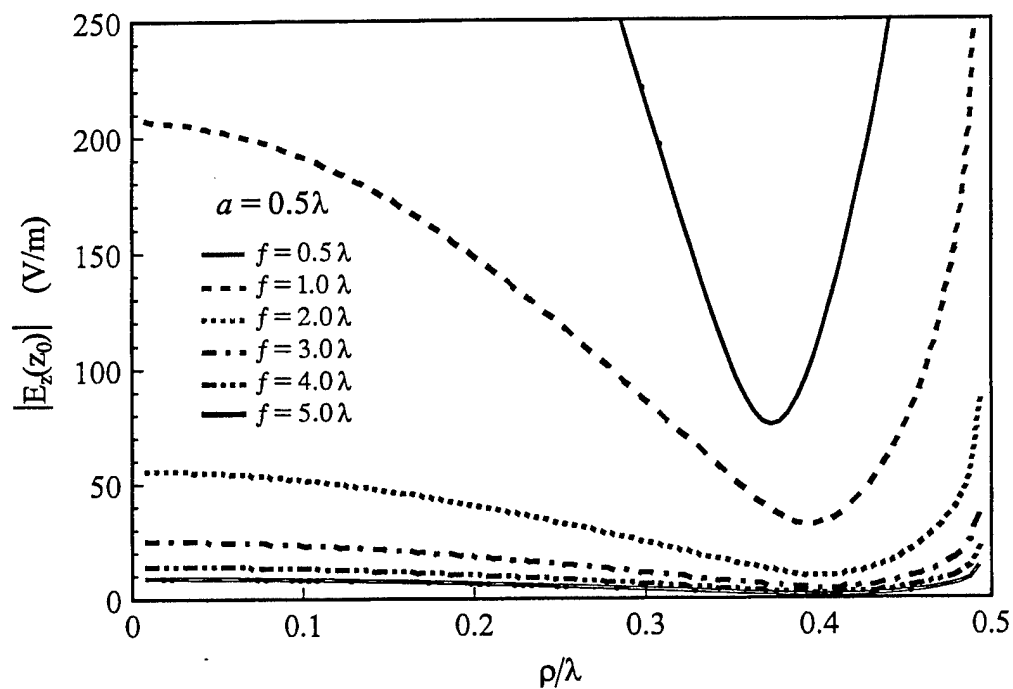


Figure 8-24. Electric field (z-directed) at the focal point of the reflector for  $a = 0.5\lambda$ .

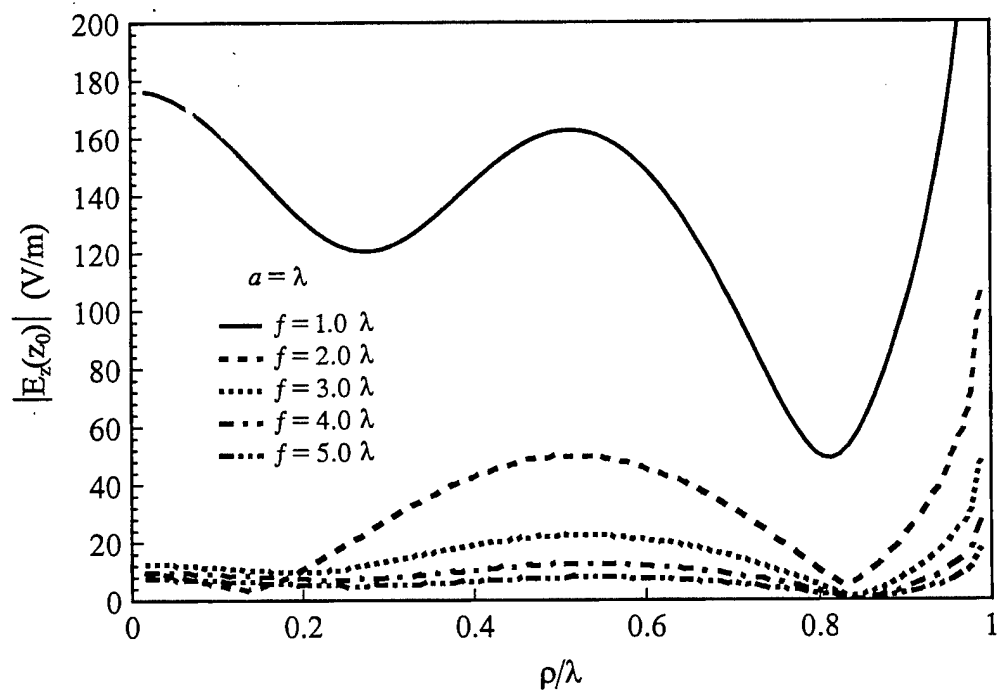


Figure 8-25. Electric field (z-directed) at the focal point of the reflector for  $a = \lambda$ .

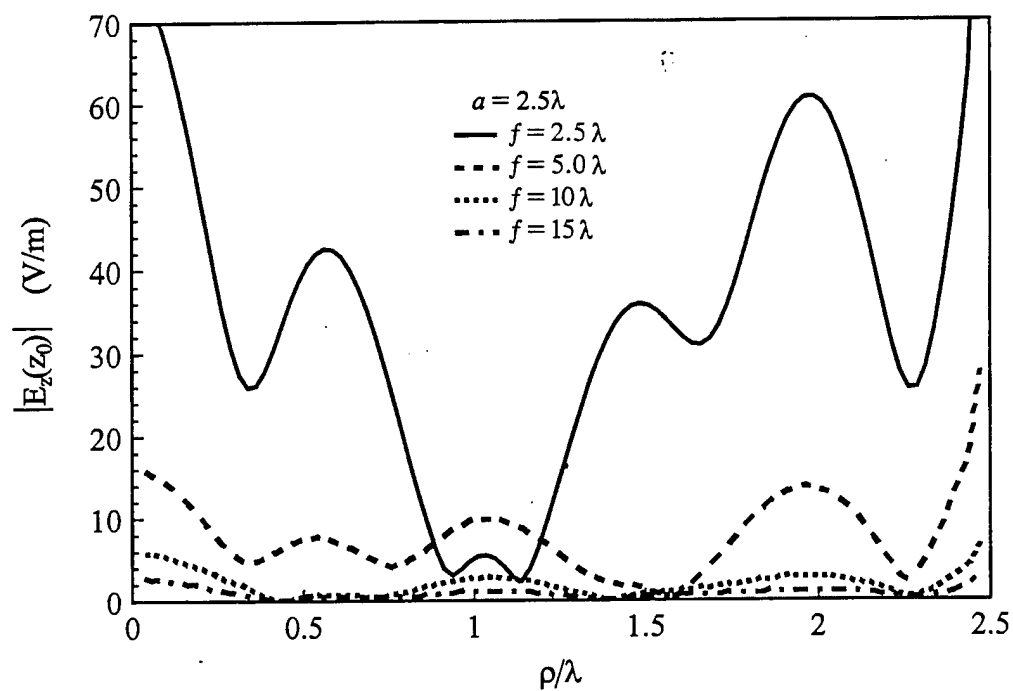


Figure 8-26. Electric field (z-directed) at the focal point of the reflector for  $a = 2.5\lambda$ .

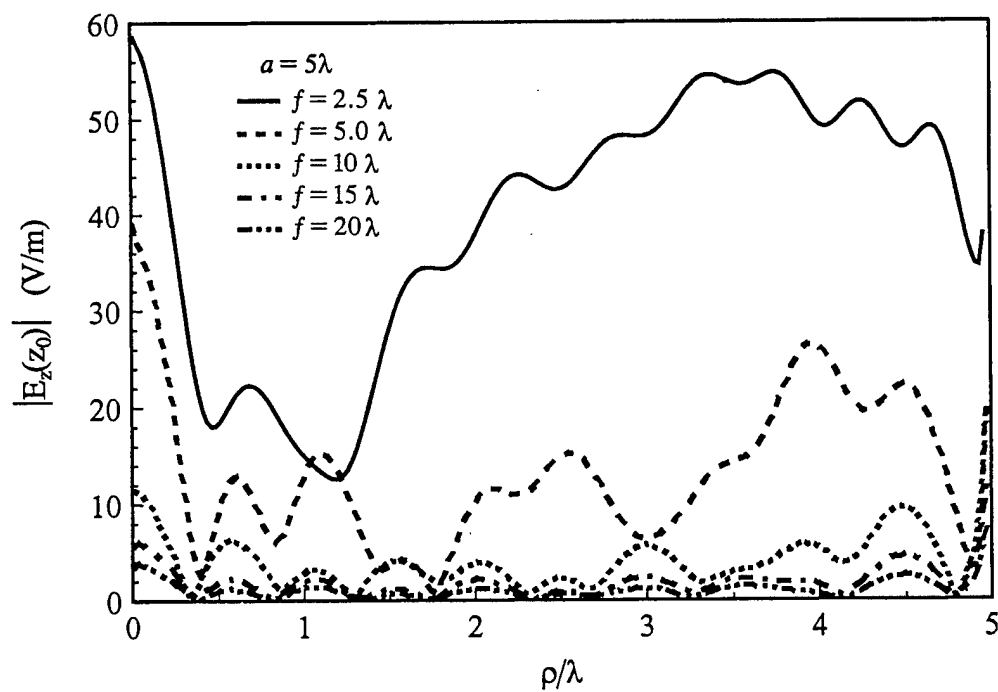


Figure 8-27. Electric field (z-directed) at the focal point of the reflector for  $a = 5\lambda$ .

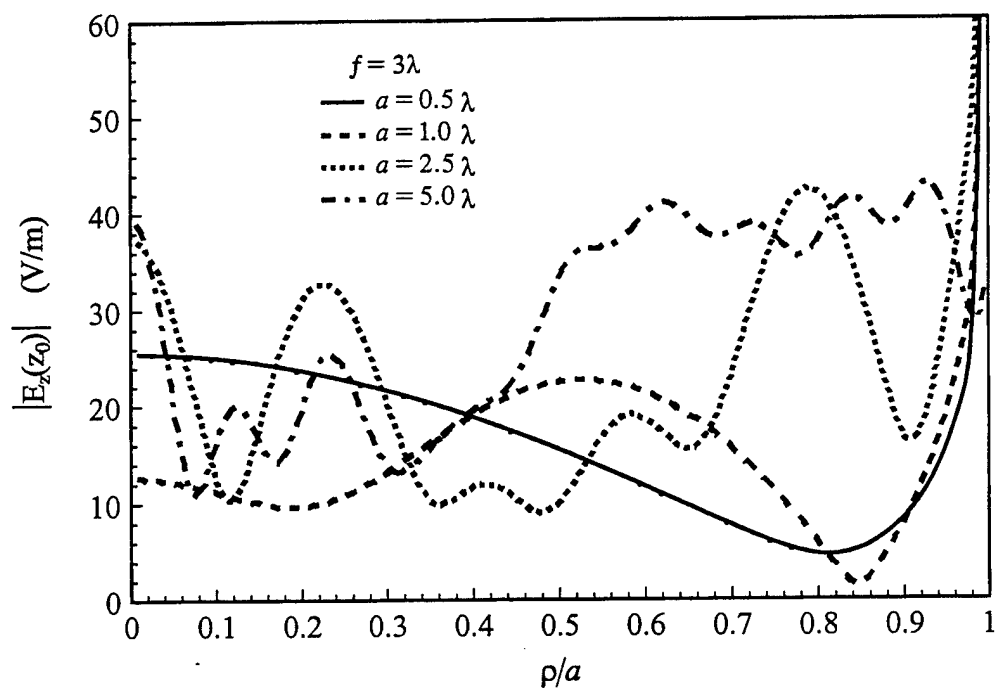


Figure 8-28. Electric field (z-directed) at the focal point of the reflector for  $f = 3\lambda$ .

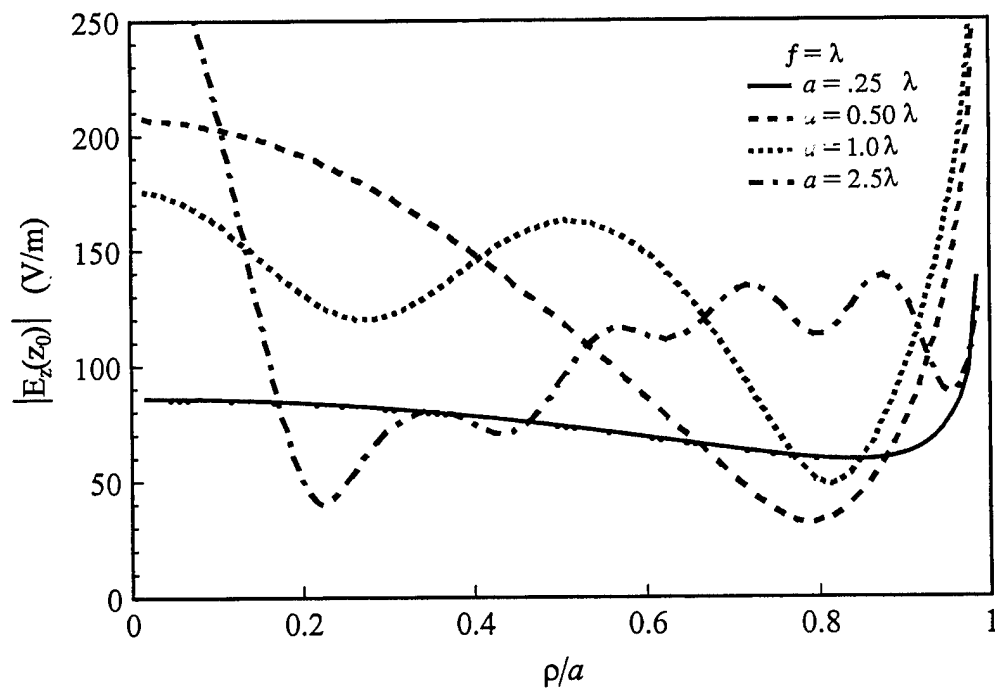


Figure 8-29. Electric field (z-directed) at the focal point of the reflector for  $f = \lambda$ .

## SUPPLEMENTARY REFERENCES

- [1] C. M. Butler and L. L. Tsai, "An alternate frill field formulation," *IEEE Trans. Antenn. Propagat.*, vol. 21, no.1, pp. 115-116, Jan 1973.
- [2] L. L. Tsai, "A numerical solution for the near and far fields of an annular ring of magnetic current," *IEEE Trans. Antenn. Propagat.*, vol. 20, no.5, pp. 569-576, Sep 1972.
- [3] C.M. Butler and A.Q. Martin, "Electromagnetic fields and currents excited by modulated laser light illumination of conducting objects, Technical Report AFOSR Grant # F49620-96-1-0005, Sept. 1, 1997.
- [4] J.R. Mautz and R.F. Harrington, "H-field, E-field and combined field solutions for conducting bodies of revolution", *AEU*, pp. 159-164, 1978.
- [5] A.Q. Martin and C.M. Butler, "Corroboration of the analysis of an axially directed antenna exciting a conducting tube", *Journal of Electromagnetic Waves and Applications* vol. 11, pp. 821-852, 1997.
- [6] A. Q. Martin, "An analytical and experimental investigation of an axially-directed antenna in the presence of an infinite conducting cylindrical tube," Ph.D. Dissertation, Clemson University 1989.

## PERSONNEL SUPPORTED, PUBLICATIONS, INTERACTIONS

### Personnel Supported

Professor Chalmers M. Butler, the P.I., and Professor Anthony Q. Martin, the Co-P.I. are the faculty supported on this grant. Two Ph.D. students, Alp Kustepeli and Cengiz Ozziam are also supported on this grant.

### Publications

None.

### Interactions

A. Kustepeli, A. Q. Martin, and C. M. Butler, "Fields and Currents Excited by a Dipole Directed Normal to the Surface of a Conducting Screen Containing a Finite-length Narrow Slot," *1996 IEEE International Symposium and URSI Radio Science Meeting*, URSI Digest, p. 195, Baltimore Maryland, July 1996.

*Technical Exchange Meeting.* During May, 1997, Dr. Michael G. Harrison of Phillips Laboratory, Kirtland AFB, visited the investigators at Clemson University to discuss project progress and findings. Dr. Harrison visited again in August, 1997, this time accompanied by Dr. David Dietz of Phillips laboratory.

Alp Kustepeli and Anthony Q. Martin, "Fields and Currents due to a Modulated Laser Beam Exciting an Array of Narrow Slots," *1997 IEEE AP-S International Digest*, pp 1240-1243, July 1997.

C. Ozzaim and C. M. Butler, "EM fields and currents due to laser-light illumination of a conducting can", *URSI National Radio Science Meeting*, Boulder, Colorado, January 1998.

A. Kustepeli and A. Q. Martin, "Fields and currents due to a modulated laser beam exciting a narrow slot backed by a rectangular waveguide," *National Radio Science Meeting Digest*, p. 123, Boulder Colorado, 5-8 January 1998.

C. Ozzaim and C. M. Butler, "EM fields and currents due to laser-light illumination of a reflector antenna ", *USNC/URSI Radio Science Meeting*, June 1998, Atlanta, GA.

C. Ozzaim and C. M. Butler, "Coupling to a Probe in a Metal Can by an Electric Dipole", *APS Symp*, Orlando, FL , June 1999,.